Searching for Continuous Gravitational Waves from Isolated Pulsars

Amy Louise Hewitt

Physics

Department of Physics

Lancaster University

June 2025

A thesis submitted to Lancaster University for the degree of
Doctor of Philosophy in the Faculty of Science and Technology

Supervised by

Prof. Isobel Hook &

Dr. Matthew Pitkin

Abstract

The work presented in this thesis focuses on the prospect of detecting continuous gravitational waves (CWs) from pulsars. It first looks at a method of obtaining evidence of CWs without the use of gravitational wave (GW) data. The braking index, n, of a pulsar is a measure of its angular momentum loss and its value corresponds to various spin-down mechanisms. For a pulsar spinning down due to GW emission from the principal mass quadrupole mode alone, the braking index would equal exactly 5. Unfortunately, for millisecond pulsars, it can be hard to measure observationally due to the extremely small second time derivative of the rotation frequency, $\ddot{f}$. This thesis examines whether it could be possible to extract the distribution of n for a whole population of pulsars rather than measuring the values individually. Simulated data is used with an injected $n = 5$ signal for 47 millisecond pulsars and the distribution is extracted using hierarchical Bayesian inference methods. It is found that while detection is theoretically possible, observation times of over 20 years and RMS noise on the order of 10^{-5} ms are needed.

Next, a targeted search for CWs from 236 pulsars using combined data from the second and third observing runs of the LIGO and Virgo interferometric GW detectors are presented. Searches for emission from the $l = m = 2$ mass quadrupole mode with a frequency at only twice the pulsar rotation frequency (single-harmonic) and from the $l = 2, m = 1, 2$ modes frequencies of both once and twice the rotation frequency (dual-harmonic) are performed using a Bayesian analysis method. No evidence of GWs is found, so for the single-harmonic

search 95% credible upper limits on the strain amplitudes h_0 are presented along with limits on the pulsars' mass quadrupole moments Q_{22} and ellipticities ε. Of the pulsars studied, 23 have strain amplitudes that are lower than the limits calculated from their electromagnetically measured spin-down rates. These pulsars include the millisecond pulsars J0437−4715 and J0711−6830 which have spin-down ratios of 0.87 and 0.57 respectively. For nine pulsars, their spin-down limits have been surpassed for the first time. For the Crab and Vela pulsars the limits are factors of ~ 100 and ~ 20 times more constraining than their spin-down limits respectively. In the dual-harmonic search, new limits are placed on the strain amplitudes C_{21} and C_{22}.

Finally, a targeted search for CWs from 45 pulsars using the first part of the fourth LIGO–Virgo–KAGRA observing run is presented. Similarly to the previous analysis, searches are performed for the single- and dual-harmonic emission models for each pulsar using a Bayesian analysis method. No evidence is found for a CW signal and so 95% credible upper limits are set on the signal amplitudes, as well as ellipticities and mass quadrupoles where applicable. For the single-harmonic search, 29 pulsars have surpassed their spin-down limits. The lowest upper limit on the amplitude is 6.4×10^{-27} for the young energetic pulsar J0537−6910, while the lowest constraint on the ellipticity is 8.8×10^{-9} for the nearby millisecond pulsar J0437−4715.

I dedicate this thesis to loved ones who never got to see me finish it.

Acknowledgements

Declaration

This thesis is my own work and no portion of the work referred to in this thesis has been submitted in support of an application for another degree or qualification at this or any other institute of learning.

Chapter 1

This chapter presents useful background knowledge in the field of gravitational waves and pulsars. Therefore, it contains information from the literature with references where applicable.

Chapter 2

This chapter introduces a novel method of retrieving the braking index from a population of pulsars. It has been published in the Astrophysical Journal, Hewitt et al. (2025). The script used for this was created by me and incorporates `Tempo2` (Edwards et al., 2006; Hobbs et al., 2006a, 2009) to generate fake pulsar arrival times based on the data from the NANOGrav 12.5-year dataset (Alam et al., 2020, 2021). This data is then modelled using `enterprise` (Ellis et al., 2020) and modified versions of `enterprise_extensions` (Taylor et al., 2021) and `enterprise_warp` (Goncharov, 2021) which were created by Matthew Pitkin (Goncharov et al., 2024; Taylor et al., 2024). The `posteriorstacker` python package (Baronchelli et al., 2020; Buchner, 2021) was used to combine the posteriors from each pulsar.

Chapter 3

This chapter represents part of the paper published in the Astrophysical Journal, Abbott et al. (2022e). The full paper includes the results of two additional analysis pipelines performed on high value pulsars which were analysed and added to the paper by other members of the LIGO-Virgo-KAGRA Collaboration (LVK) collaboration. Therefore, those pipelines have been removed from this chapter, leaving only the Bayesian analysis which was done by me. It should be noted that I led the paper writing process, with input through reviews from others in the LVK. Due to collaboration policy, authorship is given to the entire collaboration and listed alphabetically on an opt-out basis. Therefore, although I am not the first author of this paper, this chapter represents my own work.

The GW strain data used in this chapter is from the LIGO and Virgo GW detectors which has already been through a cleaning process (Acernese et al., 2022; Davis et al., 2019; Viets and Wade, 2021). Pulsar timing solutions were derived by the following EM observatories: the Canadian Hydrogen Intensity Mapping Experiment (CHIME) (Amiri et al., 2021a), the Mount Pleasant Observatory 26 m telescope, the 42 ft telescope and Lovell telescope at Jodrell Bank, the MeerKAT project (Bailes et al., 2020), the Nançay Decimetric Radio Telescope, the Neutron Star Interior Composition Explorer (NICER) and the Molonglo Observatory Synthesis Telescope (as part of the UTMOST pulsar timing programme; Jankowski et al., 2019; Lower et al., 2020). `LALSuite` (LIGO Scientific Collaboration, 2018) is used to run the Bayesian analysis, specifically `lalapps_knope` (Pitkin et al., 2017) using existing methods as described in the chapter. The tables and figures used to present the results in this chapter are produced using a modified version of code created by Matthew Pitkin.

Chapter 4

This chapter represents part of a paper published in the Astrophysical Jounal, Abac et al. (2025). Similarly to Chapter 3, the full paper includes results from additional pipelines which were performed by other members of the collaboration and have been removed from this chapter in order to represent my own work only. Additionally, Luca D'Onofrio lead the paper writing process. The main body of the paper was written more collaboratively, with paragraphs from different people being merged during editing. Therefore, I have rewritten this chapter.

As in the previous chapter, this work uses cleaned GW strain data from the LIGO detectors with detector calibration performed prior to data collection. Pulsar timing solutions were provided by Chandra (Weisskopf et al., 2002), Fermi-LAT (Atwood et al., 2009), the Neutron Star Interior Composition Explorer (NICER) (Gendreau et al., 2012), the Nancay Radio Telescope (NRT) (Desvignes et al., 2016), the Jodrell Bank Observatory (JBO), the Argentine Institute of Radio astronomy (IAR) (Gancio et al., 2020), the Mount Pleasant Radio Observatory (Lewis et al., 2003), the Five-hundred-meter Aperture Spherical Telescope (FAST) (Smits et al., 2009), and the Canadian Hydrogen Intensity Mapping Experiment (CHIME) (Amiri et al., 2021b). The Bayesian analysis was performed using `CWInPy` (Pitkin, 2022). Figure 4.1, Figure 4.2, and Figure 4.3 were produced with a modified version of the code used in the previous chapter. The analysis comparing the results of this chapter to previous results was initially performed by Luca D'Onofrio and repeated in full by me.

Chapter 5

This chapter sums up the work covered in this thesis along with a discussion of future advancements in the field. Similar to the introduction, this comes from the literature with appropriate references.

"There's always something to look at if you open your eyes!"

– Doctor Who

Contents

4 Search for Continuous Gravitational Waves from Known Pulsars in the Early Part of the Fourth LIGO-Virgo-KAGRA Observing Run

List of Figures

Chapter 1

Introduction

The current state of the field of gravitational wave (GW) astronomy is an exciting one. Since the first GW detection in 2015, each search has resulted in more detections, allowing us to hear for the first time the hidden mergers of the most massive objects in the universe. This unique observation window enables detections of events not possible from electromagnetic (EM) observations alone, and when coupled with EM detections in a multimessenger event, provides confirmation on the sources of both. And, with new evidence pointing towards the observation of a GW background, new types of GW observations are being realised. Neutron stars (NSs) are significant in both astrophysics and the wider physics field. Hidden beneath their crusts are potential answers to questions about the fundamental properties of matter under pressure. By studying continuous GWs (CWs) from pulsars, we may gain insights into the equation of state of neutron star matter, the dynamics of their interiors, and the mechanisms behind their spin-down rates.

This chapter will provide an introduction to GW astronomy before giving a more specific background into the search for CWs from pulsars. Additionally, it introduces neutron stars and our current understanding of them and how observations of CWs can help to uncover some of their many mysteries.

1.1 Gravitational Waves

Newton published his laws of motion and universal gravitation in Newton (1687), fundamentally changing our understanding of how objects interact. He identified that objects with mass attract every other object with a force directly proportional to their mass and inversely proportional to the square of their distance. He called this force gravity. These laws explained the motion of the planets in the solar system and of objects on Earth with a single coherent theory. In his theory of universal gravitation, he assumed that gravity acted instantaneously regardless of distance.

Centuries later, Einstein's theory of special relativity (SR) was published (Einstein, 1905). It relies on two core principles: a) The speed of light in a vacuum is constant regardless of the motion of the observer or the emitting body and b) the laws of physics are identical for all inertial (non-accelerating) frames of reference. From these principles, time dilation and length contraction emerge, rendering the concepts of absolute space or absolute time meaningless. To replace them, SR introduces the spacetime interval ds, the spatial and temporal difference between events in four-dimensional spacetime:

$$ds^2 = -c^2 dt^2 + dx^2 + dy^2 + dz^2 \tag{1.1}$$

where c is the speed of light; x, y, and z are the spatial coordinates; and t is the temporal coordinate. However, as SR limits the speed of information transmission to the speed of light, Newton's previous assumption that gravity acted instantaneously was no longer consistent. Gravitational information should travel at the speed of light and the information must be propagated somehow.

Ten years later, Einstein expanded on SR to include accelerating observers in his General Theory of Relativity (or general relativity, GR) (Einstein, 1915). This introduced the equivalence theory which states that gravity is equivalent to acceleration, allowing for the concept of gravity as a curvature of spacetime. A straight line across curved spacetime will itself appear curved. These straight lines through spacetime are called geodesics, and an object not being acted on by any external force will always follow a geodesic. In a non-uniform gravitational

field, the curvature of spacetime will cause two geodesics to diverge, the extent of which defines the curvature of spacetime in that area. This curvature of spacetime provides a solution to the question of how gravitational information propagates. As matter and energy move through spacetime, spacetime is warped, causing waves to ripple out at the speed of light. These are gravitational waves.

1.2 Gravitational Waves from General Relativity

The Einstein field equation describes how mass and energy curve spacetime using the Einstein tensor $G^{\mu\nu}$,

$$G^{\mu\nu} = R^{\mu\nu} - \frac{1}{2}g^{\mu\nu}R = 8\pi T^{\mu\nu}. \tag{1.2}$$

Here, natural units are used, so the gravitational constant $G = c = 1$. The right-hand side represents matter via the stress-energy tensor $T^{\mu\nu}$ which describes the density and flow of energy and momentum in spacetime. The left-hand side describes the geometry of spacetime using the Ricci scalar R and Ricci tensor $R^{\mu\nu}$ along with the space-time metric $g^{\mu\nu}$. The metric $g^{\mu\nu}$ broadly represents the geometry of spacetime. The term $R^{\mu\nu}$ describes how the curvature changes due to mass and energy while R is derived from $R^{\mu\nu}$ and gives the degree of curvature.

To understand how a gravitational wave distorts spacetime around two test masses in the most simple case, the weak field approximation, we first begin with flat spacetime, represented by the Minkowski metric

$$\eta_{\mu\nu} = \begin{pmatrix} -1 & 0 & 0 & 0 \\ 0 & 1 & 0 & 0 \\ 0 & 0 & 1 & 0 \\ 0 & 0 & 0 & 1 \end{pmatrix}. \tag{1.3}$$

This is valid for regions of space distant from strong concentrations of matter or radiation. Using this metric, we can calculate the perturbation of spacetime $g_{\mu\nu}$

due to a small ($h_{\mu\nu} \ll 1$) perturbation caused by a gravitational wave:

$$g_{\mu\nu} = \eta_{\mu\nu} + h_{\mu\nu}. \tag{1.4}$$

Through Lorentz transforms, it can be shown that $h_{\mu\nu}$ transforms as a second-rank tensor, allowing for it to be treated separately from $\eta_{\mu\nu}$. It can be redefined as the trace reverse

$$\bar{h}^{\mu\nu} = h_{\mu\nu} - \frac{1}{2}\eta^{\mu\nu}h. \tag{1.5}$$

The assumption that $h_{\mu\nu} \ll 1$ allows the non-linear terms in equation (1.2) to be ignored, producing the linear field equation

$$\Box\bar{h}^{\mu\nu} = -16\pi T^{\mu\nu}, \tag{1.6}$$

where $\Box$ is the wave operator

$$\Box = \frac{\partial^2}{\partial t^2} - \nabla^2 = \frac{\partial^2}{\partial t^2} - \frac{\partial^2}{\partial x^2} - \frac{\partial^2}{\partial y^2} - \frac{\partial^2}{\partial z^2}. \tag{1.7}$$

In free space (a vacuum with no matter or energy), $T^{\mu\nu} = 0$, allowing the simplification of equation (1.6) to

$$\left(\frac{\partial^2}{\partial t^2} - \nabla^2\right)\bar{h}^{\mu\nu} = 0, \tag{1.8}$$

which is the three-dimensional wave equation describing GWs. For the simplest plane wave, the solution to equation (1.8) is

$$\bar{h}^{\mu\nu} = A^{\mu\nu}\exp(ik_\mu x^\mu), \tag{1.9}$$

where $A^{\mu\nu}$ is the amplitude of the wave and k_μ is the wavevector. This demonstrates that small perturbations in spacetime propagate as waves. The next step is to show the effect a passing GW has on objects by deriving the change in proper distance between two test masses, as shown in Schutz (2009).

We can write $h_{\mu\nu}$ as

$$h_{\mu\nu} = \begin{pmatrix} h_{tt} & h_{tx} & h_{ty} & h_{tz} \\ h_{xt} & h_{xx} & h_{xy} & h_{xz} \\ h_{yt} & h_{yx} & h_{yy} & h_{yz} \\ h_{zt} & h_{zx} & h_{zy} & h_{zz} \end{pmatrix}, \tag{1.10}$$

which has many degrees of freedom that are not physical for GW perturbations. In order to simplify it, a transverse-traceless (TT) gauge translation is performed. This leaves the physical content of the theory unchanged while allowing for considerable reduction in the degrees of freedom. There are two properties of the TT gauge. The first is that it is transverse, meaning the perturbations are transverse to the direction of propagation. Assuming the GW is travelling in the z-direction, this means perturbations occur only in the x- and y-directions. Therefore, the terms with a z-component can be set to 0. The TT gauge makes the perturbation purely spatial, and so the temporal components are also set to 0. The second property is that the TT gauge is traceless, meaning the trace $(h_{tt}+h_{xx}+h_{yy}+h_{zz})$ equals 0, so $h_{yy} = -h_{xx}$. After this translation, $h_{\mu\nu}^{TT}$ becomes

$$h_{\mu\nu}^{TT} = \begin{pmatrix} 0 & 0 & 0 & 0 \\ 0 & h_{xx} & h_{xy} & 0 \\ 0 & h_{xy} & -h_{xx} & 0 \\ 0 & 0 & 0 & 0 \end{pmatrix} \tag{1.11}$$

which demonstrates that there are only two independent constraints, A_{xx}^{TT} and A_{xy}^{TT}. Using equation (1.4), we can look specifically at g_{xx} which can be simplified using the fact that $\eta_{xx} = 1$ for flat spacetime as shown in equation (1.3) to get:

$$g_{xx} = \eta_{xx} + h_{xx}^{TT} = 1 + h_{xx}^{TT}. \tag{1.12}$$

To find the proper distance between the two test particles along the x-axis, we can integrate the square root of the spacetime interval

$$\delta l = \int \sqrt{ds^2}. \tag{1.13}$$

The spacetime interval in equation (1.1) represents flat spacetime. In curved spacetime, the interval can be written in terms of the metric tensor

$$ds^2 = g_{\mu\nu}dx^\mu dx^\nu. \tag{1.14}$$

Since the two particles are stationary ($dt = 0$) and only separated along the x-axis ($dy = dz = 0$), the spacetime interval in equation (1.14) becomes

$$ds^2 = g_{xx}dx^2 = (1 + h_{xx}^{TT})dx^2, \tag{1.15}$$

through the substitution of g_{xx} from equation (1.12). To obtain the proper distance δl, ds^2 is integrated following equation (1.13) and, given the perturbation is small ($h_{xx}^{TT} \ll 1$), a Taylor expansion can be used to approximate

$$\delta l = \int_0^\varepsilon \sqrt{1 + h_{xx}^{TT}}dx \approx \int_0^\varepsilon \left(1 + \frac{1}{2}h_{xx}^{TT}\right)dx, \tag{1.16}$$

where ε is the initial separation of the two particles. This is evaluated at $x = 0$, giving

$$\delta l \approx \left[1 + \frac{1}{2}h_{xx}^{TT}(x = 0)\right]\varepsilon. \tag{1.17}$$

This equation tells us that the change in separation of the two test particles due to a passing GW is proportional to their initial separation, a fact that is utilised in the designs of modern GW detectors as discussed in Section 1.3. It also gives an idea of the scale of the change in proper distance, as h_{xx}^{TT} is generally on the order of 10^{-21} or smaller (Schutz, 2009).

This approximation is valid for two test masses which are not acted upon by any other force. In this case, when observed from the inertial frame of reference of one of the particles, the effect of a passing GW is like that of a tidal force, stretching and contracting the proper distance between the particles. For particles that are not free, the amount their separation is stretched depends on the strength of the other force(s). In the case of two free test masses and a ruler measuring their separation, a passing GW would cause a separation of the two masses but

the ruler, due to the much stronger forces within it, would be barely stretched at all.

From the two independent terms h_{xx}^{TT} and h_{xy}^{TT} in equation (1.11), we can infer the two polarisations of GWs. The first is referred to as + (plus) polarisation, and arises when $h_{xx}^{TT} \neq 0$ and $h_{xy}^{TT} = 0$. In this case, as the wave oscillates as $h_{xx}^{TT} = -h_{yy}^{TT}$ changes sign, the particles will be moved in the x- and y-directions as shown in Figure 1.1. If, on the other hand, $h_{xx}^{TT} = 0$ and $h_{xy}^{TT} \neq 0$, then the GW has $\times$ (cross) polarisation, and will oscillate at $45°$ from the + polsarisation.

Finally, it is important to look at what causes the emission of GWs. To do so, equation (1.6) is solved for $T^{\mu\nu} \neq 0$

$$\left(\frac{\partial^2}{\partial t^2} - \nabla^2 \right) \bar{h}^{\mu\nu} = 16\pi T^{\mu\nu}, \tag{1.18}$$

along with the following assumptions: The time-dependent part of $T^{\mu\nu}$ is sinusoidal and the typical source velocity inside the GW source region is much slower than the speed of light. These assumptions are valid for all but the most extreme GW sources. The solution to this equation is

$$h_{jk} = -2\Omega^2 D_{jk} \frac{e^{i\Omega(r-t)}}{r}, \tag{1.19}$$

where Ω is the frequency of the sinusoidal fluctuation in $T^{\mu\nu}$, r is the radial coordinate in the spherical polar coordinate system, t is time, and D_{jk} comes from the mass quadrupole moment tensor, defined as (Schutz, 2009):

$$I^{lm} := \int T^{00} x^l x^m d^3 x = D^{lm} e^{-i\Omega t}. \tag{1.20}$$

Lower order mass moments like dipole and monopole moments do not produce GWs. A monopole mass moment is the mass itself and a changing mass would violate the conservation of energy. Equally, the dipole mass moment represents the momentum of the centre of mass and so changing it would violate the conservation of momentum. Therefore, GW emitters must have some mass quadrupole moment which represents a deviation from spherical symmetry.
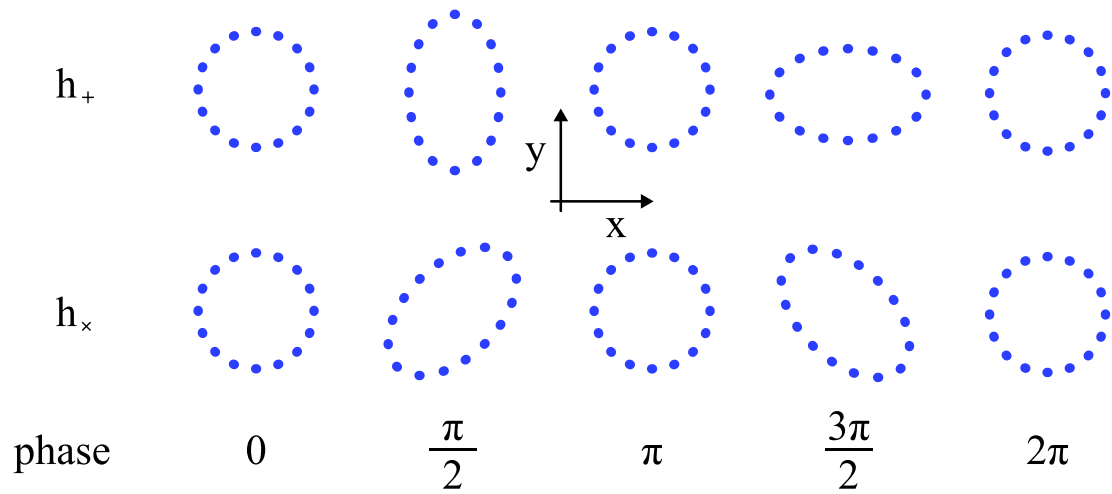
Figure 1.1 The effect of gravitational waves on a free ring of test particles for plus h_+ and cross $h_\times$ polarisations. (Credit: Zach Mason.)

1.3 Gravitational Wave Detector Design

The two behaviours of gravitational waves that have most influenced detector design are the change in spacetime interval between two test masses and the transverse nature of the wave. Current ground-based observatories are kilometre-scale laser interferometers. These utilise high-powered lasers to detect minute differences in the lengths of their two perpendicular arms by measuring interference patterns. A simplified description of a GW observatory is that of a laser, split in two by a beam splitter, where half travels down one arm and the other half travels down the other. The two beams are then reflected back and recombined. If the lengths of the two arms are perfectly equal, the two halves recombine constructively. If they are off by half a wavelength, they combine destructively, and no light is seen. Any variation between the travel times of the two beams results in some light making it into the photodetector. However, as the difference in length that must be detected in order to observe gravitational waves is on the order of $1{\times}10^{-19}$ m (smaller than the diameter of an electron) (Svitil et al., 2016), intense optimisation is required to reduce noise. Having numerous detectors also becomes important as it allows for noise in individual detectors to be ruled out as candidates.

1.3.1 Optimising the Detector

The first problem to be addressed is the length of the arms. As demonstrated in Section 1.2, the GW strain h is proportional to the initial length of the arms L

$$h \propto \frac{\Delta L}{L}. \tag{1.21}$$

Therefore, the longer the arms, the smaller the measurements that can be made. However, with extremely long arms come more practical limitations to overcome. The simplest solution is to introduce an additional mirror to each arm near the beam splitter, so that light can be reflected down each arm around 400 times, increasing the effective arm length from 4 km to about 1600 km in the case of LIGO (LIGO Caltech, 2016), seen in Figure 1.2. This allows for the laser light to
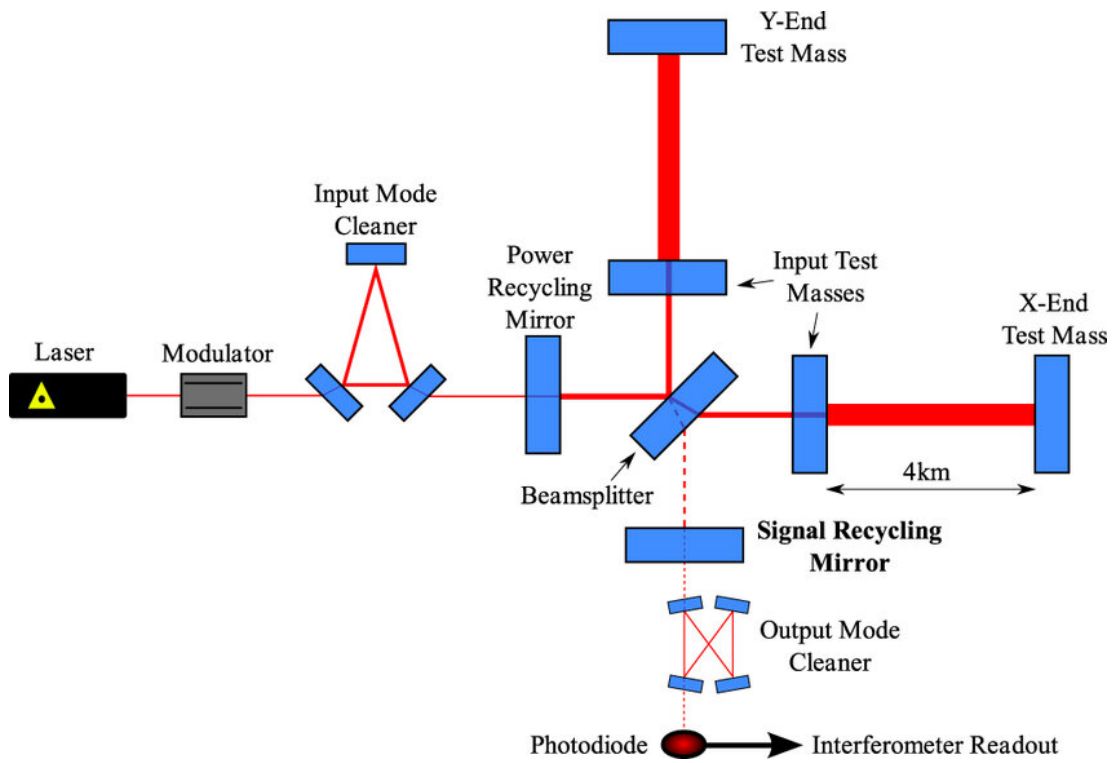
Figure 1.2 A simplified diagram showing the setup for Advanced LIGO detectors. Taken from Nuttall et al. (2015).

travel larger distances without the need to build longer arms. The space between mirrors also constitutes a Fabry-Perot cavity. Only light which is in resonance with such a cavity can pass through it. It is important to keep the Fabry-Perot cavities in resonance with the laser beam to avoid loss of power. This means ensuring the length of the arms L are related to the laser wavelength λ via

$$L = \frac{n\lambda}{2}, \tag{1.22}$$

where n is an integer. Such changes in arm length can occur from a variety of sources, such as seismic vibrations, thermodynamic mirror surface fluctuations, and fluctuations of the laser frequency itself. The length of the arms is controlled through the Pound-Drever-Hall (PDH) technique. This involves modulating the laser so that radio frequency (RF) sidebands with frequencies not in resonance with the cavity are produced and reflected down the arms. Through comparison of the phase difference between the input and reflected sidebands, deviations from resonance can be identified and corrected (Black, 2001).

The laser power is also a crucial factor to consider. Higher laser power results in more photons and sharper interference fringes measured by the photodetector due to a reduction in shot noise (the statistical uncertainty in the arrival times of photons at the detector) (Buikema et al., 2020). Due to the physical limitations of building lasers of the desired power, the power of the laser beam is increased using power recycling mirrors. These mirrors sit after the laser and before the beam is split into the two arms. Any light which has already been through the instrument will be reflected back into the interferometer by the power recycling mirror allowing it to be recycled. A similar method can be performed on the other end of the interferometer, before the photodetector. In this case, it is called signal recycling, as the signal is reflected back into the interferometer to improve the broadness of the frequency response (Aasi et al., 2015).

Due to their high sensitivities, current interferometers are limited by quantum noise, the fluctuation in the electromagnetic field due to the uncertainty in phase and amplitude required by the Heisenberg uncertainty principle. Shot noise is caused by phase vacuum fluctuations and is the dominant noise at high frequencies, while amplitude vacuum fluctuations are called quantum radiation pressure

noise and are dominant at low frequencies. While increasing the laser power improves the sensitivity at higher frequencies by reducing the shot noise, it also results in higher quantum radiation pressure noise which reduces sensitivity at lower frequencies. In order to overcome this, quantum squeezing can be used over certain frequency ranges. This is the use of the uncertainty principle to restrict the uncertainty in phase in exchange for larger uncertainty in amplitude and vice versa. Frequency dependent optical squeezing allows for different types of squeezing at different frequencies, meaning shot noise can be reduced by squeezing the phase at high frequencies and quantum radiation pressure noise can be reduced by squeezing amplitude at low frequencies (Ganapathy et al., 2023).

Additional sources of noise include seismic and thermal noise. Seismic noise sources can include nearby traffic, trains, earthquakes, and even weather patterns across the continent. In order to reduce the effect of such noise, the optical components of the interferometer are suspended as quadruple-pendulums. These suspensions are themselves mounted on larger isolation systems. In addition to the passive damping provided by the pendulum system, active vibration isolation is also employed to oppose unwanted vibrations through feedback loops, preventing the vibrations from reaching the passive suspension system in the first place (Matichard et al., 2015). Together, this system of isolated suspension allows the test masses to be considered as free-falling in the plane of the detector. As the interferometer is kept in a vacuum, thermal noise predominantly results from thermal fluctuations within the mirror coating and test mass itself. Constructing the mirrors out of materials with very high quality factors like fused silica maintains reflectivity and concentrates thermally induced vibrations in a narrow frequency range that can be designed to be outside the detector sensitivity range (Harry et al., 2002). Another simple way to reduce the effects of thermal noise is to increase the mass of the test masses as much as possible. In Advanced LIGO, each test mass is 40 kg.

1.3.2 Calibration Methods

With the interferometer optimised to detect GWs at the required sensitivities through the above enhancements, it is then important to ensure the instrument

is properly calibrated. One important calibration method uses a photon radiation pressure actuator. This involves using an additional laser reflected off the test masses. By varying the power of the laser, the recoil of the photons hitting the mirror can be varied, resulting in known movement of the mirror and consequent change in arm length. Models of actual GW signals can be constructed and passed into the detector through these precise movements of the mirrors. The models can then be compared to the actual interferometer response, allowing for calibration of the instrument and estimation of uncertainties (Abbott et al., 2017b). For the most recent LIGO observing run the strain calibration uncertainty was measured to be 10% in magnitude and 10° in phase (Capote et al., 2024).

Additionally, there can be slow changes in the detector response over time, which must also be accounted for. These can be caused by drifts in the alignment and thermal state of the optics in the interferometer. To track these changes over time, modulated excitations are injected into the interferometer arms. These cause peaks at the modulation frequency which will be affected by any slow temporal variation. Monitoring changes in the peaks allows for the identification and subsequent compensation of any temporal variations (Tuyenbayev et al., 2017).

1.3.3 LIGO and Current Gravitational Wave Detectors

The largest and most sensitive GW detectors to date are those of the Laser Interferometer Gravitational-Wave Observatory (LIGO). This consists of two detectors based in the USA: one in Hanford, Washington (H1) and one in Livingston, Louisiana (L1) (Aasi et al., 2015) operated by the Caltech and MIT LIGO Laboratory via a cooperative agreement with the NSF. They are separated by $\sim$ 3000 km, corresponding to a difference in GW arrival time of up to 10 milliseconds, which is useful for estimating the direction of the source. Additionally, as they are separated by a large distance and situated in different climates, they are subject to different noise while signals will be common in both detectors. Both observatories are Michelson interferometers with 4 km long arms.

Another crucial GW detector is Virgo, in Cascina, Pisa in Italy (Acernese et al., 2015). This is a single Michelson interferometer with 3 km arms which can

provide even more accurate source location estimations when combined with the LIGO detectors. It is operated by the European Gravitational Observatory and funded by INFN (Italy), CNRS (France) and Nikhef (Netherlands).

A second detector with 3 km arms is the Kamioka Gravitational Wave Detector (KAGRA) in Hida, Japan (Akutsu et al., 2021). In contrast to LIGO and Virgo which are all overground interferometers, KAGRA is underground. It is operated by ICRR, KEK and NAOJ and funded by MEXT (Japan). It was formerly known as the Large Scale Cryogenic Gravitational Wave Telescope (LCGT) due to its use of cryogenic mirrors.

Other notable detectors include GEO600, a 600 m interferometer in Hanover, Germany operated by German and British LSC institutions and funded by MPG (Germany) and STFC (UK) (Lueck, 2010). It is often used to test new technologies and collect data while other, larger, detectors are offline for upgrades and maintenance. Another two test detectors are in Japan: TAMA 300, a 300 m detector in Tokyo (Kozai and TAMA-300 Team, 1999) and the Cryogenic Laser Interferometer Observatory (CLIO), a 100 m detector in Hida (Yamamoto et al., 2008).

The LIGO Scientific Collaboration (LSC) and Virgo collaboration have been carrying out joint analyses when joint data is available since 2010. In 2021, KAGRA joined to form the LIGO-Virgo-KAGRA Collaboration (LVK). The current era is the advanced (2nd-generation) detector era, of which there have been four observing runs so far, as seen in Figure 1.3. The first observing run (O1) took place between September 2015 and January 2016 and was purely LIGO. O2 took place between November 2016 and August 2017 in which Virgo joined for the final month (Abbott et al., 2019c). O3 took place between April 2019 and March 2020 and contained both LIGO and Virgo (The LIGO Scientific Collaboration et al., 2021) (see Chapter 3 for more details). O4 has been split into multiple sections, the first (O4a) running from May 2024 to January 2024 as discussed in Chapter 4. Virgo joined in April 2024 and KAGRA aims to rejoin before the end of O4 (LVK, 2025). For upcoming and planned detectors, see Chapter 5.
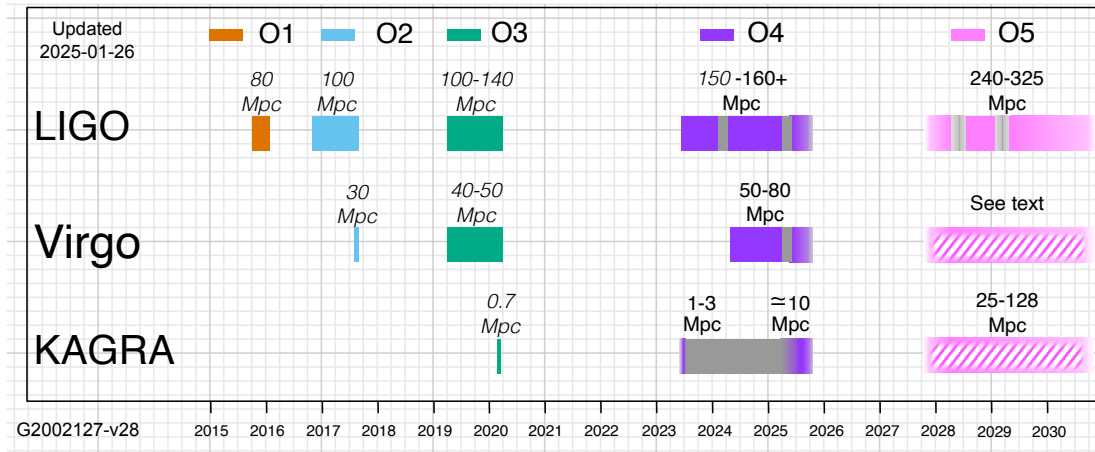
Figure 1.3 The LVK observing runs during the advanced detector era along with the detector activity throughout. Grey represents down-times for min-run maintainance, while the hashed sections represent unconfirmed activity. O5 is the best guess and is subject to change. Virgo is currently reassessing its plans for O5. The value in Mpc represents the estimated range to which the detectors would detect a binary neutron star merger. Taken from: LVK (2025).

1.4 Gravitational Wave Searches

On the 12th September 2015, the newly upgraded Advanced LIGO observatories, LIGO Hanford and LIGO Washington, began their first observing period, set to run until 19th January 2016. Two days later, on the 14th September 2015, the first GW was detected, named GW150914. An alert was sounded within three minutes and was independently confirmed by a second online burst search a few hours later (Abbott et al., 2016b,c,d). It was a transient signal, produced by the merger of two black holes around 400 Mpc away. The two detectors both picked up the event within the 10 ms intersite propagation time with a combined signal-to-noise ratio (SNR) of 24. The event itself lasted less than 0.2 seconds. The frequency-time signal from both detectors can be seen in Figure 1.4, taken from Abbott et al. (2016a). The observation of GW150914 would win Rainer Weiss, Barry C. Barish, and Kip S. Thorne the 2017 Nobel Prize in Physics, demonstrating the realisation of a vision of almost fifty years and kickstarting a new era of gravitational wave astronomy.

Only two years later, the first multimessenger event to be observed in both GW and EM was observed. The GW event GW170817 was observed on the 17th August 2017 at 12:41:04 UTC, the first observation consistent with a binary neutron star merger (Abbott et al., 2017c). Only 1.74 seconds later, the gamma ray burst (GRB) GRB 170817A was observed independently by both the Fermi Gamma-ray Burst Monitor (Fermi-GBM, Goldstein et al., 2017) and the Anti-Coincidence Shield for the Spectrometer for the INTErnational Gamma-Ray Astrophysics Laboratory (INTEGRAL, Savchenko et al., 2017). This temporal offset between the GW and photon arrival times had major implications on fundamental physics: from constraining the difference between the speed of gravity and the speed of light, to placing new limits on the violation of Lorentz invariance, to constraining the Shapiro delay between gravitational and electromagnetic radiation. The multimessenger observation also confirmed that neutron star mergers are the progenitors of short gamma-ray bursts (Abbott et al., 2017c). Currently, this is still the only multimessenger observation involving GWs.
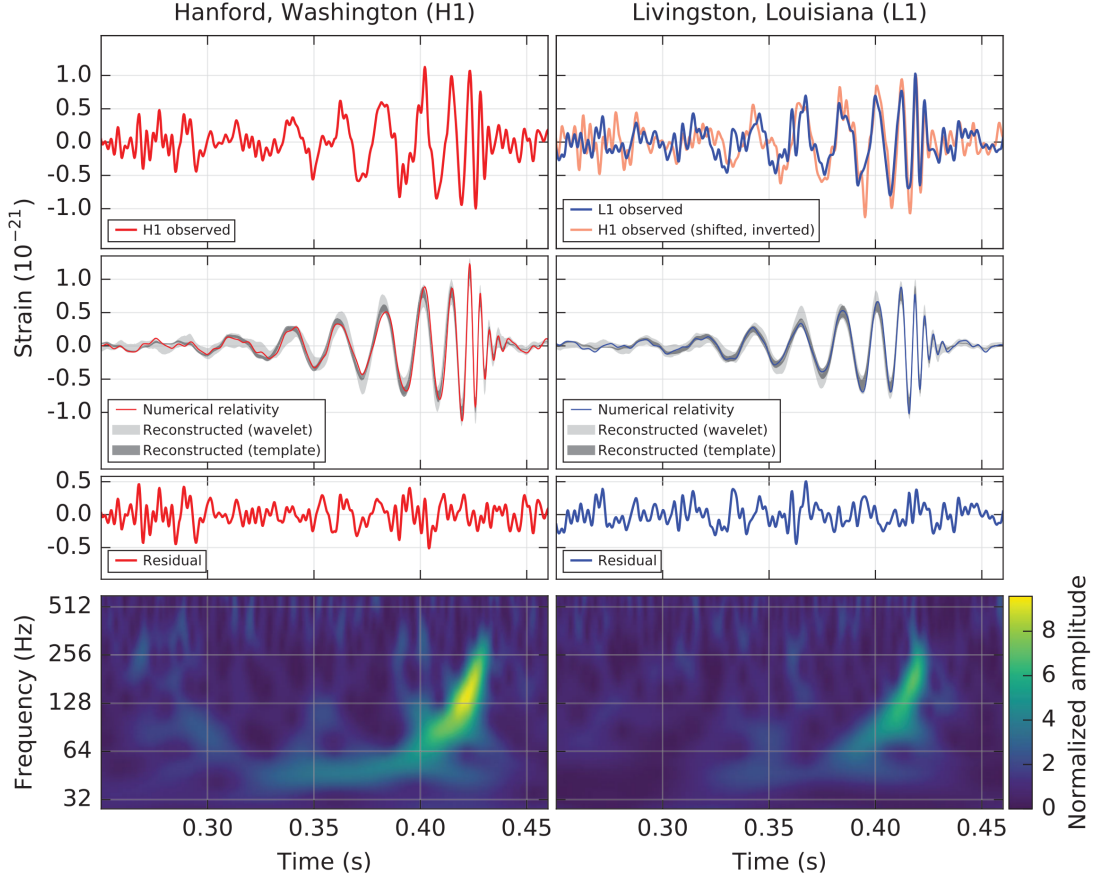
Figure 1.4 The GW event GW150914 observed by the LIGO Hanford (H1, left column panels) and Livingston (L1, right column panels) detectors. Top: the observed strain, with the L1 signal being flipped and shifted before being overlaid with the H1 signal for comparison. Upper middle: the numerical relativity result for a system with parameters consistent with those calculated for GW150914. The two shaded areas are the 90% credible regions for two independent waveform reconstructions. Dark grey shows the model of the signal using binary black hole template waveforms while the light grey model calculates the signal as a linear combination of sine-Gaussian wavelets. Lower middle: the residuals after the numerical relativity waveform is subtracted. Bottom: the time-frequency representation of the strain data. Taken from: Abbott et al. (2016a).

1.4.1 Transient Gravitational Waves

Both of these detections, and all detections from LIGO to date, are transient signals. These are GW emissions from massive events which are only detectable for brief periods of time (on the order of 0.1 - 100 s). In the years following GW150914, hundreds of these GW signals have been detected by the LVK collaboration (Abbott et al., 2023), all of which have been produced by inspiral and subsequent mergers of compact objects. Transient GWs from compact binary coalescences (CBCs) are characterised by increasing frequency and amplitude as the two objects spiral into each other. At the moment of merger, the frequency and amplitude peak, followed by a subsequent ring down, as seen in Figure 1.4. When shifted into an audible frequency, these GWs sound like a chirping sound, hence their nickname 'chirps'.

The compact objects involved in transient GW events have involved either neutron stars or black holes. They have been observed in all configurations, including neutron star-neutron star, neutron star-black hole and black hole-black hole mergers. The graphic in Figure 1.5 shows all announced GW detections up until the end of O3. Also included are the masses of neutron stars and black holes which have been observed through EM observations. They provide a sense of scale for the types of objects being detected through GWs.

As can be seen from Figure 1.5, the majority of compact objects being detected are black holes, with many of them being more massive than those observed through EM observations. A number of neutron stars have been detected as both primary and secondary objects (Abbott et al., 2021b,d). Some compact objects have been detected in the observed mass gap between the most massive neutron stars and the least massive black holes to have been observed in the galaxy. This gap may be due to observational bias or due to fundamental physical constraints on the formation of compact objects of this mass range. New observations of mass gap objects can provide clues towards the formation and evolution of compact objects as they challenge current models. These mass gap objects have been involved in the transient events as both the remnants and as the secondary objects (Abbott et al., 2017e, 2020a,c). Recently, the merger of a neutron star and an intermediate mass object has been detected. This is most likely to be a low

Masses in the Stellar Graveyard

LIGO-Virgo-KAGRA Black Holes   *LIGO-Virgo-KAGRA Neutron Stars*   *EM Black Holes*   *EM Neutron Stars*

LIGO-Virgo-KAGRA | Aaron Geller | Northwestern
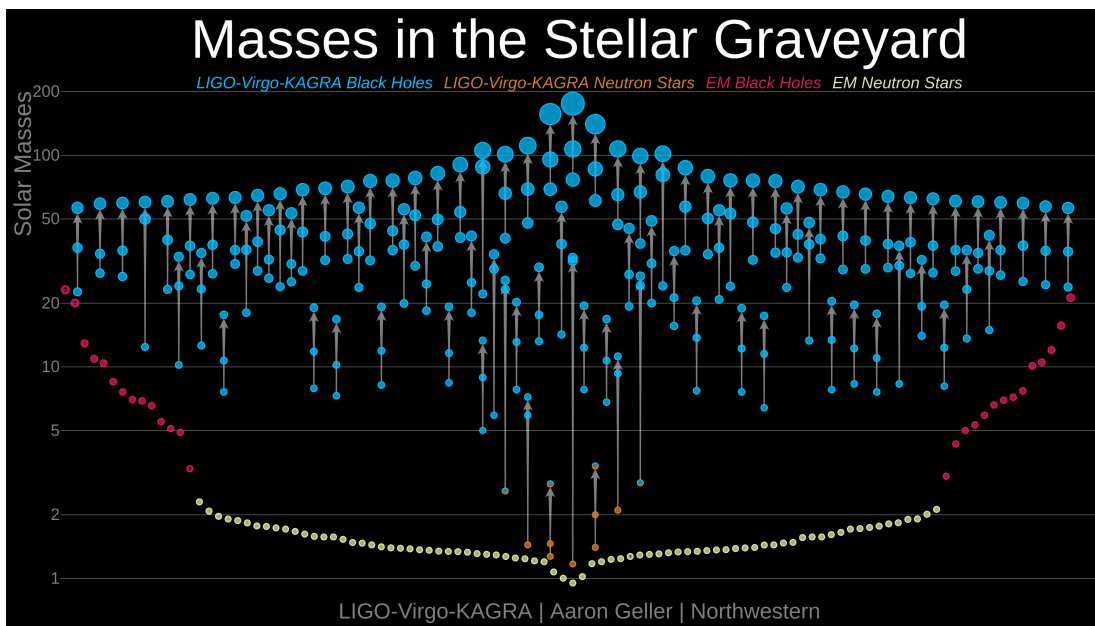
Figure 1.5 The masses of announced GW detections up to and including O3 that have a probability of astrophysical origin greater than 0.5. For each event, the primary and secondary objects are represented with arrows indicating the remnant. The x-axis is meaningless and events have been placed in an aesthetically pleasing way. The y-axis shows objects' masses. Also included are neutron stars and black holes which have been observed via EM observation. Credit: LIGO-Virgo / Aaron Geller / Northwestern University.

mass black hole due to the stricter upper limit on neutron stars. Furthermore, neutron stars have a non-zero tidal deformability compared to zero for black holes. Analysis of the mass gap object found its tidal deformability to be consistent with a black hole (The LIGO Scientific Collaboration et al., 2024). Observations of these rare mass gap objects provide valuable insights into the population of compact objects and provide updated estimates for merger rates and populations.

1.4.1.1 Searches for Transient Gravitational Waves

Transient events cannot be predicted and, in order to increase the likelihood of a multimessenger observation through simultaneous EM observations, real-time alerts are desired. Therefore, transient searches are performed in two modes: online and offline. The online searches are performed with low-latency and provide public alerts within minutes of a possible detection. The offline search is then performed in the following days using updated data quality and calibration to improve the detection confidence and develop an astrophysical interpretation.

There are two methods of extracting a GW signal from data. The first method uses a database of CBCs and compares the data to the templates to identify matches. These templates cover the parameter space defined by the two component masses of the compact binary and their dimensionless spins. It covers systems with total masses ranging from 2 $M_\odot$ to 758 $M_\odot$ and spins ranging from 0 (non-spinning) to 1 (the Kerr limit (Reynolds, 2021) at which a singularity would have no event horizon, which is forbidden). The second method does not assume any waveform template and instead searches coherently for transient signals across multiple detectors. Both methods can be used to rapidly identify signals in the online search and be used to reconstruct signals and estimate their significance during offline searches (The LIGO Scientific Collaboration et al., 2021).

1.4.2 Stochastic Gravitational Waves

While transient GWs have become commonplace, they are no longer the only type of GW with compelling observational evidence. Searches for a stochastic

GW background have been performed using ground-based GW detectors, however these have not resulted in any detection (Abbott et al., 2021f). Instead, success has been seen through pulsar timing arrays (PTAs). Recently the independent collaborations of the North American Nanohertz Observatory for Gravitational Waves (NANOGrav) (Agazie et al., 2023), a joint European-Indian effort (EPTA/InPTA) (EPTA Collaboration and InPTA Collaboration et al., 2023), the Chinese PTA (Xu et al., 2023), and the Parkes PTA in Australia (Reardon et al., 2023) all reported evidence of the stochastic GW background (GWB). A large contributor to the potential GWB observed through PTAs are supermassive black hole binaries (SMBHBs) which occur after mergers of galaxies in hierarchical structure formation when the two SMBHs eventually fall into each other and form a binary. These binary systems will emit GWs similarly to the compact binaries discussed in Section 1.4.1 (McWilliams et al., 2014). Potential sources of the GWB that could be detected using interferometric detectors would produce GWs at higher frequencies and may have origins such as cosmic strings or phase transitions in the early universe (Christensen, 2019), allowing us to observe events that occurred even earlier than what is possible through observations of the cosmic microwave background radiation (CMBR), which is restricted to the time of last scattering (Domènech, 2021).

1.4.2.1 Pulsars as Gravitational Wave Detectors

PTAs depend on the precision of pulsars as natural clocks. Their spin period and its derivative remain stable and predictable, barring any glitches (refer to Section 1.6.4) and timing noise (refer to Section 1.6.3). However, one source of timing noise are GWs themselves. As pulsar signals traverse space on their way to Earth, they can be distorted by GWs passing through the same region of spacetime. This distortion is correlated among signals from different pulsars, based on the GW's form and direction. However, in the case of the GWB, the signal could not be detected as a distinctive phase-coherent signal like an individual GW as, while the Earth term of the observed signal would be coherent due to signals arriving at the same time, the individual GW signals from the SMBHBs sources would be incoherent. Instead, the GWB is observed across multiple pulsars as excess

low-frequency residual power with consistent amplitude and spectral shape (Pol et al., 2021; Romano et al., 2021).

To verify the signal, the consistent amplitude and spectral shape is not enough, as this could be caused by other effects such as intrinsic pulsar processes of a similar amplitude (Goncharov et al., 2022) or common systematic noise like clock errors (Tiburzi et al., 2016). Hellings and Downs (1983) derived that, for an isotropic GWB, the correlation between the timing delays of any two pulsars is a universal, quasi-quadrupolar function of their angular separation in the sky. This behaviour is used to confirm the GWB signal in Agazie et al. (2023).

1.4.3 Continuous Gravitational Waves

The form of GW focused on in this thesis is the continuous gravitational wave (CW). These are characterised by a steady frequency and amplitude in the observable frequency range of detectors for an extended period of time. They are generally emitted by long-lived periodic motion. In particular, a promising source of CWs are neutron stars (NSs, see Sections 1.5 to 1.7 for more information). As discussed in Section 1.2, a changing mass quadrupole will result in the emission of GWs. This is characterised by some changing deviation from spherical symmetry about the centre of mass, typically as a result of rotation or the orbit of a binary system (Mirasola et al., 2024). In the case of an isolated NS, this asymmetry could manifest in a variety of ways. One is that of solid deformations, such as mountains on the crust. These can be produced during cooling (Ushomirsky et al., 2000), form as a result of binary accretion (Gittins and Andersson, 2021b), or due to strong magnetic fields (Bonazzola and Gourgoulhon, 1996; Cutler, 2002). These 'mountains' are only millimetres tall for a typical NS with a radius of 10 km (Gittins, 2024), as the crust will crack under anything taller[1]. A common way of quantifying the solid deformation of a NS is through its ellipticity.

Another mechanism behind potential CWs from neutron stars is through oscillation modes. In particular, r-modes are unstable to GW emission and are therefore considered the most likely oscillation for observable CW emission (Andersson, 1998; Friedman and Morsink, 1998). These modes are analogous to

---

[1]The maximum height depends on the equation of state, see Section 1.7

Rossby waves on Earth which are caused by the Coriolis force (an inertial force which acts on objects in motion from a rotating frame of reference) and pressure gradients. On neutron stars, r-modes are fluid modes for which the restorative force is the Coriolis force. These oscillations are able to reach amplitudes such that the emitted CWs are potentially observable (Haskell, 2015).

An advantage of CWs rather than transient GWs is that observations can be stacked up over time to increase the signal-to-noise ratio. The signal will also be present in historical data, allowing for verification without needing to compare results from multiple detectors. However, no evidence of CWs has been detected to date. There are three main types of searches for CWs:

1.4.3.1 All-sky Searches

All-sky searches look for CW signals from EM-silent sources in all sky directions over a broad range of frequencies and rotational parameters (e.g., Abbott et al., 2018, 2019a, 2021a, 2022c; Dergachev and Papa, 2020; Steltner et al., 2021, 2023). This large parameter space is computationally expensive and less sensitive than other searches due to a higher trials factor. The trials factor is a quantification of the 'look-elsewhere effect' which is a statistical phenomenon where apparently significant results can be caused simply by large parameter spaces or repeat measurements.

All-sky searches are not limited to signals from deformed neutron stars. In addition to expected alternative sources like compact binaries in stable orbits (Singh et al., 2019) and scalar boson clouds surrounding spinning black holes (Abbott et al., 2022d), it therefore allows for the discovery of unknown or unexpected sources. All-sky searches use multiple semi-coherent analysis methods with hierarchical follow-up. This involves breaking the data into smaller sections and regions of parameter space and running jobs in parallel in order to improve computation time. The Einstein@Home project (Einstein@Home, 2005) uses the idle time of volunteers' computers to perform these searches, proving greater computational power and allowing for more sensitive searches, such as the coherent search of the whole dataset used in the final hierarchical analysis step in Steltner et al. (2023).

1.4.3.2 Directed Searches

Directed searches look for signals from small sky locations with high probabilities of containing neutron stars, such as supernova remnants and the galactic centre (e.g., Abbott et al., 2021e, 2022b,f; Lindblom and Owen, 2020; Liu and Zou, 2022; Papa et al., 2020; Piccinni et al., 2020). They usually focus on a single area of interest rather than whole populations and are therefore less computationally expensive and more sensitive than all-sky searches. Like all-sky searches, directed searches are generally semi-coherent, with data divided into segments which are processed and then incoherently combined without taking the signal phase into account. They also usually use a hierarchical approach to perform follow-up analyses on potential signals. As they search a large parameter space within a specific sky region, directed searches can also be valid for CWs from binary systems and boson clouds (Abbott et al., 2022f).

1.4.3.3 Targeted Searches

Targeted searches look for signals from pulsars whose timing solutions can be calculated from known rotation phases and spin-down rates using fully-coherent methods (e.g., Abac et al., 2025; Abbott et al., 2017a, 2019b, 2020b, 2021c, 2022e; Ashok et al., 2021; Nieder et al., 2019, 2020). By assuming that the GW phase evolution follows the EM solution, the parameter space can be reduced to the unknown signal amplitude and orientation. This allows for less computational cost and higher sensitivities but relies on the assumed source parameters. A subset of targeted searches aims to account for small deviations from the observed values by relaxing the assumption that the GW evolution follows the EM. In this case, the search is performed in a narrow band around the frequency and spin-down rate. These are referred to as narrowband searches (e.g., Abbott et al., 2017d, 2019d, 2022a). However, because this decreases the sensitivity and increases the computational cost, these are often performed on fewer, specific targets.

As discussed in Section 3.1.2, an isolated triaxial pulsar emitting CWs through rotation will emit GWs at twice their rotation frequency $f_{\rm rot}$. Therefore, targeted searches look for signals at the $2f_{\rm rot}$ harmonic in 'single-harmonic' analyses. Additionally, GW emission at $f_{\rm rot}$ is possible due to certain mechanisms, in which

case emission would be seen at both f_{rot} and $2f_{\text{rot}}$ (Jones, 2010). Searches at both harmonics are referred to as 'dual-harmonic' searches.

The analyses in Chapters 3 and 4 are regular (not narrowband) targeted searches using a time-domain Bayesian method. Bayesian analysis is introduced in Section 1.4.3.4 and the targeted Bayesian search method is described in Abbott et al. (2019b) and repeated in Chapter 3. There are additional analysis pipelines which run alongside the Bayesian analysis which are not discussed in the later chapters but are included in the corresponding papers Abbott et al. (2022e) and Abac et al. (2025) along with a narrowband search. In both cases, the additional pipelines provide increased robustness and an opportunity for cross-validation of potential signals. They will be briefly described here.

The 5-vector method is a frequentist approach derived in (Astone et al., 2010). This means the significance of a candidate signal is characterised by the p-value: the probability of obtaining a larger statistical value from noise only. This is achieved using off-source frequencies as background noise. The 5-vector method involves splitting the frequency of the expected CW using the Earth sidereal motion (movement with respect to the stars) into a central peak and four side-bands at $\pm 1f_{\oplus}$ and $\pm 2f_{\oplus}$ where $f_{\oplus}$ is the Earth's sidereal frequency. Then, matched filters for the $+$ and $\times$ GW harmonics are applied to obtain a detection statistic for which the p-value is calculated. The 5-vector method cannot easily be applied to the dual-harmonic emission model, which is more complicated than the single-harmonic model. Instead, a search at only f_{rot} is performed in the dual-harmonic search. This is consistent with a pulsar with a biaxial moment of inertia and an angle between its symmetry and rotation axes (Jones, 2010). The 5-vector method is also used in narrowband searches (Astone et al., 2014).

The $\mathcal{F}/\mathcal{G}/\mathcal{D}$-statistic method uses the heterodyned data used in the Bayesian method (see Section 3.2 for details on the heterodyne steps in the Bayesian method) to obtain the $\mathcal{F}$-statistic derived in Jaranowski et al. (1998), the $\mathcal{G}$-statistic derived in Jaranowski and Królak (2010), and the $\mathcal{D}$-statistic derived in Verma (2021). Which statistic is used depends on the known parameters of the search. When amplitude, phase, and polarisation are unknown, as in most cases, the $\mathcal{F}$-statistic is used. When polarisation is known but amplitude and phase are unknown (as in searches with restricted priors described in Section 3.2.2), the

$\mathcal{G}$-statistic is used. The $\mathcal{D}$-statistic is used to search for dipole radiation from Brans-Dicke theory, a competitor to GR with a varying gravitational constant G, which would produce an additional scalar polarisation of the GW. The statistics are calculated for each detector separately and then combined incoherently by adding the respective statistics. A signal is considered to be detected if any of these statistics surpass a threshold for acceptable false alarm rate (FAR), which is generally a probability of 1%. All methods described in this section can set upper limits on the GW signal amplitude in the absence of a signal. A comparison of the 5-vector and $\mathcal{F}$-statistic methods can be found in D'Onofrio et al. (2024) and a review of targeted, directed, and all-sky methods and previous searches can be found in Tenorio et al. (2021).

1.4.3.4 Bayesian Statistics

Bayesian statistics provides a robust method for calculating the probability of a hypothesis given some prior belief and observed data, and is used throughout this thesis. Fundamentally, it computes the posterior probability using Bayes' theorem:

$$p(\theta|d, H) = \frac{p(d|\theta, H)}{p(d|H)} p(\theta|H),$$ (1.23)

where $p(\theta|d, H)$ is the posterior probability distribution on the parameters θ that define hypothesis H, given the observed data d, $p(d|\theta, H)$ is the likelihood function of the data, $p(\theta|H)$ is the prior probability distribution for the model parameter given hypothesis H, and $p(d|H)$ is the evidence for the data given the model hypothesis.

The model evidence $P(d|H)$ is given by:

$$P(d|H) = \int P(d|\theta, H) \cdot P(\theta|H) \, d\theta,$$ (1.24)

where θ represents the parameters of the model. For models with multiple parameters, this can be difficult to solve analytically, and therefore is often estimated numerically via methods like nested sampling algorithms, which explore the parameter space to estimate the evidence and posterior distribution.

When comparing two hypotheses, H_1 and H_2, the odds ratio $\mathcal{O}_{12}$ can be computed as

$$\mathcal{O}_{12} = \frac{P(d|H_1)}{P(d|H_2)} \cdot \frac{P(H_1)}{P(H_2)}, \qquad (1.25)$$

which describes how much more likely the data are under one hypothesis than the other, adjusted for prior beliefs. When the two models have equal prior probabilities, $P(H_1)/P(H_2) = 1$, and the odds ratio reduces to the ratio of the model evidences $P(d|H_1)/P(d|H_2)$, also known as the Bayes factor (Pitkin et al., 2015). This odds ratio allows for comparisons between different models, such as those used in Section 2.2.2 to compare models with different pulsar braking indices, and Chapters 3 and 4 to calculate the ratio of a coherent GW signal versus incoherent noise.

1.5 Neutron Stars

Neutron stars (NSs) are small, dense stellar remnants formed when stars with initial masses of over 9 $M_\odot$ can no longer support themselves via nuclear fusion and collapse via a core-collapse supernova (Heger et al., 2003). If the mass of the remnant is not sufficient to overcome the Chandrasekhar limit, it can support itself via electron degeneracy pressure, a quantum mechanical effect where fermions (in this case electrons) cannot occupy the same quantum state as one another (Shapiro and Teukolsky, 1983) and results in a white dwarf star. However if the mass is sufficient, high temperatures and pressures allow for electrons to combine with protons to form neutrons through electron capture (Chandrasekhar, 1931). This leaves a remnant made of neutrons, hence the term 'neutron' star. At this point, the collapse is halted by neutron degeneracy pressure which relies on the same fermionic behaviour as electron degeneracy pressure (Bombaci, 1996). However, if the core still has sufficient mass, it can overcome this pressure and collapse indefinitely, resulting in a black hole. These mass requirements during formation enforce a range of masses of the NSs themselves. Any less than ~ 1.44 $M_\odot$ and they would have become a white dwarf. Any more than ~ 3 $M_\odot$ and they would overcome neutron degeneracy pressure and become a black hole (Kalogera and Baym, 1996).

There are various conditions under which a NS is created. For less massive stars (those under 10 $M_\odot$) they must be created through O/Ne/Mg core collapse rather than the iron core collapse which can create neutron stars from progenitors with higher initial mass. At the other end of the mass spectrum, stars which are very high in metallicity can lose their hydrogen envelope during supernova explosions, leading to enough mass loss to result in neutron stars rather than black holes even when the initial mass is over 25 $M_\odot$ (Heger et al., 2003).

These massive objects are compacted into a radius on the order of tens of kilometres. This, coupled with the fact that they are at stellar distances from Earth, make it difficult to resolve the NS itself via EM observations. Although neutron stars were theorised by Walter Baade and Fritz Zwicky as early as 1934 (Baade and Zwicky, 1934), they were not discovered until Jocelyn Bell and Antony Hewish identified a uniquely periodic radio 'pulse' (that they jokingly suggested might be due to 'little green men') in 1968 which became the discovery of the first 'pulsar' (Hewish et al., 1968).

1.6 Observing Neutron Stars as Pulsars

The precise mechanisms behind these pulses are unknown. However, the following is a broad description. When the progenitor star undergoes a supernova explosion and its radius decreases from millions of kilometres to tens of kilometres, its angular momentum is conserved. This leads to rotational frequencies in the range of tens to hundreds of hertz. Consequently, the surface of the neutron star can achieve relativistic speeds. The magnetic field of the star rotates at the same speed. Plasma near the neutron star is caught in the magnetic field and must rotate with it. At a certain radius, the plasma would need to be rotating at the speed of light to corotate with the pulsar. The region in which this happens is called the light cylinder. Field lines within the light cylinder remain open, no longer being closed lines which loop back into the pulsar. Particles which are travelling along these field lines at relativistic speeds will emit radiation in their direction of movement. This causes beams to be emitted from a certain radius above the surface and aligned with the direction of the open field lines (Goldreich

and Julian, 1969). These are the radio beams which Bell and Hewish observed and remain the defining characteristic of pulsars.

Another factor which is important for generating the observed pulsar beams is their strong magnetic fields. During the core collapse, the magnetic field is compressed into a much smaller volume. This increased density of magnetic flux strengthens the magnetic field. The high rotation speeds can also cause magnetic currents in the conductive pulsar fluid, increasing the field strength through the dynamo effect. Magnetic field strengths of $\sim 10^{12}$ G are typical for radio pulsars and $\sim 10^8$ G for the faster spinning millisecond pulsars (MSPs) (Mukherjee et al., 2015). These values can be estimated using the pulsar spin-down rate (described in Section 1.6.1) by assuming that all the loss of angular momentum is due to magnetic dipole breaking (Kim et al., 2023). For MSPs, strong surface fields also results in observable cyclotron radiation in their X-ray spectra (Staubert et al., 2019).

1.6.1 Spin-Down

The spin-down rate of a pulsar is not only used to estimate their magnetic field strength. By observing pulsar timings over extended periods, we can learn a lot about their lifecycles. From the moment of their creation, their rotation frequency decreases at a predictable rate due to loss of angular momentum. There are multiple potential causes of this loss of momentum, or 'spin-down', with magnetic dipole radiation being generally considered the dominant cause. However, as described in Section 1.4.3, pulsars are also expected to emit gravitational radiation, which would in turn contribute to the loss of angular momentum.

The spin-down rate can also be used to estimate the pulsar age. In this case, we refer to a characteristic age τ, as it is only an approximation of the pulsar's true age. First, we assume that the energy loss of a pulsar can be modelled as

$$\dot{P} = kP^{2-n}, \tag{1.26}$$

where P and $\dot{P}$ are the pulsar rotation period and its derivative, k is a constant, and n is known as the braking index (Jiang et al., 2013). Rearranging this

equation gives

$$dt = \frac{dP}{kP^{2-n}},$$
(1.27)

which, when integrated with the limits P and P_0, gives the following expression for characteristic age τ,

$$\tau = \frac{P}{(n-1)\dot{P}} \left[1 - \left(\frac{P_0}{P} \right)^{n-1} \right],$$
(1.28)

where P_0 is the rotation period at the time of NS formation t_0. We can assume that $P \gg P_0$ as the pulsar spins down over time, which allows the equation to be simplified to

$$\tau = \frac{P}{(n-1)\dot{P}},$$
(1.29)

in the rest frame of the observer.

For a pulsar losing angular momentum due to magnetic dipole radiation alone, this corresponds to a braking index of $n = 3$ (see Section 2.1) which gives $\tau = P/2\dot{P}$. However, as the focus of this thesis is GWs from pulsars, it is more interesting to consider a pulsar whose spin-down is caused by GW emission alone. These theoretical pulsars are referred to as gravitars and have a braking index of $n = 5$ if the GW emission is caused by 'mountains' on the pulsar surface as discussed in Section 1.4.3 (r-modes result in $n = 7$), therefore giving a characteristic age of $\tau = P/4\dot{P}$. This is discussed in more detail in Chapter 2.

However, pulsars are also able to gain angular momentum during their lifetimes. Indeed, a significant fraction of pulsars ($\sim 10\%$) have periods shorter than 10 milliseconds, which is far shorter than the expected period at birth of ~ 40 ms (van der Swaluw and Wu, 2001). These frequencies can also correspond to characteristic ages older than the universe itself. The first millisecond pulsar to be observed was B1937+21 in 1982 with a period of 1.558 ms (frequency of 642 Hz) (Backer et al., 1982). This was also the fastest pulsar before the observation of J1748-2446ad in 2004 which has a frequency of 716 Hz (Hessels et al., 2006). There must be processes through which these millisecond pulsars can be spun up. Pulsars in close binary systems which accrete matter from their companion can gain angular momentum and become 'recycled' pulsars. These pulsars can be in

a binary system with a Sun-like star from their formation or, when in globular clusters where stellar density is high, old pulsars can interact with regular stellar binaries to kick one star out and begin accretion of the remaining star once it evolves into a red giant (Bhattacharya and van den Heuvel, 1991).

1.6.2 Pulsar Timing Model

As most pulsar properties are derived from radio pulse observations, measuring them with accuracy is vital. In most cases, the individual pulses observed from a pulsar are very weak. For very bright pulsars, individual pulses may be observed, but there are still a variety of effects which cause slight variations on the pulse time of arrival (TOA) and the strength of the signal. Therefore, to account for these issues, hundreds of pulses are integrated together. This creates an integrated pulse profile which is then extremely consistent over time even when individual pulses are not. This stability allows for pulsars to be used in the pulsar timing arrays described in Section 1.4.2.1.

The process of obtaining TOAs using an integrated pulse profile is summarised as follows: First a mask is applied to the data to remove radio frequency interferences (RFIs). Then, individual pulse observations are folded with respect to their frequency to obtain a high signal-to-noise ratio template of the shape and features of the pulse. These folded profiles are then compared to new observations to obtain the precise moment that each pulse reaches Earth.

The TOAs are used to fit the parameters that define the phase evolution $\phi(t)$ of the pulsar, which is well described by a Taylor expansion:

$$\phi(t) = \phi_0 + f_{\rm rot}(t - t_0) + \frac{1}{2}\dot{f}_{\rm rot}(t - t_0)^2 + \frac{1}{6}\ddot{f}_{\rm rot}(t - t_0)^3 + ... , \qquad (1.30)$$

where t_0 is the reference epoch and ϕ_0 is the phase at t_0, and $f_{\rm rot}$, $\dot{f}_{\rm rot}$, and $\ddot{f}_{\rm rot}$ are the pulsar rotation frequency and frequency first and second derivatives respectively. However, there are many mechanisms which introduce noise, complicating this process.

A crucial step in determining pulsar timing parameters is the transformation from observed arrival time to emission time, which is performed by the commonly

used pulsar timing package TEMPO2 via the following equation (Edwards et al., 2006):

$$t_e^{\mathrm{psr}} = t_a^{\mathrm{obs}} - \Delta_\odot - \Delta_{\mathrm{IS}} - \Delta_{\mathrm{B}}, \tag{1.31}$$

where $\Delta_\odot$ accounts for delays due to propagation through the solar system and the conversion to the solar system barycentre (SSB), Δ_{IS} accounts for delays due to propagation through interstellar space and the conversion to the binary barycentre (BB), and Δ_{B} contains delays due to any binary companion. Each term is a combination of various effects:

The solar system delay $\Delta_\odot$ includes:

$$\Delta_\odot = \Delta_A + \Delta_{R\odot} + \Delta_p + \Delta_{D\odot} + \Delta_{E\odot} + \Delta_{S\odot}, \tag{1.32}$$

where Δ_A is the atmospheric propagation delay due to a different speed of light in the atmosphere, $\Delta_{R\odot}$ is the Roemer delay from the distance between Earth and the SSB, Δ_p is the annual parallax, $\Delta_{D\odot}$ is the Solar system dispersion due to the electrons in the solar wind, $\Delta_{E\odot}$ is the Einstein delay due to time dilation in the solar system, and $\Delta_{S\odot}$ is the Shapiro delay due to the passage through curved spacetime in the solar system.

The Δ_{IS} term is

$$\Delta_{\mathrm{IS}} = \Delta_{\mathrm{VP}} + \Delta_{\mathrm{ISD}} + \Delta_{\mathrm{FDD}} + \Delta_{\mathrm{ES}} \tag{1.33}$$

where Δ_{VP} is the vacuum propagation delay caused by secular motion such as proper motion, radial velocity, and acceleration (like the Shklovskii effect), Δ_{ISD} is the interstellar dispersion delay, Δ_{FDD} represent the frequency-dependent propagation delays, and Δ_{ES} is the Einstein-like time-dilation due to relative motion between the SSB and BB.

Finally, for binary systems Δ_{B} is included:

$$\Delta_{\mathrm{B}} = \Delta_{\mathrm{RB}} + \Delta_{\mathrm{AB}} + \Delta_{\mathrm{EB}} + \Delta_{\mathrm{SB}}, \tag{1.34}$$

where Δ_{RB} is the Roemer delay due to binary orbital motion, Δ_{AB} is the aberra-

tion of the radio beam by the companion, Δ_{EB} is the Einstein delay due to the binary, and Δ_{SB} is the Shapiro delay due to the binary.

1.6.3 Timing Noise

The timing model as described in Section 1.6.2 predicts the exact times that each pulsar pulse should be observed on Earth based on the pulsar's fitted parameters. The difference between the predicted TOA and the observed TOAs is called a residual:

$$\mathrm{Residual} = \mathrm{TOA}_{\mathrm{observed}} - \mathrm{TOA}_{\mathrm{expected}} \tag{1.35}$$

For a perfectly modelled pulsar and observation instrument, these residuals will be zero. However, unmodelled processes will appear as some identifiable feature. These can be classified into two types of noise, red and white. White noise is independent between observations and generally caused by unmodelled instrumental errors and pulse jitter intrinsic to the pulsar (Liu et al., 2011; Parthasarathy et al., 2021). Red noise is time-dependent and appears over longer timescales. This type of irregularity is termed 'timing noise' and is seen as a random walk in phase, frequency, or frequency derivative away from the regular spin-down as described in Section 1.6.1. In equation (1.30), the $\dddot{f}_{\mathrm{rot}}$ term is the most affected by the timing noise. Timing noise is strongly correlated to the spin-down rate and therefore shows up most clearly in younger pulsars with higher spin-down rates. The Crab pulsar, which is the one of the youngest known pulsars, experiences larger timing noise compared to other pulsars. Although MPSs experience less timing noise than other pulsars, it can still be of significant consideration when it comes to using them in PTAs like those discussed in Section 1.4.2.1.

The root-mean-square (RMS) of the timing residuals is commonly used as a measure of their overall variation and therefore represents the timing precision achieved for a given pulsar. It can be influenced both by intrinsic timing noise sources and observational limitations such as the cadence of observations and instrument sensitivity. This is discussed in more detail in Chapter 2. The RMS

value can be calculated from a set of residuals using:

$$\text{RMS} = \sqrt{\frac{1}{N} \sum_{i=1}^{N} r_i^2} \qquad (1.36)$$

where N is the number of residuals and r_i is the i-th residual. The signal-to-noise ratio for a single pulse profile can then be calculated from the pulse profile RMS noise values and the peak pulse amplitude A_i,

$$\text{S/N}_i = \frac{A_i}{\sigma_i}. \qquad (1.37)$$

When combining N individual pulse profiles into a folded profile, (1.37) can then be extrapolated to find the signal-to-noise for the folded pulse profile:

$$\text{S/N} = \frac{\sum_i A_i}{\sqrt{\sum_i \sigma_i^2}}, \qquad (1.38)$$

which gives a $\text{S/N} \propto \sqrt{N}$ scaling relation when all pulses are the same (Liu et al., 2011).

Additionally, there is a similar relationship between the white RMS noise of a pulsar and the number of observations of that pulsar, such that $\text{RMS} \propto \sqrt{N_{\text{obvs}}}$ where N_{obvs} is the number of timing observations. However, as red noise begins to dominate at longer observation lengths, a 'time factor' can be defined to specify the limit to which increasing the number of timing observations (with a fixed cadence) improves the RMS noise. This can be calculated as

$$\text{Time Factor} = \frac{\sigma_0^2}{\sigma_r^2} \qquad (1.39)$$

where σ_0 is the unweighted RMS of timing residuals and σ_r is the level of red noise (Perrodin et al., 2013). This gives the factor by which the number of observations can be increased without the residuals becoming dominated by red noise. However increasing the number of observations through a higher cadence does not have this limitation in the same way, as it increases the number of

observations without increasing the timing baseline.

The type of timing noise is relevant for the detection of CWs from pulsars. An early look into this effect is considered in Jones (2004). If the region of the star responsible for GW emission is strongly coupled to the region of the star producing the EM pulses, then both signals will exhibit the same phase wandering due to timing noise, such that the GW phase residuals $\Delta\Phi_{\mathrm{GW}}$ and the EM phase residuals $\Delta\Phi_{\mathrm{EM}}$ are equal. However, if the coupling is imperfect, this may not be true, and Jones defines the ratio between the phase residuals as

$$\alpha = \frac{\Delta\Phi_{\mathrm{GW}}}{\Delta\Phi_{\mathrm{EM}}}. \tag{1.40}$$

On short timescales, it is expected that the EM and GW emitting parts of the pulsar are coupled, giving $\alpha = 1$. On the other hand, if sources of the timing noise are processes in the magnetosphere and therefore above the surface of the pulsar, this would not cause any residuals in the GW phase, leading to $\alpha = 0$. A third scenario involves weak, random exchanges of angular momentum between the GW emitting and EM emitting parts of the pulsar. In this case, conservation of angular momentum leads to

$$I_{\mathrm{EW}}\Delta\dot{\Omega}_{\mathrm{EW}} + I_{\mathrm{GW}}\Delta\dot{\Omega}_{\mathrm{GW}} = 0. \tag{1.41}$$

This can be integrated twice and rearranged to find

$$\alpha = -\frac{I_{\mathrm{EW}}}{I_{\mathrm{GW}}}, \tag{1.42}$$

where I is the relative moment of inertia of the emitting part. For example, if the EM emission is produced in the crust while the GW emission comes from a superfluid core, a typical value for α would be ~ -0.01.

Jones (2004) found that, under the assumption that $\alpha = 1$, timing noise must be accounted for in the case of younger pulsars (like the Crab) in order to detect CWs emitted from them. With sufficient measurements, it is possible to account for such timing noise by including higher order terms in equation (1.30).

For the Crab pulsar this means going up to the 12th order term (Abbott et al., 2019b). In other cases, multiple sinusoidal harmonics can be fit to the timing noise in the arrival times during a process called 'harmonic whitening'. This means obtaining the residuals after fitting up to the $\dddot{f}_{\text{rot}}$ term and then fitting the harmonic sinusoids to them. The fundamental frequency can be specified or derived from the time-span of the data (Hobbs et al., 2004, 2006b). The curve produced by the sum of these curves is removed from the residual to obtain mostly white noise.

While the origin of red timing noise is still largely unknown, some processes which contribute to it have been identified. Pulsars may have unknown companions with which they interact, causing features not included in the model (Pitkin and Woan, 2007). Additionally, the density of the interstellar medium (ISM) can change as the line of sight between the pulsar and Earth shifts, causing variations in the dispersion of the pulse (You et al., 2007). Even GWs themselves, such as the stochastic GW background, can disrupt the pulsar signal, leading to red timing noise (Hellings and Downs, 1983). On the other hand, timing noise may be random unknown processes, such as micro-glitches (see Section 1.6.4) (Cordes and Downs, 1985).

1.6.4 Glitches

While micro-glitches may contribute to timing noise, regular glitches deserve their own classification. Despite having very predictable timings, pulsars can occasionally experience random 'glitches' where the rotation frequency suddenly increases before slowly returning to a stable frequency. Figure 1.6 shows the location of all glitching pulsars as of September 2022 on a $P - \dot{P}$ plane. The younger pulsars are those in the top right of the plot with higher frequency derivatives. These are where the majority of glitches have been observed, although some glitches have been observed in millisecond pulsars like J0613−0200 (McKee et al., 2016) and B1821−24 (Cognard and Backer, 2004). Roughly 6% of known pulsars have been observed to glitch, and the majority have been observed to glitch only once or twice (Zhou et al., 2022). However some younger, high spin-down rate pulsars have exhibited frequent glitches. In particular, the pulsars J0534+2200 (Crab),

36
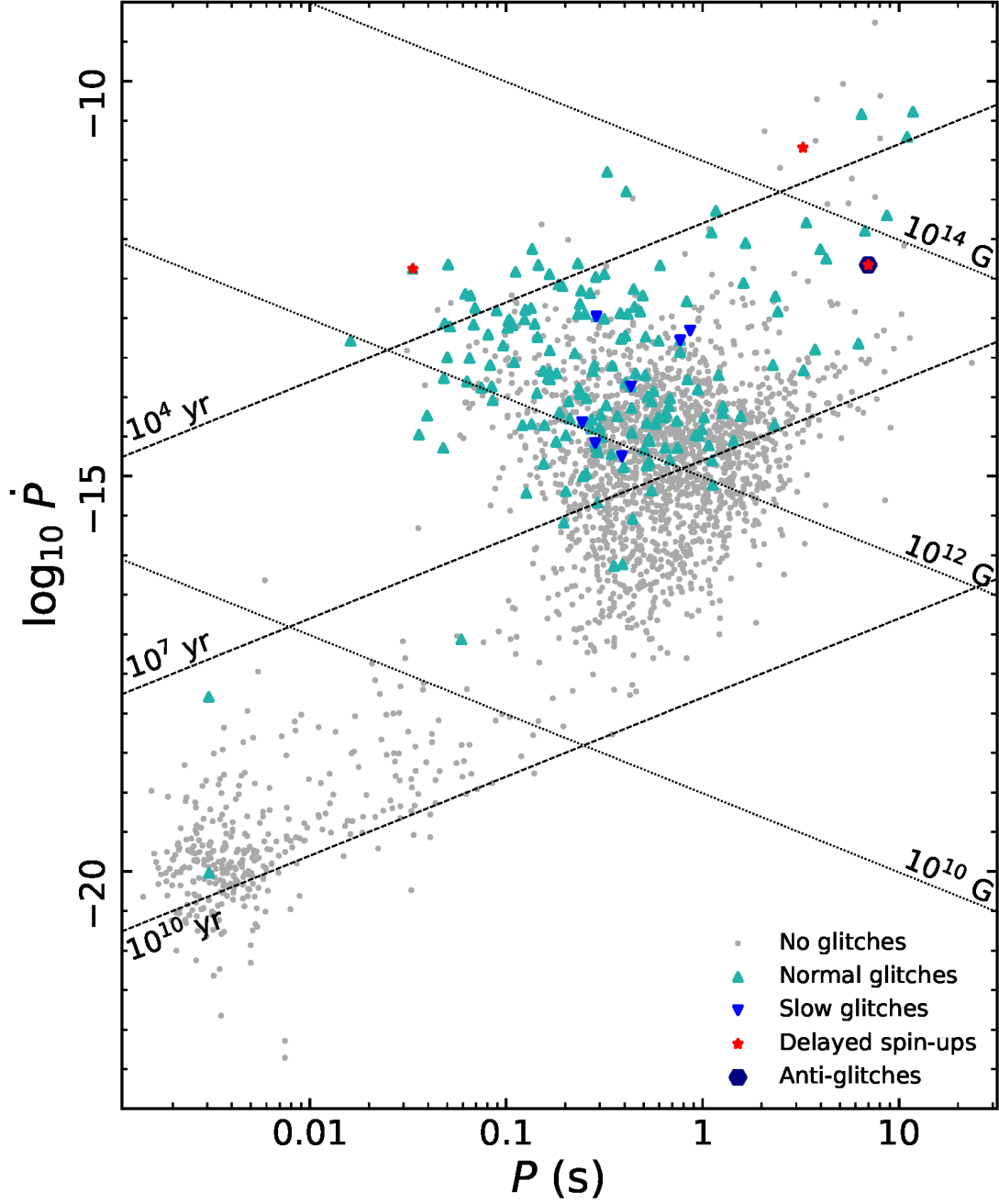
Figure 1.6 Period-period derivative plot for all pulsars in the ATNF Pulsar Catalogue and their detected glitches as of September 2022. The legend describes the type of glitch subclass as described in Section 1.6.4. Taken from Zhou et al. (2022).

J0537−6910, and J0835−4510 (Vela) have been seen to undergo tens of glitches so far.

As seen in Figure 1.6, there are four classifications of glitches. Normal glitches are by far the most common. They are classified as having a fast spin-up (on the order of seconds) with a longer recovery ranging from days to years depending on the shape of the recovery. The causes of glitches are not known, but popular theories include starquakes (where the crust cracks) (Baym et al., 1969) and brief couplings between a superfluid core and a solid crust, leading to the transfer of angular momentum to the slower-moving crust (Antonelli et al., 2022). Slow glitches have decreased rates of spin-up and spin-down compared to normal glitches. These cannot be explained by the angular momentum exchange model and may be either a type of timing noise (Hobbs et al., 2004) or due to a sudden increase in angular momentum of the neutron star crust after a quake (Link and Epstein, 1996). Delayed spin-up glitches display a short period of frequency increase immediately after the glitch, followed by a rapid decrease in the frequency derivative. They have only been detected in large glitches of young pulsars (Zhou et al., 2022). Anti-glitches are sudden decreases in pulsar frequency accompanied by an X-ray outburst. As they have so far been observed in magnetars (pulsars with extremely strong magnetic fields), this suggests that anti-glitches are related to the magnetosphere (Manchester, 2018).

1.6.5 Measuring Pulsar Distances

Pulsar beams give us insights into rotation parameters such as the pulsar frequency and its derivatives, but we must rely on additional observations to determine parameters such as pulsar distance and mass. Distance is of particular interest in the field of CWs, as it allows for the calculation of the spin-down limit: the maximum GW amplitude possible under the assumption that the observed pulsar spin-down rate is caused by GW emission alone.

The most common method of measuring pulsar distances is the YMW16 model described in Yao et al. (2017). As a pulsar pulse travels through the galaxy, Magellanic Clouds, and/or intergalactic medium (IGM), it interacts with free electrons through electrostatic interactions and is delayed. This causes the pulse

to be dispersed, which can be measured. The arrival time delay can be calculated as:

$$\Delta t = \frac{e^2}{2\pi m_e c\, f^2} \mathrm{DM} \tag{1.43}$$

where e and m_e are the charge and mass of an electron respectively, f is the radio frequency of the pulse and c is the speed of light. DM is the dispersion measure, or column density along the path of the pulse, which can be calculated as:

$$\mathrm{DM} = \int_0^D n_e\, dl \tag{1.44}$$

where D is the distance to the pulsar and n_e is the local free electron density. YMW16 provides a model for the density of free electrons in the galaxy, Magellanic Clouds and IGM which is calibrated using pulsars whose distances have been calculated independently. Then, for other pulsars, YMW16 can be used with the measured pulse dispersion to obtain an estimate for the distance. For 95% of pulsars YMW16 distance values have a typical fractional uncertainty of up to 90%.

While YMW16 is especially useful for obtaining distance measurements for any pulsar with an observable TOA dispersion, there are other methods which may be more accurate. Some pulsars are associated with other objects for which the distance is known, such as globular clusters or supernova remnants, allowing for the pulsar distance to be estimated in comparison. Then there are parallax measurements, where the perceived movement of the pulsar in the sky over the course of the year in arcseconds θ is used to estimate the distance in parsecs D_θ using $D_\theta = 1/\theta$. As the parallax is greater for pulsars close to Earth, this method becomes less accurate for more distant sources. Smits et al. (2011) found that uncertainties of below 20% could be achieved for close pulsars (< 13 kpc).

Most pulsar distances used to calibrate YMW16 used the absorption of the pulsar emission by Hɪ gas. Only gas between the pulsar and Earth will cause absorption. The velocities of regions of Hɪ can be derived from the spectrum of the absorption and these velocities can be correlated with the galactic rotation model to obtain a distance. The absorption with a velocity corresponding to the furthest distance from Earth is used as the pulsar distance measurement. This

method is more applicable for pulsars with brighter apparent magnitudes which tend to be close to Earth. Verbiest et al. (2012) found that their HI distance measurements could be overestimated by up to $\sim 20\%$.

Another method involves the Shklovskii effect where a pulsar's transverse velocity causes a change in radial acceleration, resulting in an apparent doppler-shift of both the orbital and spin period derivative (Shklovskii, 1970). This is directly correlated with the pulsar distance, allowing for a Shklovskii distance estimate D_{shk} to be calculated from:

$$D_{\mathrm{shk}} = \frac{c}{\mu^2} \frac{\dot{P}^{\mathrm{shk}}}{P} \tag{1.45}$$

where μ is the proper motion of the pulsar, P is the pulsar period (orbital or spin) and $\dot{P}^{\mathrm{shk}}$ is the contribution to the observed period derivative from the Shklovskii effect (Reardon et al., 2021). In Yao et al. (2017), for the three pulsars with Shklovskii distance measurements, those were the most accurate distances measurements, with errors ranging from $\sim 1\%$ to $\sim 90\%$.

1.7 Neutron Star Equation of State

So far, I have discussed the rotational parameters like frequency and its derivatives, the distance to pulsars, and some complex processes occurring within and around these intense objects, but there is a property about which little is known: density. An equation of state (EOS) describes the density and pressure relationship in a medium. For NSs, it relates their mass and radius and describes what form matter takes within the star. As NS conditions exceed what is possible to recreate on Earth, their interiors are of particular note to fields outside GW physics or even astrophysics.

Mass can be calculated for some pulsars using a variety of methods. For pulsars in binaries, the doppler shifts of the pulse period and of the spectral features of the companion can reveal the orbital period and radial velocity from which the mass function can be calculated. Then, if the mass of the companion and inclination is known, the NS mass can be measured, otherwise only limits

can be produced (Zhang et al., 2011). For NS-NS binaries, relativistic effects such as Shapiro delay (the increase in travel time of radio signals in the presence of a massive object due to the curving of spacetime) and periastron advances (the change in orbit due to spacetime curvature) can be used to calculate the pulsar masses to higher precisions (Kramer et al., 2021). For isolated pulsars, glitches (see Section 1.6.4) can play a role in the calculation of mass. Pizzochero et al. (2017) showed how the maximum observed glitch amplitude of a pulsar can constrain its mass based on the assumption that superfluid vortices inside the star are pinned to the underside of the crust. Angular momentum is stored as the superfluid at the crust lags behind the deeper superfluid until the vortices are unpinned, releasing that angular momentum in a glitch. In this case, the maximum possible glitch depends on the mass of the pulsar.

Radius, on the other hand, is much harder to measure. The Neutron Star Interior Composition Explorer (NICER) telescope (Gendreau et al., 2016) has allowed for the measurement of both mass and radius for some X-ray-bright MSPs: J0030+0451 (Miller et al., 2019; Riley et al., 2019), J0740+6620 (Miller et al., 2021; Riley et al., 2021; Salmi et al., 2022), and J0437-4715 (Reardon et al., 2024). This method involves measuring the X-ray emission from hot spots on the pulsar surface as it rotates (accounting for the relativistic bending of light which can allow hot spots on the other side of the NS to still be visible) to calculate the radius. This is possible due to NICER's high accuracy of 100 ns for X-ray arrival times.

The main difference between various EOS models is their rigidity. A model is more rigid if the addition of matter results mostly in an increase in radius. On the other hand, a softer EOS would result in other effects like increased pressure and density. The observations from NICER have so far ruled out both the most rigid and the softest EOSs. The ability for a pulsar to support certain levels of ellipticity (or mountain heights) is also dependent on the EOS. As described briefly in Section 1.4.3.3 and more deeply in Section 3.1.2, the ellipticity of an isolated pulsar can be calculated using the GW strain amplitude and pulsar distance. Even in the absence of detections, the amplitude upper limits can constrain the ellipticies, which in turn can constrain the EOS.

Current models of neutron star interiors include a solid iron outer crust with superfluid below it. However, the precise form of matter in the core is unknown. There are many proposals, the simplest of which is nucleonic matter. The extreme density may allow for additional degrees of freedom, which would allow for nucleonic matter alongside hyperons (a baryon with strangeness) (Zachariou et al., 2024). The matter in the core may undergo a phase transition where the nuclear matter breaks down into deconfined quarks and gluons (Annala et al., 2023). If there is quark matter in NSs, it is possible that this matter is in a colour superconducting phase, where colour transitions can take place without loss if the effective temperature is low enough (Tanimoto et al., 2020). Similarly, another possibility is for the core to be made up of pairs of neutrons in Bose-Einstein condensates (Rodríguez Concepción and Quintero Angulo, 2024). On the underside of the crust, there may be a so-called 'pasta' phase, where the nucleonic matter takes forms such as rods (spaghetti), voids (anti-gnocchi), and sheets (lasagne) which strongly resemble varieties of pasta (Caplan and Horowitz, 2017). With plenty of exciting physics waiting to be understood in the centres of these intense objects, all methods of further constraining the EOS are of interest.

1.8 Summary

In this chapter, I have provided a brief description of the field of GW astrophysics today, along with methods of observations with a focus on searching for CWs from isolated NSs. I have also given a description of NSs, the methods we have of observing these unique objects and the many mysteries and exotic processes occurring within them. It should now be clear why the prospect of observing CWs from pulsars is both interesting and promising. In the following chapter, I will discuss the opportunity to search for evidence of CWs from pulsars without the use of GW observations through the measurement of the pulsar braking index. In the chapters following this, I will describe the search for a direct measurement of CWs from known pulsars in targeted searches using the third (Chapter 3) and first part of the fourth (Chapter 4) LVK observing runs. Finally, I will conclude with the future of GW observations in Chapter 5.

Chapter 2

Recovering Pulsar Braking Index from a Population of Millisecond Pulsars

2.1 Introduction

Pulsars are objects of great interest in the world of gravitational waves (GWs). As their pulses are very regular, they can be used as cosmic clocks, and due to small, coherent variations over whole populations of pulsars in pulsar timing arrays (PTAs), they have been used as tools to identify the stochastic GW background as described in Section 1.4.2.

However, as well as being useful for detecting GWs, pulsars are predicted to emit them themselves (Ostriker and Gunn, 1969). The LIGO-Virgo-KAGRA (LVK) collaboration has already detected several transient GW signals from the inspiral and subsequent mergers of neutron stars in binary systems with black holes or other neutron stars (Abbott et al., 2021b,d, 2023) as described in Section 1.4.1. While observing transient GWs has become commonplace, it is not the only form of GW expected to be produced by neutron stars. Another category of GWs which remain unobserved to date are continuous waves (CWs), i.e., very long-lived

quasi-monochromatic signals. A promising candidate source for such a signal is an individual neutron star spinning with some non-axisymmetric deformation. Such a deformation could take the form of a mountain on the crust caused by cooling (Ushomirsky et al., 2000), binary accretion (Gittins and Andersson, 2021a) or due to strong magnetic fields (Bonazzola and Gourgoulhon, 1996; Cutler, 2002). Oscillations beneath the crust, such as r-modes, can also cause GW emission from a single pulsar (Andersson, 1998; Friedman and Morsink, 1998). More information on CWs can be found in Section 1.4.3. Although these signals are currently yet to be observed, it is possible to obtain evidence of their existence observationally without requiring a GW detection. One method is to measure the braking index n of a pulsar, which I will discuss in this chapter.

The braking index is a measure of a pulsar's angular momentum loss as seen in equation (1.26). This can be rewritten in terms of frequency rather than period to get:

$$\dot{f} \propto -f^n, \tag{2.1}$$

where f is the pulsar's rotation frequency and $\dot{f}$ is the first time derivative of the frequency, i.e., the spin-down rate. The value of n depends on the mechanism of angular momentum loss. For example, a pulsar losing angular momentum through magnetic dipole radiation follows

$$\dot{f}_{\text{dip}} = -\frac{8\pi^2}{3c^3}\frac{B^2}{I_{zz}}R^6 f^3 \sin^2 \alpha, \tag{2.2}$$

which gives a braking index of 3 (Hamil et al., 2015). Here, c is the speed of light, B represents the magnitude of the dipolar magnetic field at the magnetic pole, I_{zz} is the moment of inertia, α is the angle between the magnetic field axis and the rotation axis, and R is the star's radius at the magnetic pole.

Similarly, if the spin-down of a non-axisymmetric pulsar was instead dominated by emission of GWs (as in the case of a 'gravitar') the angular momentum loss would follow

$$\dot{f}_{\text{GW}} = -\frac{512\pi^4}{5}\frac{G}{c^5}I_{zz}\varepsilon^2 f^5, \tag{2.3}$$

where $\varepsilon \equiv |I_{xx} - I_{yy}|/I_{zz}$ is the ellipticity of the pulsar, (I_{xx}, I_{yy}, I_{zz}) are the

source's principle moments of inertia (Palomba, 2005), and G represents the gravitational constant. In this case, the braking index is equal to 5. Woan et al. (2018) observed a possible minimum ellipticity for millisecond pulsars (MSPs) consistent with $n = 5$, suggesting that the spin-down of pulsars near this limit is dominated by GW emission. It is also possible for pulsars to have a braking index of 7 if GWs are emitted via r-modes described in 1.4.3 (Abbott et al., 2021g). Most realistic systems are expected to have a mixture of several processes such that $\dot{f} = -af^3 - bf^5 - cf^7$, where a, b, and c are coefficients that define the amount of mixing.

By solving the differential in equation (2.1), the value of n can be determined from observational parameters using

$$n = \frac{f\ddot{f}}{\dot{f}^2}. \tag{2.4}$$

This requires knowledge of both the first and second derivatives of f. Although several pulsars have measured braking indices (Lower et al., 2021; Parthasarathy et al., 2020), the second derivative for MSPs is usually small, often around the order of $10^{-30}\,\mathrm{s}^{-3}$, making it difficult to observe over current timescales.

Rather than trying to directly measure the braking index of single pulsars, this chapter discusses the possibility of using a population of pulsars to infer the distribution of n for the whole sample. This could allow the underlying energy loss process to be inferred without needing precise values of $\ddot{f}$ for individual sources. This method is similar to that used in Pitkin et al. (2018) to search for CWs from a population of pulsars. If the braking index distribution could be determined in this way, it would give valuable insight into whether pulsar populations are spinning down due to GW emission.

In this chapter, I discuss the method used to obtain and extract the braking index from the pulsar population in Section 2.2, present and discuss the results in Section 2.3, and comment on the feasibility of this method now and for future observations in Section 2.4.

2.2 Analysis

I create simulated time of arrival data (TOAs) for simplified pulsar models with injected braking indices of primarily $n = 5$ (see 2.3.6 for analysis using other values of n), representing pulsars with spin-down dominated by GW emission. Posteriors on n for each pulsar are then obtained from their TOAs without an informed assumption on the value of n. These posteriors are combined to extract the distribution of n for the entire population. I look at how factors like noise levels, observation length, and observation frequency affect the accuracy and confidence of the recovered distribution.

2.2.1 Creating TOAs

The 47 pulsars from the wideband NANOGrav 12.5-year data set (Alam et al., 2020, 2021) are used as example pulsars for this analysis. All pulsars in this sample are MSPs, meaning they have a rotation frequency of over $100\,\mathrm{Hz}$. This puts the sample closer to the cut-off described in Woan et al. (2018) which is caused by $n = 5$ processes than if it contained pulsars with lower frequencies. It may be noted that 30 of the pulsars are in binary systems; however, this information is not used in this study, and they are treated as isolated pulsars.

I take the pulsar parameter files provided by NANOGrav and strip them of unnecessary parameters, leaving a basic imitation of the original pulsar: binary information is removed, so all pulsars appear isolated and glitches (see Section 1.6.4) are ignored. The effect that glitches would have on the braking index is discussed briefly in Section 2.4. The parameters retained are chosen as only those required for the production of the fake TOAs by the pulsar timing software package `Tempo2` (Edwards et al., 2006; Hobbs et al., 2006a, 2009). A list of the parameters can be seen in Table 2.1. The values `F0` and `F1` (representing f and $\dot{f}$) are used as provided, while `F2` ($\ddot{f}$) is fixed at the value corresponding to a braking index of $n = 5$ by rearranging equation (2.4). This provides realistic TOA data for pulsars with an injected $n = 5$ for us to test the analysis method on.

Using simulated TOAs instead of real data decreases the number of variables, allowing the analysis to be performed with fewer unknown effects. It also allows

Table 2.1 Pulsar parameters kept in the stripped parameter files used to create simulated TOAs with `Tempo2`.

Parameter	Details
PSR	Pulsar name
LAMBDA	Ecliptic longitude
BETA	Ecliptic latitude
POSEPOCH	Position epoch
F0	Frequency of pulsar rotation
F1	Derivative of frequency
PEPOCH	Period epoch
DM	Dispersion measure
EPHEM	Which solar system ephemeris to use
CLK	Definition of clock to use
TZRSITE	Telescope site code corresponding to TZR
F2	Second frequency derivative

us to vary parameters such as noise and frequency of observations. I can investigate beyond current observational constraints, performing the analysis with observation times that exceed the 12.5 years of the NANOGrav sample. Importantly, it allows us to know the true value of n so I can verify the accuracy of my results.

Real pulsar TOAs are subject to noise, which is generally classified into two types: white (uncorrelated in time) and red (correlated in time). Red noise is prevalent at low frequencies and so affects data with longer timescales. There are several sources of red noise: stochastic GWs which will induce correlated red noise in the residuals (the difference between the predicted TOAs and the actual TOAs) of multiple pulsars, processes intrinsic to each pulsar (such as companions), and the varying effects of the interstellar medium (ISM). The spin down of younger pulsars is caused by various complex methods (Palomba, 2000), leading to stronger red noise than their older MSP counterparts. Although sources of red noise can be hard to identify, the noise properties of the MSPs in the NANOGrav sample can mostly be described as white noise (Perrodin et al., 2013), with Gaussian noise present at all frequencies. White noise represents instrumental errors that have not been modelled and intrinsic pulse jitter (Liu et al., 2011; Parthasarathy et al., 2021). The impact of noise, especially red noise,

on high-precision pulsar timing and its effect on the measurability of $\ddot{f}$, can be seen in Liu et al. (2019).

In this analysis, I allow my simulated TOAs to be created with a root-mean-square (RMS) noise value for white noise alone. For each pulsar, the noise value is taken from Table 5 in Alam et al. (2020). In cases where the source has a separate red noise value, the value for white noise is taken only. These noise value used for each pulsar is listed in Table A.1. As the effect of timing noise on the accuracy of this method will be tested, I need to be able to vary the average noise of the sample to any desired value $\text{RMS}_{\text{desired}}$. Therefore, I scale the RMS noise of each individual pulsar using

$$\text{RMS}_{i,\text{scaled}} = \mu_{\text{desired}} \times \frac{\text{RMS}_i}{\mu}, \tag{2.5}$$

where RMS_i is the RMS noise value for pulsar i taken from Alam et al. (2020), μ is the mean across all pulsars in the original dataset, and μ_{desired} is the mean the target mean across all pulsars after scaling. This retains the realistic natural variation of RMS noise throughout the population.

The number of days between observations is kept at 28 throughout this analysis, despite it being one of the parameters which I wish to vary. Instead, I simulate changing it using the known relationship between frequency of observations and RMS noise for a pulsar assuming only white noise:

$$\text{RMS}_{\text{eqv}} = \frac{\text{RMS}}{\sqrt{N}}, \tag{2.6}$$

where N is the factor by which the cadence of observations is increased and RMS_{eqv} is the RMS noise equivalent to such an increase in observations (Perrodin et al., 2013). This allows us to simulate a higher cadence without increasing the computational load. The full list of parameters used in generating the fake TOAs are listed in Table 2.2.

Table 2.2 Run parameters used to generate TOAs. Unless otherwise stated, these parameters were kept constant between pulsars.

Parameter	Details	Value
NDOBS	Number of days between observations	28
NOBSD	Number of observations per day	1
RANDHA	Random hour angle (y/n)	n
START	Start date of observation (MJD)	Varied
END	End date of observation (MJD)	58850 (Jan 2020)
RMS	RMS noise to be added (ms)	Varied

2.2.2 Bayesian Odds

The first iteration of this method involves a bespoke script written to calculate the Bayesian odds of specific values of n given a set of residuals. To do this, TEMPO2 is given the simulated TOAs for each pulsar along with a parameter file containing identical information as is used to create the TOAs with the exception of F2, which is varied to create models with assumed braking indices between 0 and 10. Other parameters are given, as shown in Table 2.2.

An example of residuals produced using this method is shown in Figure 2.1. The top panel shows the residuals for the assumption that $n = 0$ and $n = 5$ plotted on the same graph. To the naked eye, there is little variation between the two models. In the bottom panel, the difference between the residuals is plotted for each TOA. The cubic F2 term can now be clearly seen. This is because the assumption in the $n = 0$ model does not correct for the F2 term, therefore leaving it in the residuals[1].

Since the signal from F2 is difficult to detect by eye, the Bayesian odds of a model with a braking index of n being preferred over a model with a braking index of 0 can be used to assess the support for the presence of a signal. These odds are defined as

$$\mathcal{O} = \frac{p(\vec{D}|M_n)}{p(\vec{D}|M_0)} \frac{p(M_n)}{p(M_0)}, \tag{2.7}$$

where M_n represents the model with an assumed braking index, n, with M_0

---

[1]The difference is actually a polynomial up to 3rd order, as F0 and F1 are allowed to be fit by TEMPO2.
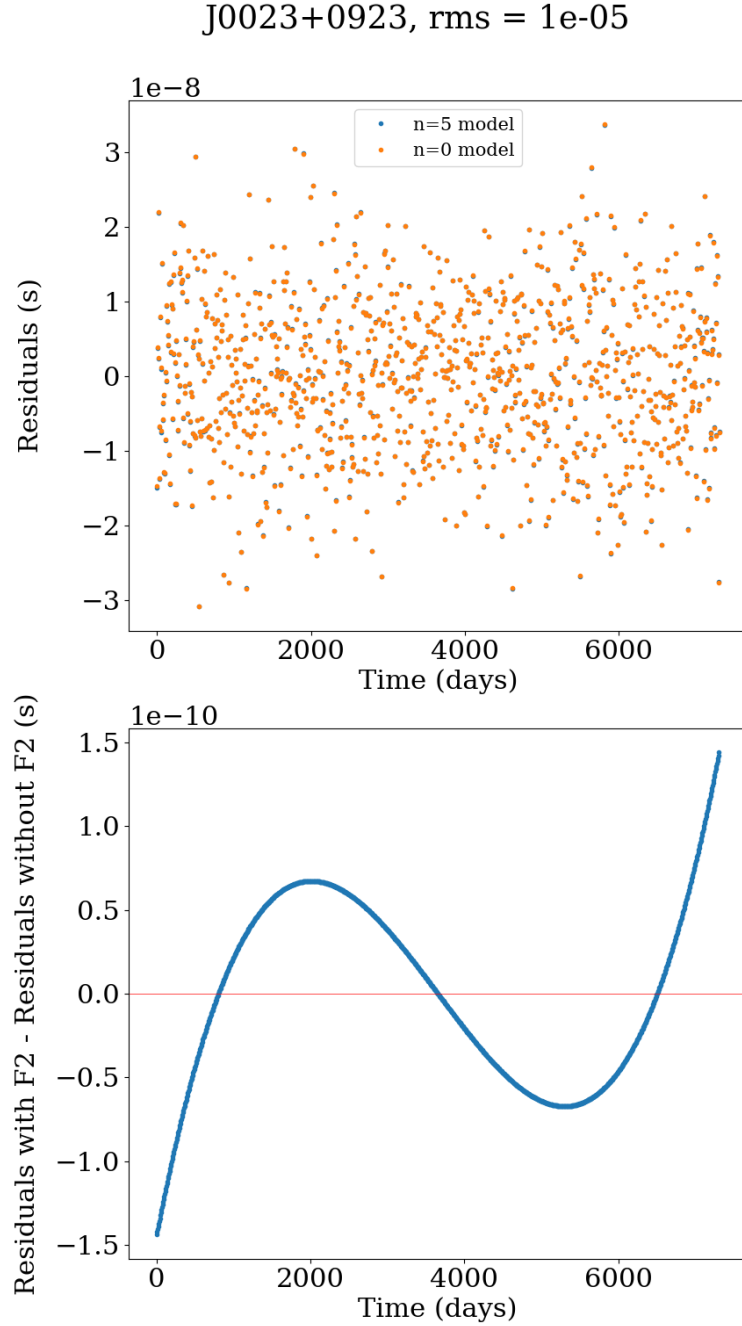
Figure 2.1 Top: The residuals for pulsar J0023+0923 for each model plotted over time. Bottom: The difference between the residuals for each model. A cubic signal can clearly be seen, though on a scale much smaller than the noise on the residuals.

being the assumption that $n = 0$. $\vec{D}$ is the set of residuals for all pulsars such that $\vec{D} = \{\vec{d_1}, \ldots, \vec{d_N}\}$ with $\vec{d_i}$ representing the set of residuals for one of the N pulsars in the sample. As mentioned in Section 1.4.3.4, the fraction $p(M_n)/p(M_0)$ is the prior odds which can be set to 1 if there is no prior preference between the models, as is the case here. This leaves the term $p(\vec{D}|M_n)/p(\vec{D}|M_0)$, which is also known as the Bayes factor.

As the residuals for each pulsar are independent, the probability of the full set of residuals for a given assumption of n can be calculated as the product of the probability of the residuals of each individual pulsar

$$p(\vec{D}|M_n) = \prod_{i=1}^{N} p(\vec{d_i}|M_n). \tag{2.8}$$

The probability for pulsar, i, can be calculated as

$$p(\vec{d_i}|M_n) = \left(2\pi\sigma_i^2\right)^{-n_i/2} \exp\left(-\sum_{j=1}^{n_i} \frac{r_{(n)_i}^2(t_j)}{2\sigma_i^2}\right), \tag{2.9}$$

where σ_i is the rms noise on the residuals, n_i is the number of residuals for that pulsar, and $r_{(n)_i}(t_j)$ is the residual at time t_j.

It is sometimes more useful to calculate the natural log of the Bayesian odds, which is equivalent to

$$\ln(\mathcal{O}) = \ln(p(\vec{D}|M_n)) - \ln(p(\vec{D}|M_0)), \tag{2.10}$$

with $\ln(p(\vec{D}|M_n))$ being calculated as

$$\ln(p(\vec{D}|M_n)) = \sum_{i=0}^{N} \left(-\frac{n_i}{2}\ln(2\pi\sigma_i^2) - \sum_{j=0}^{n_i} \frac{r_{(n)_i}(t_j)^2}{2\sigma_i^2}\right). \tag{2.11}$$

These odds values are then plotted against n for varying numbers of pulsars and observation lengths, providing a plot as seen in Figure 2.2[1]. These early re-

---

[1]Note that this early script only used pulsars whose names begin with 'J', hence 44 being the maximum amount.

sults demonstrate the key ideas that with greater observation length and number of pulsars, it should be easier to determine the braking index. It suggests that even for long observation lengths, having 20 rather than 10 pulsars can make a significant difference. The results for larger numbers of pulsars appear to become increasingly correlated to each other, likely due to them having increasing proportions of pulsars in common.

2.2.3   Obtaining Posteriors

The method discussed in Section 2.2.2 can be easily improved upon. First, it requires running `TEMPO2` for every desired value of n between 0 and 10. Before the script was fully refined, the decision was made to switch to a more robust method which produces posteriors on n for each pulsar. It also allows for n to be treated as continuous rather than discrete.

I choose to use `enterprise` (Ellis et al., 2020) and `enterprise_extensions` (Taylor et al., 2021) to model TOAs and provide likelihoods using the simulated TOAs for each pulsar[1]. `enterprise_warp` (Goncharov, 2021), a set of tools which allow Bayesian inference via the `bilby` package (Ashton et al., 2019; Romero-Shaw et al., 2020) in combination with `enterprise`, is used to produce posteriors on the rotational parameters that I require. `enterprise_warp` can only sample over non-derived pulsar parameters, i.e., the rotational frequency and its derivatives. However, the strong correlation between $\dot{f}$ and $\ddot{f}$ means it is difficult to draw samples from their joint posterior. Therefore, `enterprise_warp` (Goncharov et al., 2024) is modified to allow it to draw samples directly from the braking index so, for each pulsar, I sample from the posterior on f (`F0`), $\dot{f}$ (`F1`), n, and a constant white noise variance. I use priors on f and $\dot{f}$ defined by the `enterprise_extensions` defaults: uniform priors that are constant between $\pm 5\sigma$ (where σ is taken from the values from the fit provided in the PTA parameter files). For the braking index I use a uniform prior that is constant between

---

[1] I have used a modified version of `enterprise_extensions` (Taylor et al., 2024) that retains 128 bit floating point precision for parameter values to avoid numerical truncation errors which were noticed when running analyses for very low RMS noise values.
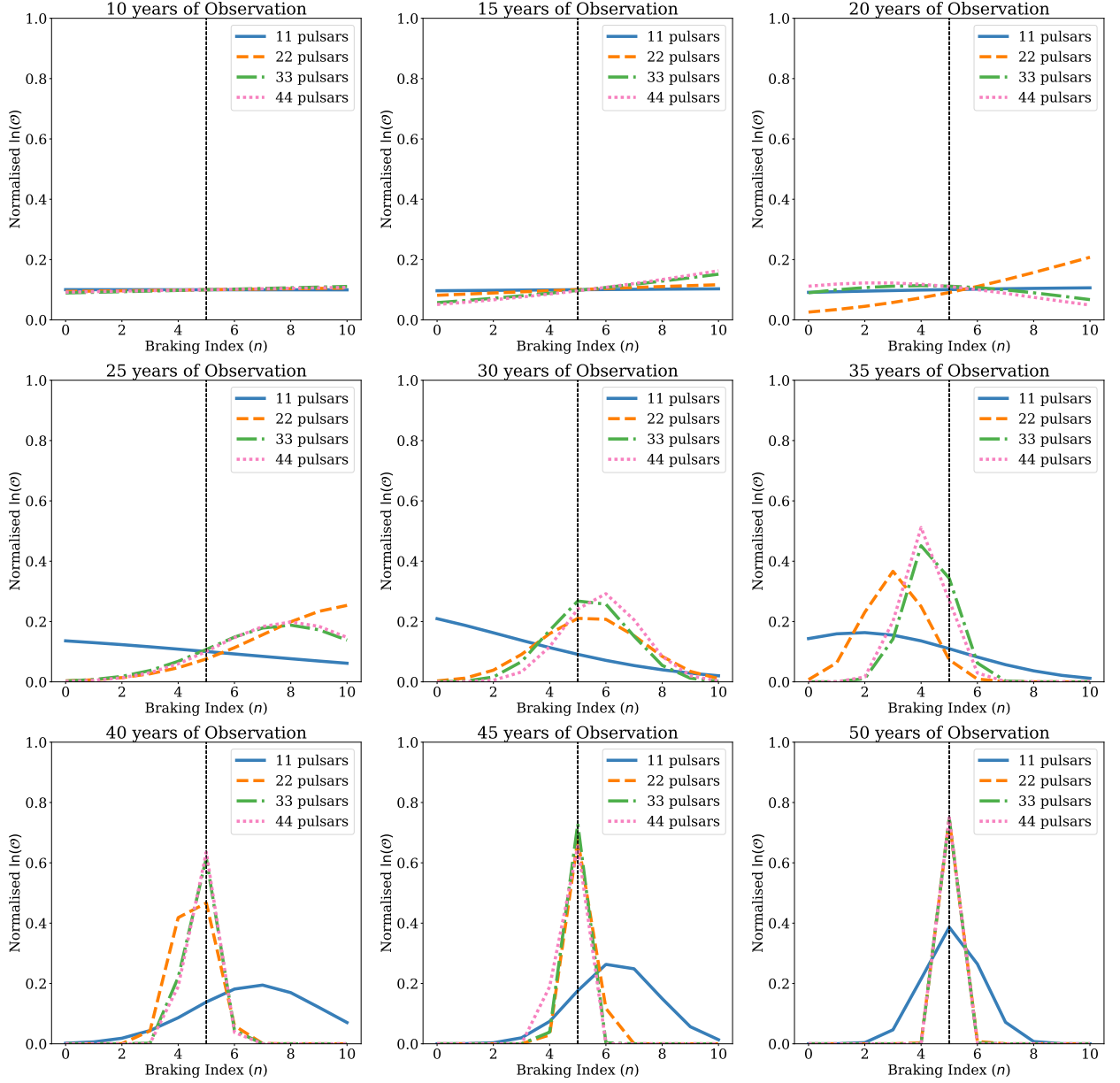
Figure 2.2 Bayesian odds for each model of n compared to $n = 0$ for different numbers of pulsars observed over varying lengths of time. The black dotted line shows $n = 5$, the true braking index of the sample. The RMS noise was kept at 1×10^{-5}.

53

$0 \leq n \leq 10$. For the sampling I use the `dynesty` nested sampling package (Speagle, 2020), via `bilby`. Despite not being required for my subsequent analysis, $\ddot{f}$ samples can be recreated from those I obtain via equation (2.4).

2.2.4 Recovering the Underlying Distribution

Finally, the posteriors on n can be 'stacked' using the `posteriorstacker` python package (Baronchelli et al., 2020; Buchner, 2021) to infer and plot the underlying distribution of n for the entire population.

`Posteriorstacker` uses the hierarchical Bayesian model described in Appendix A of Baronchelli et al. (2020) to infer the intrinsic distribution for desired parameters given posteriors for a sample of objects. I briefly describe the method here. The parent distribution of a value n for all objects is assumed to be a Gaussian $N(n_i | \mu, \sigma)$ with unknown mean μ and standard deviation σ (the hierarchical model's hyperparameters); in this case the objects are pulsars and n_i is the braking index for each pulsar i. As the parent distribution should hold for all pulsars, the hierarchical Bayesian modelling likelihood for the hyperparameters can be calculated as the product of the individual pulsar likelihoods marginalised over n_i

$$\mathcal{L} \equiv P(\mathbf{D} | \mu, \sigma) = \prod_i \int P(D_i | n_i) N(n_i | \mu, \sigma) \mathrm{d}n_i, \qquad (2.12)$$

where $\mathbf{D}$ refers to the full dataset of all 47 pulsars used in this analysis. The posterior distributions on the braking index, $P(n|D_i)$, for each pulsar, i, can be used as likelihoods in equation (2.12), i.e.,

$$P(D_i | n_i) \propto P(n_i | D_i), \qquad (2.13)$$

which is valid due to having used a uniform prior on n_i in the posterior inference, with the associated constant of proportionality being unimportant. As I have a finite number of posterior samples rather than a functional form of the posterior,

the `posteriorstacker` package makes use of the useful observation that

$$\int P(D_i|n_i)N(n_i|\mu,\sigma)\mathrm{d}n_i \propto \sum_{j=1}^{m_i} N(n_{ij}|\mu,\sigma), \qquad (2.14)$$

where m_i is the number of samples (usually on the order of 20,000 per pulsar when using `dynesty` for the parameter estimation) and n_{ij} are the posterior sample values of the braking index for the ith pulsar, i.e., it is the expectation value/mean of the parent distribution evaluated at the posterior sample values. So, the likelihood that `posteriorstacker` evaluates over μ and σ can be approximated by

$$\mathcal{L} \propto \prod_i \sum_{j=1}^{m_i} N(n_{ij}|\mu,\sigma). \qquad (2.15)$$

Equation (2.12) or (2.15), can be converted to a posterior over μ and σ by multiplying by appropriate priors on these hyperparameters. In this case, the priors are uniform for μ and log-uniform for σ.

Posteriorstacker requires a single file containing the posteriors for each pulsar in separate lines, with the same number of samples given for each pulsar. Since `enterprise_warp` returns varying numbers of samples (this was on the order of 20,000 samples for each pulsar), I must randomly remove surplus samples from the pulsars based on the pulsar with the lowest number of samples.

Posteriorstacker provides two model distributions: histogram (using a Dirichlet prior distribution) and Gaussian. The histogram distribution is more agnostic of the true underlying distribution, but it is therefore also less constraining. I use the Gaussian distribution as it provides better constraints and has fewer parameters to infer (i.e., it is a 'simpler' model) with 0 and 10 being the lower and upper ends of the distribution respectively. For the Gaussian model, `posteriorstacker` estimates the distributions for the mean and standard deviation for the braking index. Posteriorstacker can provide an evaluation of the parent Gaussian distribution at different percentiles of the sampled hyperparameters, i.e., the median (50th percentile) distribution.

To summarise Section 2.2 so far, for each analysis presented below, I perform

the following steps: i) generate simulated TOAs for a set of pulsars, ii) for each pulsar, use the simulated TOAs to draw posterior samples on f, $\dot{f}$, and n using a nested sampling algorithm, and iii) use the combined posterior samples on n from all pulsars to infer posterior samples on the mean μ and standard deviation σ of a parent Gaussian distribution for n.

2.2.5 Quantifying the Results

The results obtained in this analysis are mostly represented as plots, which provide easy visual analysis of the degree to which recovering n is successful. It is also useful to accompany these plots with more quantitative values for easier comparison between results. One method is by calculating the odds ratio that a randomly drawn braking index would be within a given range about the desired value. To achieve this, I begin with the following equation

$$
\int_a^b \frac{\sigma}{\sqrt{2\pi}} \exp\left(-\frac{(x-\mu)^2}{2\sigma^2}\right) dx =
$$
$$
\frac{\sigma^2}{2}\left[\text{erf}\left(\frac{(\mu-a)}{\sqrt{2}\sigma}\right) - \text{erf}\left(\frac{(\mu-b)}{\sqrt{2}\sigma}\right)\right] \tag{2.16}
$$

which is the analytical solution to integrating the Gaussian distribution from a to b, where μ and σ are the mean and standard deviation.

First, I decide on an arbitrary grid on the braking index. Then for each grid bin I evaluate equation (2.16) using the grid bin boundaries, b_{min} and b_{max}, as the limits of integration for the equally weighted posterior sample values distributions. I then sum the probabilities within each bin. For each bin, this gives the odds, $O_{b_{\text{min}}-b_{\text{max}}}$, that a braking index randomly drawn from my distributions would be within that bin:

$$
O_{b_{\text{min}}-b_{\text{max}}} =
$$
$$
\sum_k^{N_k} \frac{\sigma_k^2}{2}\left[\text{erf}\left(\frac{(\mu_k-b_{\text{max}})}{\sqrt{2}\sigma_k}\right) - \text{erf}\left(\frac{(\mu_k-b_{\text{min}})}{\sqrt{2}\sigma_k}\right)\right], \tag{2.17}
$$

where N_k is the number of samples from the posterior of the underlying distribution hyperparameters μ and σ.

To find the equivalent probability within an arbitrary range, for example $[4, 6]$, I can sum up the probabilities for the bins within that range. I can then also sum together the probabilities for all bins, O_{all} (in my case, this is $[0, 10]$) to obtain the odds ratio:

$$OR_{a-b} = \frac{O_{a-b}}{O_{\text{all}} - O_{a-b}}. \tag{2.18}$$

It is important to note that this is not a Bayesian odds ratio, rather it is a straightforward ratio between probabilities. As these values are for comparing the results of analyses with differing parameters, the choice of metric is arbitrary. It must only be consistent and allow for meaningful comparisons. In this analysis, I choose to use 100 bins and calculate the odds ratio within the range $[4, 6]$, denoted as OR_{4-6}. While the choice is arbitrary, this range is chosen as it excludes the $n = 3$ case where the spin-down is due to magnetic dipole radiation alone and $n = 7$ case where it is due to GW emission via r-modes. Figure 2.3 visualises the results of this process for a run with an observation length of 20 years and an RMS noise value of 1×10^{-5} ms using all 47 pulsars. For this run, $OR_{4-6} = 1.00$, meaning there is a 50% chance of drawing a value of n between 4 and 6 from the distributions.

2.3 Analysis Results

Following the methods described in Section 2.2, I repeat the analysis several times, changing the RMS noise, observation length, and number of pulsars to identify the parameters with the greatest impact on the recoverability of the braking index using this method. In the following sections, the "default" parameters will be an observation length of 20 years with a mean RMS noise of 1×10^{-5} ms using all 47 pulsars. The run using these parameters is depicted as the solid blue line in each plot.
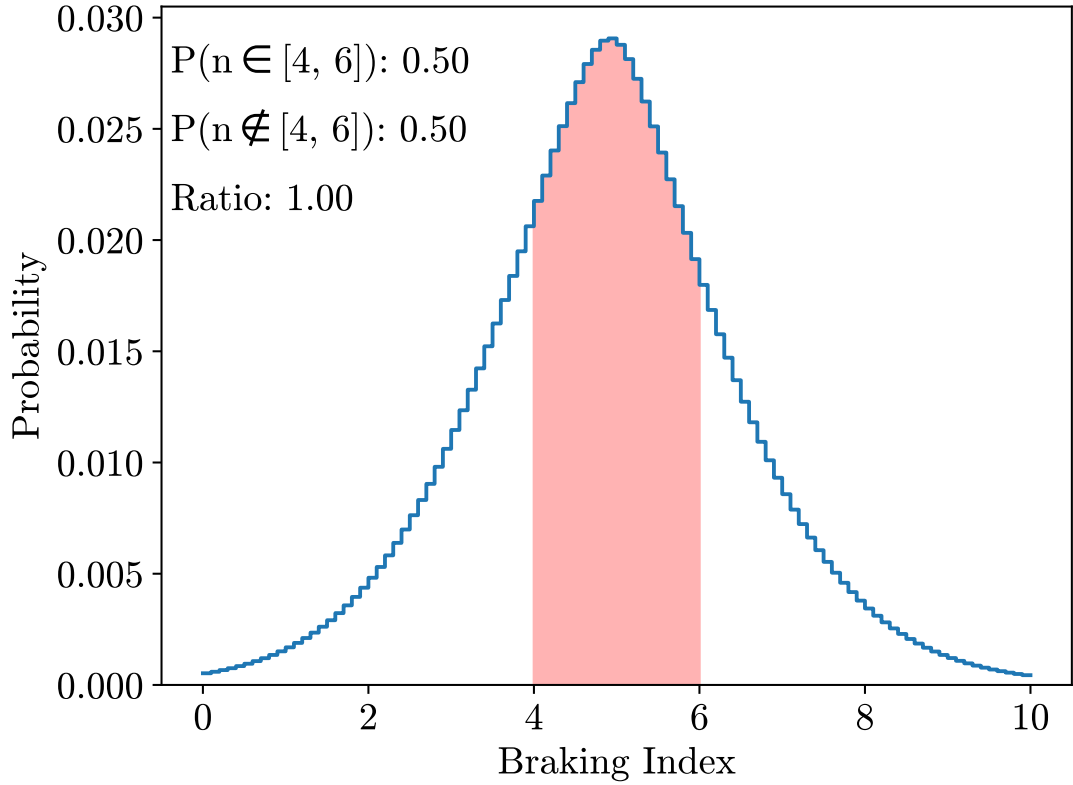
Figure 2.3 A normalised histogram of the equally weighted posterior samples binned into 100 bins for an observation length of 20 years and an RMS noise value of 1×10^{-5} ms using all 47 pulsars. Using equation (2.16), the probability that n lies in the bins between 4 and 6 (shaded in red) and the probability that it lies outside that region is calculated to find OR_{4-6}.
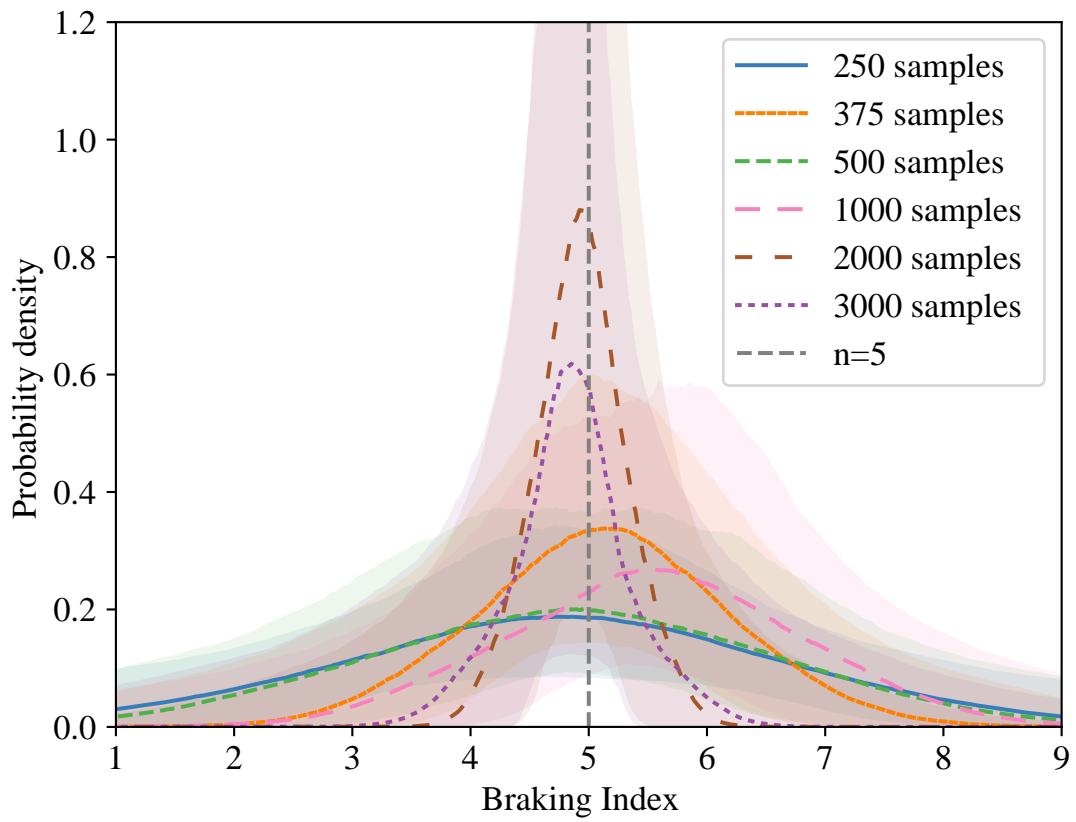
Figure 2.4 The result of varying the number of samples produced by MCMC. The lines represent the median values while the shaded regions are bounded by the 5th and 95th percentiles.

2.3.1 MCMC samples

Before settling on `dynesty` as the sampler, a Markov chain Monte Carlo (MCMC) sampler called `bilby-MCMC` was used. While `dynesty` has its own stopping criteria which causes an arbitrary number of samples to be produced, `bilby-MCMC` takes a desired number of samples selected by the user. This introduces a new parameter to be considered in these analyses. This Section, and Section 2.3.1.1, describe tests performed using the `bilby-MCMC` version of the code which are not relevant when performing this analysis with `dynesty`.

I vary the number of MCMC samples for the bilby sampler to find a good compromise between computation time and producing converged MCMC chains. This allows us to fix the number of samples while varying the other parameters. Unlike the other parameters, the number of samples can be improved without needing advancements in instruments or observations; therefore, it is best to identify a suitable value before looking at the parameters which are more difficult to achieve in reality. I note that the overall number of samples that I can run the MCMC for is also limited by memory constraints, due to the implementation of data storage within the `enterprise` software. Due to this, I limit the maximum samples in a run to 3000.

Figure 2.4 shows the variation in results for different sample sizes. Simulated TOAs are created for all 47 pulsars for an observation length of 20 years and a mean RMS of 1×10^{-5} ms. The solid lines come from generating Gaussians using the median values from the distributions on the braking index, while the shaded bands come from the values at the 95th and 5th percentiles of the distributions. These same TOAs are then used to create each set of samples. This approach mimics the scenario where the analysis would be performed repeatedly on one set of real observational data. The analysis is performed three times for each sample size and the result with the smallest standard deviation on n for each is plotted to help account for random variations (see Section 2.3.1.1). The observation time and mean RMS is chosen for illustrative purposes as it shows a clear variation of confidences across the range of samples.

As can be seen from Figure 2.4, there is evidence for a signal at $n = 5$ and there is a general improvement with increasing sample size. This occurs because

larger sample numbers are more likely to produce convergent MCMC chains. However, there are a few anomalies. For example, the analysis with 375 samples is more confident than the 1000 sample analysis and the 2000 sample analysis is more confident than the analysis with 3000 samples. This is due to random variations introduced both during the analysis to generate posteriors on n and when surplus samples are removed before `posteriorstacker` is used.

2.3.1.1 Selecting samples

As demonstrated in Figure 2.4, there can be large variations in results which sometimes go against expected trends. I investigate sources of random variation and identify that randomly removing excess samples has a much larger effect than anticipated. This is likely due to the samples having a high correlation, meaning that by randomly removing certain values I am skewing the overall distribution.

Figure 2.5 shows the result of the investigation. The same TOA data for all 47 pulsars is used as in Section 2.3.1 for both the 375 (blue) and 3000 (orange) sample runs. However, the sample file given to `posteriorstacker` is generated 5 separate times, so each file contains a different selection of samples. The effect of this selection can be seen in the variation in lines of each colour. It can also be seen that for the larger number of samples, this variation is less significant.

However, the wide variation in these results is suggestive of the MCMC chains not fully converging even for the larger sample sizes. Figure 2.6 shows the trace and posterior histogram plots for the pulsar rotation parameters f, $\dot{f}$, and $\ddot{f}$ for J1713+0747 for a 20-year run with an RMS value of 1×10^{-5} ms, and 2000 samples. The red points at the start represent the burn-in. Stable behaviour can be seen in the trace plots with no evidence of drift. The histograms for $\dot{f}$ and $\ddot{f}$ are both smooth and unimodal, suggesting that the sampler has converged. In comparison, Figure 2.7 shows the trace and histogram plots for B1953+29 for the same analysis. Here, the burn-in period is significant, and the histogram for $\ddot{f}$ is relatively flat, suggesting that the chain may not have fully converged. These examples illustrate that while some pulsars have converged, this cannot be assumed for the whole sample.
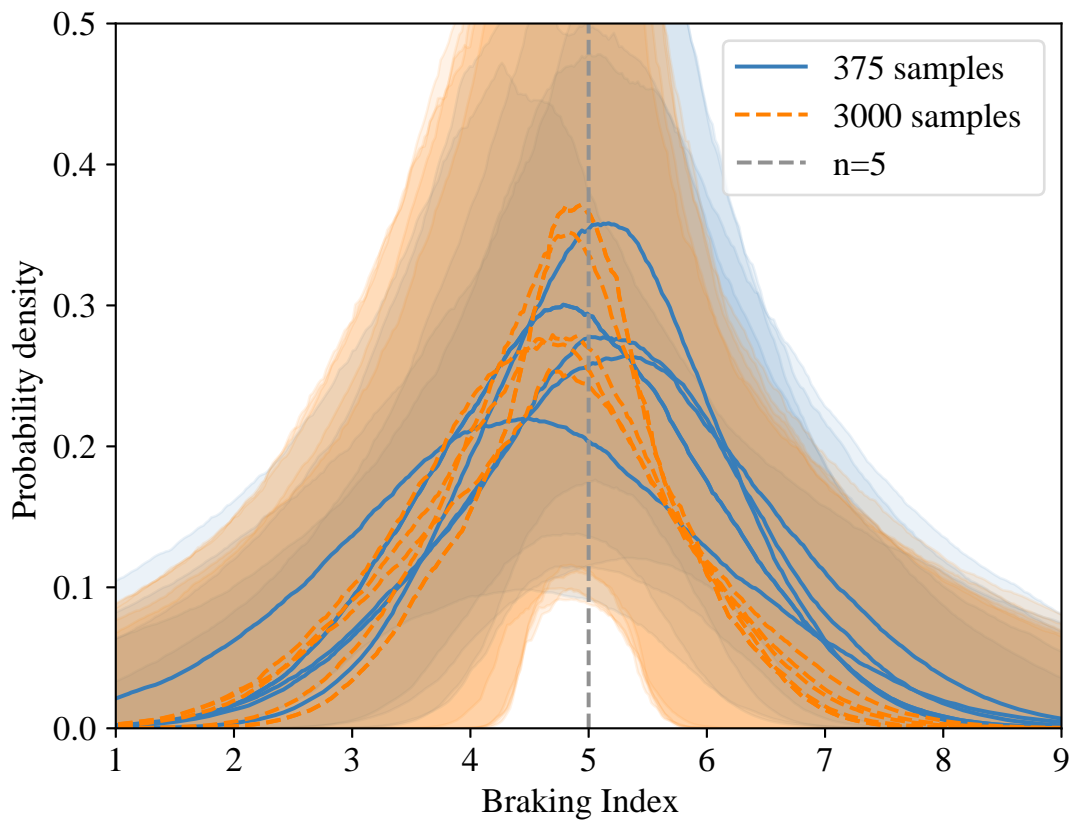
Figure 2.5 The result of identical analyses except for the removal of different excess samples for use in `posteriorstacker`. The blue lines represent results from keeping 375 samples while orange represents keeping 3000 samples. The lines represent the median values while the shaded regions are bounded by the 5th and 95th percentiles.
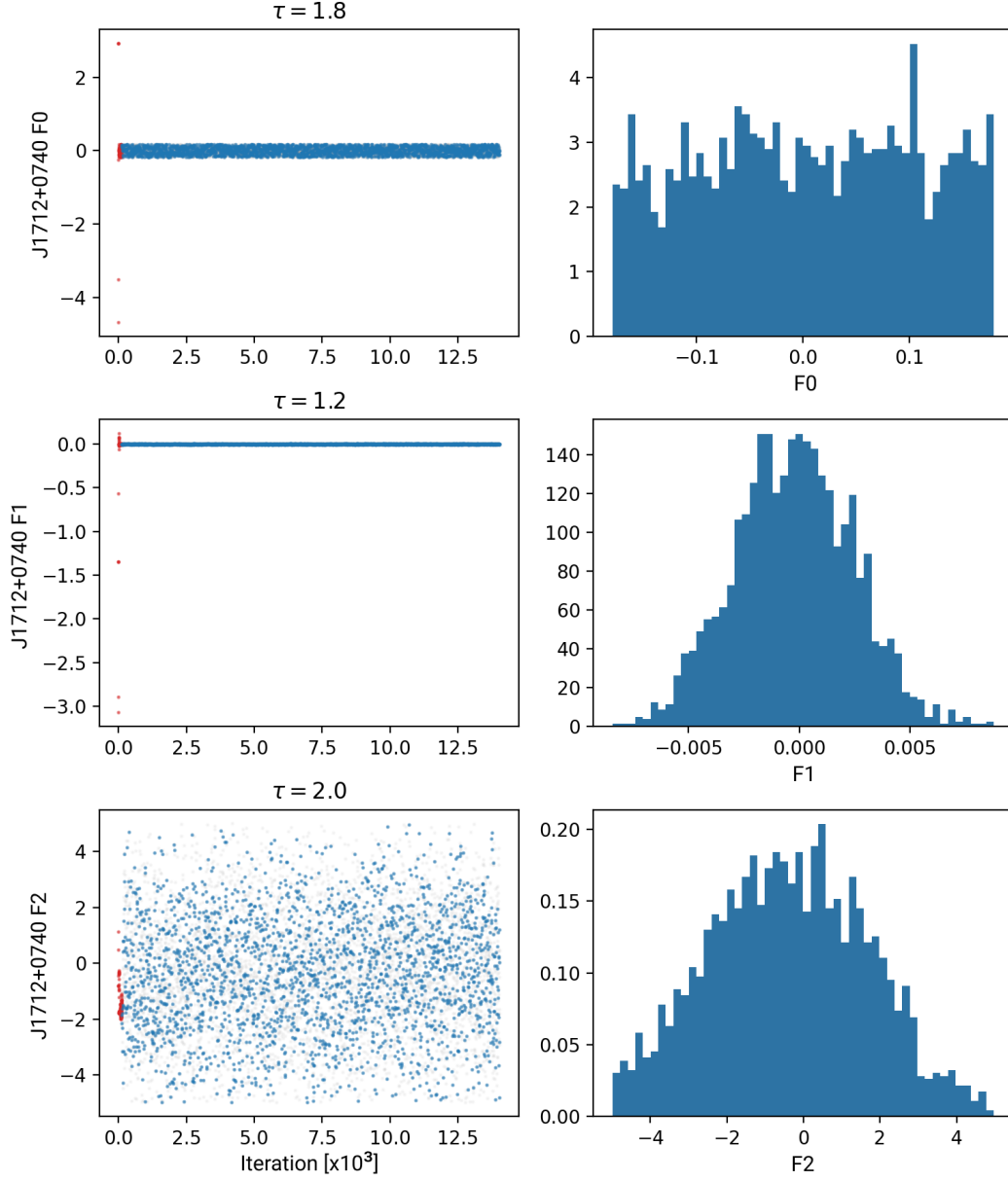
Figure 2.6 The MCMC trace diagram for J1713+0747, with 2000 samples and an average RMS of 1×10^{-5} ms. The red dots represent burn-in and τ is the autocorrelation time. It can be seen that for this pulsar, the MCMC chains appear to have converged.

63
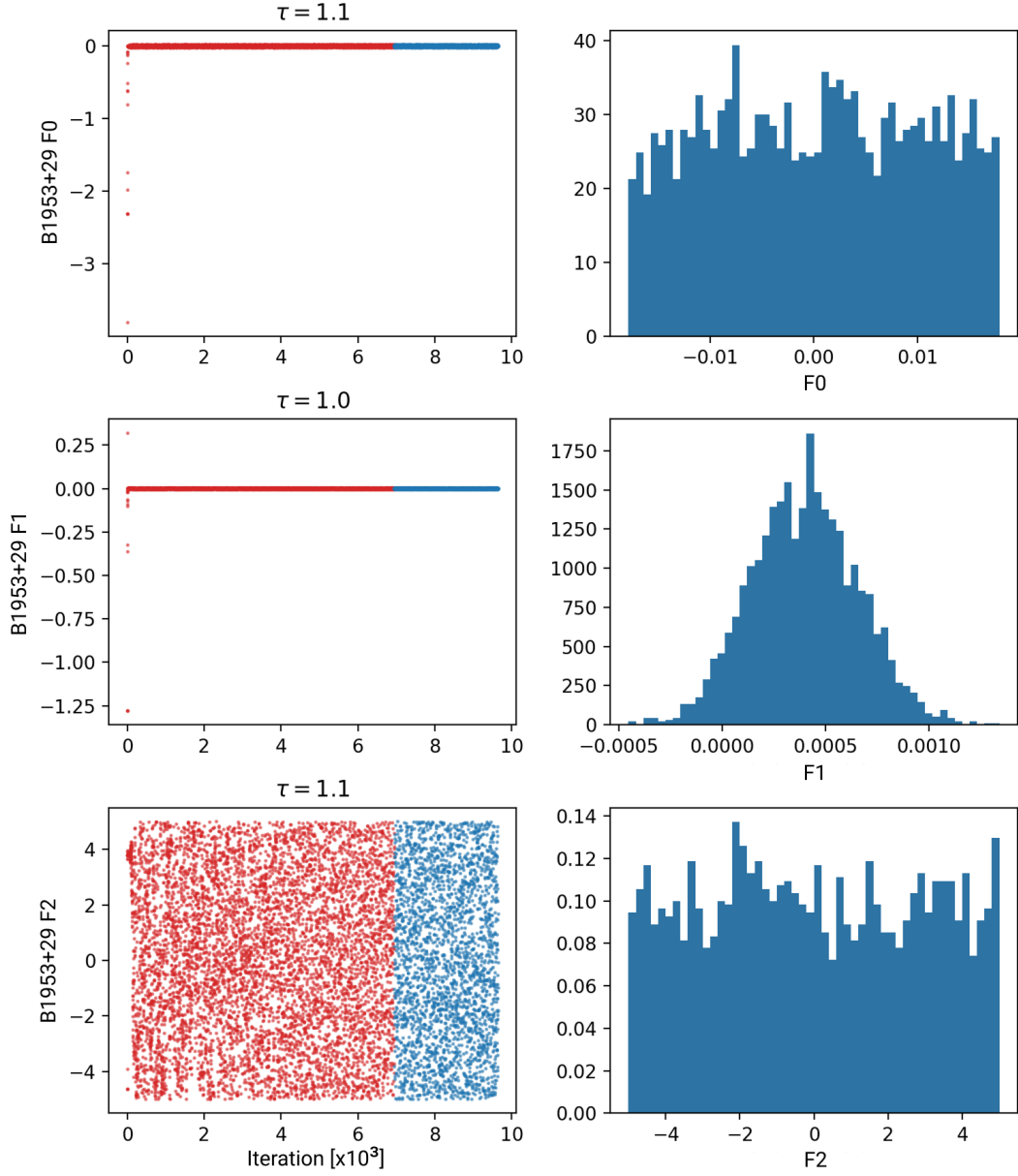
Figure 2.7 The MCMC trace diagram for B1953+29, with 2000 samples and an average RMS of 1×10^{-5} ms. The red dots represent burn-in and τ is the autocorrelation time. It can be seen that for this pulsar, the MCMC chains do not appear to have converged.

These findings indicate that the number of samples tested are insufficient, but as larger sample sizes are infeasible, a new method is required. Instead, a nested sampling method was chosen. By using `dynesty`, 20,000 samples are produced on average before the stopping criteria is met with similar runtimes to those of `bilby-MCMC`, which vastly reduces the effect of removing excess samples for `posteriorstacker`. Additionally, `dynesty` simplifies the process by removing the number of samples from consideration. Therefore, the following sections describe the results obtained using `dynesty` as described in Section 2.2.3.

2.3.2 TOAs and Posteriors

In Figure 2.8, I investigate the variation caused at various stages in the analysis. Each colour represents a different set of TOAs produced by `Tempo2` given identical parameters. These three sets of TOAs are then put through the rest of the analysis five times to see the variation introduced when obtaining posteriors. The variation on each TOA itself is produced during either the `enterprise` or `posteriorstacker` stage while the differences between each TOA would be introduced by `Tempo2`. I calculate the mean and standard deviation of OR_{4-6} for each TOA set to be 0.96 ± 0.03, 0.94 ± 0.02, and 1.04 ± 0.06 for blue, orange, and green respectively. While the green TOA set had higher odds ratios overall, its lowest was still well within the range of the other two. Blue and orange are additionally within each other's ranges, suggesting that the variation from post-processing dominates the variation from the TOA set used.

I conclude that there is little correlation between the TOA data used and the probability density after the full analysis pipeline. Each set of TOAs demonstrates a similar amount of variation with no TOA producing consistently better results. To rule out the amount of variation introduced by `posteriorstacker`, the script is additionally run repeatedly on the same posteriors. This results in negligible variation, so it is concluded that most of the variation is introduced when using `enterprise` to obtain posteriors on n.
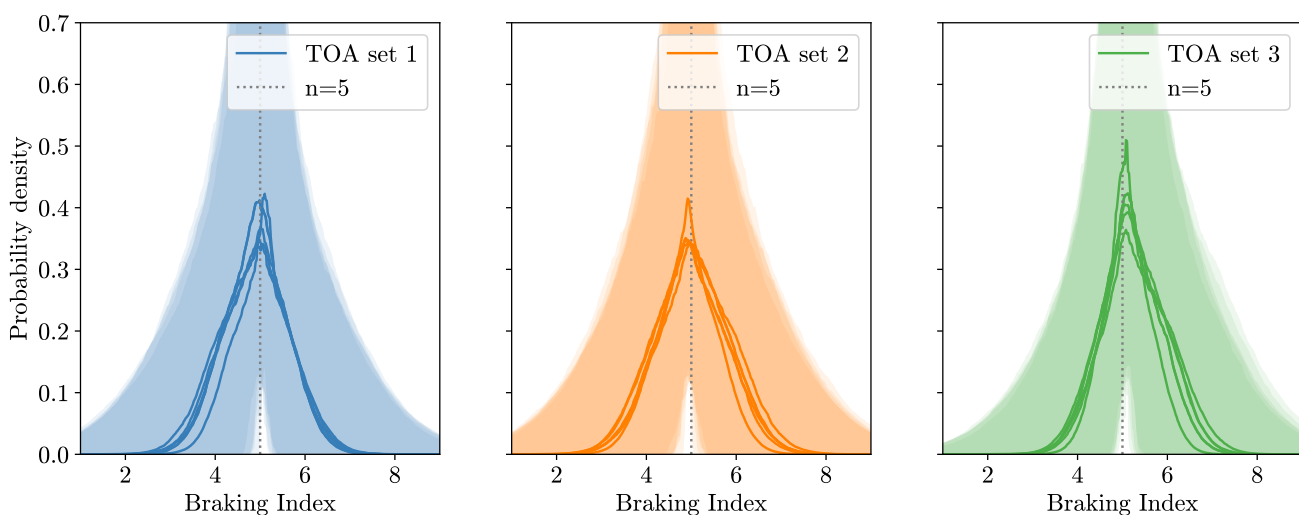
Figure 2.8 The result of identical analyses performed on three sets of TOAs produced by `Tempo2` given identical parameters. It demonstrates the variation introduced during the TOA generation step and posterior analysis. The lines represent the median values while the shaded regions are bounded by the 5th and 95th percentiles. The mean OR_{4-6} for the blue, orange, and green TOAs are: 0.96 ± 0.03, 0.94 ± 0.02, and 1.04 ± 0.06 respectively.
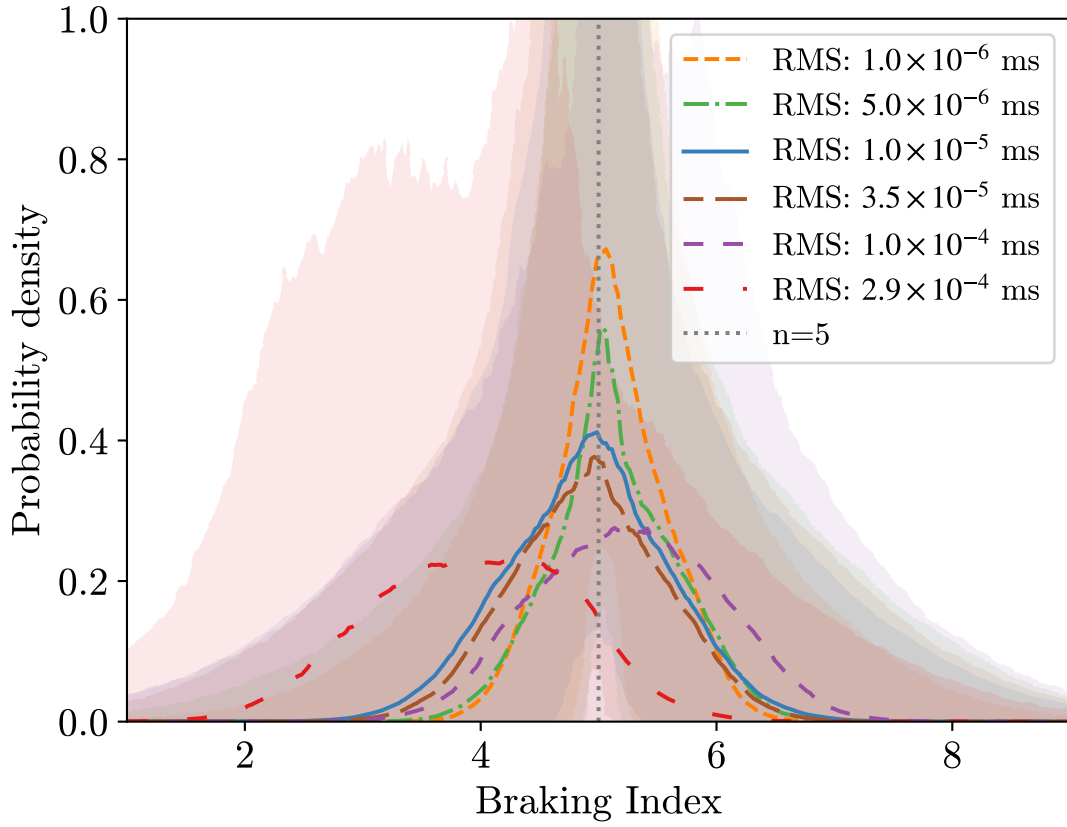
Figure 2.9 Analyses with identical parameters aside from varying the mean RMS noise, calculated using equation (2.5), in the simulated TOAs. The lines represent the median values while the shaded regions are bounded by the 5th and 95th percentiles. The OR_{4-6} for these runs, in order from highest rms to lowest, are: 0.62, 0.88, 0.98, 1.00, 1.06, 1.76.

2.3.3 RMS Noise

Of the three main factors I want to investigate, I look at the RMS noise value first. It makes sense to include the full pulsar population for these comparisons, since pulsars can be analysed in parallel so they do not affect the runtime. Performing this analysis for a 50-year observation length could cost over 262 GB of memory and take on the order of a week to run, so care was taken to avoid running lots of expensive analyses. Therefore, an observation length of 20 years was chosen for repeat analyses. This value is also ideal as in a few years the pulsars in this sample will have 20 years of observations. Changing the mean RMS noise has two effects, as discussed in Section 2.2.1. While it represents white noise on the pulsar TOA data, it can also represent changing the cadence of observations using equation (2.6). It is important to note that the cadence of observations is fixed at 1 per month for all analyses. The following values for RMS (in ms) are chosen:

- 2.9×10^{-4} ms: The mean RMS for the NANOGrav sample.

- 1×10^{-4} ms: It is estimated that the Square Kilometer Array (SKA) will produce this RMS for 50 pulsars (Stappers et al., 2018). The SKA is discussed in more depth in Section 5.2.

- 3.5×10^{-5} ms: The smallest RMS for a pulsar in the NANOGrav sample (J2234+0611).

- 1×10^{-5} ms: The SKA could provide this RMS value for five pulsars (Stappers et al., 2018).

- 5×10^{-6} ms: The equivalent RMS corresponding to a true RMS noise of 1×10^{-5} ms but with an observation every week rather than every month.

- 1×10^{-6} ms: Chosen to demonstrate what kinds of rms values would have a strong effect on the confidence.

Where possible, one set of TOAs is produced and repeated analyses performed on that set with the parameters for the inference analysis varied as desired. This ensures the least amount of random error is introduced. However, with the RMS and observation time comparisons, new TOA data must be produced for each run

as those parameters are used in the production of the simulated data. This means these analyses are subject to additional variation caused by the independent noise realisations. This is likely to be minimal, as discussed in Section 2.3.2.

The results for the various RMS values can be seen in Figure 2.9. The lines represent the median values of a Gaussian braking index distribution for each RMS value and the shaded regions are bounded by the 5th and 95th percentiles. The RMS noise values below 3.5×10^{-5} ms are able to recover the $n = 5$ signal with OR_{4-6} over 1.00, representing a higher likelihood that the braking index is between 4-6 than outside that range (such as $n = 3$ or $n = 7$, which would be expected from magnetic dipole radiation or r-modes respectively). This suggests reasonable accuracy and confidence. The difference between OR_{4-6} for the factor of 10 improvement between 1×10^{-5} ms and 1×10^{-6} is a factor of 1.76. This suggests that for current optimistic projections, decreases to TOA noise will not greatly improve the viability of this analysis method. The RMS noise value of 1×10^{-6} was included to verify that the braking index could be recovered with vast improvements in noise. Values even smaller than this have been tested and, using the change to `enterprise_extensions` described in Section 2.2.3, they continue this trend.

A mean RMS noise value of 1×10^{-5} calculated using equation (2.5) is chosen to be kept constant for the subsequent analyses as it represents a balance between optimistic but still realistic. Table A.1 shows the braking index results for the 20-year run with an RMS noise value of 1×10^{-5} along with the pulsar parameters used to derive it. The individual braking index values come from taking the mean and standard deviation of each pulsar's posterior samples.

2.3.4   Observation Length

Since n depends on the frequency double derivative, which changes very slowly over time, I expect more accurate and confident results with increased observation length. This is especially true as $\ddot{f}$ will have a cubic increase with time. Additionally, $\ddot{f}$ decorrelates with $\dot{f}$ over greater observation periods, making it easier to measure. Figure 2.10 shows the results of five runs of varying observation lengths. In this case, new simulated TOAs are created for each analysis

with different specified lengths going backwards in time. This could theoretically result in slightly better results due to higher pulsar f, $\dot{f}$, and $\ddot{f}$ values than in future measurements. However, this, and the location of the epoch within the observation length, was verified to make negligible difference. The mean RMS noise is kept at 1×10^{-5} ms and I include all 47 pulsars. Identical posterior analyses are performed.

It can be seen that the confidence increases with length of observation. For 10 or fewer years, the correct braking index is not recovered with any significant confidence as reflected by $\mathrm{OR}_{4-6} < 1.00$. In the 20-year run, the mean n is correct, but with a OR_{4-6} value of 1.00 exactly. For longer observation lengths, the correct n is recovered with an OR_{4-6} of 1.46 and 9.65 for 30 and 50 years, respectively. The signal at $n = 5$ for the 50-year run is very significant, although multiple decades must pass before such an observation length is achievable. That time-frame would doubtlessly also herald advances in timing precision which would also improve the probability of a signal. However, it should be remembered that these runs were performed assuming an already optimistic RMS noise value.

2.3.5 Number of Pulsars

Figure 2.11 shows the results of running the analysis with different numbers of pulsars. In this case, the same TOA and posterior data is used for all analyses with an observation time of 20 years and an RMS noise of 1×10^{-5} ms. Originally, the pulsars to be included were chosen randomly, but it was identified that one pulsar with a well-constrained braking index dominates the results, causing improvements the moment it is included. To limit this effect, the pulsar is automatically included in the dataset for the first 10 pulsars, and all subsequent datasets. Reproducing this plot results in variation only due to the random selection of pulsars added to each run.

Increasing the number of pulsars is shown to improve the confidence of the detection of n as expected. While the signal is dominated by one exceptional source which is included from the start, it can be further improved by increasing the population size. There is roughly a factor of 2 improvement between the maximum probability densities for the 10- and 47-pulsar runs, which demonstrates
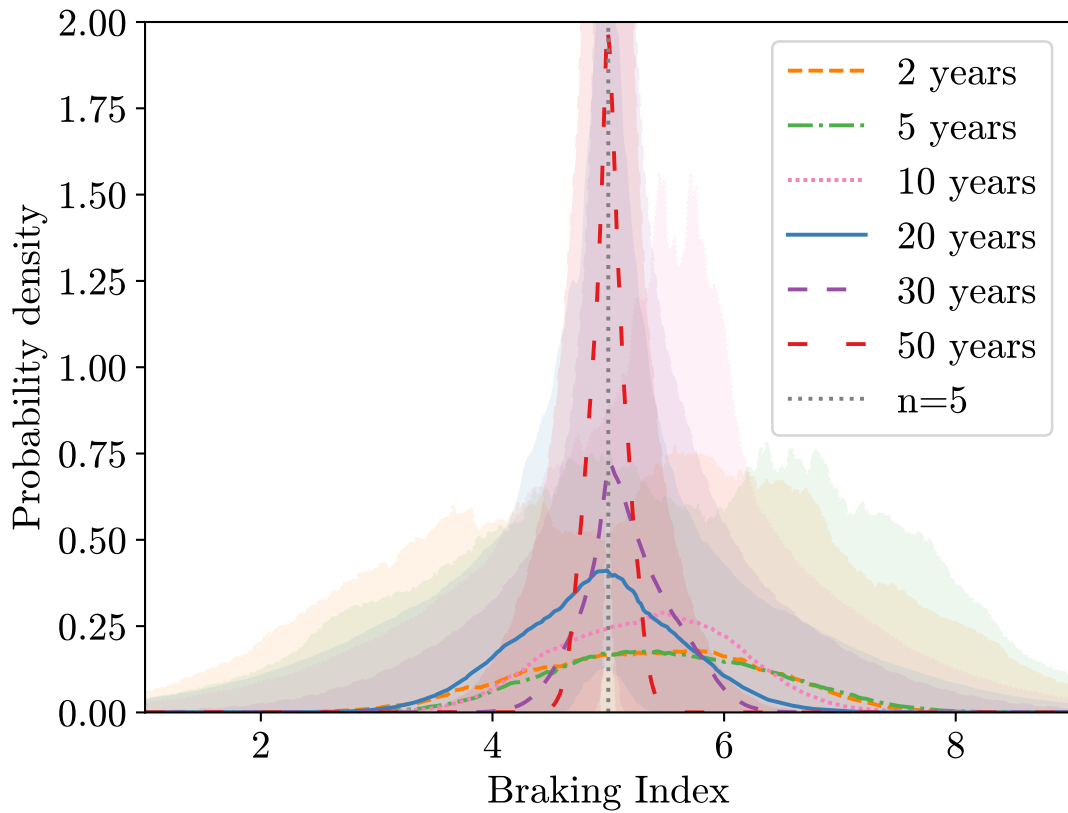
Figure 2.10 Analyses with identical parameters aside from varying observation time. The lines represent the median values while the shaded regions are bounded by the 5th and 95th percentiles. The OR_{4-6} for these runs, in order from shortest to longest observation length, are: 0.69, 0.69, 0.92, 1.00, 1.46, 9.65.
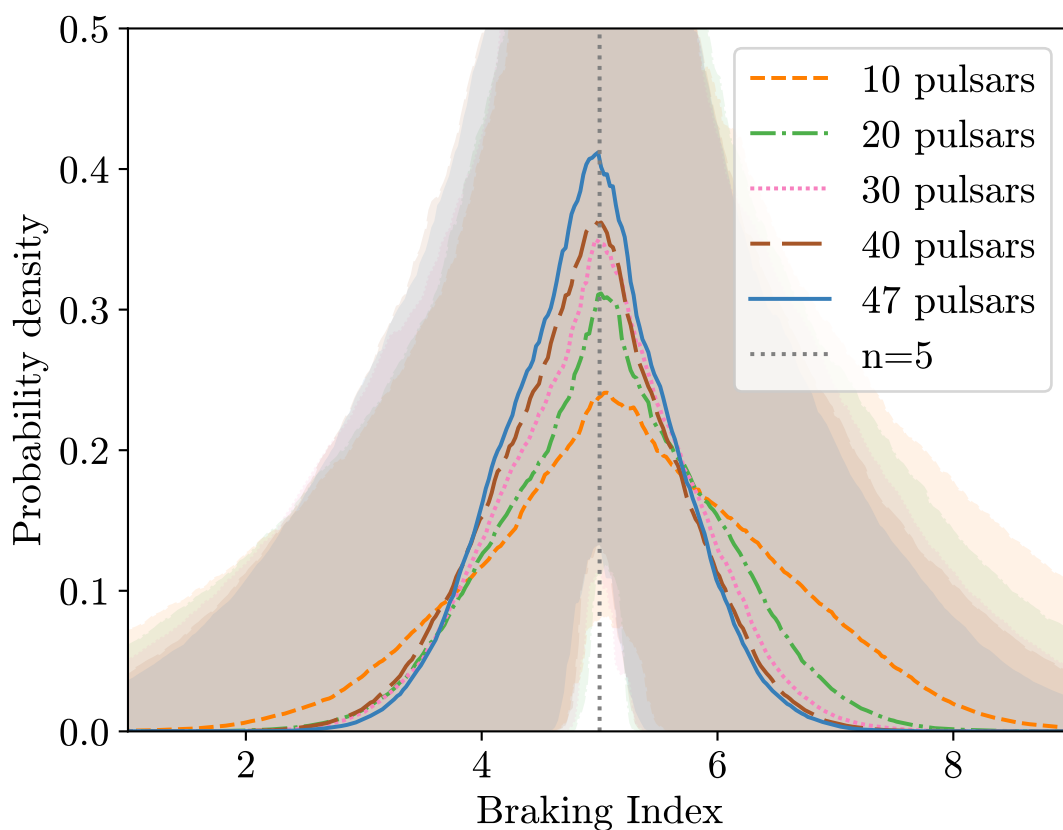
Figure 2.11 Analyses with identical parameters aside from varying the number of pulsars. For each set, additional pulsars are picked at random except for the pulsar with the strongest signal, which was included in all runs. The lines represent the median values while the shaded regions are bounded by the 5th and 95th percentiles. The OR_{4-6} for these runs, in order from fewest to the most pulsars, are: 0.53, 0.70, 0.81, 0.90, 1.00.

the significance of sample size, even if the added pulsars are not better constrained than those already included in the sample.

The pulsar selected to be included in the 10-pulsar run is B1937+21 with $n = 5.01 \pm 0.06$. This pulsar has the highest frequency derivative and therefore also the highest double derivative, as can be seen in Table A.1.

2.3.6 Varying Braking Index

So far, all analyses have been run on simulated TOAs with n fixed at 5. To test the ability of this method to identify any value of n, runs are performed on TOAs with different true values of n. I perform three analyses with 20 years of observation at an RMS noise level of 1×10^{-6}. These values are chosen as they produce accurate and confident results in the other analyses. Tests for $n = 3$ and $n = 7$ are chosen as they represent the braking indices due to magnetic dipole radiation and r-mode GWs respectively (see 2.1). Figure 2.12 shows that a strong signal is found for all three analyses with similar confidences and accuracies, verifying that this method is not biased towards a braking index of 5.

2.4 Discussion

This analysis looks at purely simulated data from reduced pulsar parameters to represent simple, isolated versions of real pulsars. Therefore, when performing this analysis on real data it is reasonable to expect that it would be harder to extract the underlying distribution of n. Specifically, the inclusion of parameters which are correlated with $\ddot{f}$, such as the proper motion of the pulsar or non-white timing noise, would make this more complicated. I also assume that the measured $\dot{f}$ is dominated by the intrinsic spin-down and not contaminated by acceleration effects. The results in this chapter therefore represent an optimistic scenario, but are presented as a proof-of-principle study.

Of the factors considered, improvement of some are more achievable than others. Although some pulsars, such as Vela, have been observed for 50 years, having a large sample with consistent observations and small timing residuals for
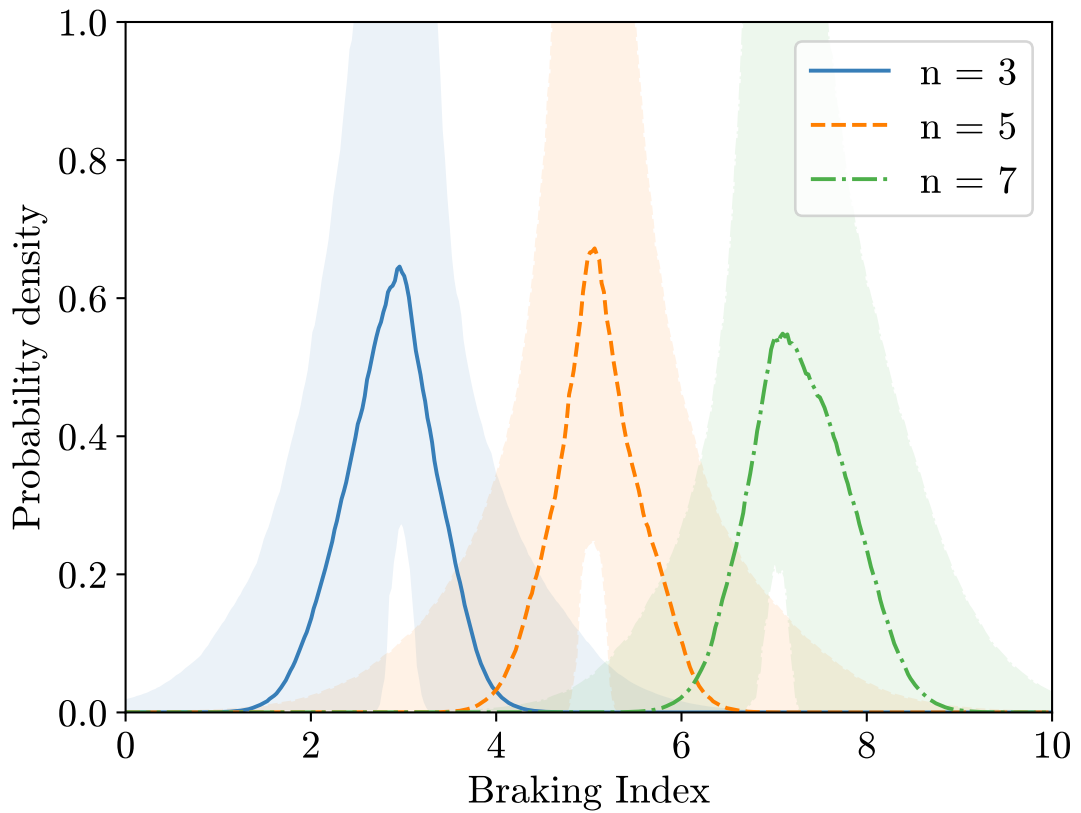
Figure 2.12 Analyses with identical parameters aside from varying the braking index used to set $\dddot{f}$ when generating the simulated TOAs. The lines represent the median values while the shaded regions are bounded by the 5th and 95th percentiles.

such a timescale will not happen soon. For example, the NANOGrav dataset (Alam et al., 2020) used in this analysis has 12.5 years of observations for 47 pulsars, while the EPTA has 24 years for 6 pulsars (Chen et al., 2021) and the PPTA as observed 30 MSPs spanning up to 18 years (Reardon et al., 2023). The newest NANOGrav dataset, the 15-year dataset, has 67 pulsars (Agazie et al., 2023). These three groups are part of the International Pulsar Timing Array (IPTA). In the future, combined arrays will allow for much larger populations of pulsars to be analysed for longer periods of time, thus increasing the likelihood that this analysis would observe the underlying distribution on the braking index.

Increasing the cadence of observations is known to have the same effect as reducing the RMS noise. However, even with collaborations such as the IPTA, it may be more beneficial to have individual telescopes observing different pulsars than for multiple telescopes observing the same source (Lam, 2018). Therefore, improving the RMS noise itself would be preferable as it would free observation time for other targets. The SKA, which is currently in construction and expected to enter operation by the end of the decade, could provide an RMS noise of 1×10^{-4} ms for 50 pulsars and potentially 1×10^{-5} ms for five more (Stappers et al., 2018).

2.5 Summary

This chapter looks at the feasibility of observing the braking index, n of a population of pulsars in order to identify the types of processes involved in angular momentum loss. Simulated pulsar TOA data with an injected braking index of $n = 5$ is produced using `Tempo2` (Edwards et al., 2006; Hobbs et al., 2006a, 2009). Without assuming any prior knowledge of n, posteriors are produced by `enterprise` (Ellis et al., 2020) for each pulsar, which are then combined using the hierarchical Bayesian model in `posteriorstacker` (Buchner, 2021). The effect of RMS noise, observation length, and number of pulsars in the sample are investigated.

It is found that with realistically optimistic values for RMS noise, I am able to accurately recover the braking index from the sample, but with a low OR_{4-6} of around 1.0, which means it is equally likely that n is between $4 - 6$ as it is

outside that range. Decreasing the RMS noise to values better than predicted for upcoming detectors enables us to recover the signal accurately and confidently, but order of magnitude improvements would be needed to increase the ratio by a factor of 1.5. Due to the difficulty of such an improvement, this parameter is likely to have the least effect on the feasibility of this method in the near future.

The observation length is found to have a significant impact on how well n is recovered with this method. Using an optimistic value for the RMS noise, a 20-year observation length enables accurate identification of n with an OR_{4-6} of 1.00. For longer observation lengths, the odds ratio increases significantly to 9.65 for the 50-year run. This parameter has a big impact on the feasibility of this method, but by definition requires many years to pass.

The number of pulsars is also found to increase the likelihood of confidently recovering a signal significantly, with a factor of four increase in the number of pulsars resulting in a factor of 2 increase in OR_{4-6}. With more telescopes being built and the increase in large collaborations, this parameter should not be too difficult to improve and therefore is likely to have a substantial impact on the feasibility of this method.

In conclusion, I have developed a method for extracting the braking index distribution for a set of millisecond pulsar observations. In my proof-of-principle studies, I have shown that this works for a simplified scenario under some optimistic assumptions. While this may not provide a way to confidently constrain a particular pulsar braking mechanism if applied to current real timing datasets, this may be possible with future observations. It is still worthwhile testing the method on real datasets, with some of my assumptions and simplifications relaxed, to see what constraints can be placed on values of the braking index.

Chapter 3

Searches for Gravitational Waves from Known Pulsars in the Second and Third LIGO-Virgo Observing Runs

3.1 Introduction

To date, the LIGO and Virgo observatories have made detections of numerous sources of gravitational radiation. These detections have been of transient gravitational waves (GWs) from the inspiral and subsequent mergers of compact binary objects including binary black holes and binary neutron stars (Abbott et al., 2021b). Recently, the list of observed events expanded to include neutron star-black hole binaries (Abbott et al., 2021d). There remain other types of GW sources that are yet to be observed such as continuous GW (CW) sources. Unlike transients, CW signals are almost monochromatic, with their amplitude and frequency changing negligibly over year-long timescales. The mass quadrupoles of these sources, such as deformed neutron stars, are expected to be far smaller than those involved in compact binaries and therefore only local galactic sources

are likely to produce detectable signals.

As discussed in Section 1.4.3, likely candidates for producing such signals are neutron stars spinning with some non-axisymmetric deformation (Zimmermann and Szedenits, 1979), particularly solid deformation which can manifest as NS ellipticities or 'mountains'. GW radiation can also be caused by fluid modes of oscillation beneath the crust such as r-modes. By detecting CWs, light can be shed on the structure of the star. Additionally, detections of such GWs can be used to test general relativity via the constraint of non-standard GW polarisation (Abbott et al., 2019e; Isi et al., 2017). A more thorough discussion of various methods of GW emission from neutron stars can be found in Riles (2017) and Glampedakis and Gualtieri (2018).

The structure of this chapter is as follows. Section 3.1.1 outlines the types of CW searches. Section 3.1.2 describes the types of signal models used in this analysis. Section 3.2 describes the search method used. Section 3.3 covers both the GW and EM data used. I present my results in Section 3.4 with conclusions in Section 3.5.

3.1.1   Continuous-Wave Searches

The three types of CW searches are described in more detail in Section 1.4.3 but summarised here for completeness. Targeted searches look for signals from known pulsars for which their rotational phases can be accurately determined from electromagnetic (EM) observations (e.g., Abbott et al., 2017a, 2019b, 2020b, 2021c; Ashok et al., 2021; Nieder et al., 2019, 2020). This simplifies the search as the EM observations can be used to derive a timing solution and it is assumed that the GW phase evolution is locked to the EM evolution. This means the search is over a small parameter space, generally limited to the unknown signal amplitude and orientation of the source, which allows a more sensitive search than other methods. In some targeted searches, the assumption that the GW evolution follows the EM evolution is relaxed and the search is performed in a narrow band around the expected frequency and spin-down rate (Abbott et al., 2017d, 2019d). In this case, the search is more computationally expensive due to the larger parameter range being searched and slightly less sensitive because

of a higher trials factor. To overcome this, narrowband searches often look at fewer targets. Directed searches look for signals from small sky regions that are believed to have a high probability of containing a neutron star, such as supernova remnants. As the timing solution cannot be derived from EM observations, a wide range of rotational parameters (such as rotation frequency and its derivative) must be searched. All-sky searches look for signals in all sky directions and over a wide range of rotational parameters. Both these methods suffer increasing computational costs and decreasing sensitivity of the searches as parameter space increases.

Searches of all three types have been performed and so far no convincing evidence for CWs has been observed. However, searches have probed new regimes, such as providing upper limits on emission that are more stringent (i.e., smaller) than those based on energetics arguments. For example, for several pulsars including the Crab pulsar, Vela pulsar (Abbott et al., 2019b), J0537−6910 (Abbott et al., 2021c,g) and two millisecond pulsars (Abbott et al., 2020b) the direct upper limits set on the GW amplitude are more constraining than limits based on the assumption that all the pulsars' spin-down luminosity is radiated through GWs, known as the spin-down limit.

In this chapter I report the results of a targeted search for CW signals from 236 pulsars using the second and third LIGO-Virgo observing runs (O2 and O3 respectively). A description of these detectors can be found in Section 1.3, while Section 3.3.1 details the observing runs. The ephemerides for the pulsars have been derived from observations using the CHIME, Hobart, Jodrell Bank, MeerKAT, Nancay, NICER and UTMOST observatories. More details on these EM observations can be found in Section 3.3.2.

3.1.2 Signal Models

I assume that the GW emission is locked to the rotational phase of the pulsar. For the ideal case of a triaxial star rotating steadily about a principal moment of inertia axis, the GW emission is at twice the star's spin frequency, $f_{\rm rot}$. However, there are mechanisms that can produce variations to this $2f_{\rm rot}$ frequency. For example, a superfluid component with a misaligned spin axis within the star

could produce a dual-harmonic emission at both once and twice the rotation frequency without leaving an imprint on the EM emission (Jones, 2010). Therefore, I perform two searches: one at just twice the pulsar rotation frequency called a single-harmonic search, and one at both one and two times the frequency referred to as a dual-harmonic search.

The waveform used in the dual-harmonic search is detailed in Jones (2010) and used in Pitkin et al. (2015), Abbott et al. (2017a), Abbott et al. (2019b), and Abbott et al. (2020b). The signals h_{21} and h_{22} at once and twice the pulsar rotation frequency can be defined as

$$
\begin{aligned}
h_{21} &= -\frac{C_{21}}{2}\Big[\; F_+^D(\alpha, \delta, \psi; t)\sin\iota\cos\iota\cos\left(\Phi(t) + \Phi_{21}^C\right) + \\
&\qquad\qquad F_\times^D(\alpha, \delta, \psi; t)\sin\iota\sin\left(\Phi(t) + \Phi_{21}^C\right)\Big], \qquad (3.1) \\
h_{22} &= -C_{22}\Big[\; F_+^D(\alpha, \delta, \psi; t)(1 + \cos^2\iota)\cos\left(2\Phi(t) + \Phi_{22}^C\right) + \\
&\qquad\qquad 2F_\times^D(\alpha, \delta, \psi; t)\cos\iota\sin\left(2\Phi(t) + \Phi_{22}^C\right)\Big], \qquad (3.2)
\end{aligned}
$$

where C_{21} and C_{22} are the dimensionless constants that give the component amplitudes, the angles (α, δ) are the right ascension and declination of the source, while the angles (ι, ψ) describe the orientation of the source's spin axis with respect to the observer in terms of inclination and polarisation respectively, Φ_{21}^C and Φ_{22}^C are phase angles at a defined epoch, and $\Phi(t)$ is the rotational phase of the source. The antenna functions F_+^D and $F_\times^D$ describe how the two polarisation components (plus and cross as derived in Section 1.2) are projected onto the detector.

For the ideal case of a steadily spinning triaxial star emitting GWs only at twice the rotation frequency, the equatorial ellipticity can be defined as

$$
\varepsilon \equiv \frac{|I_{xx} - I_{yy}|}{I_{zz}}, \qquad (3.3)
$$

where (I_{xx}, I_{yy}, I_{zz}) are the source's principal moments of inertia, with the star rotating about the z-axis. The mass quadrupole of the source Q_{22} is often quoted

and is related to the ellipticity as

$$Q_{22} = I_{zz}\varepsilon\sqrt{\frac{15}{8\pi}}. \tag{3.4}$$

For single-harmonic emission, C_{21} from equation (3.1) can be set as 0, leaving only C_{22} in equation (3.2). The amplitude can then be parameterised as the dimensionless h_0: the amplitude of the circularly polarised signal that would be observed if the source lay directly above or below the plane of the detector and had its spin axis pointed directly towards ($\iota = 0$) or away ($\iota = \pi$) from the detector. In this configuration, the plus and cross polarisations have equal amplitude and a phase difference of $\pi/2$, equivalent to circular polarisation. The polarisation angle ψ described how the circularly polarised wave projects onto the detector arms via the antenna functions. When $\psi = 0$, $\mathrm{F}_+ = 1, \mathrm{F}_\times = 0$ and when $\psi = \pi/4$, $\mathrm{F}_+ = \mathrm{F}_\times = 1/\sqrt{2}$.

The following equations are defined in Aasi et al. (2014):

$$h_0 = 2C_{22} = \frac{16\pi^2 G}{c^4}\frac{I_{zz}\varepsilon f_{\mathrm{rot}}^2}{d}, \tag{3.5}$$

where d is the distance of the source, c is the speed of light in a vacuum and G is the gravitational constant. The spin-down limit h_0^{sd} of a source is given by:

$$h_0^{\mathrm{sd}} = \frac{1}{d}\left(\frac{5GI_{zz}}{2c^3}\frac{|\dot{f}_{\mathrm{rot}}|}{f_{\mathrm{rot}}}\right)^{1/2}, \tag{3.6}$$

where $\dot{f}_{\mathrm{rot}}$ is the first derivative of the rotational frequency, i.e., the spin-down rate, and provides an amplitude limit assuming that all the rotational energy lost by the pulsar is converted to GW energy (Owen, 2005). When h_0 is smaller than h_0^{sd}, the spin-down limit can be said to have been surpassed. This information is most often represented by quoting the 'spin-down ratio', i.e., the ratio between h_0 and h_0^{sd}. If, assuming that there is no mechanism (e.g., accretion) providing some additional spin-up torque, the direct amplitude constraints probe a new physical regime only when the spin-down limit is surpassed. There are two types of spin-

down rate: intrinsic and observed. The observed spin-down rate can be affected by the transverse velocity of the source, e.g., the Shklovskii effect (Shklovskii, 1970), so where possible the intrinsic spin-down rate is used to calculate the spin-down limit.

3.2 Analysis

In this analysis, I perform a time-domain Bayesian analysis method. This method searches for two signal models: a single-harmonic signal emitted by the $l = m = 2$ mass quadrupole mode at twice the pulsar rotation frequency and a dual-harmonic signal emitted by the $l = m = 2$ and $l = 2, m = 1$ modes at twice and once the frequency.

The raw GW strain data are heterodyned using their expected phase evolution, which includes both corrections for the relative motion of the source with respect to the detector and relativistic effects (Dupuis and Woan, 2005). This results in the data being centred about the expected signal frequency now at $0\,\mathrm{Hz}$. They are then low-pass filtered using a cut-off frequency of $0.25\,\mathrm{Hz}$ and then down-sampled to one sample per minute. For the dual-harmonic search this is repeated so that time series are obtained centred at both f_{rot} and $2f_{\mathrm{rot}}$. Bayesian inference is used to estimate the remaining unknown signal parameters and the evidence for the signal model (Pitkin et al., 2017). For the parameter inference, the prior distributions used are those given in Appendix 2 of Abbott et al. (2017a). They are uninformative uniform priors for the orientation angles, unless restricted ranges are appropriate as discussed in Section 3.2.2. For the amplitude parameters, Fermi-Dirac distribution priors are used (see Section 2.3.5 of Pitkin et al., 2017). The Fermi-Dirac distributions for each pulsar are set such that they are close to flat over the bulk of the likelihood while penalising very large values. This choice of prior means that the amplitude posteriors will be dominated by the likelihood even when no signal is observed. Any upper limits derived from the posteriors will be more conservative than those that would be found from using an uninformative Jeffreys prior that is uniform in the logarithm

of the amplitude, i.e., $p(h_0) \propto 1/h_0$. To avoid basing the priors on current detector data, the priors are constructed by choosing Fermi-Dirac parameters that give distributions for which the 95% probability upper bound is equivalent to the estimated upper limit sensitivity of the combined LIGO S6 and Virgo VSR4 science runs at the particular pulsar GW signal frequency.[1]

This method also considers the effect of glitches on the pulsars (Section 1.6.4) and can perform searches with restrictions on the pulsar orientation (Section 3.2.2).

3.2.1   Glitches

Although their frequency is usually very stable, pulsars occasionally experience a transient increase in rotation frequency and frequency derivative called glitches. These are discussed in more detail in Section 1.6.4. Some of the sample of pulsars glitched during the course of O2 and O3. I assume that glitches affect the GW phase identically to the EM phase, but with the addition of an unknown phase offset at the time of the glitch. This phase offset is included in the parameter inference. For glitches that occur before or after the range of the data, no phase offset is needed. The pulsars which experienced glitching during the course of this analysis are J0534+2200, also known as the Crab pulsar (Shaw et al., 2021), J0908−4913 (Lower et al., 2019) and J1105−6107. They are shown in Table 3.1 along with the time (MJD) of the glitch.

Table 3.1 Pulsars with glitches occurring during the course of the runs used in this analysis.

PSR	Epoch (MJD)
J0534+2200 (Crab)	58687.6448 ± 0.0033
J0908−4913	58767.34 ± 4.5
J1105−6107	58582.24

---

[1]For the dual-harmonic search for pulsars with signal components below 20 Hz, the C_{21} priors are constructed without using the estimated VSR4 Virgo sensitivity. This is to prevent the prior from dominating over the likelihood in this frequency region.

3.2.2 Restricted Orientations

Occasionally, the orientation of a pulsar can be determined from modelling of X-ray observations of its pulsar wind nebula (Ng and Romani, 2004, 2008). In such cases, these values can be included as narrow priors on inclination ι and polarisation Ψ angle rather than using an uninformative uniform prior. Results still assuming uniform priors are also included. Such pulsars are shown in Table 3.2 (below) along with their restricted prior ranges (Abbott et al., 2017a), which are assumed to be Gaussian with the given mean and standard deviation.

Table 3.2 Pulsars with observations sufficient to restrict their orientation priors in terms of inclination ι and polarisation Ψ angles and the values used as the constraints. The two values for ι are to incorporate the unknown rotation direction in the search by using a bimodal distribution. The additional ι_2 is simply $\pi - \iota_1$ radians.

PSR	Ψ (rad)	ι_1 (rad)	ι_2 (rad)
J0534+2200 (Crab)	2.1844 ± 0.0016	1.0850 ± 0.0149	2.0566 ± 0.0149
J0835-4510 (Vela)	2.2799 ± 0.0015	1.1048 ± 0.0105	2.0368 ± 0.0105
J1952+3252	0.2007 ± 0.1501		
J2229+6114	1.7977 ± 0.0454	0.8029 ± 0.1100	2.3387 ± 0.1100

In the case of the Crab pulsar, which both experienced a glitch and has sufficient observations for restricted priors, four individual analyses are performed. Each analysis accounts for the glitch, with combinations of dual/single-harmonic search and restricted/unrestricted priors.

3.3 Data Sets Used

3.3.1 Gravitational-Wave Data

The data set used O2 and O3 runs. The O2 run took place between 2016 October 30 (MJD: 57722.667) and 2017 August 25 (MJD: 57990.917). Virgo joined O2 on 2017 August 1. The duty factors for L1, H1, and V1, were 57%, 59%, and 80%, respectively. O3 took place between 2019 April 1 (MJD: 58574.625) and 2020 March 27 (MJD: 58935.708). Virgo was operational for the whole of the

O3 run. The duty factors for this run were 76%, 71%, and 76% for L1, H1, and V1, respectively. The uncertainties on the amplitude and phase calibration of the detectors for O2 can be found in Cahillane et al. (2017) and Acernese et al. (2018) and those for O3 can be found in Sun et al. (2020), Sun et al. (2021), and Acernese et al. (2022). For O2, the maximum 1σ amplitude uncertainties over the range 10-2000 Hz were between about $[-2.5, +7.5]\%$ and $[-8, +4]\%$ for H1 and L1, respectively, and for Virgo the maximum uncertainty was 5.1%. For O3, the maximum 1σ amplitude uncertainties over the range 10-2000 Hz were between about $[-5, +7]\%$ and $[-5.5, +5.5]\%$ for H1 and L1, respectively, and for Virgo the maximum uncertainty was 5%. These ranges are the extremes of the upper and lower bound over the full frequency range and over different measurement epochs over the run, so at specific frequencies/times the uncertainty can be far smaller.

The data used underwent cleaning processes (Acernese et al., 2022; Davis et al., 2019; Viets and Wade, 2021), specifically the removal of narrowband spectral artifacts at the calibration line frequencies and power line frequencies. A discussion on the consequences of performing a search using LIGO data with versus without the narrowband cleaning of Viets and Wade (2021) applied can be found in Section 3.4.2.

3.3.2 Electromagnetic Data

EM observations of pulsars produce the timing solutions used as input to the GW searches. These observations have been made in radio and X-ray wavelengths. The observatories which have contributed to the data set are: the Canadian Hydrogen Intensity Mapping Experiment (CHIME) (as part of the CHIME Pulsar Project; Amiri et al., 2021a), the Mount Pleasant Observatory 26 m telescope, the 42 ft telescope and Lovell telescope at Jodrell Bank, the MeerKAT project (as part of the MeerTime project; Bailes et al., 2020), the Nançay Decimetric Radio Telescope, the Neutron Star Interior Composition Explorer (NICER) and the Molonglo Observatory Synthesis Telescope (as part of the UTMOST pulsar timing programme; Jankowski et al., 2019; Lower et al., 2020). Pulsar timing solutions

were determined from this data using TEMPO (Nice et al., 2015) or TEMPO2 (Edwards et al., 2006; Hobbs et al., 2006a, 2009) to fit the model parameters[1].

Pulsars whose rotation frequency is greater than 10 Hz are selected so they are within the sensitivity band of the GW detectors. This leads to primarily targeting millisecond pulsars and fast spinning young pulsars. Of the 236 pulsars in this analysis, 74 are different from the 221 used in the O2 analysis (Abbott et al., 2019b). There are 168 pulsars in binary systems and 161 are millisecond pulsars (see Section 1.6.1 for more detail about millisecond pulsars). The pulsar J0537−6910 is not included due to the recently published searches for it in Abbott et al. (2021c,g).

For some pulsars, ephemerides were only available for the course of O3. In such cases, only GW data from O3 was used. This is the case for 102 out of the 236 pulsars in this analysis.

3.4 Analysis Results

No evidence for GW signals from any of the included pulsars is found. The results for all except the high-value targets are shown in Table A.2. The pulsars which surpass their spin-down limits are labelled as 'high-value' pulsars and are shown in Table A.3 and discussed in Section 3.4.1. As no CWs are observed, I present the 95% credible upper limits on the GW amplitudes C_{22} and C_{21} for the dual-harmonic run (searching for the mass quadrupole modes $l = 2$, $m = 1, 2$) and the GW amplitude h_0 for the single-harmonic ($l = 2$, $m = 2$) search. These are calculated using coherently combined data from all three detectors over the O2 and O3 observing runs or just the O3 run, as appropriate. Due to the calibration amplitude systematic uncertainties for the detectors, the amplitude estimates can have uncertainties of up to $\sim 8\%$.

Figure 3.1 shows the 95% credible upper limits on the GW amplitudes C_{22} and C_{21} for all pulsars. In addition, it shows joint detector sensitivity estimates for the two amplitudes based on the representative power spectral densities for

---

[1]While TEMPO2 is an updated and more flexible version of TEMPO, the latter may be used in legacy workflows or due to its stability over time.

the detectors over the course of O3. For an explanation of how these estimates are calculated, see Section 4.4 or Appendix C in Abbott et al. (2019b).

The 95% credible upper limits for the GW amplitude h_0 from the single-harmonic analysis for all pulsars are shown as stars in Figure 3.2. The spin-down limit for each pulsar is represented as a grey triangle. If the observed upper limit for a pulsar is below the spin-down limit, this is shown via a dotted green line from the spin-down limit to the h_0 limit which is plotted within a shaded circle. The solid line gives the joint detector sensitivity estimate over the course of O3.[1]

Figure 3.3 shows a histogram of the spin-down ratio $h_0^{95\%}/h_0^{\mathrm{sd}}$ for every pulsar for which calculating a spin-down rate is possible.[2] These values rely on the pulsar distance, frequency derivative and principal moment of inertia, which all have associated uncertainties. These uncertainties are not taken into account in this study, for which I use the best-fit values listed in Table A.2 and A.3 and a fiducial moment of inertia I_{zz}^{fid} of $10^{38}\,\mathrm{kg\,m^2}$, but their presence should be kept in mind. Distance errors are primarily based on uncertainties in the galactic free electron distribution (Yao et al., 2017), which can lead to distance errors on the order of a factor of two. Nearby pulsars, for which parallax measurements are possible, will generally have smaller distance uncertainties. Table A.2 provides a reference for the distance to each pulsar, which can be used to find an estimate of the associated error as required. The relative uncertainties in frequency derivative are generally much smaller than the distance uncertainties. The principal moment of inertia is equation of state dependent and could range between $\sim (1-3) \times 10^{38}\,\mathrm{kg\,m^2}$ (see, e.g., Abbott et al., 2007). The mass quadrupole Q_{22} and the ellipticity ε limits also rely on these values; for example, the given ellipticity upper limits are inversely proportional to $I_{zz}/10^{38}\,\mathrm{kg\,m^2}$.

The single-harmonic search is used to place limits on the mass quadrupole $Q_{22}^{95\%}$ which can be used to find the pulsar's ellipticity $\varepsilon^{95\%}$ using equations (3.5) and (3.4). However, for pulsars that did not surpass their spin-down limits these Q_{22} and ε values would lead to spin-down rates $\dot{P}_{\mathrm{rot}}$ that are greater than (and thus are in violation of) their measured values. The results are shown in terms

---

[1]The sensitivity estimate for O3 alone is used as it dominates compared to the estimate for the O2 run.

[2]Spin-down rates cannot be calculated for pulsars with insufficient distance, frequency or frequency derivative data (see equation (3.6)).
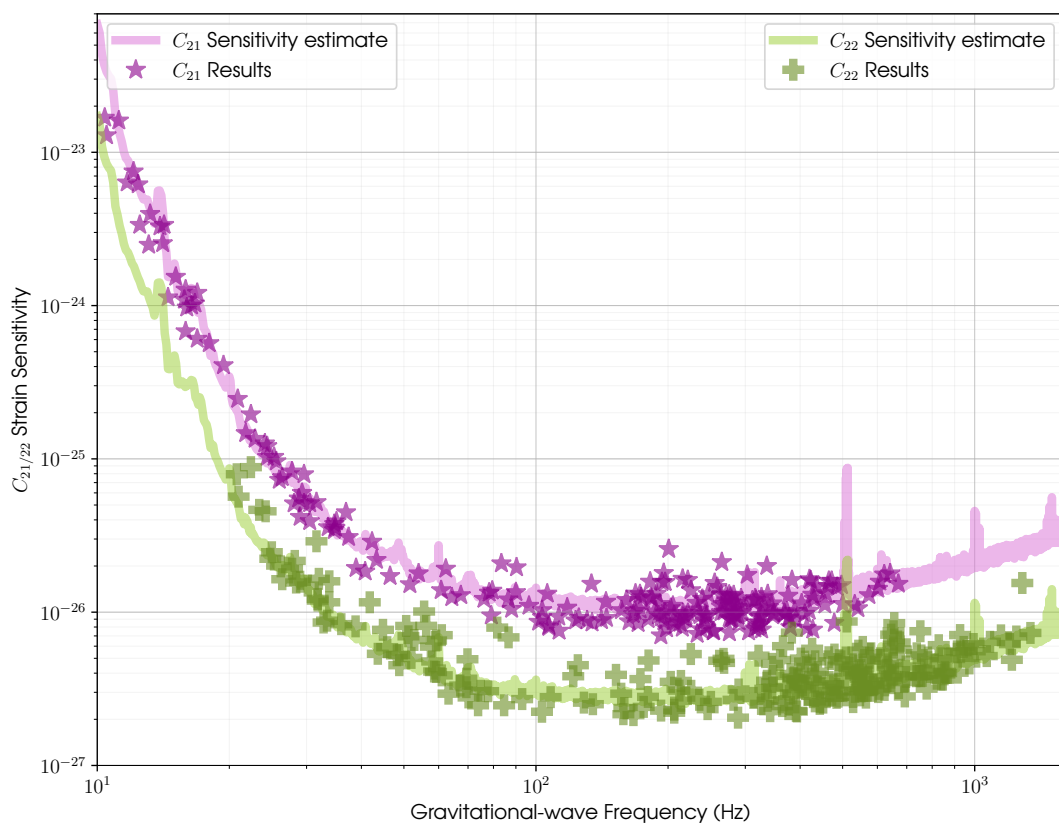
Figure 3.1 The 95% credible upper limits on the GW amplitudes for all 236 pulsars. The pink stars and green crosses show the 95% credible upper limits for the GW amplitudes (C_{22} and C_{21} respectively) for the dual-harmonic search. The solid lines show the estimated sensitivity of all three detectors combined over the course of O3.
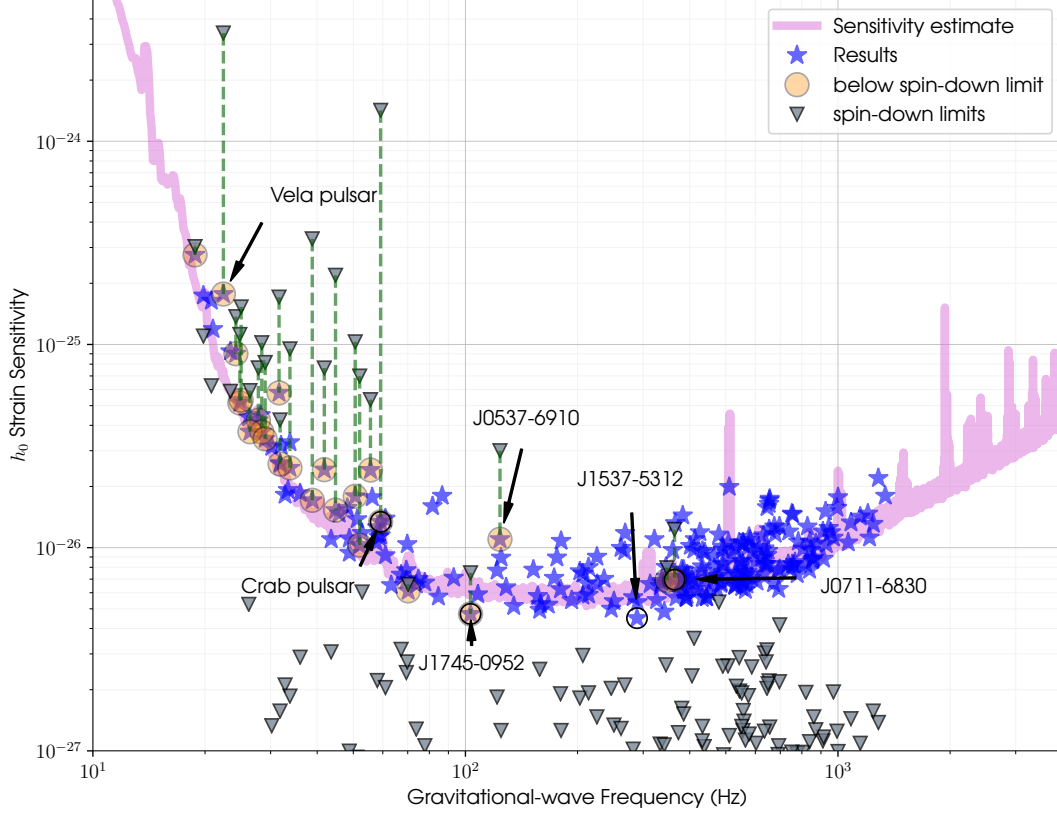
Figure 3.2 Upper limits on h_0 for the 236 pulsars in this analysis. The stars show 95% credible upper limits on the amplitudes of h_0. Grey triangles represent the spin-down limits for each pulsar (based on the distance measurement stated in Table A.2 and assuming the canonical moment of inertia). For those pulsars which surpass their spin-down limits, their results are plotted within shaded circles. The pink curve gives an estimate of the expected strain sensitivity of all three detectors combined during the course of O3. The highlighted pulsars are those with the best h_0, Q_{22} and spin-down ratio out of the pulsars which surpassed their spin-down limit, as well as the best h_0 limit out of the whole sample. The Vela pulsar is highlighted and the pulsar J0537−6910 upper and spin-down limits calculated in Abbott et al. (2021c) are also included for completeness.
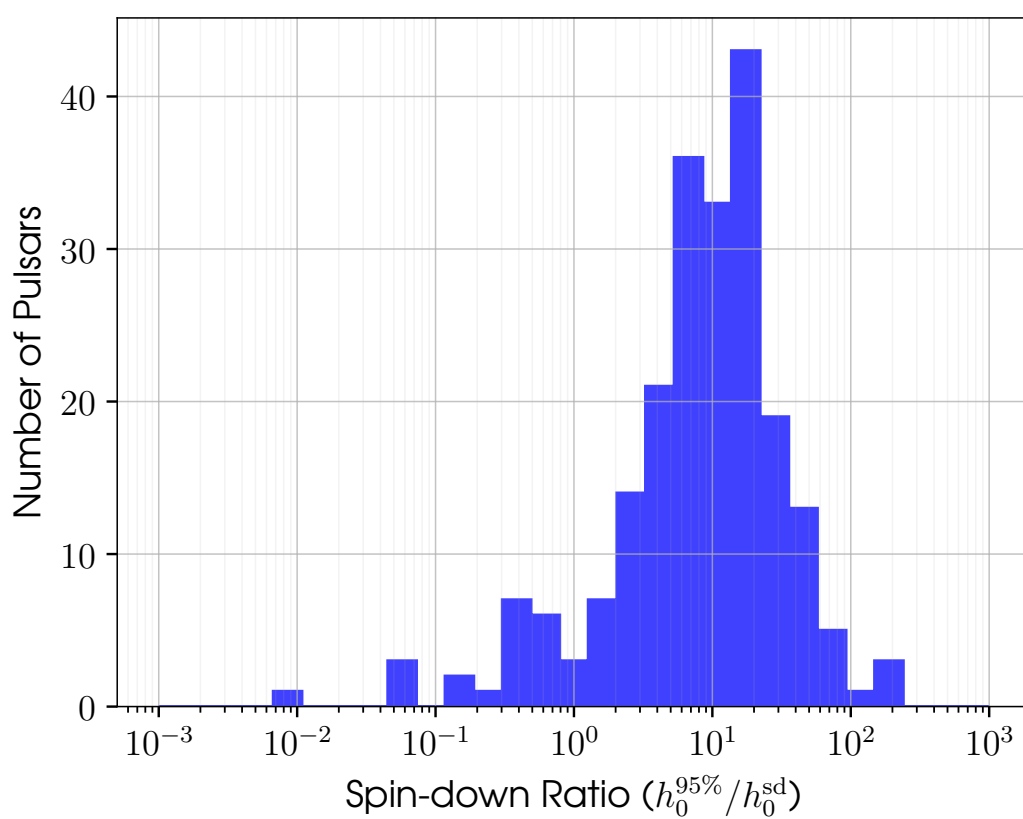
Figure 3.3 A histogram of the spin-down ratio for the 195 pulsars for which a spin-down ratio is calculated.

of the mass quadrupole Q_{22} and ellipticity ε in Figure 3.4. Also included are histograms of the upper limits and spin-down limits as well as contour lines of equal characteristic age τ calculated under the assumption that all spin-down is due to energy loss through GW emission, i.e., the braking index is $n = 5$.

Twenty-three pulsars have direct upper limits that are below their spin-down limit, with 89 pulsars within a factor of 10 of their spin-down limit. There are 90 millisecond pulsars with a spin-down ratio less than 10. For the dual-harmonic search, the most constraining upper limit for C_{21} is J2302+4442 with 7.05×10^{-27}. The smallest C_{22} upper limit is 2.05×10^{-27} for J1537−5312. As physically meaningful constraints for the single-harmonic search are only achieved once the spin-down limit has been surpassed, the following best limits are taken from the 23 pulsars that have $h_0^{95\%}/h_0^{sd} < 1$. The smallest spin-down ratio is 0.009 for J0534+2200 (the Crab pulsar). The pulsar with the smallest upper limit on h_0 is J1745−0952 with 4.72×10^{-27}. The best Q_{22} upper limit is achieved by J0711−6830 with $4.07 \times 10^{29} \, \mathrm{kg \, m^2}$ which leads to the best limit on ellipticity of 5.26×10^{-9}. This pulsar has a dispersion measure distance of $0.11 \, \mathrm{kpc}$, which makes it relatively close-by. However, its high ecliptic latitude makes it very insensitive to parallax measurement (Reardon et al., 2021).

For each pulsar, a model comparison between the assumption of the data being consistent with a coherent signal compared to the assumption of an incoherent signal *or* noise is performed. This is calculated for both the dual-harmonic ($l = 2$, $m = 1, 2$) and single-harmonic ($l = 2$, $m = 2$) searches. Specifically, the base-10 logarithm of the Bayesian odds between models is calculated assuming a prior odds ratio of 1, which will be referred to as $\mathcal{O}$. Of all the pulsars in this search, none have $\mathcal{O} > 0$, meaning in all cases incoherent noise is more likely than a coherent signal. The pulsar with the highest $\mathcal{O}$ overall is J2010−1323 with -0.77.

3.4.1 High-Value Targets

Table A.3 shows the results for the analyses on the high-value targets. For each pulsar with either a glitch or restricted priors, individual analyses are performed assuming GW emission at both $2f_{\mathrm{rot}}$ and f_{rot} and just $2f_{\mathrm{rot}}$. In the case of the Crab pulsar, which both experienced a glitch and has sufficient observations
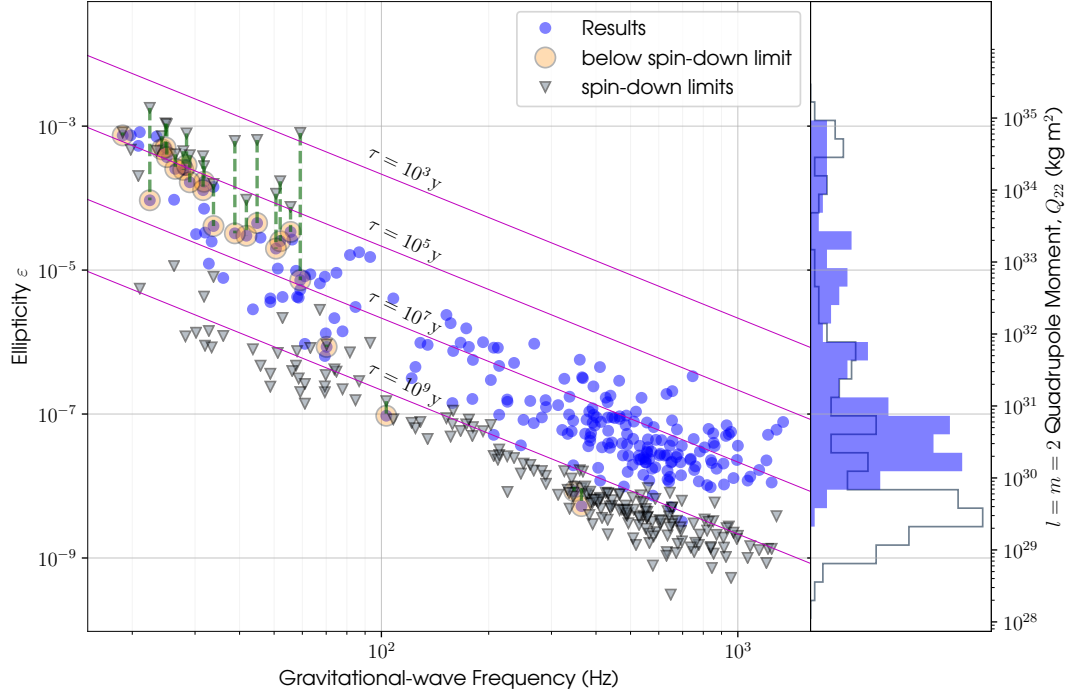
Figure 3.4 95% credible upper limits on ellipticity ε and mass quadrupole Q_{22} for all 236 pulsars. The upper limits for each pulsar are represented by blue circles while their spin-down limits are shown as grey triangles. Pulsars for which my direct upper limits have surpassed their spin-down limits are highlighted within a shaded circle with a dotted green line linking the limit to its spin-down limit. Also shown are pink contour lines of equal characteristic age $\tau = P/4\dot{P}$ assuming that GW emission alone is causing spin-down. To the right of the plot, histograms of both these direct limits and spin-down limits are shown by filled and empty bars respectively.

for restricted priors, four individual analyses are performed. Each analysis accounts for the glitch, with combinations of dual/single-harmonic search and restricted/unrestricted priors. The values shown in Table A.3 are from the searches with glitches accounted for via an unknown phase offset where applicable. When a pulsar has a restricted prior search, the results are shown in the restricted priors row.

By definition, all high-value pulsars surpassed their spin-down limits. Several pulsars glitched during the course of the runs: J0534+2200 (Crab pulsar), J0908$-$4913 and J1105$-$6107. The times of the glitches are shown in Table 3.1 and the process for dealing with them is outlined in Section 3.2.1. Additionally, some have sufficient information from EM observations on their orientation to restrict their priors: J0534+2200 (Crab pulsar), J0835$-$4510 (Vela), J1952+3252 and J2229+6114. This is discussed in 3.2.2 and the pulsars' restricted ranges are quoted in Table 3.2.

The Crab pulsar is of interest due to its high spin-down luminosity. For the single-harmonic analysis and with the glitch accounted for by a phase offset, its upper limit as a fraction of the spin-down limit is only 0.0094 (0.0085 in the restricted analysis). The fraction of spin-down luminosity emitted as gravitational waves is given by

$$\eta = \frac{\dot{E}_{\mathrm{GW}}}{\dot{E}_{\mathrm{sd}}} = \left(\frac{h_0}{h_0^{\mathrm{sd}}}\right)^2, \tag{3.7}$$

meaning that the spin-down ratio for the Crab pulsar corresponds to a GW luminosity of less than 0.009% of the available spin-down luminosity. This is consistent with previous studies that also surpassed the spin-down limit (Abbott et al., 2017d, 2019b). Its $h_0^{95\%}$ upper limit is found to be $1.3(1.2)\times10^{-26}$. With a distance of $2\,\mathrm{kpc}$ and period derivative of $4.2\times10^{-13}\,\mathrm{s\,s^{-1}}$, the upper limits on the mass quadrupole and ellipticity are calculated to be $Q_{22}^{95\%} = 5.6(5.0)\times10^{32}$ kg m^2 and $\varepsilon^{95\%} = 7.2(6.5)\times10^{-6}$. The base-10 logarithm of the Bayesian odds for this analysis favouring a coherent signal over incoherent noise is -2.6(-2.7), which clearly favours incoherent noise by a factor of ~ 400. As a visual example of the results, Figure 3.5 shows the corner plots for the search parameters for both the single- and dual-harmonic searches for the Crab pulsar.
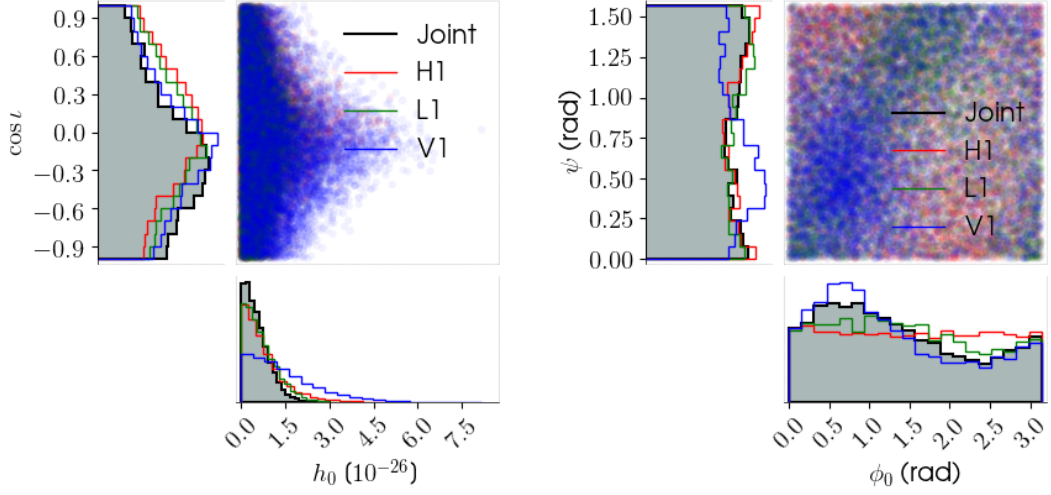
(a) Single harmonic
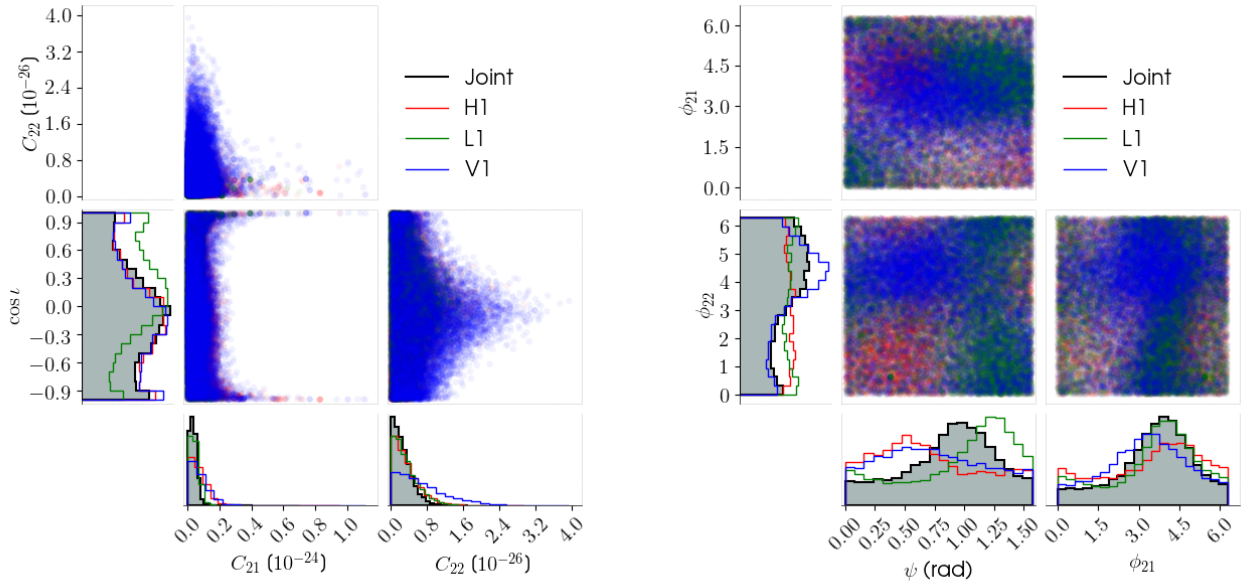
(b) Dual harmonic

Figure 3.5 Corner plots of the parameters sampled over for the Crab pulsar from the single-harmonic (top) and dual-harmonic (bottom) searches. These are the results with non-restricted priors and with the glitch taken into account. Each detector is plotted along with the joint result.

The Vela pulsar also has a very high spin-down luminosity and is considered another source of interest. Unlike the Crab pulsar, the Vela pulsar did not experience any glitches over the course of this analysis. In the single-harmonic analysis, the spin-down limit is surpassed with a ratio of 0.052(0.051), with $h_0^{95\%} = 1.8(1.7){\times}10^{-25}$. This ratio corresponds to a maximum of 0.27% of the spin-down luminosity being emitted by GWs. The previous known pulsar search by Abbott et al. (2019b) found the spin-down ratio to be 0.042 with $h_0^{95\%} = 1.4{\times}10^{-25}$ which is lower than in this analysis. This is due to significant noise in the LIGO Hanford detector at twice Vela's rotational frequency in O3, with an angular sensing control dither line being the most likely culprit[1]. However, this analysis is an improvement on the more recent measurement of the spin-down ratio of 0.067 and $h_0^{95\%} = 2.2{\times}10^{-25}$ produced in Abbott et al. (2020b). The upper limits on the mass quadrupole $Q_{22}^{95\%}$ and ellipticity ε are calculated to be $7.2(7.1){\times}10^{33}$ kg m^2 and $9.3(9.2){\times}10^{-5}$, respectively. These values are calculated assuming a distance of $0.28\,\mathrm{kpc}$ and a period derivative of $1.2\times10^{-13}\,\mathrm{s\,s^{-1}}$. The base-10 logarithm of the Bayesian odds for this pulsar in the single-harmonic analysis is -1.1(-1.0).

The pulsar J0537−6910 has the highest spin-down luminosity but has not been included in this search due to recently published searches for it in Abbott et al. (2021c,g). The limits, which can be found in Table 3 of Abbott et al. (2021c), are shown for comparison. They found $h_0^{95\%} = 1.1(1.0)\times10^{-26}$ with a spin-down ratio of $h_0^{95\%}/h_0^{sd} = 0.37(0.33)$ and $\varepsilon^{95\%} = 3.4(3.1)\times10^{-5}$ while for the dual-harmonic search $C_{21}^{95\%} = 2.2(1.8)\times10^{-26}$ and $C_{22}^{95\%} = 5.6(5.0)\times10^{-27}$.

3.4.2 Cleaned versus Uncleaned Data Comparison

The data used in this analysis was subject to a cleaning process described in Viets and Wade (2021) which focused on the removal of various narrowband spectral artifacts at calibration line frequencies. For any pulsars with GW frequencies very close to these lines, this cleaning would be expected to provide an improvement in sensitivity. In this section, I present the comparison of results using this cleaned

---

[1]This contamination was removed for the final third of O3, although its presence at earlier times still has a detrimental effect on the result.

data against results using data without this cleaning process (which I will refer to as 'uncleaned') for a sample of pulsars.

Uncleaned O3 LIGO data is used for a dual-harmonic analysis of 95 pulsars which had ephemeris data only overlapping with O3. This is compared to the O3-only analysis performed in this chapter using the cleaned data. The Virgo data used is the same in both cases. For comparison, the ratio of h_0 upper limits for each pulsar using uncleaned $h_{0,\text{uncleaned}}$ versus cleaned $h_{0,\text{cleaned}}$ data are shown in Figure 3.6.

The mean ratio of upper limit for uncleaned data versus cleaned data is 0.9966 (with a standard deviation of 0.0486) which suggests no major effect of the line cleaning on the majority of results. It should be noted that for this analysis there is a statistical uncertainty on the upper limits of around 1% due to the use of a finite number of posterior samples when calculating them (Abbott et al., 2020b). When performing parameter estimation on h_0 using multiple data sets consisting of independent noise realisations drawn from the same distribution, it has been observed emperically that the resultant upper limits will vary by on order of 30%. Due to the cleaning, the cleaned and uncleaned datasets will contain different, albeit highly correlated, noise. So, a spread of upper limit ratios that are larger than expected from the pure statistical uncertainty on each limit, but smaller than one would get from independent data, is to be expected. The pulsar with the highest ratio was J1753-1914 with over 1.3. This pulsar has a rotation frequency of 15.8 Hz corresponding to a GW frequency of 31.6 Hz. There were spectral lines at 31.4 Hz and 31.8 Hz for L1 and H1 respectively (LIGO Scientific Collaboration, 2020), which were filtered out in the cleaned data, leading to the improvement seen.

As the upper limit ratio spread can be explained as being consistent with expectations from statistical fluctuations, it suggests that very few pulsars have GW frequencies close enough to the cleaned lines for the cleaning to have a significant effect overall. However, to be consistent for all pulsars being analysed, I choose to use the narrowband cleaned data.
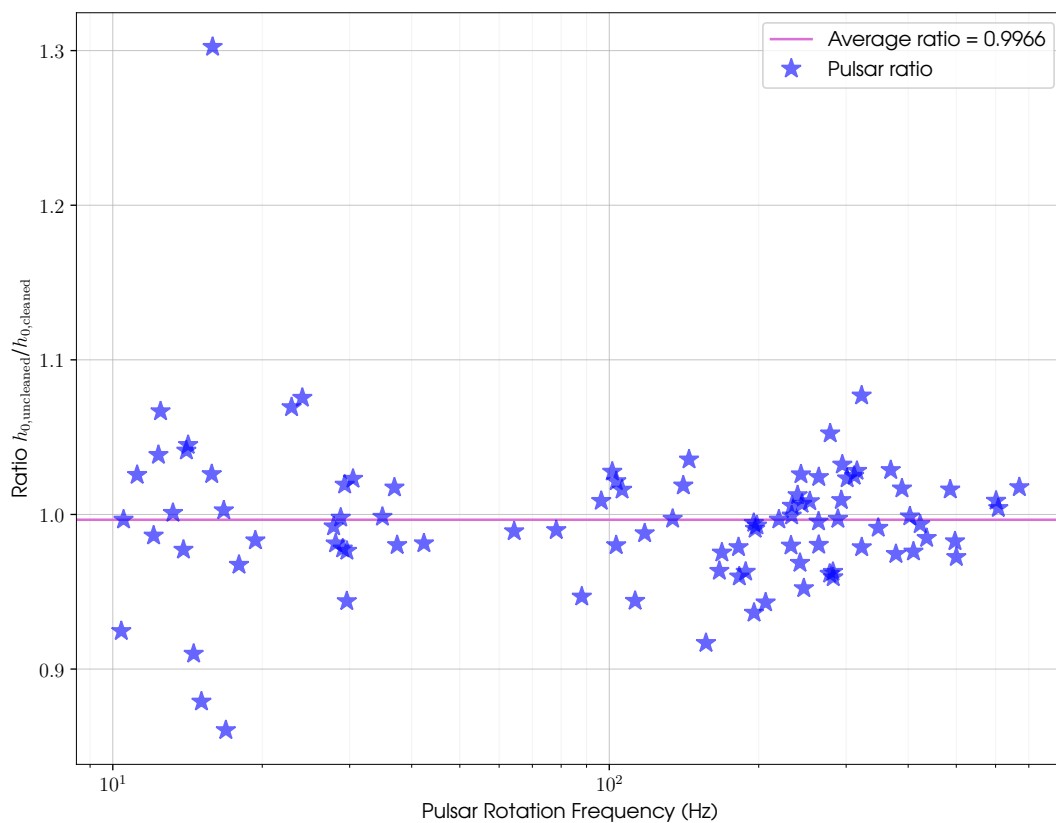
Figure 3.6 The ratio of uncleaned versus cleaned upper limits against pulsar rotational frequency. The h_0 upper limits for both data sets are calculated from the C_{22} limit determined in dual-harmonic searches using O3 data only. The mean ratio is represented by the solid pink line and ratios above zero represent an improvement in the cleaned data.

3.5 Summary

In this chapter, I search for evidence of GWs from 236 pulsars over the course of the LIGO and Virgo O2 and O3 runs and across all three detectors (LIGO Hanford, LIGO Livingston and Virgo). This is an improvement on the 221 pulsars from the O1 and O2 analysis in Abbott et al. (2019b). Searches are carried out for two different emission models. One assumes GW emission from the $l = m = 2$ mass quadrupole mode and the other assumes emission from the $l = 2, m = 1, 2$ modes. For the single-harmonic search, new upper limits on h_0 are produced and a total of 23 pulsars surpass their spin-down limits (24 if one includes J0537-6910 from Abbott et al. (2021c)). This is an improvement from the 20 pulsars in Abbott et al. (2019b) and includes 9 pulsars for which their spin-down limit had not previously been surpassed. For the dual-harmonic search, new limits on C_{21} and C_{22} are found.

The millisecond pulsars that surpass their spin-down limits, J0437−4715 and J0711−6830, have ellipticity upper limits of 8.5×10^{-9} and 5.3×10^{-9}, respectively. Comparing these values to those in Figure 3.7, I find that my results are lower than the maximum values predicted for a variety of neutron star equations of state. While this does not yet rule any EOS out, it demonstrates that these results are therefore providing new constraints in physically realistic parts of the ellipticity parameter space.

This search found no strong evidence of GW emission from any of the pulsars. However, with so many pulsars now surpassing their spin-down limit, including the millisecond pulsars J0437−4715 and J0711−6830 (Abbott et al., 2020b), the next observing run O4 could add more pulsars to this count and bring us closer to observing CWs from pulsars for the first time.
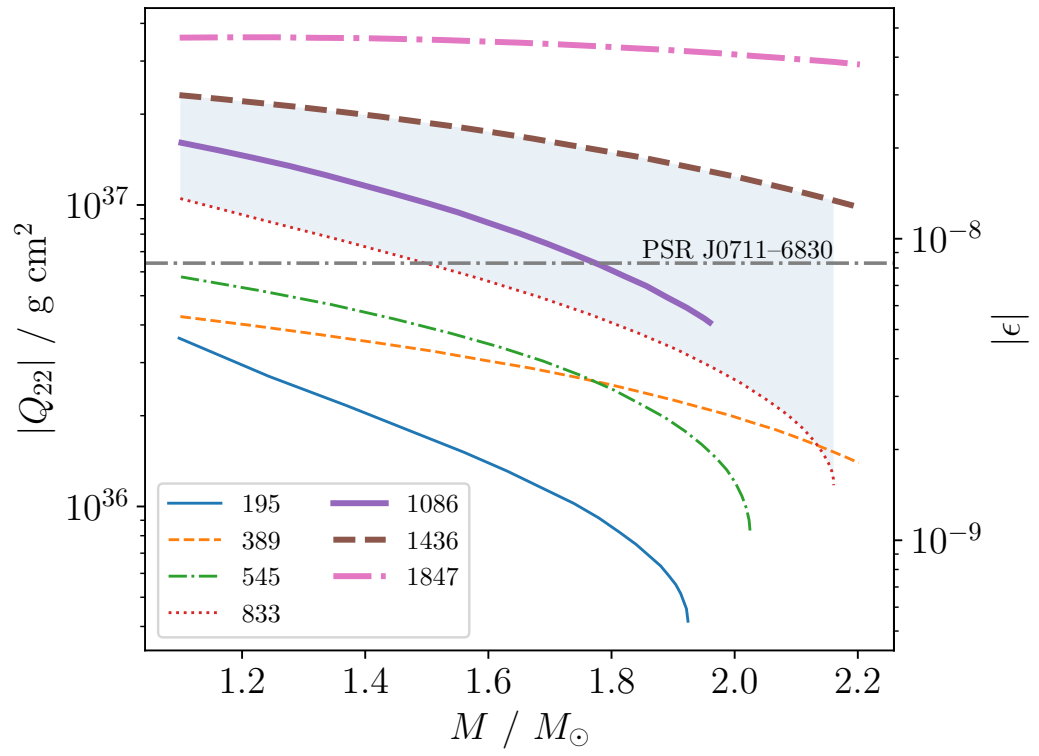
Figure 3.7 Maximum ellipticities predicted by a variety of neutron star EOSs. Taken from the left-hand panel of Figure 3 in Gittins and Andersson (2021b)

Chapter 4

Search for Continuous Gravitational Waves from Known Pulsars in the Early Part of the Fourth LIGO-Virgo-KAGRA Observing Run

4.1 Introduction and Methods

This chapter is a repeat of the analysis performed on the second and third LIGO-Virgo observing runs described in Chapter 3 (subsequently referred to as the O3 analysis). This time, the analysis is performed on the first part of the fourth LIGO-Virgo-KAGRA observing run (O4a). Due to the similarities in the two analyses, only their differences are highlighted in this section. For full details and motivations for both targeted searches, see Sections 3.1 and 3.2.

As in the O3 analysis, a time-domain Bayesian analysis is performed searching for continuous GWs at two harmonics. The signal models remain the same,

as does the analysis method involving two heterodyne phases: course and fine, followed by parameter estimation. However, the primary difference in the analysis method is that while the O3 analysis was performed using `LALSuite` (LIGO Scientific Collaboration, 2018), this O4a analysis uses the new Continuous (gravitational) Wave Inference in Python (`CWInPy`) software package (Pitkin, 2022) which uses the `dynesty` (Skilling, 2004, 2006) sampler within `bilby` (Ashton et al., 2019). The `CWInPy` software, written in Python rather than C, is designed to supersede `LALSuite`, providing greater ability to control various aspects of the analysis along with improved robustness and efficiency.

4.1.1 Prior Assumptions

Bayesian inference is used to estimate the unknown prior parameters and the evidence for the signal model. The majority of the priors used in this analysis are the same as those detailed in O3 and listed in Appendix 2 of Abbott et al. (2017a). However, for the amplitude priors I use a flat prior with an upper cutoff of 1.0×10^{-21} for all pulsars. This value is much higher than the detector sensitivity. The Bayesian stochastic sampling algorithm `dynesty` is used with 1024 live points. These live points represent the number of samples initially drawn from the prior which are repeatedly updated by replacing the point with the lowest likelihood with a new point with a higher likelihood in order to efficiently explore the posterior.

4.1.2 Restricted Priors

For some pulsars, there is sufficient information to restrict my uninformative prior assumptions on their inclination and polarisation angles. For example, I can use restricted priors if I have electromagnetic observations of their pulsar wind nebulae or, in the case of J1952+3252, proper motion measurements and observations of Hα lobes bracketing the bow shock (Ng and Romani, 2004). In these cases, the parameter estimation is repeated using these restricted priors and the results are listed alongside the results obtained using the original uninformed priors. Table 4.1 shows the pulsars for which I could restrict the priors and the values used

101

for the restrictions. In addition to those with restricted priors in O3, there are four new pulsars: J0205+6449, J0537-6910, J0540-6919, and J2021+3651. The orientation values for these pulsars were obtained using the data from Table 2 of Ng and Romani (2008) and the methods described in Appendix B of Abbott et al. (2017a). Each prior range is assumed to be Gaussian with the given mean and standard deviation. The two values for ι are to incorporate the unknown rotation direction in the search by using a bimodal distribution. The additional ι_2 is simply $\pi - \iota_1$ radians.

Table 4.1 Pulsars for which I can restrict their orientation priors using electromagnetic observations. Ψ is the polarisation and ι is the inclination.

PSR	Ψ (rad)	ι_1 (rad)	ι_2 (rad)
J0205+6449	1.5760 ± 0.0078	1.5896 ± 0.0219	1.5519 ± 0.0219
J0534+2200 (Crab)	2.1844 ± 0.0016	1.0850 ± 0.0149	2.0566 ± 0.0149
J0537-6910	2.2864 ± 0.0383	1.6197 ± 0.0165	1.5219 ± 0.0165
J0540-6919	2.5150 ± 0.0144	1.6214 ± 0.0106	1.5202 ± 0.0106
J0835-4510 (Vela)	2.2799 ± 0.0015	1.1048 ± 0.0105	2.0368 ± 0.0105
J1952+3252	0.2007 ± 0.1501	...	...
J2021+3651	0.7854 ± 0.0250	1.3788 ± 0.0390	1.7628 ± 0.0390
J2229+6114	1.7977 ± 0.0454	0.8029 ± 0.1100	2.3387 ± 0.1100

4.1.3 Glitches

During the course of the second and third LIGO-Virgo observing runs, three pulsars experienced sudden increases in both their rotation frequency and its derivative, referred to as a glitch. In this analysis, only two pulsars in the sample experienced glitches during the length of O4a: J0537$-$6910 with a glitch epoch of 60223 MJD and J0540$-$6919 with an epoch of 60150 MJD. I assume that the GW phase is affected in the same way as the EM phase. However, as the phase offset is unknown at the time of the glitch, it is included in the parameter inference for those pulsars as a uniform prior.

4.2 Datasets

4.2.1 The GW Dataset

The dataset used in this analysis is referred to as O4a. This is the first part of the fourth observing run from the LIGO collaboration, taking place between 15:00:00 UTC 24th May 2023 and 16:00:00 UTC 16th January 2024. O4 in total will be a joint observation using the LIGO Livingston (L1) and LIGO Hanford (H1) observers in the United States, Virgo (V1) in Italy, and KAGRA in Japan[1]. However, as Virgo only joined O4 on 10th April 2024 and KAGRA is scheduled to join by the end of O4, only L1 and H1 data is used in this analysis[2]. The duty factors for these detectors are 69% and 67.5% respectively. A description of the upgrades to the Advanced LIGO, Advanced Virgo, and KAGRA detectors in preparation to the O4 run can be found Appendix A of Abac et al. (2024).

As described in Section 1.3.2, the two LIGO detectors are calibrated using photon radiation pressure actuation (Karki et al., 2016; Viets et al., 2018). For the O4a data over the 10-2000 Hz range, the worst 1σ calibration uncertainty is within 10% for amplitude and 10 degrees for phase. This uncertainly can be significantly smaller at specific frequencies and times. The Bayesian pipeline also performs a cleaning step where outliers are removed before the heterodyne step using a median-absolute-deviation (MAD) method as described in Chapter 3 of Iglewicz and Hoaglin (1993), with a threshold of 3.5.

4.2.2 The EM Dataset

The inputs for the GW search are produced from timing solutions from a wide range of wavelengths. Chandra (Weisskopf et al., 2002) and Fermi-LAT (Atwood et al., 2009) provide the gamma-ray ephemerides. X-ray ephemerides are provided by the Neutron Star Interior Composition Explorer (NICER, Gendreau

---

[1]As seen in Figure 1.3, KAGRA has still not joined O4, however it still hopes to join before the end.

[2]Specifically, the channels L1:GDS–CALIB_STRAIN_CLEAN_AR and H1:GDS–CALIB_STRAIN_CLEAN_AR are used, with CAT1 vetoes for L1 and H1, respectively.

et al., 2012). The radio ephemerides are extracted from the Nancay Radio Telescope (NRT, Desvignes et al., 2016), the Jodrell Bank Observatory (JBO), the Argentine Institute of Radio astronomy (IAR, Gancio et al., 2020), the Mount Pleasant Radio Observatory (Lewis et al., 2003), the Five-hundred-meter Aperture Spherical Telescope (FAST, Smits et al., 2009) and the Canadian Hydrogen Intensity Mapping Experiment (CHIME, Amiri et al., 2021b).

`PSRCHIVE` (van Straten et al., 2012) or `PRESTO` (Ransom, 2011) are used to fold observations. Radio-frequency interferences (RFIs) are mitigated using `pazi` or `rfifind`. TOAs are then obtained by cross-correlating the folded observations with template profiles that have high signal-to-noise ratios. The TOAs during the course of O4a are selected, meaning the solutions are valid for this analysis. `Tempo` (Nice et al., 2015), due to varying workflows between groups,`Tempo2` (Edwards et al., 2006; Hobbs et al., 2006a, 2009) or PINT (Luo et al., 2019, 2021) are then used to fit the model parameters used in this search.

For most pulsars, their distances were taken from the Australia Telescope National Facility (ATNF) catalogue. Of these, the majority have been calculated using the Galactic electron density distribution model YMW16 (Yao et al., 2017). This can result in uncertainties as large as a factor of two. Another method involves measuring parallax with the timing solution (Smits et al., 2011) and can produce an uncertainty ranging from 5-50% (Shamohammadi et al., 2024). Other methods include using the orbital period derivatives of binary systems (Verbiest et al., 2008), which can produce uncertainties of 0.1%, and Very Long Baseline Interferometry (Lin et al., 2023). The uncertainty in pulsar distances is not accounted for in this analysis.

A few pulsar distances were not in the ATNF catalogue at the time of analysis (version 2.1.1). The pulsars J1412+7922 and J1849−0001 did not yet have distance values, and so their distances are taken from Mereghetti et al. (2021) and H. E. S. S. Collaboration et al. (2018) respectively. The pulsar J2016+3711 was not in the catalogue at all, so its values are taken directly from Liu et al. (2024).

In order to ensure that the pulsars selected are both in the bandwidth of the LIGO detectors and in a region where the expected targeted search sensitivity for the strain amplitude is within a factor of 3 of the spin-down limit, I choose pulsars

with rotation frequencies close to, or greater than, 10 Hz. Of the 45 pulsars in this analysis, 11 belong to binary systems and 10 are millisecond pulsars with frequencies higher than 100 Hz.

4.3 Results

I detect no statistical evidence of a CW signal in the O4a data for any of the pulsars. Therefore, I present the 95% credible upper limits in the absence of a detection. The results of the analysis on the 45 pulsars are shown in Table A.4. The 95% credible upper limits on the strain amplitude $h_0^{95\%}$ are given for the single-harmonic search along with the mass quadrupole $Q_{22}^{95\%}$ and ellipticity $\varepsilon^{95\%}$ upper limits calculated using the distances listed in the table (not taking into account the uncertainty on the distance) and a fiducial moment of inertia $I_{zz} = 10^{38}$ kg m^2. For pulsars that do not surpass their spin-down limits, $Q_{22}^{95\%}$ and $\varepsilon^{95\%}$ are not physical as they would lead to spin-down rates that are greater than observed. Using $h_0^{95\%}$ and the spin-down limit from equation (3.6), I also calculate the spin-down ratio as $h_0^{95\%}/h_0^{\mathrm{sd}}$. The upper limits for the dual-harmonic search are included as $C_{21}^{95\%}$ and $C_{22}^{95\%}$. Finally, the base-10 logarithmic odds of a coherent signal versus incoherent noise are given for both the single-harmonic $\mathcal{O}_{m=2}^{l=2}$ and dual-harmonic $\mathcal{O}_{m=1,2}^{l=2}$ searches.

For J0537−6910 and J0540−6919, the pulsars that experienced glitches during O4a, the results in this table are produced when incorporating an additional phase offset in the parameter inference. For pulsars with sufficient observational data (listed in Table 4.1), results using restricted priors of inclination and polarisation angles are listed in separate rows.

Figure 4.1 shows the upper limits from the single-harmonic analysis alongside the combined sensitivity curve of both detectors during O4a. The results from this analysis for each pulsar are represented by the blue stars, with their corresponding spin-down limit shown by the grey triangles at the same frequency. The sensitivity curve is shown as a pink line. Some pulsars have been highlighted: the Crab pulsar (J0534+2200) which has the lowest spin-down ratio of 0.0078, Vela (J0835−4510), J2021+3651 which has the highest base-10 logarithmic odds
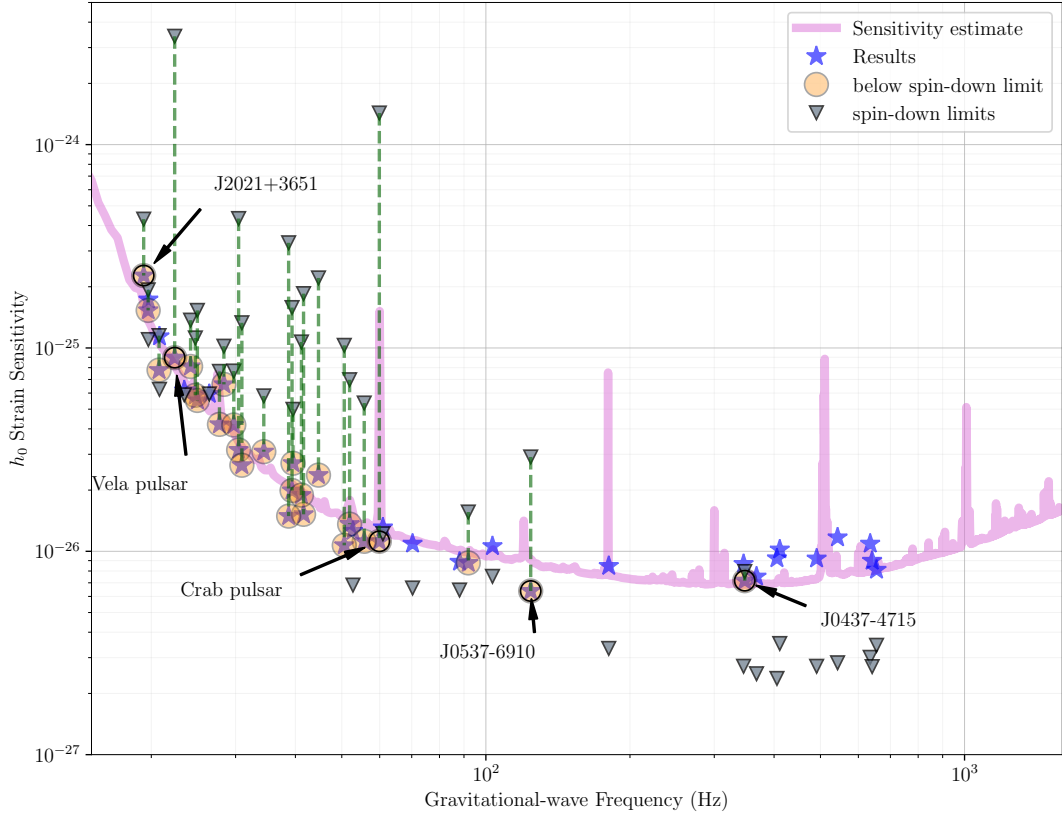
Figure 4.1 Upper limits on h_0 for the 45 pulsars in this analysis from the single-harmonic search. The blue stars show 95% credible upper limits on the amplitudes of h_0. Grey triangles represent the spin-down limits for each pulsar (based on the distance measurement stated in Table A.4 and assuming the canonical moment of inertia). The pink curve gives an estimate of the expected strain sensitivity of both detectors combined during the course of O4a.

of coherent signal versus incoherent noise with -3.1, J0537$-$6910 which has the most constraining amplitude upper limit of 6.4×10^{-27}, and J0437$-$4715 which has the most constraining ellipticity upper limit of 8.8×10^{-9}. The distribution of spin-down ratios for these results is shown in Figure 4.2, with all pulsars having a spin-down ratio below 5 and 29 pulsars surpassing their spin-down limits.

The ellipticity $\varepsilon^{95\%}$ and mass quadrupole $Q_{22}^{95\%}$ upper limits are plotted against the GW frequency in Figure 4.3. The results from this analysis are represented by blue dots while the spin-down limits are represented by grey triangles at the corresponding frequencies. Additionally, the contours of equal characteristic age are represented as pink lines. They are calculated using $\tau = P/4\dot{P}$ which can be derived with the assumption that GW emission alone is driving the spin-down. It should be noted that although all the results are plotted, only those which surpass their spin-down limit are physically meaningful.

4.4   Discussion

This section compares the results in this analysis with those of previous targeted searches (Abbott et al., 2017a, 2019b, 2021c, 2022e) which used combinations of the first three observing runs. The ratio between the O4a 95% credible upper limits and the equivalent upper limits from previous runs are shown in Figure 4.4.

The expected sensitivity of targeted searches is expressed as the minimum detectable amplitude $h_{\min}$. This can be calculated for a multi-detector analysis averaged over sky positions and polarisation parameters, using

$$h_{\min} \approx C \sqrt{\left(\sum_{i=1}^{n} \frac{T_i}{S_i} \right)^{-1}},\tag{4.1}$$

where n is the number of detectors and T_i and S_i are the effective observation time and average power spectral density (PSD) for the i-th detector respectively. The PSD is dependent on frequency, meaning there is a value of $h_{\min}$ for each pulsar, reflecting the frequency-dependent performance of the detector. The factor C depends on the search pipeline used, but in targeted analyses is $\simeq 11$, which
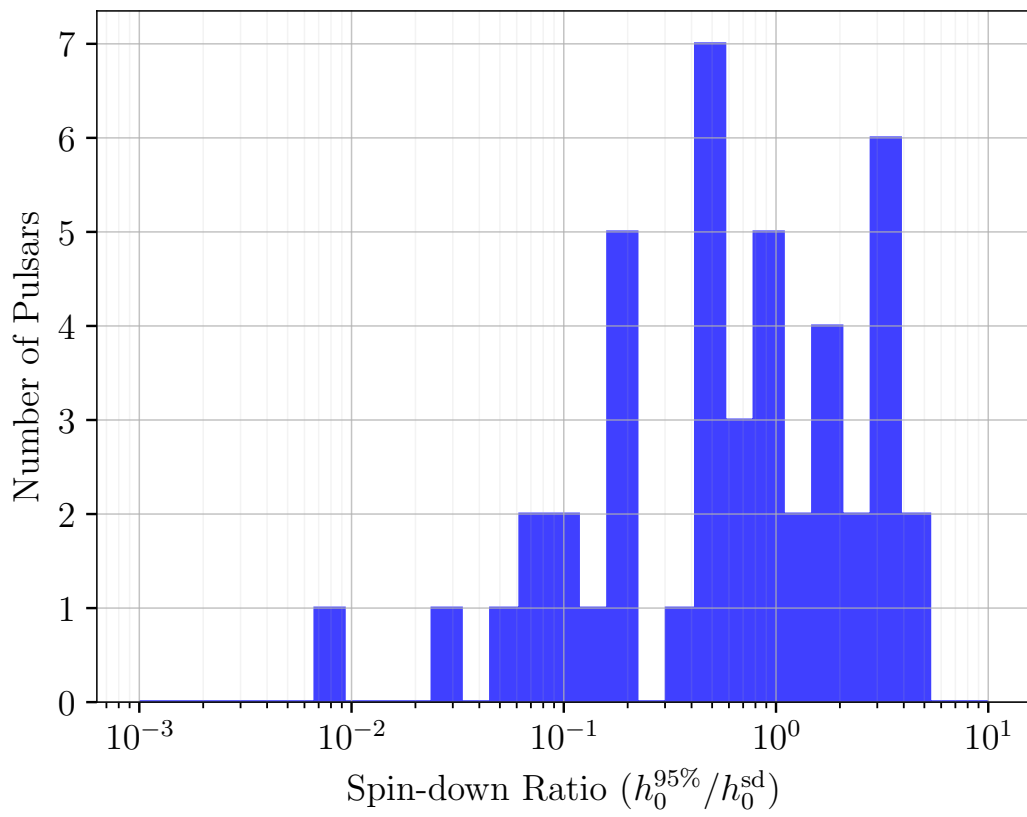
Figure 4.2 A histogram of the spin-down ratio for 45 pulsars from the single-harmonic analysis.
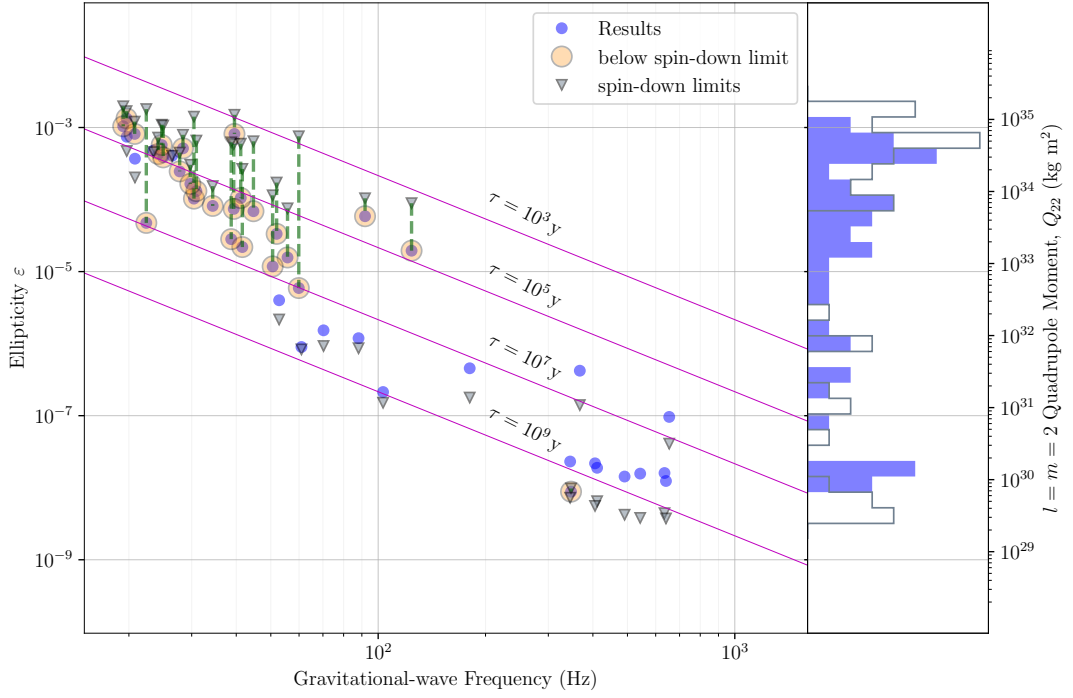
Figure 4.3 95% credible upper limits on ellipticity $\varepsilon^{95\%}$ and mass quadrupole $Q_{22}^{95\%}$ for all 45 pulsars using the Bayesian analysis method. The upper limits for each pulsar are represented by blue circles while their spin-down limits are shown as grey triangles. The upper limits are also shown in the histogram in solid blue along with their upper limits in hollow grey. Also included are pink contour lines of equal characteristic age $\tau = P/4\dot{P}$ assuming that GW emission alone is causing spin-down. Only the results for pulsars which surpassed their spin-down limits are physically meaningful.
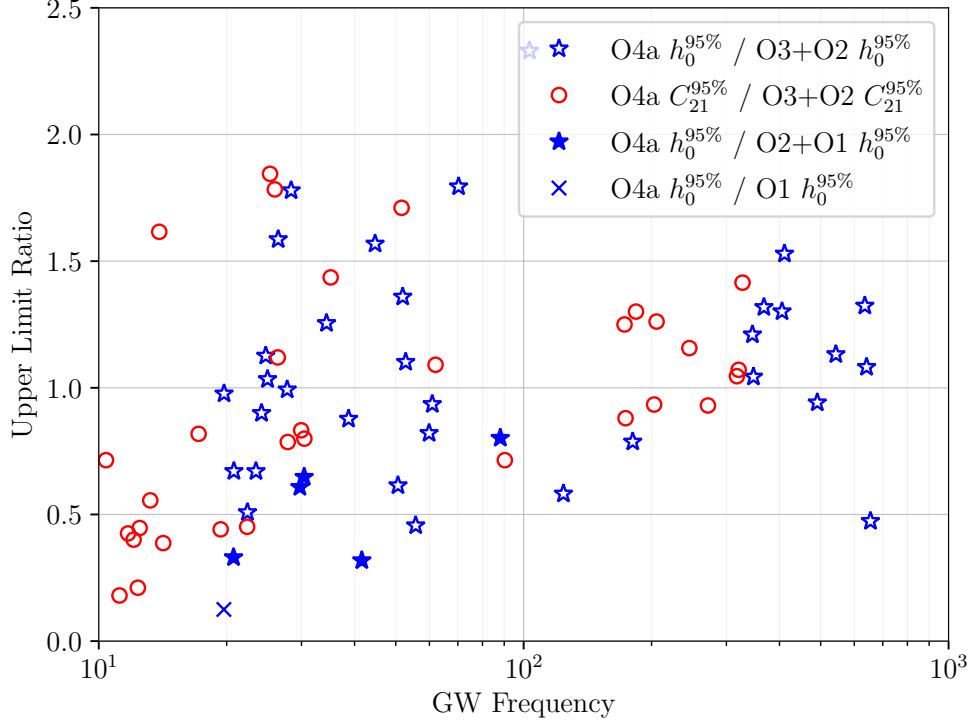
Figure 4.4 Comparisons of GW strain upper limits from this O4a analysis versus previous analyses including the same pulsars plotted against the GW frequency. The hollow blue stars represent the h_0 upper limits assuming the single-harmonic emission model produced in O4a divided by the equivalent upper limits produced using O3 and O2 data in Abbott et al. (2022e). The red circles represent the comparison of the C_{21} upper limit from the dual-harmonic analyses in the same datasets. Filled blue stars show the h_0 upper limit ratio for J0205+6449, J0737−3039A, J1813−1246, J1831−0952, J1837−0604 from the O4a analysis compared to the study including O2 and O1 data (Abbott et al., 2019b). The blue cross represents the comparison for J1826−1334, which was included in the search using just O1 data Abbott et al. (2017a). Points below 1 represent improved upper limits.

corresponds to a 90% detection probability at a 1% false alarm rate calculated under the assumption of a matched-filter coherent search (Krishnan et al., 2004; Leaci et al., 2012).

While the PSD for L1 and V1 in O4a is generally $1.5 - 2$ times better than the corresponding PSD for O3, depending on the frequency band, the effective observation time of O4a is reduced by factor of 1.6 compared to O3. This means the effect of the improved PSD is decreased. However, the O4a sensitivity is still greatly improved for frequencies below 20 Hz. This leads to an expected similar sensitivity to O3 for the single-harmonic search and improved sensitivity for C_{21} in the dual-harmonic search which is at lower frequencies.

Of the 45 pulsars in this analysis, 33 were also analysed in the previous targeted search using O3 and O2 (Abbott et al., 2022e), including J0537$-$6910 derived from Abbott et al. (2021c). Of the remaining pulsars, 5 (J0205+6449, J0737$-$3039A, J1813$-$1246, J1831$-$0952, and J1837$-$0604) were included in the joint O2 and O1 search (Abbott et al., 2019b). Finally, J1826$-$1334 was only previously included in the O1 search (Abbott et al., 2017a).

The $h_0^{95\%}$ upper limit ratio between O4a and O3+O2 is shown in Figure 4.4 as hollow blue stars, while the $C_{21}^{95\%}$ upper limit ratio is shown as red circles. In general, the amplitudes are comparable between the two analyses, with some pulsars showing improved results in O4a and others having worse results. The majority of the pulsars seeing improvements are at low frequencies. This is to be expected due to the improvements in sensitivity at low frequencies in O4a and comparable sensitivities at other frequencies.

For the pulsars from O2+O1 (shown in blue filled stars) and J1826$-$1334 from O1 only (shown as a blue cross), there is a clear improvement in the upper limits from O4a. While the remaining targets which were not included in Figure 4.4 (J0058$-$7218, J0540$-$6919, J1811$-$1925, J1826$-$1334, J2016+3711, J2021+3651, J2022+3842) have not been analysed in any other recent targeted searches, they all surpassed their spin-down limits in the O4a analysis.

The upper limits are subject to uncertainties from detector calibration as described in 4.2.1.

4.5 Summary

In this analysis, I present a targeted search for CWs from 45 known pulsars in the O4a data from the two LIGO detectors, H1 and L1. I perform a time-domain Bayesian analysis with the pulsars' parameters constrained by EM observations during the O4a period. I search at two harmonics, a single-harmonic search looking for CW signals at $2f_{\rm rot}$ and a dual-harmonic search looking for signals at both $f_{\rm rot}$ and $2f_{\rm rot}$.

No evidence of CWs are detected, and so I present 95% confidence upper limits on the strain amplitude, as seen in Figure 4.1 and Table A.4. Of the 45 pulsars in this analysis, 29 surpass their theoretical spin-down limits, allowing us to place further constraints on their ellipticities and mass quadrupoles. Compared to the last LVK targeted search (Abbott et al., 2022e), the C_{21} component of the dual-harmonic search has seen an improvement on average across the pulsars included in both analyses. For the single-harmonic search, the upper limits are comparable to O3 due to the improved sensitivity but shorter observation time of O4a. There has been a notable improvement in the upper limits for all pulsars included in LVK targeted searches prior to O3. Additionally, I surpass or equal the theoretical spin-down limit for all these pulsars.

Analysis on the full O4 dataset will improve the sensitivity of CW searches using known pulsars due to the longer effective observation time and continued improvement to the PSD, allowing even further constraints and more pulsars to surpass their spin-down limits. I am optimistic that further analyses, such as those discussed in Section 5 will lead to the observation of a CW signal.

Chapter 5

Conclusion

This thesis has presented a novel method for retrieving the braking index from a population of pulsars via Bayesian inference (Chapter 2). While this method has its limitations under current observation lengths and noise values, it shows promise with potential future advancements. As the proof of concept described in this thesis uses simulated data only, the next logical steps would be to run a more sophisticated model including binary systems, astrometric measurements such as proper motion and parallax, and more complicated noise profiles; and to run the analysis on real TOA datasets. With the newest NANOGrav dataset being the 15-year dataset containing 67 pulsars compared to the 47 pulsars in the 12.5-year dataset used in Chapter 2, it is already likely that some improvement could be seen. Further upcoming advancements which would contribute to the improved efficacy of this result are discussed in Section 5.2. If the method described in this thesis is successful, obtaining the braking index would give key insights into the mechanisms for pulsar spin-down rates and how much of a part GW emission plays.

This thesis has also described the two most recent targeted CW searches on LVK datasets. Although these searches have not found evidence of CWs, there remains optimism for the prospects of the upcoming full O4 search and, failing that, the subsequent O5 search which may begin in 2028. As can be seen in Figure 1.3, the latter parts of O4 will involve Virgo, with KAGRA joining towards the end of the run. As of March 2025, KAGRA is still yet to join O4, but with the

observing run continuing until October 2025, it still aims to join before the end (LVK, 2025). Since detector sensitivities are already surpassing the spin-down limits for many pulsars, a detection is very possible. However, the spin-down limit assumes that all pulsars are gravitars. Pitkin (2011) calculated that, assuming pulsars emit only 10% of their spin-down as GWs, 3 currently known pulsars would emit CWs detectable by Advanced LIGO-Virgo and 6 to 11 detectable by upcoming detectors, specifically the Einstein Telescope described in Section 5.1.1. This number is likely to have improved as more pulsars are now known and the design of ET has been updated. More recently, Cieślar et al. (2021) modelled the Galactic neutron star population assuming a supernova rate of 1 per 100 years, an initial ellipticity of 10^{-5} with no decay, and 10 million stars, predicting that 0.15 neutron stars would emit CWs detectable by advanced LIGO. This number increases to 26.4 neutron stars for ET. Additionally, the detection of new pulsars through advancements in EM astronomy (described in Section 5.2) could increase this number further. As described in Section 4.4, sensitivity for targeted searches depends on the observation time as well as the power spectral density of the detectors. Therefore, in comparison to the O3 and O4a runs, the full O4 run will have a greater sensitivity both due to the longer effective observing time and the sensitivity improvements made during the break between O4a and O4b[1]. The full O4 search will also contain more pulsars, as additional up-to-date pulsar ephemerides are provided by EM astronomers for full searches. A full analysis of O4 detector performance so far can be found in (Capote et al., 2024). Even without a CW detection, this dataset will provide new strain amplitude upper limits and ellipticity constraints for numerous pulsars. Additionally, O5 boasts further significant sensitivity improvements over O4 with the possibility of both Virgo and KAGRA participating. However, specifics are not yet known.

Continuous improvements will also be made in the data analysis side. The move from `LALSuite` to `CWInPy` in Chapter 4 has already sped up the analysis method with greater robustness and customisability. This program will continue to be improved and new analysis methods will appear, alongside improvements in

---

[1]In particular, the end test masses of the Livingston detector were cleaned, reducing scatter by 20-40% compared to O4a

computing hardware, which will allow for more computationally expensive analyses. This will benefit both the method of recovering the braking index in Chapter 2 and the upcoming targeted CW searches. For example, `CWInPy` allows for searches of continuous-transient signals, signals with varying amplitude but which are long-lasting, on timescales of days to months (Abbott et al., 2022a). These may be emitted as a result of pulsar glitches, so searches for continuous-transient GWs can be performed alongside targeted searches on any pulsar glitches. Also, a method which might be able to detect a signal earlier than traditional targeted searches involves combining results for individual searches into an ensemble as in Pitkin et al. (2018), which uses a similar hierarchical approach as used in Chapter 2, and D'Onofrio et al. (2023).

5.1 Future Gravitational Wave Detectors

While the existing LVK detectors will continue to be upgraded, pushing their sensitivities to new limits for each observing run, there are other exciting prospects for GW detectors on the horizon. As discussed in Section 1.4.2, interferometric detectors have the potential to observe a GW background which is cosmological in origin. By pushing the observing distance further and improving sensitivity at lower frequencies, we can observe GW sources throughout the history of the universe, allowing for lifecycle and population studies. In the search for CWs, the spin-down limit for many pulsars sits below current detectors' sensitivities, as seen in Figure 3.1. An order of magnitude sensitivity improvement would put the spin-down limit for the majority of pulsars included in the O3 targeted analysis within detector sensitivity.

5.1.1 Ground-Based Detectors

There are multiple planned ground-based GW detectors which will probe new sensitivities and frequency ranges. Figure 5.1 shows the amplitude spectral densities (ASDs) for a variety of upcoming detectors along with the advanced-plus upgrades to the current LIGO (A+), Virgo (V+), and KAGRA (K+) detectors.
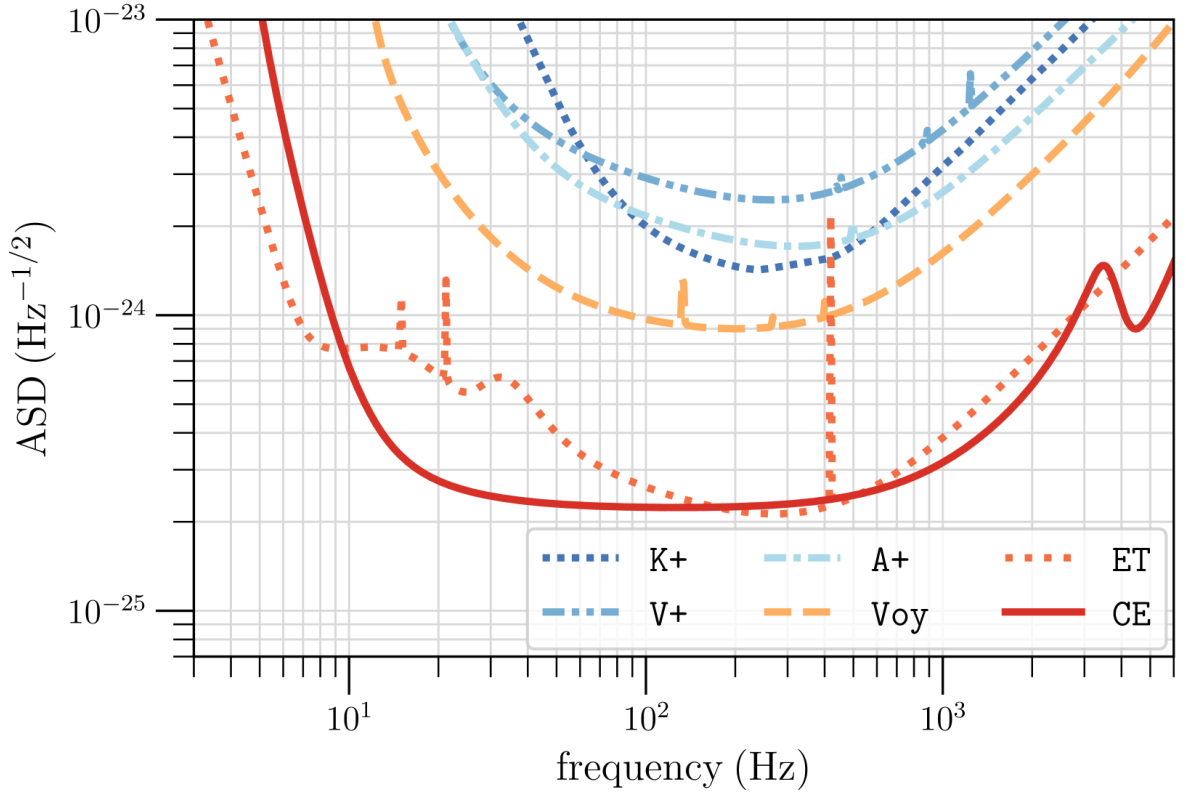
Figure 5.1 The amplitude spectral densities (ASDs) for various upcoming ground-based detectors. A+: Advanced-plus LIGO Hanford, LIGO Livingston, and LIGO India. V+: Advanced-plus Virgo. K+: Advanced-plus KAGRA. Voy: Voyager upgrade of LIGO. ET: Einstein Telescope. CE: Cosmic Explorer. Taken from Borhanian and Sathyaprakash (2024).

A+ will include a new detector in Aundha, India called A1. The additional detector, with a similar sensitivity to H1 and L1, will help to further improve the detector signal-to-noise ratio and baseline duty factor (the fraction of the time at least one of the detectors are operational over the length of the observing run) (Saleem et al., 2022). It is estimated that the number of CBC detections will increase by $\sim 70\%$ with the inclusion of A1 versus just H1, L1, and Virgo (Soni et al., 2024). In fully coherent searches (such as targeted CW searches), combining multiple identical detectors with known phase corrections results in a sensitivity improvement of $\sqrt{N}$ compared to a single detector (Riles, 2023). The inclusion of A1 therefore has twofold benefit to CW searches: improved duty factor and improved sensitivity. LIGO India is expected to be completed by 2030.

Figure 5.1 also shows the ASDs for the Voyager upgrade for LIGO. This technology can be installed in the current detectors with an aim to improve sensitivities by a factor of ~ 2 to ~ 4 compared to advanced LIGO, as they approach the thermodynamic and quantum mechanical limits of their current designs (Borhanian and Sathyaprakash, 2024). The most significant changes involve reducing the quantum noise through squeezed light and increased optical power in the arms, reducing thermal noise via mirror coatings with higher thermal conductivity and lower dissipation, and lowering the test mass temperature to 123 K to mitigate thermo-elastic noise (random heat flow within the masses) (Adhikari et al., 2024). This upgrade has already been partially implemented in O4a with the inclusion of vacuum squeezing and should be implemented in O5. Beyond this is A#, which will aim to further upgrade the detectors after O5 (Gupta et al., 2024; LIGO Scientific Collaboration, 2024).

In addition to the upcoming advancements to LIGO, there are also two new detectors shown in Figure 5.1: The Einstein Telescope (ET) and Cosmic Explorer (CE). The former will be made up of three cryogenically-cooled underground detectors with three 10 km arms nested together in a triangular shape. In the optimal design, each detector will have two interferometers, one tuned to high frequencies and one tuned to low frequencies (Branchesi et al., 2023). This arrangement can be seen in Figure 5.2. These enhancements will not only increase sensitivities at the frequencies of current detectors, but will also probe much lower frequencies. It will be able to detect GWs originating from redshifts of
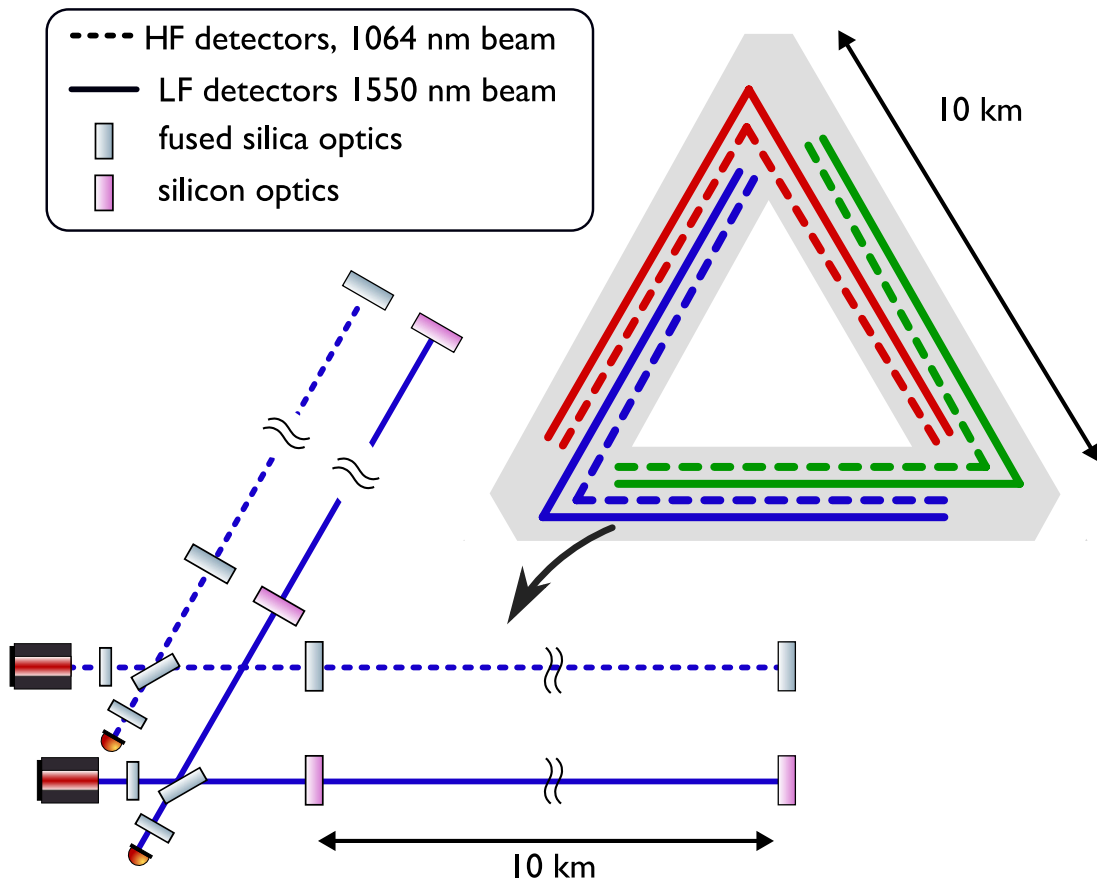
Figure 5.2 The geometry for the Einstein Telescope. Taken from Rowlinson et al. (2021).
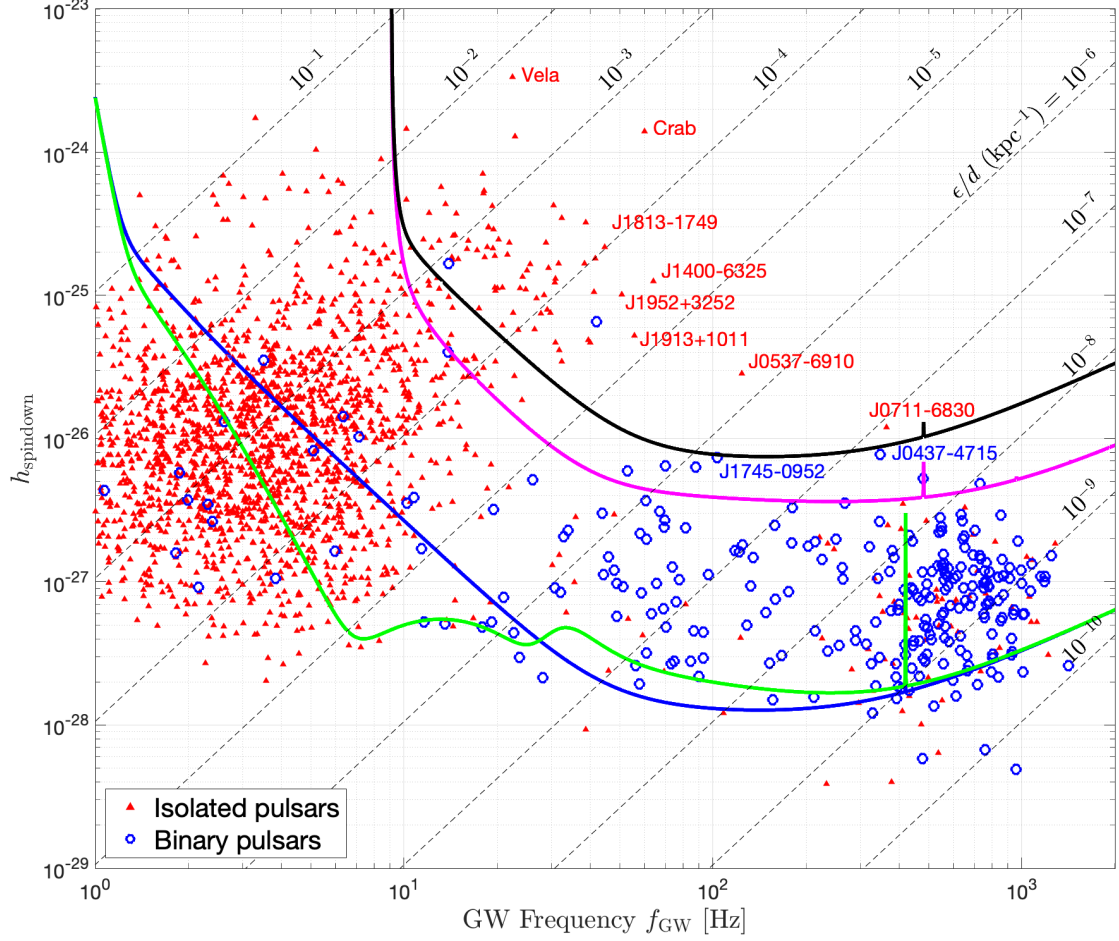
Figure 5.3 Pulsar spin-down limits plotted with sensitivity curves for O3 (black), an O4-like run using two detectors for two full years (magenta), and ET with two possible designs (blue and green). The green line represents the geometry described in Figure 5.2 (ET-C) while blue describes a geometry similar to LIGO (ET-B). Closed triangles represent isolated stars while open circles are binary systems. The grey dotted lines are quotients of ellipticity/distance. Taken from Riles (2023).

up to $z = 1000$ (during the cosmological dark ages). This allows it to see the entire population of stellar and intermediate black holes throughout history, giving valuable information about their demographics, origins, and evolution. Great improvements can also be made in CW searches. Figure 5.3 shows where various pulsar spin-down limits sit against the expected sensitivity curve of ET. Assuming that GW emission is contributing significantly to the spin-down for these pulsars (although this is unlikely), the sensitivity would be low enough to detect CWs from the majority of pulsars. ET aims to begin observations in 2035.

Cosmic Explorer is a planned US-based observatory consisting of two L-shaped detectors, one with 40 km arms and one with 20 km arms. The L-shaped design allows CE to utilise the mature technology which has already been used reliably in the LVK detectors. The large arm lengths will allow it to achieve similar sensitivities to ET at most frequencies and better in some, while an order of magnitude better than Advanced LIGO (Reitze et al., 2019). A benefit of being above ground is easier access for the purpose of topological upgrades in the future (Evans et al., 2021). It is envisioned to begin operation some time in the 2030s (Hall et al., 2021).

5.1.2 Space-Based Detectors

While upcoming detectors include new ground-based detectors like those in the LVK, they are not limited to Earth. Figure 5.4 shows the sensitivity curves for various space-based GW detectors on a plot of characteristic strain amplitude h_c against GW frequency f. One exciting prospect is the Laser Interferometer Space Antenna (LISA). This will be the first space-based GW observatory with a planned launch in ~ 2035 and operation from 2037 for at least 4.5 years. Led by the European Space Agency (ESA), it will have a duty factor of $> 82\%$ (Colpi et al., 2024). The LISA mission is also a collaboration between ESA, NASA, and the LISA consortium. LISA will comprise three spacecraft in a triangular formation trailing behind the Earth in its orbit, with each spacecraft separated by 2.5×10^6 km. Due to the distances involved, it is not feasible to use a Michelson interferometer design where a single laser is split and reflected. Instead, each spacecraft in LISA will have two lasers which travel one-way to the neighbouring
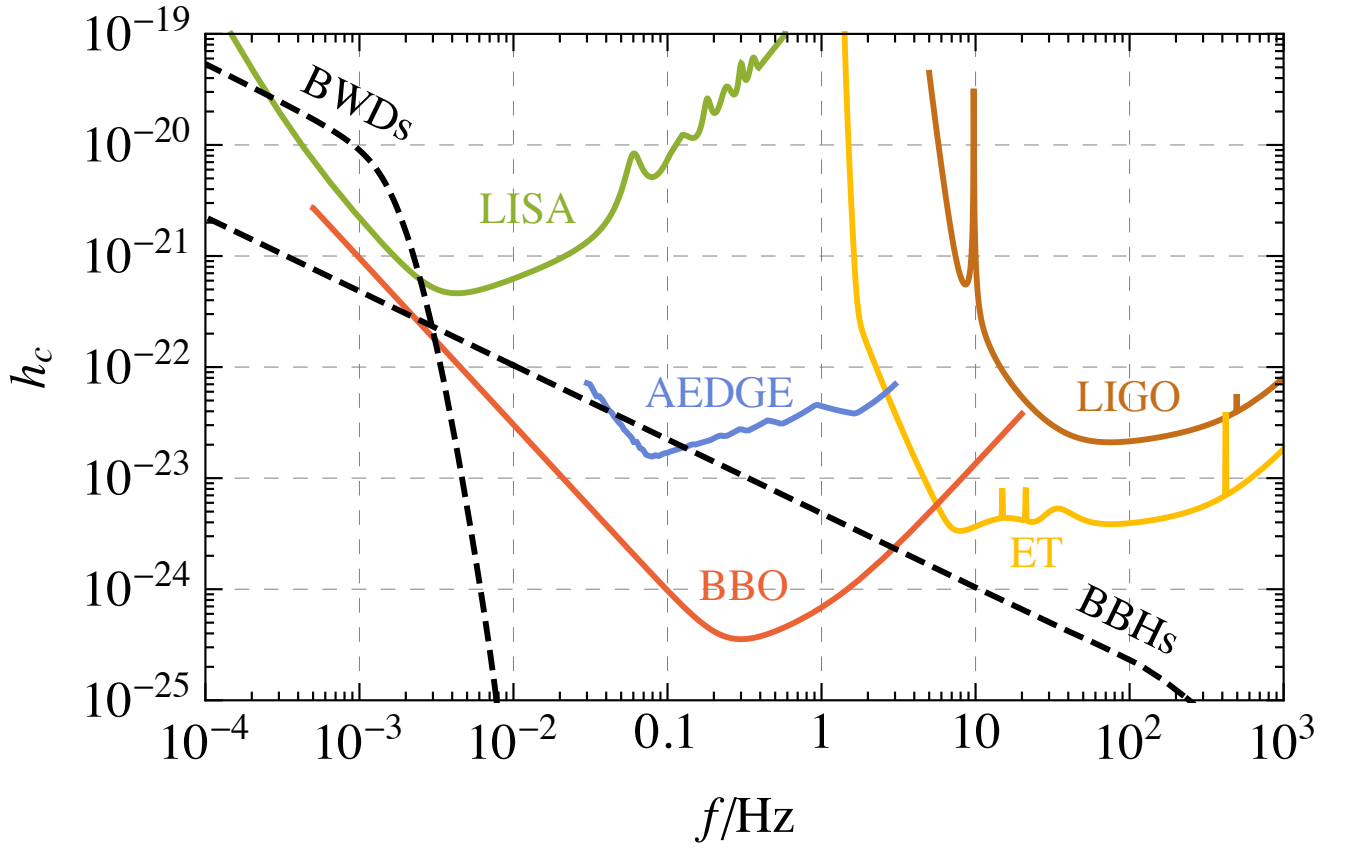
Figure 5.4 The sensitivity curve of LISA compared to LIGO and ET along with the GW foregrounds from binary white dwarfs (BWDs) and binary black holes (BBHs). Also included are the Atomic Experiment for Dark Matter and Gravity Exploration (AEDGE) and Big Bang Observer. Taken from Lewicki and Vaskonen (2021).
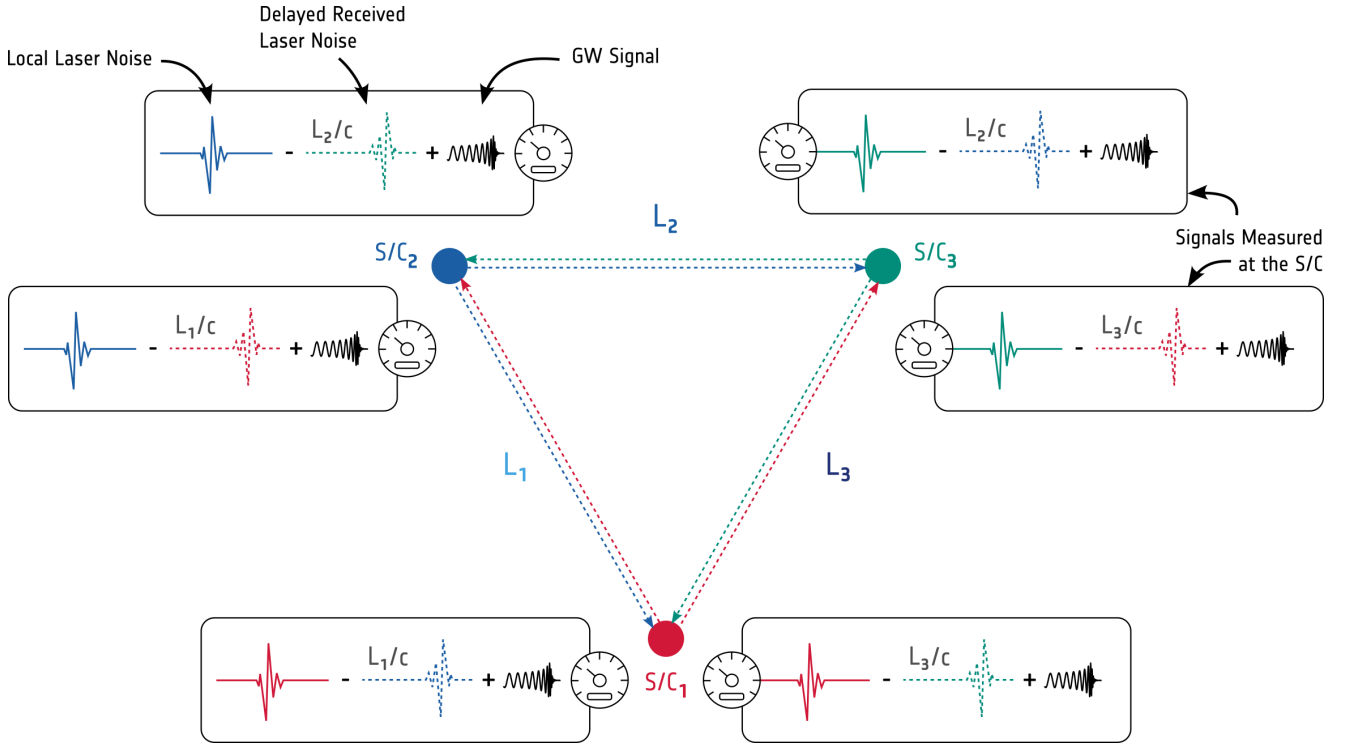
Figure 5.5 The geometry for LISA. Each spacecraft (S/C) measures the phase of interference between its local laser and neighbours which will contain a time-delayed copy of the neighbour's laser noise plus any GW signal. The noise can be suppressed by combining measurements from all three spacecraft along with corrections for the time delays. Taken from Colpi et al. (2024).

spacecraft as seen in Figure 5.5. This formation is passively stable for the duration of LISA's lifetime. LISA aims to detect a host of new low-frequency GW sources, achieving high sensitivity in the low-frequency range, between 20 μHz and 1 Hz, as seen in Figure 5.4. While LISA is not sensitive to the frequency region of CWs from deformed neutron stars, its frequency range puts it in the realm of CWs from binary white dwarfs.

LISA has already been tested in the LISA Pathfinder mission launched by the ESA in 2015. The aim of this mission was to demonstrate that the test masses would follow a geodesic (and therefore be free-falling) to a sufficient noise level. This mission used two 2 kg test masses separated by tens of centimetres. The mission exceeded the noise levels required, showing great promise for the prospects of the full LISA observatory (Armano et al., 2024).

The TAIJI program, a Chinese GW observatory with similar geometry and sensitivity to LISA (Hu and Wu, 2017), is likely to work in partnership with LISA, forming an even greater network. Wang et al. (2021) found that the most complimentary orientation would be for TAIJI to lead the Earth in its orbit by 20° with a −60° inclination in comparison to LISA, which trails the Earth by 20° with an inclination of +60°. This would provide the most accurate sky localisation and polarisation measurement. Another Chinese detector is TianQin (Luo et al., 2016). This detector would consist of three satellites in an equillateral triangle formation around Earth (An et al., 2022) It is possible that LISA, TAIJI and TianQin may be operational simultaneously, and if operating together in a network, could detect mergers of SMBHBs as standard sirens, precise contraints on the cosmological constant to 0.9 - 1.2 % (Jin et al., 2024).

The Big Bang Observer (Harry et al., 2006) is the proposed successor to LISA with three clusters of LISA-like detectors as seen in Figure 5.6. These would be launched in stages, starting with the pair of constellations in the star-like formation and following up with the 'outrigger' constellations. The two star constellations provide maximum cross-correlation while minimising cross-correlated noise, and the outrigger constellations primarily aid in improving angular resolution of foreground sources. The primary goal of the BBO is to detect the GW background, but it will still be sensitive to foreground sources. As seen in Figure 5.4, it is capable of achieving greater sensitivities than any of the other
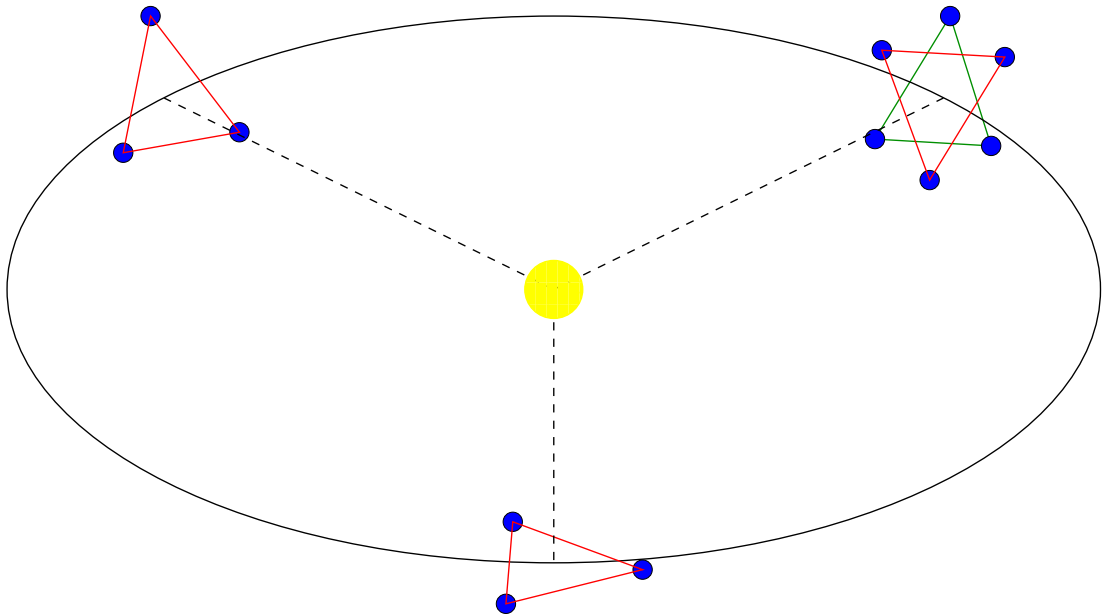
Figure 5.6 The geometry for BBO. Three sets of interferometers like those in LISA are positioned in an Earth-like orbit, with one pair rotated with respect to each other to form a star shaped configuration. Taken from Crowder and Cornish (2005).

observatories discussed here, though in a frequency range which only reaches slow-spinning neutron stars. While its primary aim will not be the detection of CWs from pulsars themselves, it will also be sensitive to CWs from both binary white dwarfs and binary black holes.

Also seen in Figure 5.4 is the Atomic Experiment for Dark Matter and Gravity Exploration (AEDGE) (Abou El-Neaj et al., 2020). This experiment will be sensitive in the range between that of LISA and ground-based observers like Advanced LIGO with the aim of detecting both GWs from sources such as SMBHs (Ellis et al., 2023), cosmic strings (Chang and Cui, 2022), and first-order phase transitions (Badziak and Nałecz, 2023); and bosonic dark matter (Arvanitaki et al., 2016). Rather than using laser interferometers, it will use cold atom interferometers, which involve measuring the phase shift as laser light travels across strontium atoms and excites them (Graham et al., 2016). It could be realised in the ESA Voyage 2050 Science Program, building on knowledge gained by LISA and other cold atom interferometers.

5.2 Electromagnetic Advancements

The future of GW astronomy is clearly filled with novel ideas for observatories which can push the boundaries of GW detection towards the edges of the universe. However, in the realm of CW searches for known pulsars, a vital part of the puzzle comes from the EM detections used to constrain the priors. As discussed briefly in Section 2.4, constant advancements to PTAs are being achieved. The observation length and frequency have a significant impact on obtaining accurate pulsar timing models, which will naturally increase with time and the development of more telescopes.

The International Pulsar Timing Array (IPTA) is a consortium containing the European Pulsar Timing Array (EPTA), the North American Nanohertz Observatory for Gravitational Waves (NANOGrav), the Indian Pulsar Timing Array Project (InPTA), and the Parkes Pulsar Timing Array (PPTA). Its most recent data release described in Perera et al. (2019) involved 65 MSPs. This includes the 9-year NANOGrav dataset of 37 pulsars. Already, the 15-year NANOGrav

dataset has 67 MSPs itself. While potential observations of the GWB benefit from high quality pulsar timing rather than pure quantity, the large number of smaller telescopes provides opportunities to observe increasing numbers of pulsars which is useful in CW searches.

The Square Kilometre Array Observatory (SKAO) offers major advancements in radio astronomy. It consists of two radio telescopes in South Africa and Australia, with the SKAO headquarters in the UK. The Australian telescope is called SKA-Low as it features 131,072 low-frequency radio antennas spread between 512 stations for a total collecting area of 419,000 m^2. Each antenna is a log-periodic antenna which features triangular teeth of increasing scale (like a Christmas tree). This variation in teeth size gives SKA-Low a wide frequency range of 50 - 350 MHz (Grainge et al., 2017). Compared to LOFAR, a similar radio telescope in the Netherlands, SKA-Low will have a 25% better resolution with 8 times greater sensitivity and be able to survey the sky 135 times faster, allowing for frequent observations of more pulsars and faster responses for multimessenger observations (Braun et al., 2019). SKA-Mid is in South Africa and contains 197 mid-frequency 15 m-diameter radio dishes. These dishes are arranged in a pattern radiating out from a central point in three spiral arms with a total collecting area of 33,000 m^2 which contributes to greater sensitivity and a baseline (distance between two furthest dishes) of 150 km contributing to greater resolution. It has a frequency range of 350 MHz - 15.4 GHz and aims to reach 24 GHz. The existing MeerKAT radio telescope with its 13.5 m-diameter dishes will also form part of the SKA-Mid array (Grainge et al., 2017). Compared to the Karl G. Jansky Very Large Array (VLA) in the US, SKA-Mid will have 5 times the resolution, 5 times the sensitivity and 60 times the survey speed (Braun et al., 2019). In 2024, four of the SKA-Low stations have been populated and the synchronisation of the first SKA-Mid dish with MeerKAT has been tested. Construction on both is scheduled to finish by 2030. These improvements in sensitivity will lead to better pulsar timing models with reduced uncertainties, which in turn can lead to better constraints on the pulsar parameters used in targeted CW searches, increasing their sensitivities. Additionally, the SKA may result in the observation of more pulsars, leading to more candidates for observable CWs.

5.3 Summary

This thesis has described the current state of physics from the perspective of GW observations, in particular searches for CWs from known pulsars, an area in which there have been no observations to date. Chapter 2 introduced a novel Bayesian method for determining the braking index from a population of pulsars, the measurement of which would indicate the source of pulsar spin-down, possibly identifying GW emission as a contributor. Moving forward, the next steps would be using a more sophisticated model followed by real pulsar TOAs. While this method is unlikely to uncover the braking index from current datasets, the advancements discussed in Section 5.2 increase the likelihood that this method will be viable in the future.

In Chapters 3 and 4, two Bayesian searches using the most recent data releases from the LIGO-Virgo-KAGRA collaboration are presented, surpassing the spin-down limits for 23 and 29 pulsars respectively. In the O3 search, the pulsar with the lowest $h_0^{95\%}$ upper limit was J1745$-$0952 with 4.72×10^{-27} corresponding to an ellipticity of 9.5×10^{-8} and a mountain size of 0.01 - 0.02 cm depending on the EOS and assuming a mass of 1.4 M$_\odot$[1]. Meanwhile, in the O4a search, J0537$-$6910 had the most constraining amplitude upper limit of 6.4×10^{-27} which corresponds to an ellipticity of 1.95×10^{-5} and a mountain size of 2 - 4 cm following the same method and assumptions.

While no signals were found, upcoming advancements in both analysis methods and current detectors, and the inclusion of the new observatories as discussed throughout Chapter 5, will increase the prospect of a future detection in upcoming LVK runs and beyond.

---

[1]This is calculated using Equation 11 and Figures 1 and 2 from Johnson-McDaniel (2013)

Appendix A

A.1   Pulsar braking index table

Name	F0 (s)	F0 err (s)	F1	F1 err (s^{-1})	F2 (s^{-1})	RMS ms	Mean n*	Std n*
J0023+0923	327.8	3.45e-13	-1.23e-15	1.49e-20	2.30e-32	0.000288	5.17	2.83
J0030+0451	205.5	7.74e-11	-4.30e-16	2.78e-19	4.49e-33	0.0002	5.03	2.83
J0340+4130	303.1	9.67e-13	-6.47e-16	4.17e-20	6.91e-33	0.000449	4.79	2.82
J0613-0200	326.6	1.63e-12	-1.02e-15	1.71e-20	1.60e-32	0.000188	4.67	2.80
J0636+5128	348.6	8.68e-13	-4.19e-16	7.25e-20	2.52e-33	0.000596	5.05	2.83
J0645+5158	112.9	1.23e-13	-6.28e-17	4.49e-21	1.74e-34	0.000196	5.10	2.82
J0740+6620	346.5	1.18e-12	-1.46e-15	7.91e-20	3.09e-32	0.000106	4.49	2.80
J0931-1902	215.6	8.77e-13	-1.69e-16	5.35e-20	6.60e-34	0.000424	5.08	2.84
J1012+5307	190.3	1.49e-12	-6.20e-16	1.75e-20	1.01e-32	0.000209	5.17	2.82
J1024-0719	193.7	6.18e-13	-6.96e-16	8.38e-21	1.25e-32	0.00024	5.19	2.83
J1125+7819	238.0	2.35e-12	-3.93e-16	1.61e-19	3.25e-33	0.000614	5.02	2.88
J1453+1902	172.6	2.09e-12	-3.47e-16	1.15e-19	3.50e-33	0.000798	5.02	2.85
J1455-3330	125.2	3.59e-13	-3.81e-16	4.40e-21	5.80e-33	0.000544	4.94	2.85
J1600-3053	277.9	1.58e-13	-7.34e-16	3.63e-21	9.69e-33	0.000213	4.99	2.80
J1614-2230	317.4	2.21e-13	-9.69e-16	5.20e-21	1.48e-32	0.000175	5.06	2.85
J1640+2224	316.1	1.50e-13	-2.82e-16	2.53e-21	1.25e-33	0.000142	5.13	2.79
J1643-1224	216.4	4.21e-12	-8.64e-16	5.39e-20	1.73e-32	0.000292	5.34	2.80
J1713+0747	218.8	7.93e-14	-4.08e-16	1.11e-21	3.81e-33	8.1e-05	4.75	2.86
J1738+0333	170.9	4.12e-13	-7.05e-16	1.08e-20	1.45e-32	0.000272	4.54	2.83
J1741+1351	266.9	2.13e-13	-2.15e-15	8.23e-21	8.68e-32	0.000148	6.77	2.36
J1744-1134	245.4	1.78e-12	-5.38e-16	1.68e-20	5.90e-33	0.000278	4.99	2.83
J1747-4036	607.7	2.03e-10	-4.85e-15	2.21e-18	1.94e-31	0.000767	5.25	2.81
J1832-0836	367.8	5.82e-13	-1.12e-15	3.16e-20	1.70e-32	0.000195	5.10	2.82
J1853+1303	244.4	2.79e-12	-5.21e-16	5.36e-20	5.55e-33	9.2e-05	5.15	2.88
B1855+09	186.5	4.05e-12	-6.20e-16	2.41e-20	1.03e-32	0.000357	5.13	2.84
J1903+0327	465.1	2.03e-11	-4.07e-15	3.70e-19	1.78e-31	0.000394	4.93	2.82
J1909-3744	339.3	1.21e-12	-1.61e-15	9.76e-21	3.84e-32	5.8e-05	3.48	2.50
J1910+1256	200.7	3.83e-13	-3.90e-16	8.10e-21	3.79e-33	0.000399	5.03	2.83
J1911+1347	216.2	2.15e-13	-7.91e-16	1.31e-20	1.45e-32	0.000115	5.28	2.77
J1918-0642	130.8	1.11e-13	-4.39e-16	1.45e-21	7.38e-33	0.000296	4.83	2.85
J1923+2515	264.0	4.93e-13	-6.66e-16	1.41e-20	8.40e-33	0.000237	4.95	2.83
B1937+21	641.9	3.26e-11	-4.33e-14	1.79e-19	1.46e-29	0.000103	5.01	0.06
J1944+0907	192.9	4.13e-13	-6.45e-16	6.20e-21	1.08e-32	0.000375	5.11	2.80
J1946+3417	315.4	6.12e-12	-3.15e-16	2.18e-19	1.57e-33	0.000143	4.90	2.83
B1953+29	163.0	7.93e-13	-7.91e-16	2.76e-20	1.92e-32	0.000475	5.33	2.85
J2010-1323	191.5	1.48e-13	-1.77e-16	4.31e-21	8.17e-34	0.00025	4.95	2.82
J2017+0603	345.3	5.14e-13	-9.53e-16	3.30e-20	1.32e-32	9.7e-05	4.42	2.81
J2033+1734	168.1	9.20e-13	-3.15e-16	5.71e-20	2.95e-33	0.00052	4.93	2.87
J2043+1711	420.2	3.04e-13	-9.26e-16	9.33e-21	1.02e-32	0.000122	4.69	2.78
J2145-0750	62.3	9.24e-13	-1.16e-16	8.99e-21	1.07e-33	0.000274	4.95	2.82
J2214+3000	320.6	1.13e-12	-1.51e-15	3.71e-20	3.57e-32	0.000419	5.17	2.87
J2229+2643	335.8	7.18e-13	-1.72e-16	4.84e-20	4.40e-34	0.000196	5.01	2.87
J2234+0611	279.6	3.94e-13	-9.39e-16	2.25e-20	1.58e-32	3.5e-05	4.21	2.68
J2234+0944	275.7	8.77e-13	-1.53e-15	3.77e-20	4.23e-32	0.000165	5.22	2.80
J2302+4442	192.6	7.64e-13	-5.14e-16	3.52e-20	6.87e-33	0.000693	4.95	2.84
J2317+1439	290.3	3.20e-11	-2.05e-16	1.14e-19	7.22e-34	0.000204	4.97	2.85
J2322+2057	208.0	9.85e-13	-4.18e-16	1.02e-19	4.19e-33	0.000237	5.11	2.85

Table A.1 Pulsar values used in the analysis in Chapter 2. Columns denoted by *
include values calculated from individual pulsar posterior samples in a simulated 20-
year run with an average RMS of 1×10^{-5} ms scaled using the listed RMS value and
equation (2.5) and assuming all pulsars have a braking index of exactly $n = 5$.

A.2   O3 analysis tables

Table A.2: Limits on Gravitational-wave Amplitude and Derived Quantities from O3 (Chapter 3) for 213 Pulsars.

Pulsar Name (J2000)	$f_{\rm rot}$ (Hz)	$\dot{P}_{\rm rot}$ (s s^{-1})	Distance (kpc)	$h_0^{\rm sd}$	$C_{21}^{95\%}$	$C_{22}^{95\%}$	$h_0^{95\%}$	$Q_{22}^{95\%}$ (kg m^2)	$\varepsilon^{95\%}$	$h_0^{95\%}/h_0^{\rm sd}$	$\mathcal{O}_{m=1,2}^{l=2}$	$\mathcal{O}_{m=2}^{l=2}$
J0023+0923[a,e]	327.8	1.0×10^{-20}	1.11 (a)	1.3×10^{-27}	9.6×10^{-27}	8.5×10^{-27}	1.7×10^{-26}	3.3×10^{30}	4.2×10^{-8}	13	-3.2	-1.0
J0030+0451[a,e]	205.5	1.0×10^{-20}	0.33 (a)	3.6×10^{-27}	8.7×10^{-27}	3.1×10^{-27}	6.5×10^{-27}	9.2×10^{29}	1.2×10^{-8}	1.8	-4.4	-2.3
J0034−0534[a,e]	532.7	4.2×10^{-21}	1.35 (b)	8.9×10^{-28}	1.1×10^{-28}	5.2×10^{-27}	1.1×10^{-26}	9.2×10^{29}	1.2×10^{-8}	12	-4.7	-2.4
J0101−6422[a,δ]	388.6	3.7×10^{-21}	1.00 (b)	9.7×10^{-28}	1.0×10^{-28}	3.2×10^{-27}	7.4×10^{-27}	9.0×10^{29}	1.2×10^{-8}	7.6	-4.7	-2.5
J0102+4839[e]	337.4	1.1×10^{-20}	2.31 (b)	6.8×10^{-28}	1.3×10^{-28}	6.3×10^{-27}	1.3×10^{-26}	4.7×10^{30}	6.1×10^{-8}	19	-3.7	-1.6
J0117+5914[αα]	9.9	5.9×10^{-15}	1.77 (b)	1.1×10^{-25}	···	···	1.7×10^{-25}	5.8×10^{34}	7.5×10^{-4}	1.6	···	-2.5
J0125−2327[e]	272.1	1.8×10^{-20}	0.92 (b)	2.0×10^{-27}	1.2×10^{-27}	4.2×10^{-27}	8.5×10^{-27}	1.9×10^{30}	2.5×10^{-8}	4.3	-4.1	-2.1
J0154+1833[a,e]	422.9	1.1×10^{-21}	1.62 (b)	3.4×10^{-28}	1.6×10^{-28}	3.6×10^{-27}	9.7×10^{-27}	1.6×10^{30}	2.1×10^{-8}	29	-4.3	-2.5
J0218+4232[a,e]	430.5	7.6×10^{-20}	3.15 (c)	1.5×10^{-27}	1.2×10^{-27}	4.0×10^{-27}	8.9×10^{-27}	2.8×10^{30}	3.6×10^{-8}	6.1	-4.5	-2.5
J0340+4130[a,e]	303.1	6.7×10^{-21}	1.60 (b)	7.2×10^{-28}	1.7×10^{-28}	3.2×10^{-27}	6.8×10^{-27}	2.2×10^{30}	2.8×10^{-8}	9.5	-3.7	-2.4
J0348+0432[a,e]	25.6	2.3×10^{-19}	2.10 (d)	9.3×10^{-28}	9.6×10^{-28}	7.0×10^{-26}	1.4×10^{-26}	8.1×10^{32}	1.1×10^{-5}	15	-4.5	-2.4
J0406+3039[e]	383.3	8.3×10^{-21}	···	···	1.6×10^{-26}	4.2×10^{-27}	8.5×10^{-27}	···	···	···	-3.9	-2.4
J0407+1607[e]	38.9	7.9×10^{-20}	1.34 (b)	1.1×10^{-27}	1.9×10^{-26}	3.0×10^{-27}	6.7×10^{-27}	1.1×10^{32}	1.4×10^{-6}	6.4	-5.4	-2.6
J0453+1559[a,e]	21.8	1.8×10^{-19}	0.52 (b)	3.1×10^{-27}	1.5×10^{-27}	5.4×10^{-27}	1.1×10^{-26}	2.2×10^{32}	2.8×10^{-6}	3.6	-5.5	-3.0
J0509+0856[a,e]	246.6	3.8×10^{-21}	0.82 (b)	9.6×10^{-28}	1.3×10^{-26}	3.1×10^{-27}	8.3×10^{-27}	2.0×10^{30}	2.6×10^{-8}	8.6	-4.2	-2.2
J0509+3801[e]	13.1	7.9×10^{-18}	1.56 (b)	5.3×10^{-27}	2.5×10^{-27}	2.0×10^{-26}	4.4×10^{-26}	7.3×10^{33}	9.5×10^{-5}	8.3	-9.2	-2.7
J0557+1550[e]	391.2	7.4×10^{-21}	1.83 (b)	7.5×10^{-28}	9.0×10^{-27}	5.1×10^{-27}	1.1×10^{-26}	2.3×10^{30}	3.0×10^{-8}	14	-4.5	-2.2
J0557−2948[δ]	22.9	7.3×10^{-20}	4.27 (b)	2.4×10^{-28}	1.4×10^{-28}	5.9×10^{-27}	1.5×10^{-26}	2.2×10^{33}	2.8×10^{-5}	60	-5.2	-2.7
J0609+2130[α]	18.0	2.4×10^{-19}	0.57 (b)	2.9×10^{-27}	5.7×10^{-25}	8.4×10^{-27}	1.8×10^{-26}	6.0×10^{32}	7.8×10^{-6}	6.4	-8.7	-2.9

Table A.2: Limits on Gravitational-wave Amplitude and Derived Quantities from O3 (Chapter 3) for 213 Pulsars.

Pulsar Name (J2000)	$f_{\rm rot}$ (Hz)	$\dot{P}_{\rm rot}$ (s s^{-1})	Distance (kpc)	$h_0^{\rm sd}$	$C_{21}^{95\%}$	$C_{22}^{95\%}$	$h_0^{95\%}$	$Q_{22}^{95\%}$ (kg m^2)	$\varepsilon^{95\%}$	$h_0^{95\%}/h_0^{\rm sd}$	$\mathcal{O}_{m=1,2}^{l=2}$	$\mathcal{O}_{m=2}^{l=2}$
J0610−2100[ae]	259.0	1.1×10^{-21}	3.26 (b)	1.3×10^{-28}	1.5×10^{-26}	4.3×10^{-27}	9.4×10^{-27}	8.3×10^{30}	1.1×10^{-7}	71	-3.8	-2.1
J0613−0200[ae]	326.6	8.3×10^{-21}	0.60 (f)	2.2×10^{-27}	1.2×10^{-26}	7.5×10^{-27}	1.6×10^{-26}	1.7×10^{30}	2.2×10^{-8}	7.4	-3.2	-1.2
J0614−3329[ae]	317.6	1.8×10^{-20}	0.63 (g)	3.0×10^{-27}	8.5×10^{-27}	4.2×10^{-27}	8.3×10^{-27}	9.5×10^{29}	1.2×10^{-8}	2.7	-4.5	-2.3
J0621+1002[ae]	34.7	4.6×10^{-20}	0.42 (b)	2.4×10^{-27}	3.4×10^{-27}	3.7×10^{-27}	7.7×10^{-27}	4.9×10^{31}	6.4×10^{-7}	3.2	-5.3	-2.6
J0636+5129[ae]	348.6	3.4×10^{-21}	0.21 (b)	4.2×10^{-27}	9.7×10^{-27}	3.8×10^{-27}	7.8×10^{-27}	2.5×10^{29}	3.2×10^{-9}	1.9	-5.2	-2.5
J0636−3044[δ]	253.4	2.1×10^{-20}	0.71 (b)	2.6×10^{-27}	7.5×10^{-27}	3.8×10^{-27}	7.5×10^{-27}	1.5×10^{30}	2.0×10^{-8}	2.8	-4.5	-2.3
J0645+5158[ae]	112.9	2.7×10^{-21}	1.20 (a)	3.7×10^{-28}	7.6×10^{-27}	3.1×10^{-27}	6.6×10^{-27}	1.1×10^{31}	1.5×10^{-7}	18	-4.4	-2.1
J0709+0458[ae]	29.0	3.8×10^{-19}	1.20 (b)	2.2×10^{-27}	4.2×10^{-27}	4.8×10^{-27}	1.3×10^{-26}	3.3×10^{32}	4.3×10^{-6}	5.7	-5.7	-2.5
J0721−2038[ε]	64.3	4.4×10^{-20}	2.68 (b)	5.1×10^{-28}	1.2×10^{-28}	2.6×10^{-27}	6.4×10^{-27}	7.5×10^{31}	9.8×10^{-7}	13	-4.7	-2.2
J0732+2314[ε]	244.5	6.0×10^{-21}	1.15 (b)	8.5×10^{-28}	7.9×10^{-28}	2.8×10^{-27}	8.3×10^{-27}	2.9×10^{30}	3.8×10^{-8}	9.7	-4.5	-2.2
J0740+6620[ae]	346.5	6.4×10^{-21}	1.14 (h)	1.1×10^{-27}	9.5×10^{-27}	2.8×10^{-27}	6.3×10^{-27}	1.1×10^{30}	1.4×10^{-8}	5.9	-5.5	-2.7
J0751+1807[ae]	287.5	6.7×10^{-21}	0.60 (i)	1.9×10^{-27}	1.1×10^{-27}	5.0×10^{-27}	1.0×10^{-26}	1.3×10^{30}	1.7×10^{-8}	5.4	-4.1	-2.1
J0824+0028[ae]	101.4	1.4×10^{-19}	1.69 (b)	1.8×10^{-27}	8.6×10^{-27}	3.5×10^{-27}	7.6×10^{-27}	2.3×10^{31}	3.0×10^{-7}	4.2	-4.2	-2.0
J0900−3144[ae]	90.0	4.9×10^{-20}	0.89 (i)	1.9×10^{-27}	1.3×10^{-27}	2.8×10^{-27}	6.2×10^{-27}	1.3×10^{31}	1.6×10^{-7}	3.3	-5.0	-3.0
J0921−5202[δ]	103.3	2.1×10^{-20}	0.40 (k)	2.9×10^{-27}	9.3×10^{-27}	2.3×10^{-27}	5.8×10^{-27}	4.0×10^{30}	5.1×10^{-8}	2	-4.4	-2.2
J0931−1902[ae]	215.6	3.2×10^{-21}	3.72 (b)	1.8×10^{-28}	7.9×10^{-27}	3.6×10^{-27}	7.7×10^{-27}	1.1×10^{31}	1.5×10^{-7}	43	-4.3	-2.1
J0955−6150[δ]	500.2	1.4×10^{-20}	2.17 (b)	9.9×10^{-28}	1.1×10^{-26}	5.6×10^{-27}	1.8×10^{-26}	2.8×10^{30}	3.6×10^{-8}	18	-4.8	-2.2
J1012+5307[ae]	190.3	1.0×10^{-20}	0.70 (j)	1.6×10^{-27}	9.5×10^{-27}	4.0×10^{-27}	7.8×10^{-27}	2.8×10^{30}	3.6×10^{-8}	4.8	-4.2	-2.1
J1012−4235[δ]	322.5	6.5×10^{-21}	0.37 (b)	3.1×10^{-27}	9.3×10^{-27}	7.1×10^{-27}	1.6×10^{-26}	1.0×10^{30}	1.3×10^{-8}	5	-3.8	-1.8

Table A.2: Limits on Gravitational-wave Amplitude and Derived Quantities from O3 (Chapter 3) for 213 Pulsars.

Pulsar Name (J2000)	$f_{\rm rot}$ (Hz)	$\dot{P}_{\rm rot}$ (s s^{-1})	Distance (kpc)	$h_0^{\rm sd}$	$C_{21}^{95\%}$	$C_{22}^{95\%}$	$h_0^{95\%}$	$Q_{22}^{95\%}$ (kg m^2)	$\varepsilon^{95\%}$	$h_0^{95\%}/h_0^{\rm sd}$	$\mathcal{O}_{m=1,2}^{l=2}$	$\mathcal{O}_{m=2}^{l=2}$
J1017$-$7156$^{a\delta}$	427.6	2.8×10^{-21}	3.50 (f)	2.5×10^{-28}	7.7×10^{-27}	4.1×10^{-27}	8.8×10^{-27}	3.1×10^{30}	4.0×10^{-8}	35	-4.7	-2.4
J1022$+$1001$^{a\delta}$	60.8	3.5×10^{-20}	0.64 (f)	1.8×10^{-27}	1.4×10^{-27}	3.8×10^{-27}	7.7×10^{-27}	2.4×10^{31}	3.2×10^{-7}	4.2	-4.6	-1.9
J1024$-$0719$^{b\epsilon}$	193.7	$\cdots$	1.20 (f)	$\cdots$	1.6×10^{-26}	3.7×10^{-27}	7.2×10^{-27}	4.2×10^{30}	5.4×10^{-8}	$\cdots$	-3.4	-2.2
J1035$-$6720$^{a\delta}$	348.2	4.5×10^{-20}	1.46 (b)	2.2×10^{-27}	9.9×10^{-27}	4.4×10^{-27}	1.3×10^{-26}	2.8×10^{30}	3.6×10^{-8}	5.8	-5.2	-2.2
J1036$-$8317$^{\delta}$	293.4	3.1×10^{-20}	0.93 (b)	2.6×10^{-27}	1.2×10^{-26}	3.3×10^{-27}	7.1×10^{-27}	1.4×10^{30}	1.8×10^{-8}	2.7	-4.4	-2.4
J1038$+$0032$^{\epsilon}$	34.7	6.7×10^{-20}	5.95 (b)	2.1×10^{-28}	3.8×10^{-27}	3.2×10^{-27}	6.9×10^{-27}	6.3×10^{32}	8.1×10^{-6}	33	-5.3	-2.6
J1045$-$4509$^{a\delta}$	133.8	1.8×10^{-20}	0.59 (f)	2.1×10^{-27}	1.5×10^{-27}	5.0×10^{-27}	9.6×10^{-27}	5.8×10^{30}	7.5×10^{-8}	4.6	-2.7	-1.3
J1101$-$6424$^{\delta}$	195.7	1.8×10^{-21}	2.17 (b)	2.2×10^{-28}	8.7×10^{-28}	2.3×10^{-27}	5.7×10^{-27}	5.9×10^{30}	7.6×10^{-8}	26	-4.6	-2.7
J1103$-$5403$^{\delta}$	294.7	3.7×10^{-21}	1.68 (b)	5.0×10^{-28}	1.0×10^{-26}	3.4×10^{-27}	9.6×10^{-27}	3.4×10^{30}	4.4×10^{-8}	19	-4.7	-3.5
J1125$+$7819$^{b\epsilon}$	238.0	$\cdots$	0.88 (b)	$\cdots$	7.7×10^{-27}	3.4×10^{-27}	7.3×10^{-27}	2.1×10^{30}	2.7×10^{-8}	$\cdots$	-4.5	-2.3
J1125$-$5825$^{a\delta}$	322.4	6.0×10^{-20}	1.74 (b)	2.0×10^{-27}	8.6×10^{-27}	3.7×10^{-27}	9.2×10^{-27}	2.8×10^{30}	3.6×10^{-8}	4.5	-4.7	-2.3
J1125$-$6014$^{\delta}$	380.2	4.0×10^{-21}	1.40 (f)	7.1×10^{-28}	8.0×10^{-28}	3.8×10^{-27}	8.2×10^{-27}	1.5×10^{30}	1.9×10^{-8}	12	-4.7	-2.4
J1142$+$0119$^{b\epsilon}$	197.0	$\cdots$	2.17 (b)	$\cdots$	1.6×10^{-26}	3.6×10^{-27}	7.4×10^{-27}	7.6×10^{30}	9.8×10^{-8}	$\cdots$	-3.4	-2.1
J1207$-$5050$^{a\delta}$	206.5	5.7×10^{-21}	1.27 (b)	6.9×10^{-28}	9.5×10^{-27}	4.4×10^{-27}	1.1×10^{-26}	6.0×10^{30}	7.8×10^{-8}	16	-4.1	-1.9
J1216$-$6410$^{\delta}$	282.5	1.6×10^{-21}	1.10 (b)	5.0×10^{-28}	9.7×10^{-27}	2.8×10^{-27}	7.3×10^{-27}	1.8×10^{30}	2.4×10^{-8}	15	-4.5	-2.4
J1231$-$1411$^{a\epsilon}$	271.5	8.3×10^{-21}	0.42 (b)	2.9×10^{-27}	1.3×10^{-26}	5.6×10^{-27}	1.1×10^{-26}	1.1×10^{30}	1.4×10^{-8}	3.7	-3.8	-2.1
J1300$+$1240$^{b\epsilon}$	160.8	$\cdots$	0.60 (j)	$\cdots$	1.2×10^{-26}	5.2×10^{-27}	1.1×10^{-26}	4.6×10^{30}	6.0×10^{-8}	$\cdots$	-3.5	-1.6
J1302$-$3258$^{\epsilon}$	265.2	6.6×10^{-21}	1.43 (b)	7.4×10^{-28}	2.1×10^{-26}	4.1×10^{-27}	7.5×10^{-27}	2.8×10^{30}	3.6×10^{-8}	10	-3.3	-2.3
J1312$+$0051$^{a\epsilon}$	236.5	8.2×10^{-21}	1.47 (b)	7.6×10^{-28}	9.6×10^{-27}	2.9×10^{-27}	6.3×10^{-27}	3.0×10^{30}	3.9×10^{-8}	8.3	-4.5	-2.4

Table A.2: Limits on Gravitational-wave Amplitude and Derived Quantities from O3 (Chapter 3) for 213 Pulsars.

Pulsar Name (J2000)	f_{rot} (Hz)	$\dot{P}_{rot}$ (s s^{-1})	Distance (kpc)	h_0^{sd}	$C_{21}^{95\%}$	$C_{22}^{95\%}$	$h_0^{95\%}$	$Q_{22}^{95\%}$ (kg m^2)	$\varepsilon^{95\%}$	$h_0^{95\%}/h_0^{sd}$	$\mathcal{O}_{m=1,2}^{l=2}$	$\mathcal{O}_{m=2}^{l=2}$
J1327+3423[ε]	24.1	1.3×10^{-19}	$\cdots$	$\cdots$	1.3×10^{-25}	5.2×10^{-27}	1.6×10^{-26}	$\cdots$	$\cdots$	$\cdots$	-5.1	-2.6
J1327−0755[bε]	373.4	$\cdots$	25.00 (b)	$\cdots$	1.0×10^{-26}	3.9×10^{-27}	7.9×10^{-27}	2.6×10^{31}	3.3×10^{-7}	$\cdots$	-4.6	-2.4
J1337−6423[aδ]	106.1	1.8×10^{-20}	5.94 (b)	1.9×10^{-28}	1.3×10^{-26}	3.1×10^{-26}	6.7×10^{-27}	6.4×10^{31}	8.3×10^{-7}	36	-4.2	-2.1
J1400−1431[aε]	324.2	9.0×10^{-23}	0.27 (n)	5.1×10^{-28}	8.2×10^{-27}	3.9×10^{-27}	8.3×10^{-27}	3.9×10^{29}	5.0×10^{-9}	16	-4.6	-2.3
J1411+2551[aε]	16.0	8.9×10^{-20}	1.13 (b)	8.5×10^{-28}	9.7×10^{-25}	1.7×10^{-25}	3.2×10^{-26}	2.6×10^{33}	3.3×10^{-5}	37	-9.3	-2.7
J1420−5625[δ]	29.3	6.8×10^{-20}	1.33 (b)	8.5×10^{-28}	6.0×10^{-28}	4.1×10^{-28}	1.1×10^{-27}	3.2×10^{32}	4.1×10^{-6}	13	-5.1	-2.7
J1421−4409[aδ]	156.6	6.0×10^{-21}	2.08 (b)	3.8×10^{-28}	1.0×10^{-26}	2.8×10^{-27}	6.6×10^{-27}	1.0×10^{31}	1.3×10^{-7}	18	-4.3	-2.2
J1431−4715[aδ]	497.0	1.1×10^{-20}	1.53 (p)	1.3×10^{-27}	1.5×10^{-27}	6.2×10^{-27}	1.6×10^{-26}	1.8×10^{30}	2.3×10^{-8}	13	-4.4	-2.2
J1431−5740[δ]	243.3	6.4×10^{-21}	3.55 (b)	2.8×10^{-28}	9.7×10^{-28}	3.1×10^{-27}	6.7×10^{-27}	7.4×10^{30}	9.5×10^{-8}	24	-4.4	-2.4
J1435−6100[δ]	107.0	2.4×10^{-20}	2.81 (b)	4.6×10^{-28}	8.2×10^{-28}	3.6×10^{-27}	8.0×10^{-27}	3.6×10^{31}	4.7×10^{-7}	17	-3.9	-1.8
J1439−5501[δ]	34.9	1.4×10^{-19}	0.65 (b)	2.7×10^{-27}	3.5×10^{-27}	4.9×10^{-27}	1.0×10^{-26}	1.0×10^{32}	1.3×10^{-6}	3.8	-5.1	-2.3
J1446−4701[aδ]	455.6	9.6×10^{-21}	1.50 (f)	1.1×10^{-27}	1.1×10^{-27}	5.6×10^{-27}	1.2×10^{-26}	1.6×10^{30}	2.1×10^{-8}	11	-4.3	-2.2
J1453+1902[aε]	172.6	9.2×10^{-21}	1.27 (b)	8.0×10^{-28}	1.3×10^{-26}	4.6×10^{-27}	8.0×10^{-27}	6.3×10^{30}	8.1×10^{-8}	10	-4.1	-2.7
J1455−3330[aε]	125.2	2.3×10^{-20}	1.01 (q)	1.3×10^{-27}	9.2×10^{-27}	2.6×10^{-27}	5.4×10^{-27}	6.4×10^{30}	8.3×10^{-8}	4.1	-4.3	-2.3
J1502−6752[aδ]	37.4	2.2×10^{-19}	7.73 (b)	3.0×10^{-28}	3.1×10^{-28}	3.1×10^{-27}	7.0×10^{-27}	7.1×10^{32}	9.2×10^{-6}	24	-5.6	-2.6
J1513−2550[ε]	471.9	2.2×10^{-20}	3.96 (b)	6.5×10^{-28}	1.6×10^{-28}	5.9×10^{-27}	1.2×10^{-26}	4.0×10^{30}	5.2×10^{-8}	19	-3.9	-2.3
J1514−4946[aδ]	278.6	1.1×10^{-20}	0.91 (b)	1.6×10^{-27}	1.2×10^{-27}	3.3×10^{-27}	1.0×10^{-26}	2.2×10^{30}	2.9×10^{-8}	6.6	-4.2	-2.2
J1518+0204A[ce]	180.1	4.4×10^{-20}	8.00 (r)	2.8×10^{-28}	9.0×10^{-27}	4.9×10^{-27}	9.7×10^{-27}	4.4×10^{31}	5.7×10^{-7}	34	-5.1	-2.2
J1518+4904[aε]	24.4	2.3×10^{-20}	0.96 (b)	6.3×10^{-28}	1.2×10^{-25}	4.5×10^{-27}	9.4×10^{-27}	2.8×10^{32}	3.6×10^{-6}	15	-5.0	-3.0

Table A.2: Limits on Gravitational-wave Amplitude and Derived Quantities from O3 (Chapter 3) for 213 Pulsars.

Pulsar Name (J2000)	$f_{\rm rot}$ (Hz)	$\dot{P}_{\rm rot}$ (s s^{-1})	Distance (kpc)	$h_0^{\rm sd}$	$C_{21}^{95\%}$	$C_{22}^{95\%}$	$h_0^{95\%}$	$Q_{22}^{95\%}$ (kg m^2)	$\varepsilon^{95\%}$	$h_0^{95\%}/h_0^{\rm sd}$	$\mathcal{O}_{m=1,2}^{l=2}$	$\mathcal{O}_{m=2}^{l=2}$
J1525−5545$^{\delta}$	88.0	1.3×10^{-19}	3.14 (b)	8.7×10^{-28}	1.1×10^{-26}	2.4×10^{-27}	8.9×10^{-27}	6.6×10^{31}	8.6×10^{-7}	10	-4.5	-1.8
J1528−3146$^{\epsilon}$	16.4	2.5×10^{-19}	0.77 (b)	2.1×10^{-27}	1.0×10^{-27}	8.6×10^{-27}	1.8×10^{-26}	9.5×10^{32}	1.2×10^{-5}	8.6	-9.6	-2.9
J1529−3828$^{\delta}$	117.8	2.7×10^{-20}	4.30 (b)	3.3×10^{-28}	1.1×10^{-28}	2.7×10^{-27}	7.0×10^{-27}	4.0×10^{31}	5.1×10^{-7}	21	-4.3	-2.1
J1536−4948$^{a\delta}$	324.7	2.1×10^{-20}	0.98 (b)	2.1×10^{-27}	9.4×10^{-27}	4.7×10^{-27}	9.7×10^{-27}	1.6×10^{30}	2.1×10^{-8}	4.5	-4.3	-2.2
J1537+1155$^{a\epsilon}$	26.4	2.4×10^{-18}	1.05 (s)	6.1×10^{-27}	7.6×10^{-26}	6.6×10^{-27}	1.2×10^{-26}	3.3×10^{32}	4.2×10^{-6}	2	-5.0	-2.7
J1537−5312$^{\delta}$	144.4	1.6×10^{-20}	3.05 (b)	4.0×10^{-28}	1.2×10^{-28}	2.1×10^{-27}	4.5×10^{-27}	1.2×10^{31}	1.6×10^{-7}	11	-4.4	-2.4
J1543−5149$^{a\delta}$	486.2	1.6×10^{-20}	1.15 (b)	2.0×10^{-27}	1.5×10^{-27}	4.6×10^{-27}	1.1×10^{-26}	9.9×10^{29}	1.3×10^{-8}	5.7	-4.5	-2.4
J1544+4937$^{\epsilon}$	463.1	2.9×10^{-21}	2.99 (b)	3.1×10^{-28}	1.5×10^{-28}	7.1×10^{-27}	1.5×10^{-26}	3.8×10^{30}	5.0×10^{-8}	48	-4.0	-2.0
J1545−4550$^{\delta}$	279.7	5.3×10^{-20}	2.20 (f)	1.4×10^{-27}	1.0×10^{-27}	3.1×10^{-27}	6.7×10^{-27}	3.4×10^{30}	4.4×10^{-8}	4.8	-4.5	-2.4
J1547−5709$^{\delta}$	233.0	7.4×10^{-21}	2.69 (b)	3.9×10^{-28}	7.2×10^{-28}	3.1×10^{-27}	7.9×10^{-27}	7.2×10^{30}	9.3×10^{-8}	20	-4.5	-2.3
J1551−0658$^{\gamma}$	141.0	2.0×10^{-20}	1.32 (b)	1.0×10^{-27}	8.9×10^{-27}	2.7×10^{-27}	5.7×10^{-27}	6.9×10^{30}	9.0×10^{-8}	5.6	-4.3	-2.3
J1600−3053^{ae}	277.9	7.9×10^{-21}	3.00 (f)	4.0×10^{-28}	1.3×10^{-28}	3.9×10^{-27}	8.3×10^{-27}	5.9×10^{30}	7.6×10^{-8}	21	-4.1	-2.3
J1603−7202$^{a\delta}$	67.4	1.7×10^{-20}	3.40 (f)	2.5×10^{-28}	1.3×10^{-28}	2.5×10^{-27}	5.2×10^{-27}	7.1×10^{31}	9.1×10^{-7}	20	-4.6	-2.3
J1614−2230^{ae}	317.4	3.7×10^{-21}	0.70 (q)	1.3×10^{-27}	1.2×10^{-27}	4.6×10^{-27}	9.9×10^{-27}	1.3×10^{30}	1.6×10^{-8}	7.9	-4.2	-2.2
J1618−3921$^{\epsilon}$	83.4	5.4×10^{-20}	5.52 (b)	3.1×10^{-28}	2.1×10^{-28}	2.1×10^{-27}	5.2×10^{-27}	7.6×10^{31}	9.8×10^{-7}	17	-3.6	-2.2
J1618−4624$^{\delta}$	168.6	3.1×10^{-21}	3.04 (b)	1.9×10^{-28}	1.3×10^{-28}	2.6×10^{-27}	6.9×10^{-27}	1.3×10^{31}	1.7×10^{-7}	36	-4.4	-2.4
J1622−6617$^{a\delta}$	42.3	5.1×10^{-20}	4.05 (b)	2.9×10^{-28}	2.9×10^{-28}	2.5×10^{-27}	5.7×10^{-27}	2.4×10^{32}	3.1×10^{-6}	20	-5.2	-2.6
J1623−2631^{ce}	90.3	8.8×10^{-20}	1.80 (t)	1.3×10^{-27}	2.0×10^{-27}	4.8×10^{-27}	1.1×10^{-26}	4.4×10^{31}	5.7×10^{-7}	8.6	-3.2	-1.5
J1628−3205$^{b\delta}$	311.4	...	1.23 (b)	...	1.2×10^{-26}	3.1×10^{-26}	8.9×10^{-27}	2.1×10^{30}	2.7×10^{-8}	...	-4.3	-2.4

Table A.2: Limits on Gravitational-wave Amplitude and Derived Quantities from O3 (Chapter 3) for 213 Pulsars.

Pulsar Name (J2000)	$f_{\rm rot}$ (Hz)	$\dot{P}_{\rm rot}$ (s s^{-1})	Distance (kpc)	$h_0^{\rm sd}$	$C_{21}^{95\%}$	$C_{22}^{95\%}$	$h_0^{95\%}$	$Q_{22}^{95\%}$ (kg m^2)	$\varepsilon^{95\%}$	$h_0^{95\%}/h_0^{\rm sd}$	$\mathcal{O}_{m=1,2}^{l=2}$	$\mathcal{O}_{m=2}^{l=2}$
J1629−6902$^\delta$	166.6	1.0×10^{-20}	0.96 (b)	1.1×10^{-20}	9.7×10^{-27}	3.2×10^{-27}	6.5×10^{-27}	4.1×10^{30}	5.3×10^{-8}	6	-4.4	-2.4
J1630+3734$^{a\alpha}$	301.4	8.5×10^{-21}	1.19 (b)	1.1×10^{-21}	1.1×10^{-26}	3.0×10^{-27}	8.6×10^{-27}	2.1×10^{30}	2.7×10^{-8}	7.9	-4.4	-2.3
J1640+2224$^{a\epsilon}$	316.1	1.3×10^{-21}	1.52 (u)	3.4×10^{-21}	1.2×10^{-26}	3.6×10^{-27}	7.5×10^{-27}	2.1×10^{30}	2.7×10^{-8}	22	-4.3	-2.4
J1641+3627A$^{c\alpha}$	96.4	8.2×10^{-20}	7.10 (r)	3.2×10^{-20}	1.1×10^{-26}	2.3×10^{-27}	5.5×10^{-27}	7.7×10^{31}	1.0×10^{-6}	17	-4.5	-2.3
J1643−1224$^{a\epsilon}$	216.4	1.8×10^{-20}	1.20 (f)	1.3×10^{-20}	9.9×10^{-27}	4.8×10^{-27}	9.6×10^{-27}	4.5×10^{30}	5.8×10^{-8}	7.3	-3.8	-1.8
J1652−4838$^\delta$	264.2	1.1×10^{-20}	...	...	1.0×10^{-26}	4.5×10^{-27}	9.9×10^{-27}	...	...	...	-4.1	-2.1
J1653−2054$^\delta$	242.2	1.1×10^{-20}	2.63 (b)	5.0×10^{-20}	8.8×10^{-27}	2.8×10^{-27}	6.6×10^{-27}	5.4×10^{30}	7.0×10^{-8}	13	-4.5	-2.4
J1658−5324$^{a\delta}$	410.0	1.1×10^{-20}	0.88 (b)	1.9×10^{-20}	9.7×10^{-27}	3.7×10^{-27}	8.3×10^{-27}	7.9×10^{29}	1.0×10^{-8}	4.3	-4.6	-2.5
J1705−1903$^\delta$	403.2	2.1×10^{-20}	2.40 (b)	9.8×10^{-21}	1.1×10^{-26}	4.3×10^{-27}	9.9×10^{-27}	2.7×10^{30}	3.4×10^{-8}	10	-4.5	-2.4
J1708−3506$^{a\epsilon}$	222.0	8.6×10^{-21}	3.32 (b)	3.3×10^{-21}	9.9×10^{-28}	2.6×10^{-27}	5.7×10^{-27}	7.0×10^{30}	9.1×10^{-8}	17	-4.4	-2.4
J1709+2313$^{a\epsilon}$	215.9	1.3×10^{-21}	2.18 (b)	1.9×10^{-21}	1.7×10^{-26}	3.9×10^{-27}	8.1×10^{-27}	6.9×10^{30}	8.9×10^{-8}	42	-3.7	-2.1
J1713+0747$^{a\epsilon}$	218.8	7.8×10^{-21}	1.00 (f)	1.1×10^{-21}	9.0×10^{-27}	3.3×10^{-27}	6.9×10^{-27}	2.6×10^{30}	3.4×10^{-8}	6.5	-4.4	-2.3
J1719−1438$^{a\epsilon}$	172.7	7.3×10^{-21}	0.34 (b)	2.7×10^{-21}	1.0×10^{-27}	3.2×10^{-27}	7.2×10^{-27}	1.5×10^{30}	1.9×10^{-8}	2.7	-4.8	-2.8
J1721−2457$^{b\epsilon}$	286.0	...	1.36 (b)	...	1.2×10^{-26}	3.7×10^{-27}	7.6×10^{-27}	2.3×10^{30}	3.0×10^{-8}	...	-4.4	-2.3
J1727−2946$^{a\delta}$	36.9	2.4×10^{-19}	1.88 (b)	1.3×10^{-20}	4.5×10^{-27}	2.5×10^{-27}	6.6×10^{-27}	1.7×10^{32}	2.2×10^{-6}	5.1	-4.9	-2.7
J1729−2117$^\gamma$	15.1	1.7×10^{-19}	0.97 (b)	1.3×10^{-19}	1.5×10^{-27}	1.5×10^{-26}	3.1×10^{-26}	2.4×10^{33}	3.2×10^{-5}	23	-9.2	-2.7
J1730−2304$^{a\epsilon}$	123.1	1.1×10^{-20}	0.47 (f)	2.0×10^{-20}	8.8×10^{-27}	2.3×10^{-27}	5.0×10^{-27}	2.8×10^{30}	3.7×10^{-8}	2.5	-4.6	-2.3
J1731−1847$^{a\epsilon}$	426.5	2.3×10^{-20}	4.78 (b)	5.2×10^{-21}	1.3×10^{-26}	3.9×10^{-27}	8.6×10^{-27}	4.2×10^{30}	5.4×10^{-8}	17	-4.5	-2.5
J1732−5049$^{a\delta}$	188.2	1.1×10^{-20}	1.88 (b)	6.2×10^{-21}	1.3×10^{-26}	2.3×10^{-27}	6.7×10^{-27}	6.5×10^{30}	8.4×10^{-8}	11	-3.7	-2.3

Table A.2: Limits on Gravitational-wave Amplitude and Derived Quantities from O3 (Chapter 3) for 213 Pulsars.

Pulsar Name	$f_{\rm rot}$	$\dot{P}_{\rm rot}$	Distance	$h_0^{\rm sd}$	$C_{21}^{95\%}$	$C_{22}^{95\%}$	$h_0^{95\%}$	$Q_{22}^{95\%}$	$\varepsilon^{95\%}$	$h_0^{95\%}/h_0^{\rm sd}$	$\mathcal{O}_{m=1,2}^{l=2}$	$\mathcal{O}_{m=2}^{l=2}$
(J2000)	(Hz)	(s s^{-1})	(kpc)					(kg m^2)				
J1737−0811$^\delta$	239.5	7.9×10^{-21}	0.21 (b)	5.4×10^{-27}	1.2×10^{-26}	5.3×10^{-27}	1.2×10^{-26}	7.6×10^{29}	9.8×10^{-9}	2.1	-3.5	-1.8
J1738+0333^{ae}	170.9	2.2×10^{-20}	1.47 (v)	1.1×10^{-27}	8.5×10^{-27}	2.3×10^{-27}	4.8×10^{-27}	4.5×10^{30}	5.8×10^{-8}	4.5	-5.0	-2.9
J1741+1351^{ae}	266.9	2.9×10^{-20}	1.08 (w)	2.1×10^{-27}	1.1×10^{-26}	3.0×10^{-27}	6.6×10^{-27}	1.8×10^{30}	2.4×10^{-8}	3.2	-4.2	-2.4
J1744−1134^{ae}	245.4	7.2×10^{-21}	0.41 (f)	2.6×10^{-27}	9.5×10^{-27}	4.9×10^{-27}	9.8×10^{-27}	1.2×10^{30}	1.6×10^{-8}	3.7	-4.1	-2.1
J1745+1017^{ae}	377.1	2.2×10^{-21}	1.21 (b)	6.0×10^{-28}	9.2×10^{-27}	3.8×10^{-27}	8.3×10^{-27}	1.3×10^{30}	1.7×10^{-8}	14	-4.6	-2.4
J1747−4036^{ad}	607.7	1.1×10^{-20}	7.15 (b)	2.9×10^{-28}	1.6×10^{-26}	4.9×10^{-27}	1.1×10^{-26}	4.0×10^{30}	5.1×10^{-8}	38	-4.5	-2.5
J1748−2446A$^{c\gamma}$	86.5	9.2×10^{-20}	6.90 (r)	3.3×10^{-28}	1.2×10^{-26}	3.7×10^{-27}	7.1×10^{-27}	1.2×10^{32}	1.5×10^{-6}	22	-4.3	-2.0
J1748−3009$^{b\gamma}$	103.3	$\cdots$	5.05 (b)	$\cdots$	1.0×10^{-26}	2.2×10^{-27}	7.5×10^{-27}	6.5×10^{31}	8.4×10^{-7}	$\cdots$	-4.4	-2.1
J1750−2536$^\gamma$	28.8	1.4×10^{-19}	3.22 (b)	5.1×10^{-27}	5.5×10^{-28}	6.0×10^{-26}	1.1×10^{-26}	7.5×10^{32}	9.8×10^{-6}	21	-5.2	-2.7
J1751−2857^{ae}	255.4	1.0×10^{-20}	1.09 (b)	1.2×10^{-27}	1.6×10^{-27}	8.7×10^{-26}	2.0×10^{-26}	6.1×10^{30}	7.9×10^{-8}	17	-3.4	-1.7
J1753−1914$^\gamma$	15.9	2.0×10^{-18}	2.92 (b)	1.6×10^{-27}	1.3×10^{-24}	1.2×10^{-26}	2.6×10^{-26}	5.5×10^{33}	7.1×10^{-5}	17	-9.4	-3.0
J1753−2240$^\gamma$	10.5	9.7×10^{-19}	3.23 (b)	8.0×10^{-28}	1.3×10^{-23}	5.7×10^{-26}	1.2×10^{-25}	6.4×10^{34}	8.2×10^{-4}	150	-8.3	-2.6
J1755−3716$^\delta$	78.2	3.1×10^{-20}	8.18 (b)	1.5×10^{-28}	1.3×10^{-26}	2.9×10^{-26}	5.8×10^{-27}	1.4×10^{32}	1.8×10^{-6}	38	-4.4	-2.2
J1757−1854$^\delta$	46.5	2.6×10^{-18}	19.56 (b)	4.6×10^{-28}	1.7×10^{-26}	2.7×10^{-26}	7.1×10^{-27}	1.2×10^{33}	1.5×10^{-5}	16	-5.1	-2.3
J1757−5322$^\delta$	112.7	2.6×10^{-20}	0.94 (b)	1.5×10^{-27}	9.3×10^{-27}	5.3×10^{-27}	9.0×10^{-27}	1.2×10^{31}	1.6×10^{-7}	6.1	-3.6	-1.8
J1801−1417^{ae}	275.9	3.8×10^{-21}	1.10 (b)	7.4×10^{-28}	7.4×10^{-28}	3.2×10^{-27}	6.9×10^{-27}	1.8×10^{30}	2.4×10^{-8}	9.3	-4.6	-2.3
J1801−3210$^{b\delta}$	134.2	$\cdots$	6.11 (b)	$\cdots$	8.5×10^{-27}	4.7×10^{-27}	1.2×10^{-26}	7.3×10^{31}	9.5×10^{-7}	$\cdots$	-3.7	-1.5
J1802−2124^{ae}	79.1	7.1×10^{-20}	0.76 (i)	2.5×10^{-27}	9.5×10^{-27}	2.2×10^{-27}	4.9×10^{-27}	1.1×10^{31}	1.4×10^{-7}	2	-4.8	-2.3
J1804−0735$^{c\gamma}$	43.3	1.8×10^{-19}	7.80 (r)	2.9×10^{-28}	2.2×10^{-26}	6.8×10^{-27}	1.8×10^{-26}	1.4×10^{33}	1.8×10^{-5}	62	-4.6	-1.2

Table A.2: Limits on Gravitational-wave Amplitude and Derived Quantities from O3 (Chapter 3) for 213 Pulsars.

Pulsar Name (J2000)	$f_{\rm rot}$ (Hz)	$\dot{P}_{\rm rot}$ (s s^{-1})	Distance (kpc)	$h_0^{\rm sd}$	$C_{21}^{95\%}$	$C_{22}^{95\%}$	$h_0^{95\%}$	$Q_{22}^{95\%}$ (kg m^2)	$\varepsilon^{95\%}$	$h_0^{95\%}/h_0^{\rm sd}$	$\mathcal{O}_{m=1,2}^{l=2}$	$\mathcal{O}_{m=2}^{l=2}$
J1804−2717$^{a\epsilon}$	107.0	3.5×10^{-20}	0.81 (b)	1.9×10^{-27}	8.0×10^{-27}	2.6×10^{-27}	5.9×10^{-27}	7.5×10^{30}	9.8×10^{-8}	3	-4.3	-2.2
J1804−2858$^{b\delta}$	669.9	...	8.19 (b)	...	1.5×10^{-26}	7.3×10^{-27}	1.8×10^{-26}	6.0×10^{30}	7.7×10^{-8}	...	-4.5	-2.2
J1807−2459A$^{c\gamma}$	326.9	2.4×10^{-20}	3.00 (r)	7.6×10^{-28}	7.7×10^{-27}	5.9×10^{-27}	1.2×10^{-26}	6.3×10^{30}	8.1×10^{-8}	16	-4.1	-1.7
J1810+1744$^{\gamma}$	601.4	4.4×10^{-21}	2.36 (b)	5.5×10^{-28}	1.4×10^{-26}	6.2×10^{-27}	1.5×10^{-26}	1.8×10^{30}	2.3×10^{-8}	27	-4.5	-2.3
J1810−2005$^{a\delta}$	30.5	5.3×10^{-20}	3.51 (b)	2.9×10^{-27}	3.9×10^{-28}	3.9×10^{-26}	9.2×10^{-27}	6.3×10^{32}	8.2×10^{-6}	31	-5.6	-2.8
J1811−2405$^{a\epsilon}$	375.9	1.3×10^{-20}	1.83 (b)	9.9×10^{-28}	1.3×10^{-28}	7.5×10^{-27}	1.5×10^{-26}	3.5×10^{30}	4.5×10^{-8}	15	-3.8	-1.9
J1813−2621$^{b\gamma}$	225.7	...	3.16 (b)	...	1.4×10^{-26}	2.6×10^{-26}	6.0×10^{-27}	6.8×10^{30}	8.8×10^{-8}	...	-4.0	-2.4
J1821+0155$^{\alpha}$	29.6	2.9×10^{-20}	1.72 (b)	4.3×10^{-28}	5.1×10^{-28}	4.1×10^{-26}	1.1×10^{-26}	4.1×10^{32}	5.3×10^{-6}	26	-5.5	-2.8
J1823−3021A$^{c\epsilon}$	183.8	4.3×10^{-20}	7.90 (r)	2.9×10^{-28}	1.2×10^{-28}	2.7×10^{-27}	5.7×10^{-27}	2.4×10^{31}	3.1×10^{-7}	20	-4.2	-2.3
J1824−2452A$^{c\gamma}$	327.4	2.4×10^{-20}	5.50 (z)	4.1×10^{-28}	1.1×10^{-28}	6.6×10^{-27}	1.7×10^{-26}	1.6×10^{31}	2.1×10^{-7}	41	-4.0	-1.7
J1825−0319$^{\delta}$	219.6	6.8×10^{-21}	3.86 (b)	2.6×10^{-27}	9.5×10^{-28}	4.1×10^{-27}	9.5×10^{-27}	1.4×10^{31}	1.8×10^{-7}	37	-4.1	-2.0
J1826−2415$^{\delta}$	213.0	1.7×10^{-20}	2.73 (b)	5.7×10^{-28}	8.5×10^{-28}	5.8×10^{-27}	1.2×10^{-26}	1.3×10^{31}	1.7×10^{-7}	21	-3.6	-1.5
J1829+2456$^{\alpha}$	24.4	5.3×10^{-20}	0.92 (b)	1.0×10^{-27}	1.0×10^{-27}	5.3×10^{-27}	1.1×10^{-26}	3.1×10^{32}	4.0×10^{-6}	11	-5.2	-2.8
J1832−0836$^{b\epsilon}$	367.8	...	1.60 (f)	...	9.8×10^{-27}	3.8×10^{-27}	8.3×10^{-27}	1.8×10^{30}	2.3×10^{-8}	...	-4.8	-2.4
J1833−0827$^{a\eta}$	11.7	9.2×10^{-15}	4.50 (j)	5.9×10^{-26}	6.4×10^{-26}	4.6×10^{-26}	9.3×10^{-26}	5.5×10^{34}	7.2×10^{-4}	1.6	-8.1	-2.1
J1835−0114$^{\delta}$	195.5	7.0×10^{-21}	3.45 (b)	2.7×10^{-28}	1.8×10^{-28}	3.1×10^{-26}	5.6×10^{-27}	9.3×10^{30}	1.2×10^{-7}	21	-1.7	-2.5
J1840−0643$^{\gamma}$	28.1	9.5×10^{-20}	4.99 (b)	2.6×10^{-28}	5.1×10^{-28}	8.1×10^{-26}	1.8×10^{-26}	2.0×10^{33}	2.6×10^{-5}	67	-4.0	-2.0
J1841+0130$^{\gamma}$	33.6	8.2×10^{-18}	4.23 (b)	3.2×10^{-27}	3.6×10^{-27}	3.3×10^{-26}	7.4×10^{-27}	5.0×10^{32}	6.5×10^{-6}	2.3	-5.1	-2.6
J1843−1113$^{a\epsilon}$	541.8	9.3×10^{-21}	1.26 (i)	1.4×10^{-27}	1.1×10^{-26}	6.4×10^{-27}	1.3×10^{-26}	1.0×10^{30}	1.4×10^{-8}	9.2	-4.5	-2.3

Table A.2: Limits on Gravitational-wave Amplitude and Derived Quantities from O3 (Chapter 3) for 213 Pulsars.

Pulsar Name (J2000)	$f_{\rm rot}$ (Hz)	$\dot{P}_{\rm rot}$ (s s^{-1})	Distance (kpc)	$h_0^{\rm sd}$	$C_{21}^{95\%}$	$C_{22}^{95\%}$	$h_0^{95\%}$	$Q_{22}^{95\%}$ (kg m^2)	$\varepsilon^{95\%}$	$h_0^{95\%}/h_0^{\rm sd}$	$\mathcal{O}_{m=1,2}^{l=2}$	$\mathcal{O}_{m=2}^{l=2}$
J1843$-$1448$^{b\delta}$	182.8	$\cdots$	3.47 (b)	$\cdots$	1.2×10^{-26}	6.0×10^{-26}	1.3×10^{-26}	2.5×10^{31}	3.2×10^{-7}	$\cdots$	-3.0	-1.2
J1853+1303$^{a\epsilon}$	244.4	8.6×10^{-21}	1.32 (b)	8.9×10^{-28}	9.3×10^{-27}	4.5×10^{-27}	1.0×10^{-27}	4.1×10^{30}	5.3×10^{-8}	11	-4.1	-2.1
J1857+0943$^{a\epsilon}$	186.5	1.7×10^{-20}	1.18 (f)	1.2×10^{-27}	1.0×10^{-26}	3.3×10^{-27}	6.6×10^{-27}	4.1×10^{30}	5.3×10^{-8}	5.4	-4.3	-2.2
J1858$-$2216$^{\delta}$	419.5	3.8×10^{-21}	0.92 (b)	1.1×10^{-27}	1.0×10^{-26}	3.6×10^{-27}	7.8×10^{-27}	7.4×10^{29}	9.6×10^{-9}	7	-4.7	-2.4
J1902$-$5105$^{a\eta}$	573.9	8.7×10^{-21}	1.65 (b)	1.1×10^{-27}	1.3×10^{-26}	7.1×10^{-26}	1.4×10^{-26}	1.3×10^{30}	1.7×10^{-8}	13	-4.5	-2.3
J1903+0327$^{a\epsilon}$	465.1	1.9×10^{-20}	6.12 (b)	3.9×10^{-28}	1.6×10^{-26}	5.5×10^{-26}	1.0×10^{-26}	5.4×10^{30}	7.0×10^{-8}	27	-4.2	-2.4
J1903$-$7051$^{a\delta}$	277.9	7.7×10^{-21}	0.93 (b)	1.3×10^{-27}	9.0×10^{-27}	5.9×10^{-27}	1.1×10^{-26}	2.3×10^{30}	3.0×10^{-8}	8.4	-4.0	-2.0
J1904+0412$^{\gamma}$	14.1	1.1×10^{-19}	4.58 (b)	2.2×10^{-27}	2.5×10^{-24}	2.2×10^{-26}	4.5×10^{-26}	1.9×10^{34}	2.5×10^{-4}	200	-9.0	-2.6
J1905+0400$^{a\gamma}$	264.2	4.2×10^{-21}	1.06 (b)	8.0×10^{-28}	1.3×10^{-26}	2.6×10^{-27}	6.5×10^{-27}	1.8×10^{30}	2.3×10^{-8}	8.1	-4.1	-2.5
J1909$-$3744$^{a\delta}$	339.3	2.6×10^{-21}	1.15 (f)	6.6×10^{-28}	1.1×10^{-26}	5.7×10^{-27}	1.2×10^{-26}	2.1×10^{30}	2.8×10^{-8}	18	-4.4	-2.1
J1910+1256$^{a\epsilon}$	200.7	8.8×10^{-21}	1.50 (b)	7.2×10^{-28}	2.6×10^{-26}	5.0×10^{-26}	1.0×10^{-26}	7.0×10^{30}	9.0×10^{-8}	14	-2.5	-2.0
J1911+1347$^{a\epsilon}$	216.2	1.7×10^{-20}	1.36 (b)	1.1×10^{-27}	9.3×10^{-27}	2.6×10^{-27}	5.6×10^{-27}	3.0×10^{30}	3.9×10^{-8}	5	-4.6	-2.4
J1911$-$1114$^{a\epsilon}$	275.8	1.1×10^{-20}	1.07 (b)	1.3×10^{-27}	9.1×10^{-27}	3.0×10^{-27}	6.4×10^{-27}	1.6×10^{30}	2.1×10^{-8}	4.8	-4.6	-2.4
J1914+0659$^{\gamma}$	54.0	3.1×10^{-20}	8.47 (b)	1.2×10^{-27}	1.8×10^{-26}	2.8×10^{-26}	5.9×10^{-27}	3.1×10^{32}	4.0×10^{-6}	48	-5.0	-2.4
J1915+1606$^{a\gamma}$	16.9	8.6×10^{-18}	5.25 (b)	1.9×10^{-27}	6.1×10^{-27}	1.6×10^{-25}	3.3×10^{-26}	1.1×10^{34}	1.4×10^{-4}	18	-8.4	-1.8
J1918$-$0642$^{a\epsilon}$	130.8	2.4×10^{-20}	1.10 (a)	1.3×10^{-27}	8.8×10^{-27}	4.8×10^{-27}	1.0×10^{-27}	1.2×10^{31}	1.5×10^{-7}	7.7	-3.8	-1.4
J1923+2515$^{a\alpha}$	264.0	7.0×10^{-21}	1.20 (b)	9.1×10^{-28}	1.1×10^{-26}	2.8×10^{-27}	6.5×10^{-27}	2.0×10^{30}	2.6×10^{-8}	7.1	-4.4	-2.5
J1933$-$6211$^{a\delta}$	282.2	2.9×10^{-21}	0.65 (b)	1.1×10^{-27}	1.3×10^{-26}	3.1×10^{-27}	6.2×10^{-27}	9.2×10^{29}	1.2×10^{-8}	5.5	-4.1	-2.5
J1939+2134$^{a\gamma}$	641.9	1.1×10^{-19}	4.80 (f)	1.4×10^{-27}	1.8×10^{-26}	1.5×10^{-26}	2.2×10^{-26}	4.7×10^{30}	6.1×10^{-8}	16	-2.8	-2.0

Table A.2: Limits on Gravitational-wave Amplitude and Derived Quantities from O3 (Chapter 3) for 213 Pulsars.

Pulsar Name	f_{rot}	$\dot{P}_{rot}$	Distance	h_0^{sd}	$C_{21}^{95\%}$	$C_{22}^{95\%}$	$h_0^{95\%}$	$Q_{22}^{95\%}$	$\varepsilon^{95\%}$	$h_0^{95\%}/h_0^{sd}$	$\mathcal{O}_{m=1,2}^{l=2}$	$\mathcal{O}_{m=2}^{l=2}$
(J2000)	(Hz)	(s s^{-1})	(kpc)					(kg m^2)				
J1943+2210[γ]	196.7	8.8×10^{-21}	6.77 (b)	1.6×10^{-28}	9.9×10^{-28}	2.3×10^{-27}	5.8×10^{-27}	1.9×10^{31}	2.4×10^{-7}	37	-4.5	-2.4
J1944+0907[aε]	192.9	6.5×10^{-21}	1.22 (b)	7.4×10^{-28}	9.3×10^{-28}	2.9×10^{-27}	6.2×10^{-27}	3.7×10^{30}	4.8×10^{-8}	8.3	-4.4	-2.4
J1946+3417[aε]	315.4	1.0×10^{-21}	6.94 (b)	6.5×10^{-30}	7.8×10^{-29}	5.5×10^{-27}	1.2×10^{-27}	1.5×10^{31}	1.9×10^{-7}	180	-4.2	-2.0
J1946−5403[δ]	368.9	2.7×10^{-21}	1.15 (b)	7.0×10^{-29}	9.9×10^{-28}	5.4×10^{-27}	1.2×10^{-27}	1.8×10^{30}	2.4×10^{-8}	17	-4.2	-2.1
J1949+3106[aε]	76.1	9.3×10^{-20}	7.47 (b)	2.9×10^{-28}	1.2×10^{-28}	3.9×10^{-27}	7.8×10^{-27}	1.8×10^{32}	2.4×10^{-6}	27	-4.4	-2.1
J1950+2414[aγ]	232.3	2.0×10^{-20}	7.27 (b)	2.4×10^{-28}	1.2×10^{-28}	5.1×10^{-27}	9.1×10^{-27}	2.2×10^{31}	2.9×10^{-7}	38	-3.7	-2.2
J1955+2527[aε]	205.2	1.1×10^{-20}	8.18 (b)	1.5×10^{-28}	1.1×10^{-28}	4.8×10^{-27}	9.8×10^{-27}	3.5×10^{31}	4.5×10^{-7}	65	-3.5	-1.6
J1955+2908[aε]	163.0	3.1×10^{-20}	6.30 (b)	2.9×10^{-28}	8.7×10^{-28}	2.5×10^{-27}	5.5×10^{-27}	2.4×10^{31}	3.1×10^{-7}	19	-4.6	-2.5
J1959+2048[aε]	622.1	1.2×10^{-20}	1.40 (cc)	1.6×10^{-27}	1.8×10^{-27}	6.9×10^{-27}	1.3×10^{-26}	8.7×10^{29}	1.1×10^{-8}	8.3	-4.2	-2.4
J2007+2722[γ]	40.8	9.6×10^{-19}	7.10 (b)	7.1×10^{-28}	1.8×10^{-28}	7.9×10^{-27}	1.6×10^{-26}	1.2×10^{33}	1.6×10^{-5}	23	-4.1	-1.8
J2010−1323[aε]	191.5	3.0×10^{-21}	1.16 (b)	5.3×10^{-28}	1.1×10^{-28}	7.3×10^{-27}	1.4×10^{-26}	8.3×10^{30}	1.1×10^{-7}	27	-2.6	-0.8
J2017+0603[aε]	345.3	8.0×10^{-21}	1.40 (b)	9.6×10^{-28}	1.1×10^{-28}	3.5×10^{-27}	7.7×10^{-27}	1.7×10^{30}	2.1×10^{-8}	8	-5.2	-2.6
J2019+2425[aε]	254.2	1.6×10^{-21}	1.16 (b)	4.4×10^{-28}	7.5×10^{-28}	5.1×10^{-27}	1.1×10^{-26}	3.5×10^{30}	4.5×10^{-8}	24	-4.4	-2.1
J2022+2534[ε]	377.9	6.2×10^{-21}	...	...	9.2×10^{-27}	5.2×10^{-27}	1.5×10^{-26}	...	...	...	-4.6	-1.9
J2033+1734[aε]	168.1	8.4×10^{-21}	1.74 (b)	5.5×10^{-28}	1.0×10^{-28}	3.6×10^{-27}	6.7×10^{-27}	7.6×10^{30}	9.8×10^{-8}	12	-4.4	-2.4
J2039−3616[ε]	305.3	8.4×10^{-21}	1.70 (b)	7.6×10^{-28}	7.5×10^{-28}	4.9×10^{-27}	1.0×10^{-26}	3.4×10^{30}	4.3×10^{-8}	13	-4.3	-2.0
J2043+1711[aε]	420.2	4.1×10^{-21}	1.60 (a)	6.6×10^{-28}	1.6×10^{-28}	5.0×10^{-27}	1.1×10^{-26}	1.8×10^{30}	2.3×10^{-8}	16	-4.4	-2.4
J2043+2740[α]	10.4	1.3×10^{-15}	1.48 (b)	6.3×10^{-26}	1.7×10^{-23}	7.9×10^{-26}	1.6×10^{-25}	4.1×10^{34}	5.3×10^{-4}	2.6	-7.9	-2.4
J2045+3633[aε]	31.6	5.9×10^{-19}	5.63 (b)	6.2×10^{-28}	5.2×10^{-28}	2.9×10^{-27}	6.5×10^{-27}	6.8×10^{32}	8.7×10^{-6}	11	-5.3	-2.8

Table A.2: Limits on Gravitational-wave Amplitude and Derived Quantities from O3 (Chapter 3) for 213 Pulsars.

Pulsar Name (J2000)	$f_{\rm rot}$ (Hz)	$\dot{P}_{\rm rot}$ (s s^{-1})	Distance (kpc)	$h_0^{\rm sd}$	$C_{21}^{95\%}$	$C_{22}^{95\%}$	$h_0^{95\%}$	$Q_{22}^{95\%}$ (kg m^2)	$\varepsilon^{95\%}$	$h_0^{95\%}/h_0^{\rm sd}$	$\Theta^{l=2}_{m=1,2}$	$\Theta^{l=2}_{m=2}$
J2047+1053[γ]	233.3	2.1×10^{-20}	2.79 (b)	6.4×10^{-28}	1.0×10^{-28}	3.5×10^{-26}	7.1×10^{-27}	6.6×10^{30}	8.6×10^{-8}	11	-4.2	-2.3
J2051−0827[ae]	221.8	1.2×10^{-20}	1.47 (b)	9.0×10^{-28}	1.6×10^{-28}	2.5×10^{-26}	5.7×10^{-27}	3.1×10^{30}	4.0×10^{-8}	6.3	-3.9	-2.5
J2053+4650[ae]	79.5	1.7×10^{-19}	3.81 (b)	7.8×10^{-28}	1.4×10^{-28}	2.4×10^{-26}	5.3×10^{-27}	5.8×10^{31}	7.5×10^{-7}	6.8	-4.3	-2.2
J2055+3829[ae]	478.6	8.5×10^{-22}	4.59 (b)	1.1×10^{-28}	8.5×10^{-28}	5.6×10^{-27}	1.2×10^{-26}	4.4×10^{30}	5.6×10^{-8}	110	-4.7	-2.3
J2124−3358[ae]	202.8	8.0×10^{-21}	0.44 (f)	2.3×10^{-27}	1.1×10^{-27}	3.3×10^{-26}	7.1×10^{-27}	1.4×10^{30}	1.8×10^{-8}	3	-4.1	-2.3
J2129−5721[aδ]	268.4	1.9×10^{-20}	7.00 (f)	2.6×10^{-28}	1.0×10^{-28}	3.9×10^{-26}	7.3×10^{-27}	1.3×10^{31}	1.7×10^{-7}	28	-4.3	-2.3
J2144−5237[δ]	198.4	8.9×10^{-21}	1.66 (b)	6.5×10^{-28}	7.8×10^{-28}	3.6×10^{-26}	6.9×10^{-27}	5.3×10^{30}	6.9×10^{-8}	11	-4.5	-2.4
J2145−0750[ae]	62.3	2.7×10^{-20}	0.83 (f)	1.3×10^{-27}	1.9×10^{-27}	4.5×10^{-26}	8.9×10^{-27}	3.5×10^{31}	4.5×10^{-7}	7.1	-4.0	-1.9
J2150−0326[ε]	284.8	8.2×10^{-21}	...	...	9.6×10^{-28}	3.1×10^{-26}	6.6×10^{-27}	...	...	...	-4.5	-2.4
J2205+6012[ε]	414.0	2.0×10^{-20}	3.53 (b)	6.5×10^{-29}	7.9×10^{-28}	6.1×10^{-27}	1.3×10^{-26}	4.8×10^{30}	6.2×10^{-8}	20	-4.2	-1.9
J2214+3000[ae]	320.6	1.3×10^{-20}	0.60 (dd)	2.7×10^{-27}	8.0×10^{-27}	3.9×10^{-27}	8.3×10^{-27}	8.9×10^{29}	1.1×10^{-8}	3	-4.6	-2.3
J2222−0137[ae]	30.5	1.5×10^{-20}	0.27 (ee)	2.0×10^{-27}	5.1×10^{-27}	7.1×10^{-26}	1.4×10^{-26}	7.3×10^{31}	9.4×10^{-7}	6.8	-5.0	-2.5
J2229+2643[ae]	335.8	1.4×10^{-21}	1.80 (b)	3.1×10^{-28}	2.0×10^{-28}	3.2×10^{-26}	6.7×10^{-27}	1.9×10^{30}	2.5×10^{-8}	21	-3.5	-2.5
J2234+0611[ae]	279.6	8.4×10^{-21}	1.50 (a)	8.2×10^{-28}	9.1×10^{-28}	3.6×10^{-27}	7.6×10^{-27}	2.7×10^{30}	3.5×10^{-8}	9.2	-4.5	-2.4
J2234+0944[ae]	275.7	1.3×10^{-20}	0.80 (a)	1.9×10^{-27}	1.3×10^{-27}	4.2×10^{-26}	8.6×10^{-27}	1.6×10^{30}	2.1×10^{-8}	4.4	-4.1	-2.2
J2235+1506[aα]	16.7	9.2×10^{-21}	1.54 (b)	6.5×10^{-28}	1.0×10^{-27}	8.8×10^{-26}	1.9×10^{-26}	1.9×10^{33}	2.5×10^{-5}	29	-9.5	-2.8
J2236−5527[δ]	144.8	9.6×10^{-21}	2.05 (b)	4.6×10^{-28}	9.2×10^{-28}	3.1×10^{-26}	5.4×10^{-27}	9.6×10^{30}	1.2×10^{-7}	12	-4.2	-2.3
J2241−5236[aδ]	457.3	5.1×10^{-21}	1.05 (f)	1.2×10^{-27}	1.3×10^{-27}	4.0×10^{-26}	8.8×10^{-27}	8.1×10^{29}	1.0×10^{-8}	7.5	-4.6	-2.5
J2256−1024[ae]	435.8	1.0×10^{-20}	1.33 (b)	1.3×10^{-27}	1.5×10^{-27}	4.9×10^{-26}	1.0×10^{-26}	1.3×10^{30}	1.7×10^{-8}	8.3	-4.2	-2.4

Table A.2: Limits on Gravitational-wave Amplitude and Derived Quantities from O3 (Chapter 3) for 213 Pulsars.

Pulsar Name (J2000)	$f_{\rm rot}$ (Hz)	$\dot{P}_{\rm rot}$ (s s^{-1})	Distance (kpc)	$h_0^{\rm sd}$	$C_{21}^{95\%}$	$C_{22}^{95\%}$	$h_0^{95\%}$	$Q_{22}^{95\%}$ (kg m^2)	$\varepsilon^{95\%}$	$h_0^{95\%}/h_0^{\rm sd}$	$\Theta_{m=1,2}^{l=2}$	$\Theta_{m=2}^{l=2}$
J2302+4442[ae]	192.6	1.4×10^{-20}	0.86 (b)	1.5×10^{-27}	7.0×10^{-27}	3.7×10^{-27}	7.8×10^{-27}	3.3×10^{30}	4.3×10^{-8}	5.1	-4.2	-2.1
J2317+1439[ae]	290.3	2.7×10^{-21}	2.16 (b)	3.3×10^{-21}	8.7×10^{-28}	5.4×10^{-27}	1.1×10^{-26}	5.1×10^{30}	6.6×10^{-8}	33	-4.2	-2.0
J2322+2057[ae]	208.0	3.2×10^{-21}	1.01 (b)	6.5×10^{-21}	8.3×10^{-28}	2.9×10^{-27}	6.2×10^{-27}	2.7×10^{30}	3.4×10^{-8}	9.6	-4.4	-2.3
J2322−2650[aδ]	288.8	4.1×10^{-22}	0.23 (gg)	1.2×10^{-22}	9.5×10^{-27}	4.8×10^{-27}	1.1×10^{-26}	5.7×10^{29}	7.3×10^{-9}	9.3	-4.2	-2.0

The following is a list of references for pulsar distances and intrinsic period derivatives. They should be consulted for the associated uncertainties on these quantities: (a) Arzoumanian et al. (2018), (b) Yao et al. (2017), (c) Verbiest and Lorimer (2014), (d) Antoniadis et al. (2013), (e) Reardon et al. (2016), (f) Reardon et al. (2021), (g) Bassa et al. (2016), (h) Fonseca et al. (2021), (i) Desvignes et al. (2016), (j) Verbiest et al. (2012), (k) Lorimer et al. (2021), (l) Reynoso et al. (2006), (m) Negueruela et al. (2011), (n) Swiggum et al. (2017), (o) Halpern et al. (2013), (p) Bates et al. (2015), (q) Matthews et al. (2016), (r) Harris (2010), (s) Fonseca et al. (2014), (t) Braga et al. (2015), (u) Vigeland et al. (2018), (v) Freire et al. (2012), (w) Espinoza et al. (2013), (x) Ferdman et al. (2014), (y) Camilo et al. (2021), (z) Testa et al. (2001), (aa) Lin et al. (2009), (bb) Gotthelf et al. (2011), (cc) Brownsberger and Romani (2014), (dd) Guillemot et al. (2016), (ee) Deller et al. (2013), (ff) Halpern et al. (2001), (gg) Spiewak et al. (2018).

The following is a list of references for pulsar ephemeris data used in this analysis: CHIME: α, Hobart: β, Jodrell Bank: γ, MeerKAT: δ, Nancay: ϵ, NICER: ζ, UTMOST: η.

[a] The observed $\dot{P}$ has been corrected to account for the relative motion between the pulsar and observer.

[b] The corrected pulsar $\dot{P}$ value is negative, so no value is given and no spin-down limit has been calculated.

[c] This is a globular cluster pulsar for which a proxy period derivative has been derived assuming a characteristic age of 10^9 years and a braking index of $n = 5$.

Table A.3: Limits on Gravitational-wave Amplitude from O3 (Chapter 3) for 23 High-value Pulsars.

Pulsar Name (J2000)	$f_{\rm rot}$ (Hz)	$\dot{P}_{\rm rot}$ (s s^{-1})	Distance (kpc)	$h_0^{\rm sd}$	Priors	$C_{21}^{95\%}$	$C_{22}^{95\%}$	$h_0^{95\%}$	$Q_{22}^{95\%}$ (kg m^2)	$\varepsilon^{95\%}$	$h_0^{95\%}/h_0^{\rm sd}$	$\mathcal{O}_{m=1,2}^{l=2}$	$\mathcal{O}_{m=2}^{l=2}$
J0437$-$4715[aδ]	173.7	1.4×10^{-20}	0.16 (e)	8.0×10^{-27}	U	1.3×10^{-26}	3.8×10^{-26}	6.9×10^{-27}	6.6×10^{29}	8.5×10^{-9}	0.87	-4.4	-2.8
					R	...	...	...	...	...	...	...	...
J0534$+$2200[aγ]	29.6	4.2×10^{-13}	2.00	1.4×10^{-24}	U	7.9×10^{-26}	6.5×10^{-26}	1.3×10^{-26}	5.6×10^{32}	7.2×10^{-6}	0.0094	-4.8	-2.6
					R	6.2×10^{-26}	6.1×10^{-26}	1.2×10^{-26}	5.0×10^{32}	6.5×10^{-6}	0.0085	-4.9	-2.7
J0711$-$6830[aδ]	182.1	1.4×10^{-20}	0.11 (b)	1.2×10^{-26}	U	1.6×10^{-26}	2.4×10^{-26}	7.0×10^{-27}	4.1×10^{29}	5.3×10^{-9}	0.57	-3.9	-2.3
					R	...	...	...	...	...	...	...	...
J0835$-$4510[aβ]	11.2	1.2×10^{-13}	0.28 (j)	3.4×10^{-24}	U	1.6×10^{-23}	8.8×10^{-26}	1.8×10^{-25}	7.2×10^{33}	9.3×10^{-5}	0.052	-6.2	-1.1
					R	0.8×10^{-23}	8.6×10^{-26}	1.7×10^{-25}	7.0×10^{33}	9.1×10^{-5}	0.051	-2.7	-1.0
J0908$-$4913[η]	9.4	1.5×10^{-14}	1.00 (j)	3.0×10^{-25}	U	...	...	2.8×10^{-25}	5.7×10^{34}	7.4×10^{-4}	0.91	...	-2.6
					R	...	...	...	...	...	...	...	...
J1101$-$6101[ζ]	15.9	8.6×10^{-15}	7.00 (l)	4.3×10^{-26}	U	6.8×10^{-25}	1.2×10^{-26}	2.6×10^{-26}	1.3×10^{34}	1.7×10^{-4}	0.61	-9.8	-2.9
					R	...	...	...	...	...	...	...	...
J1105$-$6107[η]	15.8	1.6×10^{-14}	2.36 (b)	1.7×10^{-25}	U	1.1×10^{-24}	2.9×10^{-26}	5.8×10^{-26}	1.0×10^{34}	1.3×10^{-4}	0.34	-3.5	-1.3
					R	...	...	...	...	...	...	...	...
J1302$-$6350[aη]	20.9	2.3×10^{-15}	2.30 (m)	7.7×10^{-26}	U	2.5×10^{-25}	1.2×10^{-26}	2.4×10^{-26}	2.3×10^{33}	3.0×10^{-5}	0.32	-4.7	-2.3
					R	...	...	...	...	...	...	...	...
J1412$+$7922[ζ]	16.9	3.3×10^{-15}	2.00 (o)	9.5×10^{-26}	U	1.2×10^{-24}	1.2×10^{-26}	2.5×10^{-26}	3.2×10^{33}	4.1×10^{-5}	0.26	-8.7	-2.7
					R	...	...	...	...	...	...	...	...
J1745$-$0952[aε]	51.6	8.6×10^{-20}	0.23 (b)	7.5×10^{-27}	U	1.5×10^{-26}	2.2×10^{-27}	4.7×10^{-27}	7.3×10^{30}	9.5×10^{-8}	0.63	-5.1	-2.5
					R	...	...	...	...	...	...	...	...
J1756$-$2251[aε]	35.1	1.0×10^{-18}	0.73 (x)	6.6×10^{-27}	U	3.9×10^{-26}	2.8×10^{-26}	6.1×10^{-27}	6.6×10^{31}	8.6×10^{-7}	0.93	-5.3	-2.7
					R	...	...	...	...	...	...	...	...
J1809$-$1917[aγ]	12.1	2.6×10^{-14}	3.27 (b)	1.4×10^{-25}	U	7.5×10^{-24}	4.6×10^{-26}	9.0×10^{-26}	3.7×10^{34}	4.8×10^{-4}	0.66	-8.2	-2.1
					R	...	...	...	...	...	...	...	...

Table A.3: Limits on Gravitational-wave Amplitude from O3 (Chapter 3) for 23 High-value Pulsars.

Pulsar Name (J2000)	$f_{\rm rot}$ (Hz)	$\dot{P}_{\rm rot}$ (s s^{-1})	Distance (kpc)	$h_0^{\rm sd}$	Priors	$C_{21}^{95\%}$	$C_{22}^{95\%}$	$h_0^{95\%}$	$Q_{22}^{95\%}$ (kg m^2)	$\varepsilon^{95\%}$	$h_0^{95\%}/h_0^{\rm sd}$	$\mathcal{O}_{m=1,2}^{l=2}$	$\mathcal{O}_{m=2}^{l=2}$
J1813−1749[aζ]	22.4	1.3×10^{-13}	6.20 (y)	2.2×10^{-25}	U	1.9×10^{-25}	7.7×10^{-27}	1.5×10^{-27}	3.5×10^{33}	4.5×10^{-5}	0.07	-4.7	-2.5
					R	...	...	...	...	...	...	...	...
J1828−1101[γ]	13.9	1.5×10^{-14}	4.77 (b)	7.7×10^{-26}	U	3.3×10^{-24}	1.9×10^{-26}	4.2×10^{-26}	1.9×10^{34}	2.5×10^{-4}	0.55	-8.9	-2.6
					R	...	...	...	...	...	...	...	...
J1838−0655[ζ]	14.2	4.9×10^{-14}	6.60 (aa)	1.0×10^{-25}	U	3.4×10^{-24}	1.6×10^{-26}	3.7×10^{-26}	2.2×10^{34}	2.9×10^{-4}	0.36	-8.7	-2.7
					R	...	...	...	...	...	...	...	...
J1849−0001[ζ]	26.0	1.4×10^{-14}	7.00 (bb)	7.0×10^{-26}	U	7.3×10^{-26}	5.0×10^{-27}	1.0×10^{-26}	1.9×10^{33}	2.5×10^{-5}	0.15	-5.3	-2.7
					R	...	...	...	...	...	...	...	...
J1856+0245[γ]	12.4	6.2×10^{-14}	6.32 (b)	1.1×10^{-25}	U	6.2×10^{-24}	2.2×10^{-26}	5.2×10^{-26}	3.9×10^{34}	5.0×10^{-4}	0.46	-8.6	-2.7
					R	...	...	...	...	...	...	...	...
J1913+1011[γ]	27.8	3.4×10^{-15}	4.61 (b)	5.4×10^{-26}	U	8.3×10^{-26}	1.0×10^{-26}	2.4×10^{-26}	2.6×10^{33}	3.4×10^{-5}	0.45	-4.0	-1.5
					R	...	...	...	...	...	...	...	...
J1925+1720[γ]	13.2	1.0×10^{-14}	5.06 (b)	5.9×10^{-26}	U	4.0×10^{-24}	1.6×10^{-26}	3.7×10^{-26}	2.0×10^{34}	2.5×10^{-4}	0.63	-8.9	-2.9
					R	...	...	...	...	...	...	...	...
J1928+1746[γ]	14.5	1.3×10^{-14}	4.34 (b)	8.1×10^{-26}	U	1.1×10^{-24}	1.6×10^{-26}	3.4×10^{-26}	1.3×10^{34}	1.7×10^{-4}	0.42	-9.3	-3.1
					R	...	...	...	...	...	...	...	...
J1935+2025[γ]	12.5	6.1×10^{-14}	4.60 (b)	1.5×10^{-25}	U	3.4×10^{-24}	2.5×10^{-26}	5.3×10^{-26}	2.9×10^{34}	3.7×10^{-4}	0.35	-9.1	-2.6
					R	...	...	...	...	...	...	...	...
J1952+3252[aα]	25.3	5.8×10^{-15}	3.00 (j)	1.0×10^{-25}	U	1.0×10^{-25}	8.1×10^{-27}	1.8×10^{-26}	1.5×10^{33}	2.0×10^{-5}	0.17	-4.7	-2.1
					R	1.0×10^{-25}	8.1×10^{-27}	1.6×10^{-26}	1.4×10^{33}	1.8×10^{-5}	0.16	-4.6	-2.2
J2229+6114[α]	19.4	7.8×10^{-14}	3.00 (ff)	3.3×10^{-25}	U	4.1×10^{-25}	8.1×10^{-27}	1.7×10^{-26}	2.5×10^{33}	3.2×10^{-5}	0.052	-8.2	-2.9
					R	4.0×10^{-25}	5.5×10^{-27}	1.1×10^{-26}	1.6×10^{33}	2.1×10^{-5}	0.033	-5.2	-3.0

In the Priors column, U stands for uninformative and R stands for restricted. For references and other notes see Table A.2.

* The pulsar J0537−6910 was not analysed in this study but is included for completeness. The values listed here are taken from Abbott et al. (2021c).

A.3   O4a analysis table

Table A.4: Limits on Gravitational-wave Amplitude and Derived Quantities from O4a (Chapter 4) for 45 Pulsars.

Pulsar Name (J2000)	$f_{\rm rot}$ (Hz)	$\dot{P}_{\rm rot}$ (s s^{-1})	Distance (kpc)	$h_0^{\rm sd}$	Priors	$h_0^{95\%}$ (kg m^2)	$\varepsilon^{95\%}$	$Q_{22}^{95\%}$	$\frac{h_0^{95\%}}{h_0^{\rm sd}}$	$C_{21}^{95\%}$	$C_{22}^{95\%}$	$\mathcal{O}_{m=1,2}^{l=2}$	$\mathcal{O}_{m=2}^{l=2}$
J0030+0451$^\alpha$	205.53	-4.23×10^{-16}	0.33^a	3.52×10^{-27}	U	1.02×10^{-26}	1.89×10^{-8}	1.46×10^{30}	2.91	1.1×10^{-26}	5.19×10^{-27}	-5.14	-10.26
J0058−7218$^\beta$	45.94	-6.1×10^{-11}	59.70^b	1.56×10^{-26}	U	8.77×10^{-27}	5.87×10^{-5}	4.53×10^{33}	0.564	2.44×10^{-26}	4.4×10^{-27}	-5.32	-10.10
J0117+5914$^\gamma$	9.86	-5.69×10^{-13}	1.77^c	1.1×10^{-25}	U	1.73×10^{-25}	7.45×10^{-4}	5.76×10^{34}	1.58	7.67×10^{-23}	8.82×10^{-26}	-3.77	-4.93
J0205+6449$^\gamma$	15.22	-4.49×10^{-11}	3.20^d	4.33×10^{-25}	U	3.15×10^{-26}	1.03×10^{-4}	7.95×10^{33}	0.0728	5.58×10^{-25}	1.5×10^{-26}	-4.71	-8.26
					R	4.15×10^{-26}	1.36×10^{-4}	1.05×10^{34}	0.096	4.78×10^{-25}	1.97×10^{-26}	-4.53	-8.30
J0437−4715$^\delta$	173.69	-4.15×10^{-16}	0.16^e	7.95×10^{-27}	U	7.17×10^{-27}	8.81×10^{-9}	6.81×10^{29}	0.902	1.12×10^{-26}	3.4×10^{-27}	-5.35	-10.37
J0534+2200$^\gamma$	29.95	-3.78×10^{-10}	2.00^f	1.43×10^{-24}	U	1.12×10^{-26}	5.91×10^{-6}	4.57×10^{32}	0.00783	6.59×10^{-26}	5.41×10^{-27}	-5.14	-9.46
					R	9.54×10^{-27}	5.03×10^{-6}	3.89×10^{32}	0.00666	6.04×10^{-26}	4.48×10^{-27}	-5.22	-9.20
J0537−6910$^\beta$	62.03	-1.99×10^{-10}	49.70^g	2.91×10^{-26}	U	6.38×10^{-27}	1.95×10^{-5}	1.5×10^{33}	0.219	2.39×10^{-26}	3.02×10^{-27}	-5.47	-10.18
					R	8.86×10^{-27}	2.71×10^{-5}	2.09×10^{33}	0.305	1.42×10^{-26}	4.71×10^{-27}	-5.30	-10.35
J0540−6919$^\beta$	19.77	-1.87×10^{-10}	49.70^g	4.99×10^{-26}	U	2.71×10^{-26}	8.14×10^{-4}	6.29×10^{34}	0.542	1.91×10^{-25}	1.39×10^{-26}	-4.61	-8.50
					R	3.42×10^{-26}	1.03×10^{-3}	7.94×10^{34}	0.685	1.63×10^{-25}	1.72×10^{-26}	-4.20	-8.41
J0614−3329$^\alpha$	317.59	-1.76×10^{-15}	0.63^h	3.01×10^{-27}	U	1.09×10^{-26}	1.6×10^{-8}	1.24×10^{30}	3.61	8.91×10^{-27}	5.38×10^{-27}	-5.12	-10.46
J0737−3039A$^\alpha$	44.05	-3.41×10^{-15}	1.10^i	6.45×10^{-27}	U	8.88×10^{-27}	1.19×10^{-6}	9.2×10^{31}	1.38	1.85×10^{-26}	4.32×10^{-27}	-5.27	-10.22
J0835−4510$^\epsilon$	11.19	-1.57×10^{-11}	0.28^i	3.41×10^{-24}	U	8.96×10^{-26}	4.74×10^{-5}	3.66×10^{33}	0.0263	2.89×10^{-24}	4.09×10^{-26}	-4.12	-7.14
					R	7.66×10^{-26}	4.05×10^{-5}	3.13×10^{33}	0.0225	2.42×10^{-24}	3.65×10^{-26}	-4.08	-7.10
J1231−1411$^\alpha$	271.45	-5.92×10^{-16}	0.42^c	2.83×10^{-27}	U	1.17×10^{-26}	1.57×10^{-8}	1.22×10^{30}	4.12	1.17×10^{-26}	5.93×10^{-27}	-4.63	-9.87
J1412+7922$^\beta$	17.18	-9.72×10^{-13}	3.30^j	5.81×10^{-26}	U	3.09×10^{-26}	8.16×10^{-5}	6.3×10^{33}	0.531	9.91×10^{-26}	1.36×10^{-26}	-4.71	-8.00
J1537+1155$^\alpha$	26.38	-1.65×10^{-15}	0.93^k	6.82×10^{-27}	U	1.26×10^{-26}	4.0×10^{-6}	3.09×10^{32}	1.85	8.46×10^{-26}	5.55×10^{-27}	-5.18	-9.60
J1623−2631$^\gamma$	90.29	-5.26×10^{-15}	1.85^l	3.33×10^{-27}	U	8.47×10^{-27}	4.55×10^{-7}	3.51×10^{31}	2.55	1.42×10^{-26}	4.11×10^{-27}	-5.15	-10.21
J1719−1438$^\alpha$	172.71	-2.22×10^{-16}	0.34^c	2.72×10^{-27}	U	8.66×10^{-27}	2.31×10^{-8}	1.78×10^{30}	3.18	1.34×10^{-26}	3.72×10^{-27}	-5.27	-10.14
J1744−1134$^\alpha$	245.43	-4.34×10^{-16}	0.40^e	2.72×10^{-27}	U	9.21×10^{-27}	1.43×10^{-8}	1.1×10^{30}	3.39	1.13×10^{-26}	4.4×10^{-27}	-5.04	-10.37
J1745−0952$^\alpha$	51.61	-2.3×10^{-16}	0.23^c	7.53×10^{-27}	U	1.06×10^{-26}	2.13×10^{-7}	1.65×10^{31}	1.41	2.61×10^{-26}	4.95×10^{-27}	-5.26	-9.72
J1756−2251$^\gamma$	35.14	-1.26×10^{-15}	0.73^m	6.6×10^{-27}	U	1.09×10^{-26}	1.53×10^{-6}	1.18×10^{32}	1.65	5.65×10^{-26}	5.38×10^{-27}	-5.13	-9.35

Table A.4: Limits on Gravitational-wave Amplitude and Derived Quantities from O4a (Chapter 4) for 45 Pulsars.

Pulsar Name (J2000)	$f_{\rm rot}$ (Hz)	$\dot{P}_{\rm rot}$ (s s^{-1})	Distance (kpc)	$h_0^{\rm sd}$	Priors	$h_0^{95\%}$	$\varepsilon^{95\%}$	$Q_{22}^{95\%}$ (kg m^2)	$\frac{h_0^{95\%}}{h_0^{\rm sd}}$	$C_{21}^{95\%}$	$C_{22}^{95\%}$	$\mathcal{O}^{l=2}_{m=1,2}$	$\mathcal{O}^{l=2}_{m=2}$
J1809$-$1917$^\gamma$	12.08	-3.73×10^{-12}	3.27^c	1.37×10^{-25}	U	8.11×10^{-26}	4.29×10^{-4}	3.32×10^{34}	0.592	3.0×10^{-24}	3.88×10^{-26}	-4.19	-6.98
J1811$-$1925$^\beta$	15.46	-1.05×10^{-11}	5.00^n	1.33×10^{-25}	U	2.65×10^{-26}	1.31×10^{-4}	1.01×10^{34}	0.199	7.26×10^{-25}	1.34×10^{-26}	-4.82	-8.12
J1813$-$1246$^\beta$	20.8	-7.6×10^{-12}	2.63^o	1.85×10^{-25}	U	1.52×10^{-26}	2.19×10^{-5}	1.69×10^{33}	0.0822	1.41×10^{-25}	7.82×10^{-27}	-5.05	-9.10
J1813$-$1749$^\beta$	22.35	-6.34×10^{-11}	6.15^c	2.21×10^{-25}	U	2.37×10^{-26}	6.89×10^{-5}	5.32×10^{33}	0.107	8.79×10^{-26}	1.2×10^{-26}	-4.43	-8.70
J1823$-$3021A$^\gamma$	183.82	-1.14×10^{-13}	8.02^l	2.5×10^{-27}	U	7.51×10^{-27}	4.21×10^{-7}	3.26×10^{31}	3.00	1.61×10^{-26}	3.95×10^{-27}	-5.24	-9.71
J1824$-$2452A$^\alpha$	327.41	-1.73×10^{-13}	5.37^l	3.45×10^{-27}	U	8.11×10^{-27}	9.61×10^{-8}	7.43×10^{30}	2.35	1.51×10^{-26}	3.74×10^{-27}	-5.17	-10.00
J1826$-$1334$^\gamma$	9.85	-7.31×10^{-12}	3.61^c	1.93×10^{-25}	U	1.53×10^{-25}	1.34×10^{-3}	1.04×10^{35}	0.794	4.88×10^{-23}	7.04×10^{-26}	-3.85	-5.69
J1828$-$1101$^\gamma$	13.88	-2.85×10^{-12}	4.77^c	7.67×10^{-26}	U	4.21×10^{-26}	2.46×10^{-4}	1.9×10^{34}	0.549	5.3×10^{-24}	2.13×10^{-26}	-4.65	-7.40
J1831$-$0952$^\gamma$	14.87	-1.84×10^{-12}	3.68^c	7.7×10^{-26}	U	4.18×10^{-26}	1.65×10^{-4}	1.27×10^{34}	0.543	6.44×10^{-25}	1.92×10^{-26}	-4.62	-8.05
J1833$-$0827$^\gamma$	11.72	-1.26×10^{-12}	4.50^i	5.88×10^{-26}	U	6.19×10^{-26}	4.79×10^{-4}	3.7×10^{34}	1.05	2.7×10^{-24}	2.99×10^{-26}	-4.45	-7.19
J1837$-$0604$^\gamma$	10.38	-4.84×10^{-12}	4.78^c	1.15×10^{-25}	U	7.78×10^{-26}	8.15×10^{-4}	6.3×10^{34}	0.675	5.56×10^{-24}	3.56×10^{-26}	-4.42	-7.04
J1838$-$0655$^\beta$	14.18	-9.9×10^{-12}	6.60^p	1.02×10^{-25}	U	6.62×10^{-26}	5.14×10^{-4}	3.97×10^{34}	0.649	1.27×10^{-24}	3.41×10^{-26}	-3.78	-6.68
J1849$-$0001$^\beta$	25.96	-9.54×10^{-12}	7.00^q	6.98×10^{-26}	U	1.36×10^{-26}	3.34×10^{-5}	2.58×10^{33}	0.194	1.26×10^{-25}	6.04×10^{-27}	-5.20	-9.13
J1856$+$0245$^\gamma$	12.36	-9.49×10^{-12}	6.32^c	1.12×10^{-25}	U	5.85×10^{-26}	5.72×10^{-4}	4.42×10^{34}	0.523	1.34×10^{-24}	2.93×10^{-26}	-4.43	-7.77
J1913$+$1011$^\gamma$	27.85	-2.62×10^{-12}	4.61^c	5.36×10^{-26}	U	1.12×10^{-26}	1.57×10^{-5}	1.21×10^{33}	0.208	6.52×10^{-26}	5.18×10^{-27}	-5.20	-9.68
J1925$+$1720$^\gamma$	13.22	-1.83×10^{-12}	5.05^c	5.94×10^{-26}	U	5.94×10^{-26}	4.06×10^{-4}	3.14×10^{34}	1.00	2.18×10^{-24}	2.75×10^{-26}	-4.25	-6.16
J1935$+$2025$^\gamma$	12.48	-9.47×10^{-12}	4.60^c	1.53×10^{-25}	U	5.52×10^{-26}	3.85×10^{-4}	2.98×10^{34}	0.361	1.51×10^{-24}	2.64×10^{-26}	-4.61	-7.79
J1952$+$3252$^\gamma$	25.3	-3.74×10^{-12}	3.00^i	1.03×10^{-25}	U	1.07×10^{-26}	1.18×10^{-5}	9.15×10^{32}	0.103	1.86×10^{-25}	4.16×10^{-27}	-5.34	-8.60
					R	9.62×10^{-27}	1.07×10^{-5}	8.24×10^{32}	0.093	6.89×10^{-24}	2.81×10^{-27}	-5.35	-8.14
J2016$+$3711$^\zeta$	19.68	-2.81×10^{-11}	6.10^r	1.58×10^{-25}	U	1.99×10^{-26}	7.42×10^{-5}	5.73×10^{33}	0.126	1.57×10^{-25}	8.8×10^{-27}	-4.95	-9.06
J2021$+$3651$^\gamma$	9.64	-8.89×10^{-12}	1.80^s	4.3×10^{-25}	U	2.27×10^{-25}	1.04×10^{-3}	8.04×10^{34}	0.528	6.01×10^{-23}	1.13×10^{-25}	-3.13	-4.87
					R	2.18×10^{-25}	9.99×10^{-4}	7.72×10^{34}	0.507	5.0×10^{-23}	1.08×10^{-25}	-3.18	-5.24
J2022$+$3842$^\beta$	20.59	-3.65×10^{-11}	10.00^t	1.07×10^{-25}	U	1.89×10^{-26}	1.05×10^{-4}	8.14×10^{33}	0.176	1.4×10^{-25}	8.64×10^{-27}	-4.97	-9.06
J2043$+$2740$^\gamma$	10.4	-1.37×10^{-13}	1.48^c	6.26×10^{-26}	U	1.14×10^{-25}	3.69×10^{-4}	2.85×10^{34}	1.82	1.2×10^{-23}	5.21×10^{-26}	-4.09	-5.99

Table A.4: Limits on Gravitational-wave Amplitude and Derived Quantities from O4a (Chapter 4) for 45 Pulsars.

Pulsar Name (J2000)	$f_{\rm rot}$ (Hz)	$\dot{P}_{\rm rot}$ (s s^{-1})	Distance (kpc)	$h_0^{\rm sd}$	Priors	$h_0^{95\%}$ (kg m^2)	$\varepsilon^{95\%}$	$Q_{22}^{95\%}$	$\frac{h_0^{95\%}}{h_0^{\rm sd}}$	$C_{21}^{95\%}$	$C_{22}^{95\%}$	$\mathcal{O}_{m=1,2}^{l=2}$	$\mathcal{O}_{m=2}^{l=2}$
J2124$-$3358$^\alpha$	202.79	-2.94×10^{-16}	0.41^e	2.37×10^{-27}	U	9.23×10^{-27}	2.18×10^{-8}	1.68×10^{30}	3.90	9.93×10^{-27}	4.75×10^{-27}	-5.01	-10.25
J2214$+$3000^f	320.59	-1.31×10^{-15}	0.60^u	2.71×10^{-27}	U	8.98×10^{-27}	1.24×10^{-8}	9.58×10^{29}	3.31	8.6×10^{-27}	4.61×10^{-27}	-5.30	-10.49
J2222$-$0137$^\alpha$	30.47	-4.99×10^{-16}	0.27^v	1.22×10^{-26}	U	1.31×10^{-26}	8.98×10^{-7}	6.94×10^{31}	1.08	4.09×10^{-26}	6.36×10^{-26}	-5.08	-9.72
J2229$+$6114$^\gamma$	19.36	-2.9×10^{-11}	3.00^w	3.29×10^{-25}	U	1.49×10^{-26}	2.82×10^{-5}	2.18×10^{33}	0.0453	1.79×10^{-25}	6.76×10^{-27}	-5.09	-9.20
					R	9.32×10^{-27}	1.76×10^{-5}	1.36×10^{33}	0.0283	1.62×10^{-25}	4.62×10^{-27}	-5.27	-9.39

In the Priors column, U stands for uninformative and R stands for restricted.

The following is a list of references for pulsar ephemeris data used in this analysis: Nançay: α, NICER: β, JBO: γ, IAR: δ, Hobart: ϵ, FAST: ζ, CHIME: η.

The following is a list of references for pulsar distances and intrinsic period derivatives, and they should be consulted for information on the associated uncertainties on these quantities: (a) Ding et al. (2023), (b) Storm et al. (2004), (c) Yao et al. (2017), (d) Roberts et al. (1993), (e) Reardon et al. (2016), (f) Trimble (1968), (g) Walker (2012), (h) Bassa et al. (2016), (i) Verbiest et al. (2012), (j) Mereghetti et al. (2021), (k) Ding et al. (2021), (l) Baumgardt and Vasiliev (2021), (m) Ferdman et al. (2014), (n) Green et al. (1988), (o) Torres et al. (2019), (p) Lin et al. (2009), (q) H. E. S. S. Collaboration et al. (2018), (r) Liu et al. (2024), (s) Kirichenko et al. (2015), (t) Arzoumanian et al. (2011), (u) Guillemot et al. (2016), (v) Guo et al. (2021), (w) Halpern et al. (2001).

References

Aasi, J., Abadie, J., Abbott, B.P. et al. Gravitational Waves from Known Pulsars: Results from the Initial Detector Era. *ApJ*, 785:119, Apr. 2014. doi: 10.1088/0004-637X/785/2/119.

Aasi, J., Abbott, B.P., Abbott, R. et al. Advanced LIGO. *CQGra*, 32(7):074001, Apr. 2015. doi: 10.1088/0264-9381/32/7/074001.

Abac, A.G., Abbott, R., Abouelfettouh, I. et al. Observation of Gravitational Waves from the Coalescence of a 2.5–4.5 M$_\odot$ Compact Object and a Neutron Star. *ApJL*, 970(2):L34, Aug. 2024. doi: 10.3847/2041-8213/ad5beb.

Abac, A.G., Abbott, R., Abouelfettouh, I. et al. Search for Continuous Gravitational Waves from Known Pulsars in the First Part of the Fourth LIGO-Virgo-KAGRA Observing Run. *ApJ*, 983(2):99, Apr. 2025. doi: 10.3847/1538-4357/adb3a0.

Abbott, B., Abbott, R., Adhikari, R. et al. Upper limits on gravitational wave emission from 78 radio pulsars. *PhRvD*, 76(4):042001, Aug. 2007. doi: 10.1103/PhysRevD.76.042001.

Abbott, B.P., Abbott, R., Abbott, T.D. et al. Observation of Gravitational Waves from a Binary Black Hole Merger. *PhRvL*, 116(6):061102, Feb. 2016a. doi: 10.1103/PhysRevLett.116.061102.

Abbott, B.P., Abbott, R., Abbott, T.D. et al. GW150914: First results from the search for binary black hole coalescence with Advanced LIGO. *PhRvD*, 93(12):122003, June 2016b. doi: 10.1103/PhysRevD.93.122003.

Abbott, B.P., Abbott, R., Abbott, T.D. et al. Observing gravitational-wave transient GW150914 with minimal assumptions. *PhRvD*, 93(12):122004, Sept. 2016c. doi: 10.1103/PhysRevD.93.122004.

Abbott, B.P., Abbott, R., Abbott, T.D. et al. GW150914: The Advanced LIGO Detectors in the Era of First Discoveries. *PhRvL*, 116(13):131103, Apr. 2016d. doi: 10.1103/PhysRevLett.116.131103.

Abbott, B.P., Abbott, R., Abbott, T.D. et al. First Search for Gravitational Waves from Known Pulsars with Advanced LIGO. *ApJ*, 839:12, Apr. 2017a. doi: 10.3847/1538-4357/aa677f.

Abbott, B.P., Abbott, R., Abbott, T.D. et al. Calibration of the Advanced LIGO detectors for the discovery of the binary black-hole merger GW150914. *PhRvD*, 95(6):062003, Mar. 2017b. doi: 10.1103/PhysRevD.95.062003.

Abbott, B.P., Abbott, R., Abbott, T.D. et al. Gravitational Waves and Gamma-Rays from a Binary Neutron Star Merger: GW170817 and GRB 170817A. *ApJL*, 848(2):L13, Oct. 2017c. doi: 10.3847/2041-8213/aa920c.

Abbott, B.P., Abbott, R., Abbott, T.D. et al. First narrow-band search for continuous gravitational waves from known pulsars in advanced detector data. *PhRvD*, 96(12):122006, Dec. 2017d. doi: 10.1103/PhysRevD.96.122006.

Abbott, B.P., Abbott, R., Abbott, T.D. et al. GW170817: Observation of Gravitational Waves from a Binary Neutron Star Inspiral. *PhRvL*, 119(16):161101, Oct. 2017e. doi: 10.1103/PhysRevLett.119.161101.

Abbott, B.P., Abbott, R., Abbott, T.D. et al. Full band all-sky search for periodic gravitational waves in the O1 LIGO data. *PhRvD*, 97(10):102003, May 2018. doi: 10.1103/PhysRevD.97.102003.

Abbott, B.P., Abbott, R., Abbott, T.D. et al. All-sky search for continuous gravitational waves from isolated neutron stars using Advanced LIGO O2 data. *PhRvD*, 100(2):024004, July 2019a. doi: 10.1103/PhysRevD.100.024004.

Abbott, B.P., Abbott, R., Abbott, T.D. et al. Searches for Gravitational Waves from Known Pulsars at Two Harmonics in 2015-2017 LIGO Data. *ApJ*, 879 (1):10, July 2019b. doi: 10.3847/1538-4357/ab20cb.

Abbott, B.P., Abbott, R., Abbott, T.D. et al. GWTC-1: A Gravitational-Wave Transient Catalog of Compact Binary Mergers Observed by LIGO and Virgo during the First and Second Observing Runs. *Physical Review X*, 9(3):031040, July 2019c. doi: 10.1103/PhysRevX.9.031040.

Abbott, B.P., Abbott, R., Abbott, T.D. et al. Narrow-band search for gravitational waves from known pulsars using the second LIGO observing run. *PhRvD*, 99(12):122002, June 2019d. doi: 10.1103/PhysRevD.99.122002.

Abbott, B.P., Abbott, R., Abbott, T.D. et al. Tests of general relativity with the binary black hole signals from the LIGO-Virgo catalog GWTC-1. *PhRvD*, 100 (10):104036, Nov. 2019e. doi: 10.1103/PhysRevD.100.104036.

Abbott, B.P., Abbott, R., Abbott, T.D. et al. GW190425: Observation of a Compact Binary Coalescence with Total Mass ~ 3.4 M$_\odot$. *ApJL*, 892(1):L3, Mar. 2020a. doi: 10.3847/2041-8213/ab75f5.

Abbott, R., Abbott, T.D., Abraham, S. et al. Gravitational-wave Constraints on the Equatorial Ellipticity of Millisecond Pulsars. *ApJL*, 902(1):L21, Oct. 2020b. doi: 10.3847/2041-8213/abb655.

Abbott, R., Abbott, T.D., Abraham, S. et al. GW190814: Gravitational Waves from the Coalescence of a 23 Solar Mass Black Hole with a 2.6 Solar Mass Compact Object. *ApJL*, 896(2):L44, June 2020c. doi: 10.3847/2041-8213/ab960f.

Abbott, R., Abbott, T.D., Abraham, S. et al. All-sky Search for Continuous Gravitational Waves from Isolated Neutron Stars in the Early O3 LIGO Data. *arXiv:2107.00600*, July 2021a.

Abbott, R., Abbott, T.D., Abraham, S. et al. GWTC-2: Compact Binary Coalescences Observed by LIGO and Virgo during the First Half of the Third Observing Run. *PhRvX*, 11(2):021053, Apr. 2021b. doi: 10.1103/PhysRevX.11.021053.

Abbott, R., Abbott, T.D., Abraham, S. et al. Diving below the Spin-down Limit: Constraints on Gravitational Waves from the Energetic Young Pulsar PSR J0537-6910. *ApJL*, 913(2):L27, June 2021c. doi: 10.3847/2041-8213/abffcd.

Abbott, R., Abbott, T.D., Abraham, S. et al. Observation of Gravitational Waves from Two Neutron Star-Black Hole Coalescences. *ApJL*, 915(1):L5, July 2021d. doi: 10.3847/2041-8213/ac082e.

Abbott, R., Abbott, T.D., Abraham, S. et al. Searches for Continuous Gravitational Waves from Young Supernova Remnants in the Early Third Observing Run of Advanced LIGO and Virgo. *ApJ*, 921(1):80, Nov. 2021e. doi: 10.3847/1538-4357/ac17ea.

Abbott, R., Abbott, T.D., Abraham, S. et al. Upper limits on the isotropic gravitational-wave background from Advanced LIGO and Advanced Virgo's third observing run. *PhRvD*, 104(2):022004, July 2021f. doi: 10.1103/PhysRevD.104.022004.

Abbott, R., Abbott, T.D., Abraham, S. et al. Constraints from LIGO O3 Data on Gravitational-wave Emission Due to R-modes in the Glitching Pulsar PSR J0537-6910. *ApJ*, 922(1):71, Nov. 2021g. doi: 10.3847/1538-4357/ac0d52.

Abbott, R., Abbott, T.D., Acernese, F. et al. Narrowband Searches for Continuous and Long-duration Transient Gravitational Waves from Known Pulsars in the LIGO-Virgo Third Observing Run. *ApJ*, 932(2):133, June 2022a. doi: 10.3847/1538-4357/ac6ad0.

Abbott, R., Abbott, T.D., Acernese, F. et al. Search of the early O3 LIGO data for continuous gravitational waves from the Cassiopeia A and Vela Jr. supernova remnants. *PhRvD*, 105(8):082005, Apr. 2022b. doi: 10.1103/PhysRevD.105.082005.

Abbott, R., Abe, H., Acernese, F. et al. All-sky search for continuous gravitational waves from isolated neutron stars using Advanced LIGO and Advanced Virgo O3 data. *PhRvD*, 106(10):102008, Nov. 2022c. doi: 10.1103/PhysRevD.106.102008.

Abbott, R., Abe, H., Acernese, F. et al. All-sky search for gravitational wave emission from scalar boson clouds around spinning black holes in LIGO O3 data. *PhRvD*, 105(10):102001, May 2022d. doi: 10.1103/PhysRevD.105.102001.

Abbott, R., Abe, H., Acernese, F. et al. Searches for Gravitational Waves from Known Pulsars at Two Harmonics in the Second and Third LIGO-Virgo Observing Runs. *ApJ*, 935(1):1, Aug. 2022e. doi: 10.3847/1538-4357/ac6acf.

Abbott, R., Abe, H., Acernese, F. et al. Search for continuous gravitational wave emission from the Milky Way center in O3 LIGO-Virgo data. *PhRvD*, 106(4): 042003, Aug. 2022f. doi: 10.1103/PhysRevD.106.042003.

Abbott, R., Abbott, T.D., Acernese, F. et al. GWTC-3: Compact Binary Coalescences Observed by LIGO and Virgo during the Second Part of the Third Observing Run. *Physical Review X*, 13(4):041039, Oct. 2023. doi: 10.1103/PhysRevX.13.041039.

Abou El-Neaj, Y., Alpigiani, C., Amairi-Pyka, S. et al. AEDGE: Atomic Experiment for Dark Matter and Gravity Exploration in Space. *EPJ Quantum Technology*, 7:6, Mar. 2020. doi: 10.1140/epjqt/s40507-020-0080-0.

Acernese, F., Agathos, M., Agatsuma, K. et al. Advanced Virgo: a second-generation interferometric gravitational wave detector. *CQGra*, 32(2):024001, Jan. 2015. doi: 10.1088/0264-9381/32/2/024001.

Acernese, F., Adams, T., Agatsuma, K. et al. Calibration of advanced Virgo and reconstruction of the gravitational wave signal h(t) during the observing run O2. *CQGra*, 35(20):205004, Oct. 2018. doi: 10.1088/1361-6382/aadf1a.

Acernese, F., Agathos, M., Ain, A. et al. Calibration of advanced Virgo and reconstruction of the detector strain h(t) during the observing run O3. *CQGra*, 39(4):045006, Feb. 2022. doi: 10.1088/1361-6382/ac3c8e.

Adhikari, R., Brooks, A., Shapiro, B. et al. *LIGO Voyager Upgrade: Design Concept.* Sep 2024. URL https://docs.ligo.org/voyager/voyagerwhitepaper/main.pdf.

Agazie, G., Anumarlapudi, A., Archibald, A.M. et al. The NANOGrav 15 yr Data Set: Evidence for a Gravitational-wave Background. *ApJL*, 951(1):L8, July 2023. doi: 10.3847/2041-8213/acdac6.

Akutsu, T., Ando, M., Arai, K. et al. Overview of KAGRA: Detector design and construction history. *Progress of Theoretical and Experimental Physics*, 2021 (5):05A101, May 2021. doi: 10.1093/ptep/ptaa125.

Alam, M.F., Arzoumanian, Z., Baker, P.T. et al. The NANOGrav 12.5-year Data Set: Wideband Timing of 47 Millisecond Pulsars. *arXiv e-prints*, art. arXiv:2005.06495, May 2020.

Alam, M.F., Arzoumanian, Z., Baker, P.T. et al. The NANOGrav 12.5 yr Data Set: Observations and Narrowband Timing of 47 Millisecond Pulsars. *ApJS*, 252(1):4, Jan. 2021. doi: 10.3847/1538-4365/abc6a0.

Amiri, M., Bandura, K.M., Boyle, P.J. et al. The CHIME Pulsar Project: System Overview. *ApJS*, 255(1):5, July 2021a. doi: 10.3847/1538-4365/abfdcb.

Amiri, M., Bandura, K.M., Boyle, P.J. et al. The CHIME Pulsar Project: System Overview. *ApJS*, 255(1):5, July 2021b. doi: 10.3847/1538-4365/abfdcb.

An, Z., Shao, K., Gu, D. et al. Simulation and accuracy analysis of orbit determination for TianQin using SLR data. *Classical and Quantum Gravity*, 39(24): 245016, Dec. 2022. doi: 10.1088/1361-6382/aca314.

Andersson, N. A New Class of Unstable Modes of Rotating Relativistic Stars. *ApJ*, 502(2):708–713, Aug. 1998. doi: 10.1086/305919.

Annala, E., Gorda, T., Hirvonen, J. et al. Strongly interacting matter exhibits deconfined behavior in massive neutron stars. *Nature Communications*, 14: 8451, Dec. 2023. doi: 10.1038/s41467-023-44051-y.

Antonelli, M., Montoli, A. and Pizzochero, P.M. Insights Into the Physics of Neutron Star Interiors from Pulsar Glitches. In Vasconcellos, C.A.Z., editor, *Astrophysics in the XXI Century with Compact Stars. Edited by C.A.Z. Vasconcellos. eISBN 978-981-12-2094-4. Singapore: World Scientific*, pages 219–281. 2022. doi: 10.1142/9789811220944_0007.

Antoniadis, J., Freire, P.C.C., Wex, N. et al. A Massive Pulsar in a Compact Relativistic Binary. *Sci*, 340:448, Apr. 2013. doi: 10.1126/science.1233232.

Armano, M., Audley, H., Baird, J. et al. In-depth analysis of LISA Pathfinder performance results: Time evolution, noise projection, physical models, and implications for LISA. *PhRvD*, 110(4):042004, Aug. 2024. doi: 10.1103/PhysRevD. 110.042004.

Arvanitaki, A., Graham, P.W., Hogan, J.M. et al. Search for light scalar dark matter with atomic gravitational wave detectors. *arXiv e-prints*, art. arXiv:1606.04541, June 2016. doi: 10.48550/arXiv.1606.04541.

Arzoumanian, Z., Gotthelf, E.V., Ransom, S.M. et al. Discovery of an Energetic Pulsar Associated with SNR G76.9+1.0. *ApJ*, 739(1):39, Sept. 2011. doi: 10.1088/0004-637X/739/1/39.

Arzoumanian, Z., Brazier, A., Burke-Spolaor, S. et al. The NANOGrav 11-year Data Set: High-precision Timing of 45 Millisecond Pulsars. *ApJS*, 235:37, Apr. 2018. doi: 10.3847/1538-4365/aab5b0.

Ashok, A., Beheshtipour, B., Papa, M.A. et al. New Searches for Continuous Gravitational Waves from Seven Fast Pulsars. *ApJ*, 923(1):85, Dec. 2021. doi: 10.3847/1538-4357/ac2582.

Ashton, G., Hübner, M., Lasky, P.D. et al. BILBY: A User-friendly Bayesian Inference Library for Gravitational-wave Astronomy. *ApJS*, 241(2):27, Apr. 2019. doi: 10.3847/1538-4365/ab06fc.

Ashton, G. et al. BILBY: A user-friendly Bayesian inference library for gravitational-wave astronomy. *Astrophys. J. Suppl.*, 241(2):27, 2019. doi: 10.3847/1538-4365/ab06fc.

Astone, P., D'Antonio, S., Frasca, S. et al. A method for detection of known sources of continuous gravitational wave signals in non-stationary data. *CQGra*, 27(19):194016, Oct. 2010. doi: 10.1088/0264-9381/27/19/194016.

Astone, P., Colla, A., D'Antonio, S. et al. Method for narrow-band search of continuous gravitational wave signals. *Phys. Rev. D*, 89:062008, Mar 2014. doi: 10.1103/PhysRevD.89.062008. URL `https://link.aps.org/doi/10.1103/PhysRevD.89.062008`.

Atwood, W.B., Abdo, A.A., Ackermann, M. et al. The Large Area Telescope on the Fermi Gamma-Ray Space Telescope Mission. *ApJ*, 697(2):1071–1102, June 2009. doi: 10.1088/0004-637X/697/2/1071.

Baade, W. and Zwicky, F. Remarks on Super-Novae and Cosmic Rays. *Physical Review*, 46(1):76–77, July 1934. doi: 10.1103/PhysRev.46.76.2.

Backer, D.C., Kulkarni, S.R., Heiles, C. et al. A millisecond pulsar. *Nature*, 300 (5893):615–618, Dec. 1982. doi: 10.1038/300615a0.

Badziak, M. and Nałecz, I. First-order phase transitions in Twin Higgs models. *Journal of High Energy Physics*, 2023(2):185, Mar. 2023. doi: 10.1007/JHEP02(2023)185.

Bailes, M., Jameson, A., Abbate, F. et al. The MeerKAT telescope as a pulsar facility: System verification and early science results from MeerTime. *PASA*, 37:e028, July 2020. doi: 10.1017/pasa.2020.19.

Baronchelli, L., Nandra, K. and Buchner, J. Relativistic accretion disc reflection in AGN X-ray spectra at z = 0.5-4: a study of four Chandra Deep Fields. *MNRAS*, 498(4):5284–5298, Nov. 2020. doi: 10.1093/mnras/staa2684.

Bassa, C.G., Antoniadis, J., Camilo, F. et al. Cool white dwarf companions to four millisecond pulsars. *MNRAS*, 455:3806–3813, Feb. 2016. doi: 10.1093/mnras/stv2607.

Bates, S.D., Thornton, D., Bailes, M. et al. The High Time Resolution Universe survey - XI. Discovery of five recycled pulsars and the optical detectability of survey white dwarf companions. *MNRAS*, 446(4):4019–4028, Feb. 2015. doi: 10.1093/mnras/stu2350.

Baumgardt, H. and Vasiliev, E. Accurate distances to Galactic globular clusters through a combination of Gaia EDR3, HST, and literature data. *MNRAS*, 505 (4):5957–5977, Aug. 2021. doi: 10.1093/mnras/stab1474.

Baym, G., Pethick, C., Pines, D. et al. Spin Up in Neutron Stars : The Future of the Vela Pulsar. *Nature*, 224(5222):872–874, Nov. 1969. doi: 10.1038/224872a0.

Bhattacharya, D. and van den Heuvel, E.P.J. Formation and evolution of binary and millisecond radio pulsars. *PhR*, 203(1-2):1–124, Jan. 1991. doi: 10.1016/ 0370-1573(91)90064-S.

Black, E.D. An introduction to Pound-Drever-Hall laser frequency stabilization. *American Journal of Physics*, 69(1):79–87, Jan. 2001. doi: 10.1119/1.1286663.

Bombaci, I. The maximum mass of a neutron star. *A&A*, 305:871, Jan. 1996.

Bonazzola, S. and Gourgoulhon, E. Gravitational waves from pulsars: emission by the magnetic-field-induced distortion. *A&A*, 312:675–690, Aug. 1996.

Borhanian, S. and Sathyaprakash, B.S. Listening to the Universe with next generation ground-based gravitational-wave detectors. *PhRvD*, 110(8):083040, Oct. 2024. doi: 10.1103/PhysRevD.110.083040.

Braga, V.F., Dall'Ora, M., Bono, G. et al. On the Distance of the Globular Cluster M4 (NGC 6121) Using RR Lyrae Stars. I. Optical and Near-infrared Period-Luminosity and Period-Wesenheit Relations. *ApJ*, 799:165, Feb. 2015. doi: 10.1088/0004-637X/799/2/165.

Branchesi, M., Maggiore, M., Alonso, D. et al. Science with the Einstein Telescope: a comparison of different designs. *JCAP*, 2023(7):068, July 2023. doi: 10.1088/1475-7516/2023/07/068.

Braun, R., Bonaldi, A., Bourke, T. et al. Anticipated Performance of the Square Kilometre Array – Phase 1 (SKA1). *arXiv e-prints*, art. arXiv:1912.12699, Dec. 2019. doi: 10.48550/arXiv.1912.12699.

Brownsberger, S. and Romani, R.W. A Survey for Hα Pulsar Bow Shocks. *ApJ*, 784(2):154, Apr. 2014. doi: 10.1088/0004-637X/784/2/154.

Buchner, J., 2021. URL `https://github.com/JohannesBuchner/PosteriorStacker`.

Buikema, A., Cahillane, C., Mansell, G.L. et al. Sensitivity and performance of the Advanced LIGO detectors in the third observing run. *PhRvD*, 102(6): 062003, Sept. 2020. doi: 10.1103/PhysRevD.102.062003.

Cahillane, C., Betzwieser, J., Brown, D.A. et al. Calibration uncertainty for Advanced LIGO's first and second observing runs. *PhRvD*, 96(10):102001, Nov. 2017. doi: 10.1103/PhysRevD.96.102001.

Camilo, F., Ransom, S.M., Halpern, J.P. et al. Radio Detection of PSR J1813-1749 in HESS J1813-178: The Most Scattered Pulsar Known. *ApJ*, 917(2):67, Aug. 2021. doi: 10.3847/1538-4357/ac0720.

Caplan, M.E. and Horowitz, C.J. Colloquium: Astromaterial science and nuclear pasta. *Reviews of Modern Physics*, 89(4):041002, Oct. 2017. doi: 10.1103/RevModPhys.89.041002.

Capote, E., Jia, W., Aritomi, N. et al. Advanced LIGO detector performance in the fourth observing run. *arXiv e-prints*, art. arXiv:2411.14607, Nov. 2024. doi: 10.48550/arXiv.2411.14607.

Chandrasekhar, S. The Maximum Mass of Ideal White Dwarfs. *ApJ*, 74:81, July 1931. doi: 10.1086/143324.

Chang, C.F. and Cui, Y. Gravitational waves from global cosmic strings and cosmic archaeology. *Journal of High Energy Physics*, 2022(3):114, Mar. 2022. doi: 10.1007/JHEP03(2022)114.

Chen, S., Caballero, R.N., Guo, Y.J. et al. Common-red-signal analysis with 24-yr high-precision timing of the European Pulsar Timing Array: inferences in the stochastic gravitational-wave background search. *MNRAS*, 508(4):4970–4993, Dec. 2021. doi: 10.1093/mnras/stab2833.

Christensen, N. Stochastic gravitational wave backgrounds. *Reports on Progress in Physics*, 82(1):016903, Jan. 2019. doi: 10.1088/1361-6633/aae6b5.

Cieślar, M., Bulik, T., Curyło, M. et al. Detectability of continuous gravitational waves from isolated neutron stars in the Milky Way. The population synthesis approach. *A&A*, 649:A92, May 2021. doi: 10.1051/0004-6361/202039503.

Cognard, I. and Backer, D.C. A Microglitch in the Millisecond Pulsar PSR B1821-24 in M28. *ApJL*, 612(2):L125–L127, Sept. 2004. doi: 10.1086/424692.

Colpi, M., Danzmann, K., Hewitson, M. et al. LISA Definition Study Report. *arXiv e-prints*, art. arXiv:2402.07571, Feb. 2024. doi: 10.48550/arXiv.2402.07571.

Cordes, J.M. and Downs, G.S. JPL pulsar timing observations. III. Pulsar rotation fluctuations. *ApJS*, 59:343–382, Nov. 1985. doi: 10.1086/191076.

Crowder, J. and Cornish, N.J. Beyond LISA: Exploring future gravitational wave missions. *PhRvD*, 72(8):083005, Oct. 2005. doi: 10.1103/PhysRevD.72.083005.

Cutler, C. Gravitational waves from neutron stars with large toroidal B fields. *PhRvD*, 66(8):084025, Oct. 2002. doi: 10.1103/PhysRevD.66.084025.

Davis, D., Massinger, T., Lundgren, A. et al. Improving the sensitivity of Advanced LIGO using noise subtraction. *Classical and Quantum Gravity*, 36(5):055011, Mar. 2019. doi: 10.1088/1361-6382/ab01c5.

Deller, A.T., Boyles, J., Lorimer, D.R. et al. VLBI Astrometry of PSR J2222-0137: A Pulsar Distance Measured to 0.4% Accuracy. *ApJ*, 770:145, June 2013. doi: 10.1088/0004-637X/770/2/145.

Dergachev, V. and Papa, M.A. Results from the First All-Sky Search for Continuous Gravitational Waves from Small-Ellipticity Sources. *PhRvL*, 125(17):171101, Oct. 2020. doi: 10.1103/PhysRevLett.125.171101.

Desvignes, G., Caballero, R.N., Lentati, L. et al. High-precision timing of 42 millisecond pulsars with the European Pulsar Timing Array. *MNRAS*, 458:3341–3380, May 2016. doi: 10.1093/mnras/stw483.

Ding, H., Deller, A.T., Fonseca, E. et al. The Orbital-decay Test of General Relativity to the 2% Level with 6 yr VLBA Astrometry of the Double Neutron Star PSR J1537+1155. *ApJL*, 921(1):L19, Nov. 2021. doi: 10.3847/2041-8213/ac3091.

Ding, H., Deller, A.T., Stappers, B.W. et al. The MSPSRπ catalogue: VLBA astrometry of 18 millisecond pulsars. *MNRAS*, 519(4):4982–5007, Mar. 2023. doi: 10.1093/mnras/stac3725.

Domènech, G. Scalar Induced Gravitational Waves Review. *Universe*, 7(11):398, Oct. 2021. doi: 10.3390/universe7110398.

D'Onofrio, L., De Rosa, R., Palomba, C. et al. Search for gravitational wave signals from known pulsars in LIGO-Virgo O3 data using the 5 n -vector ensemble method. *PhRvD*, 108(12):122002, Dec. 2023. doi: 10.1103/PhysRevD.108.122002.

D'Onofrio, L., Astone, P., Dal Pra, S. et al. Two sides of the same coin: the F-statistic and the 5-vector method. *arXiv e-prints*, art. arXiv:2406.09236, June 2024. doi: 10.48550/arXiv.2406.09236.

Dupuis, R.J. and Woan, G. Bayesian estimation of pulsar parameters from gravitational wave data. *PhRvD*, 72(10):102002–+, Nov. 2005. doi: 10.1103/PhysRevD.72.102002.

Edwards, R.T., Hobbs, G.B. and Manchester, R.N. TEMPO2, a new pulsar timing package - II. The timing model and precision estimates. *MNRAS*, 372 (4):1549–1574, Nov. 2006. doi: 10.1111/j.1365-2966.2006.10870.x.

Einstein, A. On the electrodynamics of moving bodies. *Annalen Phys.*, 17:891–921, 1905. doi: 10.1002/andp.200590006.

Einstein, A. Zur allgemeinen Relativitätstheorie. *Sitzungsberichte der Königlich Preussischen Akademie der Wissenschaften*, pages 778–786, Jan. 1915.

Einstein@Home. `https://einsteinathome.org/`, 2005.

Ellis, J., Fairbairn, M., Hütsi, G. et al. Prospects for future binary black hole gravitational wave studies in light of PTA measurements. *A&A*, 676:A38, Aug. 2023. doi: 10.1051/0004-6361/202346268.

Ellis, J.A., Vallisneri, M., Taylor, S.R. et al. Enterprise: Enhanced numerical toolbox enabling a robust pulsar inference suite. Zenodo, Sept. 2020. URL `https://doi.org/10.5281/zenodo.4059815`.

EPTA Collaboration and InPTA Collaboration, Antoniadis, J., Arumugam, P. et al. The second data release from the european pulsar timing array - iii. search for gravitational wave signals. *A&A*, 678:A50, 2023. doi: 10.1051/0004-6361/202346844. URL `https://doi.org/10.1051/0004-6361/202346844`.

Espinoza, C.M., Guillemot, L., Çelik, Ö. et al. Six millisecond pulsars detected by the Fermi Large Area Telescope and the radio/gamma-ray connection of millisecond pulsars. *MNRAS*, 430:571–587, Mar. 2013. doi: 10.1093/mnras/sts657.

Evans, M., Adhikari, R.X., Afle, C. et al. A Horizon Study for Cosmic Explorer: Science, Observatories, and Community. *arXiv e-prints*, art. arXiv:2109.09882, Sept. 2021. doi: 10.48550/arXiv.2109.09882.

Ferdman, R.D., Stairs, I.H., Kramer, M. et al. PSR J1756-2251: a pulsar with a low-mass neutron star companion. *MNRAS*, 443:2183–2196, Sept. 2014. doi: 10.1093/mnras/stu1223.

Fonseca, E., Stairs, I.H. and Thorsett, S.E. A Comprehensive Study of Relativistic Gravity Using PSR B1534+12. *ApJ*, 787:82, May 2014. doi: 10.1088/0004-637X/787/1/82.

Fonseca, E., Cromartie, H.T., Pennucci, T.T. et al. Refined Mass and Geometric Measurements of the High-mass PSR J0740+6620. *ApJL*, 915(1):L12, July 2021. doi: 10.3847/2041-8213/ac03b8.

Freire, P.C.C., Wex, N., Esposito-Farèse, G. et al. The relativistic pulsar-white dwarf binary PSR J1738+0333 - II. The most stringent test of scalar-tensor

gravity. *MNRAS*, 423:3328–3343, July 2012. doi: 10.1111/j.1365-2966.2012. 21253.x.

Friedman, J.L. and Morsink, S.M. Axial Instability of Rotating Relativistic Stars. *ApJ*, 502(2):714–720, Aug. 1998. doi: 10.1086/305920.

Ganapathy, D., Jia, W., Nakano, M. et al. Broadband Quantum Enhancement of the LIGO Detectors with Frequency-Dependent Squeezing. *Physical Review X*, 13(4):041021, Oct. 2023. doi: 10.1103/PhysRevX.13.041021.

Gancio, G., Lousto, C.O., Combi, L. et al. Upgraded antennas for pulsar observations in the Argentine Institute of Radio astronomy. *A&A*, 633:A84, Jan. 2020. doi: 10.1051/0004-6361/201936525.

Gendreau, K.C., Arzoumanian, Z. and Okajima, T. The Neutron star Interior Composition ExploreR (NICER): an Explorer mission of opportunity for soft x-ray timing spectroscopy. In Takahashi, T., Murray, S.S. and den Herder, J.W.A., editors, *Space Telescopes and Instrumentation 2012: Ultraviolet to Gamma Ray*, volume 8443 of *Society of Photo-Optical Instrumentation Engineers (SPIE) Conference Series*, page 844313, Sept. 2012. doi: 10.1117/12.926396.

Gendreau, K.C., Arzoumanian, Z., Adkins, P.W. et al. The Neutron star Interior Composition Explorer (NICER): design and development. In den Herder, J.W.A., Takahashi, T. and Bautz, M., editors, *Space Telescopes and Instrumentation 2016: Ultraviolet to Gamma Ray*, volume 9905 of *Society of Photo-Optical Instrumentation Engineers (SPIE) Conference Series*, page 99051H, July 2016. doi: 10.1117/12.2231304.

Gittins, F. Gravitational waves from neutron-star mountains. *Classical and Quantum Gravity*, 41(4):043001, Feb. 2024. doi: 10.1088/1361-6382/ad1c35.

Gittins, F. and Andersson, N. Modelling neutron star mountains in relativity. *MNRAS*, 507(1):116–128, Oct. 2021a. doi: 10.1093/mnras/stab2048.

Gittins, F. and Andersson, N. Modelling neutron star mountains in relativity. *MNRAS*, 507(1):116–128, Oct. 2021b. doi: 10.1093/mnras/stab2048.

Glampedakis, K. and Gualtieri, L. *Gravitational Waves from Single Neutron Stars: An Advanced Detector Era Survey*, volume 457, page 673. 2018. doi: 10.1007/978-3-319-97616-7_12.

Goldreich, P. and Julian, W.H. Pulsar Electrodynamics. *ApJ*, 157:869, Aug. 1969. doi: 10.1086/150119.

Goldstein, A., Veres, P., Burns, E. et al. An Ordinary Short Gamma-Ray Burst with Extraordinary Implications: Fermi-GBM Detection of GRB 170817A. *ApJL*, 848(2):L14, Oct. 2017. doi: 10.3847/2041-8213/aa8f41.

Goncharov, B., 2021. URL `https://github.com/bvgoncharov/enterprise_warp`.

Goncharov, B., Thrane, E., Shannon, R.M. et al. Consistency of the Parkes Pulsar Timing Array Signal with a Nanohertz Gravitational-wave Background. *ApJL*, 932(2):L22, June 2022. doi: 10.3847/2041-8213/ac76bb.

Goncharov, B., Zic, A., Reardon, D. et al. mattpitkin/enterprise_warp: Braking index sampling, Aug. 2024. URL `https://doi.org/10.5281/zenodo.13274448`.

Gotthelf, E.V., Halpern, J.P., Terrier, R. et al. Discovery of an Energetic 38.5 ms Pulsar Powering the Gamma-ray Source IGR J18490-0000/HESS J1849-000. *ApJL*, 729:L16, Mar. 2011. doi: 10.1088/2041-8205/729/2/L16.

Graham, P.W., Hogan, J.M., Kasevich, M.A. et al. Resonant mode for gravitational wave detectors based on atom interferometry. *PhRvD*, 94(10):104022, Nov. 2016. doi: 10.1103/PhysRevD.94.104022.

Grainge, K., Alachkar, B., Amy, S. et al. Square Kilometre Array: The radio telescope of the XXI century. *Astronomy Reports*, 61(4):288–296, Apr. 2017. doi: 10.1134/S1063772917040059.

Green, D.A., Gull, S.F., Tan, S.M. et al. G 11.2-0.3, an evolved Cassiopeia A. *MNRAS*, 231:735–738, Apr. 1988. doi: 10.1093/mnras/231.3.735.

Guillemot, L., Smith, D.A., Laffon, H. et al. The gamma-ray millisecond pulsar deathline, revisited. New velocity and distance measurements. *A&A*, 587:A109, Mar. 2016. doi: 10.1051/0004-6361/201527847.

Guo, Y.J., Freire, P.C.C., Guillemot, L. et al. PSR J2222−0137. I. Improved physical parameters for the system. *A&A*, 654:A16, Oct. 2021. doi: 10.1051/0004-6361/202141450.

Gupta, I., Afle, C., Arun, K.G. et al. Characterizing gravitational wave detector networks: from A¡inline-formula¿ ¡/inline-formula¿ to cosmic explorer. *Classical and Quantum Gravity*, 41(24):245001, Dec. 2024. doi: 10.1088/1361-6382/ad7b99.

H. E. S. S. Collaboration, Abdalla, H., Abramowski, A. et al. The population of TeV pulsar wind nebulae in the H.E.S.S. Galactic Plane Survey. *A&A*, 612: A2, Apr. 2018. doi: 10.1051/0004-6361/201629377.

Hall, E.D., Kuns, K., Smith, J.R. et al. Gravitational-wave physics with Cosmic Explorer: Limits to low-frequency sensitivity. *PhRvD*, 103(12):122004, June 2021. doi: 10.1103/PhysRevD.103.122004.

Halpern, J.P., Gotthelf, E.V., Leighly, K.M. et al. A Possible X-Ray and Radio Counterpart of the High-Energy Gamma-Ray Source 3EG J2227+6122. *ApJ*, 547:323–333, Jan. 2001. doi: 10.1086/318361.

Halpern, J.P., Bogdanov, S. and Gotthelf, E.V. X-Ray Measurement of the Spindown of Calvera: A Radio- and Gamma-Ray-Quiet Pulsar. *ApJ*, 778:120, Dec. 2013. doi: 10.1088/0004-637X/778/2/120.

Hamil, O., Stone, J.R., Urbanec, M. et al. Braking index of isolated pulsars. *Physical Review D*, 91(6), Mar 2015. ISSN 1550-2368. doi: 10.1103/physrevd.91.063007. URL http://dx.doi.org/10.1103/PhysRevD.91.063007.

Harris, W.E. A New Catalog of Globular Clusters in the Milky Way. *arXiv:1012.3224*, Dec. 2010.

Harry, G.M., Gretarsson, A.M., Saulson, P.R. et al. Thermal noise in interferometric gravitational wave detectors due to dielectric optical coatings. *Classical and Quantum Gravity*, 19(5):897–917, Mar. 2002. doi: 10.1088/0264-9381/19/5/305.

Harry, G.M., Fritschel, P., Shaddock, D.A. et al. Laser interferometry for the Big Bang Observer. *Classical and Quantum Gravity*, 23(15):4887–4894, Aug. 2006. doi: 10.1088/0264-9381/23/15/008.

Haskell, B. R-modes in neutron stars: Theory and observations. *International Journal of Modern Physics E*, 24(9):1541007, Aug. 2015. doi: 10.1142/S0218301315410074.

Heger, A., Fryer, C.L., Woosley, S.E. et al. How Massive Single Stars End Their Life. *ApJ*, 591(1):288–300, July 2003. doi: 10.1086/375341.

Hellings, R.W. and Downs, G.S. Upper limits on the isotropic gravitational radiation background from pulsar timing analysis. *ApJL*, 265:L39–L42, Feb. 1983. doi: 10.1086/183954.

Hessels, J.W.T., Ransom, S.M., Stairs, I.H. et al. A Radio Pulsar Spinning at 716 Hz. *Science*, 311(5769):1901–1904, Mar. 2006. doi: 10.1126/science.1123430.

Hewish, A., Bell, S.J., Pilkington, J.D.H. et al. Observation of a Rapidly Pulsating Radio Source. *Nature*, 217(5130):709–713, Feb. 1968. doi: 10.1038/217709a0.

Hewitt, A.L., Pitkin, M. and Hook, I.M. Recovering Pulsar Braking Index from a Population of Millisecond Pulsars. *ApJ*, 985(1):79, May 2025. doi: 10.3847/1538-4357/adc683.

Hobbs, G., Lyne, A.G., Kramer, M. et al. Long-term timing observations of 374 pulsars. *MNRAS*, 353(4):1311–1344, Oct. 2004. doi: 10.1111/j.1365-2966.2004.08157.x.

Hobbs, G., Edwards, R. and Manchester, R. TEMPO2: a New Pulsar Timing Package. *Chinese Journal of Astronomy and Astrophysics Supplement*, 6(S2):189–192, Dec. 2006a.

Hobbs, G., Jenet, F., Lee, K.J. et al. TEMPO2: a new pulsar timing package - III. Gravitational wave simulation. *MNRAS*, 394(4):1945–1955, Apr. 2009. doi: 10.1111/j.1365-2966.2009.14391.x.

Hobbs, G.B., Edwards, R.T. and Manchester, R.N. TEMPO2, a new pulsar-timing package - I. An overview. *MNRAS*, 369:655–672, June 2006b. doi: 10.1111/j.1365-2966.2006.10302.x.

Hu, W.R. and Wu, Y.L. The taiji program in space for gravitational wave physics and the nature of gravity. *National Science Review*, 4(5):685–686, 10 2017. ISSN 2095-5138. doi: 10.1093/nsr/nwx116. URL https://doi.org/10.1093/nsr/nwx116.

Iglewicz, B. and Hoaglin, D. *How to Detect and Handle Outliers.* ASQC basic references in quality control. ASQC Quality Press, 1993. ISBN 9780873892476. URL https://books.google.co.uk/books?id=siInAQAAIAAJ.

Isi, M., Pitkin, M. and Weinstein, A.J. Probing dynamical gravity with the polarization of continuous gravitational waves. *PhRvD*, 96(4):042001, Aug. 2017. doi: 10.1103/PhysRevD.96.042001.

Jankowski, F., Bailes, M., van Straten, W. et al. The UTMOST pulsar timing programme I: Overview and first results. *MNRAS*, 484(3):3691–3712, Apr. 2019. doi: 10.1093/mnras/sty3390.

Jaranowski, P. and Królak, A. Searching for gravitational waves from known pulsars using the {\cal F} and {\cal G} statistics. *CQGra*, 27(19):194015, Oct. 2010. doi: 10.1088/0264-9381/27/19/194015.

Jaranowski, P., Królak, A. and Schutz, B.F. Data analysis of gravitational-wave signals from spinning neutron stars: The signal and its detection. *PhRvD*, 58 (6):063001, Sept. 1998. doi: 10.1103/PhysRevD.58.063001.

Jiang, L., Zhang, C.M., Tanni, A. et al. Characteristic Age and True Age of Pulsars. In *International Journal of Modern Physics Conference Series*, volume 23 of *International Journal of Modern Physics Conference Series*, pages 95–98, Jan. 2013. doi: 10.1142/S2010194513011124.

Jin, S.J., Zhang, Y.Z., Song, J.Y. et al. Taiji-TianQin-LISA network: Precisely measuring the Hubble constant using both bright and dark sirens. *Science China Physics, Mechanics, and Astronomy*, 67(2):220412, Feb. 2024. doi: 10. 1007/s11433-023-2276-1.

Johnson-McDaniel, N.K. Gravitational wave constraints on the shape of neutron stars. *PhRvD*, 88(4):044016, Aug. 2013. doi: 10.1103/PhysRevD.88.044016.

Jones, D.I. Is timing noise important in the gravitational wave detection of neutron stars? *PhRvD*, 70(4):042002, Aug. 2004. doi: 10.1103/PhysRevD.70. 042002.

Jones, D.I. Gravitational wave emission from rotating superfluid neutron stars. *MNRAS*, 402:2503–2519, Mar. 2010. doi: 10.1111/j.1365-2966.2009.16059.x.

Kalogera, V. and Baym, G. The Maximum Mass of a Neutron Star. *ApJL*, 470: L61, Oct. 1996. doi: 10.1086/310296.

Karki, S., Tuyenbayev, D., Kandhasamy, S. et al. The Advanced LIGO photon calibrators. *Review of Scientific Instruments*, 87(11):114503, 11 2016. ISSN 0034-6748. doi: 10.1063/1.4967303. URL https://doi.org/10.1063/ 1.4967303.

Kim, V., Umirbayeva, A. and Aimuratov, Y. Estimates of the Surface Magnetic Field Strength of Radio Pulsars. *Universe*, 9(7):334, July 2023. doi: 10.3390/ universe9070334.

Kirichenko, A., Danilenko, A., Shternin, P. et al. Optical Observations of Psr J2021+3651 in the Dragonfly Nebula With the GTC. *ApJ*, 802(1):17, Mar. 2015. doi: 10.1088/0004-637X/802/1/17.

Kozai, Y. and TAMA-300 Team. Laser Interferometer for Detection of Gravitational Wave-TAMA-300 (I). In Chen, P.S., editor, *Observational Astrophysics in Asia and its Future*, volume 4, page 35, Jan. 1999.

Kramer, M., Stairs, I.H., Manchester, R.N. et al. Strong-Field Gravity Tests with the Double Pulsar. *Physical Review X*, 11(4):041050, Oct. 2021. doi: 10.1103/PhysRevX.11.041050.

Krishnan, B., Sintes, A.M., Papa, M.A. et al. Hough transform search for continuous gravitational waves. *PhRvD*, 70(8):082001, Oct. 2004. doi: 10.1103/PhysRevD.70.082001.

Lam, M.T. Optimizing Pulsar Timing Array Observational Cadences for Sensitivity to Low-frequency Gravitational-wave Sources. *ApJ*, 868(1):33, Nov. 2018. doi: 10.3847/1538-4357/aae533.

Leaci, P., LIGO Scientific Collaboration and Virgo Collaboration. Searching for continuous gravitational wave signals using LIGO and Virgo detectors. In *Journal of Physics Conference Series*, volume 354 of *Journal of Physics Conference Series*, page 012010. IOP, Mar. 2012. doi: 10.1088/1742-6596/354/1/012010.

Lewicki, M. and Vaskonen, V. Impact of LIGO-Virgo black hole binaries on gravitational wave background searches. *arXiv e-prints*, art. arXiv:2111.05847, Nov. 2021. doi: 10.48550/arXiv.2111.05847.

Lewis, D.R., Dodson, R.G., Ramsdale, P.D. et al. Pulsar Observations at Mt. Pleasant. In Bailes, M., Nice, D.J. and Thorsett, S.E., editors, *Radio Pulsars*, volume 302 of *Astronomical Society of the Pacific Conference Series*, page 121, Jan. 2003. doi: 10.48550/arXiv.astro-ph/0211010.

LIGO Caltech. Ligo's interferometers, 2016. URL `https://www.ligo.caltech.edu/page/ligos-ifo`. Accessed: 26 March 2025.

LIGO Scientific Collaboration. LIGO Algorithm Library, 2018.

LIGO Scientific Collaboration. O3a lines and combs found in c00 data, Dec 2020. URL `https://dcc.ligo.org/T2000719/public`. Accessed: 26 March 2025.

LIGO Scientific Collaboration. Report of the lsc post-o5 study group. LIGO Document T2200287-v3, LIGO Document Control Center, 2024. URL `https://dcc.ligo.org/LIGO-T2200287/public`. Accessed: 23 April 2025.

Lin, L.C.C., Takata, J., Hwang, C.Y. et al. The X-ray properties of the energetic pulsar PSR J1838-0655. *MNRAS*, 400(1):168–175, Nov. 2009. doi: 10.1111/j.1365-2966.2009.15468.x.

Lin, R., van Kerkwijk, M.H., Kirsten, F. et al. The Radio Parallax of the Crab Pulsar: A First VLBI Measurement Calibrated with Giant Pulses. *ApJ*, 952 (2):161, Aug. 2023. doi: 10.3847/1538-4357/acdc98.

Lindblom, L. and Owen, B.J. Directed searches for continuous gravitational waves from twelve supernova remnants in data from Advanced LIGO's second observing run. *PhRvD*, 101(8):083023, Apr. 2020. doi: 10.1103/PhysRevD.101. 083023.

Link, B. and Epstein, R.I. Thermally Driven Neutron Star Glitches. *ApJ*, 457: 844, Feb. 1996. doi: 10.1086/176779.

Liu, K., Verbiest, J.P.W., Kramer, M. et al. Prospects for high-precision pulsar timing. *MNRAS*, 417(4):2916–2926, Nov. 2011. doi: 10.1111/j.1365-2966.2011. 19452.x.

Liu, Q.C., Zhong, W.J., Chen, Y. et al. Discovery and timing of pulsar J2016+3711 in supernova remnant CTB 87 with FAST. *MNRAS*, 528(4):6761– 6767, Mar. 2024. doi: 10.1093/mnras/stae351.

Liu, X.J., Keith, M.J., Bassa, C.G. et al. Correlated timing noise and high-precision pulsar timing: measuring frequency second derivatives as an example. *MNRAS*, 488(2):2190–2201, Sept. 2019. doi: 10.1093/mnras/stz1801.

Liu, Y. and Zou, Y.C. Directed search for continuous gravitational waves from the possible kilonova remnant G 4.8 +6.2. *PhRvD*, 106(12):123024, Dec. 2022. doi: 10.1103/PhysRevD.106.123024.

Lorimer, D.R., Kawash, A.M., Freire, P.C.C. et al. Timing observations of three Galactic millisecond pulsars. *MNRAS*, 507(4):5303–5309, Nov. 2021. doi: 10. 1093/mnras/stab2474.

Lower, M.E., Bailes, M., Shannon, R.M. et al. Detection of a Glitch in PSR J0908-4913 by UTMOST. *RNAAS*, 3(12):192, Dec. 2019. doi: 10.3847/2515-5172/ ab621d.

Lower, M.E., Bailes, M., Shannon, R.M. et al. The UTMOST pulsar timing programme - II. Timing noise across the pulsar population. *MNRAS*, 494(1): 228–245, May 2020. doi: 10.1093/mnras/staa615.

Lower, M.E., Johnston, S., Dunn, L. et al. The impact of glitches on young pulsar rotational evolution. *MNRAS*, 508(3):3251–3274, Dec. 2021. doi: 10. 1093/mnras/stab2678.

Lueck, H. The upgrade of GEO 600. *arXiv e-prints*, art. arXiv:1004.0338, Apr. 2010. doi: 10.48550/arXiv.1004.0338.

Luo, J., Chen, L.S., Duan, H.Z. et al. TianQin: a space-borne gravitational wave detector. *Classical and Quantum Gravity*, 33(3):035010, Feb. 2016. doi: 10.1088/0264-9381/33/3/035010.

Luo, J., Ransom, S., Demorest, P. et al. PINT: High-precision pulsar timing analysis package. Astrophysics Source Code Library, record ascl:1902.007, Feb. 2019.

Luo, J., Ransom, S., Demorest, P. et al. PINT: A Modern Software Package for Pulsar Timing. *ApJ*, 911(1):45, Apr. 2021. doi: 10.3847/1538-4357/abe62f.

LVK. Ligo, virgo and kagra observing run plans, Jan 2025. URL `https:// observing.docs.ligo.org/plan/`.

Manchester, R.N. Pulsar glitches and their impact on neutron-star astrophysics. *arXiv e-prints*, art. arXiv:1801.04332, Jan. 2018. doi: 10.48550/arXiv.1801. 04332.

Matichard, F., Lantz, B., Mittleman, R. et al. Seismic isolation of Advanced LIGO: Review of strategy, instrumentation and performance. *Classical and Quantum Gravity*, 32(18):185003, Sept. 2015. doi: 10.1088/0264-9381/32/18/ 185003.

Matthews, A.M., Nice, D.J., Fonseca, E. et al. The NANOGrav Nine-year Data Set: Astrometric Measurements of 37 Millisecond Pulsars. *ApJ*, 818(1):92, Feb. 2016. doi: 10.3847/0004-637X/818/1/92.

McKee, J.W., Janssen, G.H., Stappers, B.W. et al. A glitch in the millisecond pulsar J0613-0200. *MNRAS*, 461(3):2809–2817, Sept. 2016. doi: 10.1093/mnras/stw1442.

McWilliams, S.T., Ostriker, J.P. and Pretorius, F. Gravitational Waves and Stalled Satellites from Massive Galaxy Mergers at z ¡= 1. *ApJ*, 789(2):156, July 2014. doi: 10.1088/0004-637X/789/2/156.

Mereghetti, S., Rigoselli, M., Taverna, R. et al. NICER Study of Pulsed Thermal X-Rays from Calvera: A Neutron Star Born in the Galactic Halo? *ApJ*, 922 (2):253, Dec. 2021. doi: 10.3847/1538-4357/ac34f2.

Miller, M.C., Lamb, F.K., Dittmann, A.J. et al. PSR J0030+0451 Mass and Radius from NICER Data and Implications for the Properties of Neutron Star Matter. *ApJL*, 887(1):L24, Dec. 2019. doi: 10.3847/2041-8213/ab50c5.

Miller, M.C., Lamb, F.K., Dittmann, A.J. et al. The Radius of PSR J0740+6620 from NICER and XMM-Newton Data. *ApJL*, 918(2):L28, Sept. 2021. doi: 10.3847/2041-8213/ac089b.

Mirasola, L., Leaci, P., Astone, P. et al. A new semi-coherent targeted search for continuous gravitational waves from pulsars in binary systems. *arXiv e-prints*, art. arXiv:2404.03721, Apr. 2024. doi: 10.48550/arXiv.2404.03721.

Mukherjee, D., Bult, P., van der Klis, M. et al. The magnetic-field strengths of accreting millisecond pulsars. *MNRAS*, 452(4):3994–4012, Oct. 2015. doi: 10.1093/mnras/stv1542.

Negueruela, I., Ribó, M., Herrero, A. et al. Astrophysical Parameters of LS 2883 and Implications for the PSR B1259-63 Gamma-ray Binary. *ApJL*, 732(1):L11, May 2011. doi: 10.1088/2041-8205/732/1/L11.

Newton, I. *Philosophiae Naturalis Principia Mathematica.* 1687. doi: 10.3931/e-rara-440.

Ng, C.Y. and Romani, R.W. Fitting Pulsar Wind Tori. *ApJ*, 601:479–484, Jan. 2004. doi: 10.1086/380486.

Ng, C.Y. and Romani, R.W. Fitting Pulsar Wind Tori. II. Error Analysis and Applications. *ApJ*, 673:411–417, Jan. 2008. doi: 10.1086/523935.

Nice, D., Demorest, P., Stairs, I. et al. Tempo: Pulsar timing data analysis. Astrophysics Source Code Library, record ascl:1509.002, Sept. 2015.

Nieder, L., Clark, C.J., Bassa, C.G. et al. Detection and Timing of Gamma-Ray Pulsations from the 707 Hz Pulsar J0952-0607. *ApJ*, 883(1):42, Sept. 2019. doi: 10.3847/1538-4357/ab357e.

Nieder, L., Clark, C.J., Kandel, D. et al. Discovery of a Gamma-Ray Black Widow Pulsar by GPU-accelerated Einstein@Home. *ApJL*, 902(2):L46, Oct. 2020. doi: 10.3847/2041-8213/abbc02.

Nuttall, L.K., Massinger, T.J., Areeda, J. et al. Improving the data quality of Advanced LIGO based on early engineering run results. *Classical and Quantum Gravity*, 32(24):245005, Dec. 2015. doi: 10.1088/0264-9381/32/24/245005.

Ostriker, J.P. and Gunn, J.E. On the Nature of Pulsars. I. Theory. *ApJ*, 157:1395, Sept. 1969. doi: 10.1086/150160.

Owen, B.J. Maximum Elastic Deformations of Compact Stars with Exotic Equations of State. *Physical Review Letters*, 95(21):211101, Nov. 2005. doi: 10.1103/PhysRevLett.95.211101.

Palomba, C. Pulsars ellipticity revised. *A&A*, 354:163–168, Feb. 2000.

Palomba, C. Simulation of a population of isolated neutron stars evolving through the emission of gravitational waves. *MNRAS*, 359(3):1150–1164, May 2005. doi: 10.1111/j.1365-2966.2005.08975.x.

Papa, M.A., Ming, J., Gotthelf, E.V. et al. Search for Continuous Gravitational Waves from the Central Compact Objects in Supernova Remnants Cassiopeia A, Vela Jr., and G347.3-0.5. *ApJ*, 897(1):22, July 2020. doi: 10.3847/1538-4357/ab92a6.

Parthasarathy, A., Johnston, S., Shannon, R.M. et al. Timing of young radio pulsars - II. Braking indices and their interpretation. *MNRAS*, 494(2):2012–2026, May 2020. doi: 10.1093/mnras/staa882.

Parthasarathy, A., Bailes, M., Shannon, R.M. et al. Measurements of pulse jitter and single-pulse variability in millisecond pulsars using MeerKAT. *MNRAS*, 502(1):407–422, Mar. 2021. doi: 10.1093/mnras/stab037.

Perera, B.B.P., DeCesar, M.E., Demorest, P.B. et al. The International Pulsar Timing Array: second data release. *MNRAS*, 490(4):4666–4687, Dec. 2019. doi: 10.1093/mnras/stz2857.

Perrodin, D., Jenet, F., Lommen, A. et al. Timing Noise Analysis of NANOGrav Pulsars. *arXiv e-prints*, art. arXiv:1311.3693, Nov. 2013.

Piccinni, O.J., Astone, P., D'Antonio, S. et al. Directed search for continuous gravitational-wave signals from the Galactic Center in the Advanced LIGO second observing run. *PhRvD*, 101(8):082004, Apr. 2020. doi: 10.1103/PhysRevD.101.082004.

Pitkin, M. Prospects of observing continuous gravitational waves from known pulsars. *MNRAS*, 415(2):1849–1863, Aug. 2011. doi: 10.1111/j.1365-2966.2011.18818.x.

Pitkin, M. Cwinpy: A python package for inference with continuous gravitational-wave signals from pulsars. *Journal of Open Source Software*, 7(77):4568, 2022. doi: 10.21105/joss.04568. URL `https://doi.org/10.21105/joss.04568`.

Pitkin, M. and Woan, G. Binary system delays and timing noise in searches for gravitational waves from known pulsars. *PhRvD*, 76(4):042006, Aug. 2007. doi: 10.1103/PhysRevD.76.042006.

Pitkin, M., Gill, C., Jones, D.I. et al. First results and future prospects for dual-harmonic searches for gravitational waves from spinning neutron stars. *MNRAS*, 453:4399–4420, Nov. 2015. doi: 10.1093/mnras/stv1931.

Pitkin, M., Isi, M., Veitch, J. et al. A nested sampling code for targeted searches for continuous gravitational waves from pulsars. *arXiv:1705.08978v1*, May 2017.

Pitkin, M., Messenger, C. and Fan, X. Hierarchical Bayesian method for detecting continuous gravitational waves from an ensemble of pulsars. *PhRvD*, 98(6): 063001, Sept. 2018. doi: 10.1103/PhysRevD.98.063001.

Pizzochero, P.M., Antonelli, M., Haskell, B. et al. Constraints on pulsar masses from the maximum observed glitch. *Nature Astronomy*, 1:0134, July 2017. doi: 10.1038/s41550-017-0134.

Pol, N.S., Taylor, S.R., Kelley, L.Z. et al. Astrophysics Milestones for Pulsar Timing Array Gravitational-wave Detection. *ApJL*, 911(2):L34, Apr. 2021. doi: 10.3847/2041-8213/abf2c9.

Ransom, S. PRESTO: PulsaR Exploration and Search TOolkit. Astrophysics Source Code Library, record ascl:1107.017, July 2011.

Reardon, D.J., Hobbs, G., Coles, W. et al. Timing analysis for 20 millisecond pulsars in the Parkes Pulsar Timing Array. *MNRAS*, 455:1751–1769, Jan. 2016. doi: 10.1093/mnras/stv2395.

Reardon, D.J., Shannon, R.M., Cameron, A.D. et al. The Parkes pulsar timing array second data release: timing analysis. *MNRAS*, 507(2):2137–2153, Oct. 2021. doi: 10.1093/mnras/stab1990.

Reardon, D.J., Zic, A., Shannon, R.M. et al. Search for an Isotropic Gravitational-wave Background with the Parkes Pulsar Timing Array. *ApJL*, 951(1):L6, July 2023. doi: 10.3847/2041-8213/acdd02.

Reardon, D.J., Zic, A., Shannon, R.M. et al. Search for an isotropic gravitational-wave background with the parkes pulsar timing array. *The Astrophysical Journal Letters*, 951(1):L6, jun 2023. doi: 10.3847/2041-8213/acdd02. URL https://dx.doi.org/10.3847/2041-8213/acdd02.

Reardon, D.J., Bailes, M., Shannon, R.M. et al. The Neutron Star Mass, Distance, and Inclination from Precision Timing of the Brilliant Millisecond Pulsar J0437-4715. *ApJL*, 971(1):L18, Aug. 2024. doi: 10.3847/2041-8213/ad614a.

Reitze, D., LIGO Laboratory: California Institute of Technology, LIGO Laboratory: Massachusetts Institute of Technology et al. The US Program in Ground-Based Gravitational Wave Science: Contribution from the LIGO Laboratory. *BAAS*, 51(3):141, May 2019. doi: 10.48550/arXiv.1903.04615.

Reynolds, C. Observational constraints on black hole spin. In *43rd COSPAR Scientific Assembly. Held 28 January - 4 February*, volume 43, page 1412, Jan. 2021.

Reynoso, E.M., Johnston, S., Green, A.J. et al. High-resolution HI and radio continuum observations of the SNR G290.1-0.8. *MNRAS*, 369(1):416–424, June 2006. doi: 10.1111/j.1365-2966.2006.10325.x.

Riles, K. Recent searches for continuous gravitational waves. *MLPA*, 32(39): 1730035-685, Dec. 2017. doi: 10.1142/S021773231730035X.

Riles, K. Searches for continuous-wave gravitational radiation. *Living Reviews in Relativity*, 26(1):3, Dec. 2023. doi: 10.1007/s41114-023-00044-3.

Riley, T.E., Watts, A.L., Bogdanov, S. et al. A NICER View of PSR J0030+0451: Millisecond Pulsar Parameter Estimation. *ApJL*, 887(1):L21, Dec. 2019. doi: 10.3847/2041-8213/ab481c.

Riley, T.E., Watts, A.L., Ray, P.S. et al. A NICER View of the Massive Pulsar PSR J0740+6620 Informed by Radio Timing and XMM-Newton Spectroscopy. *ApJL*, 918(2):L27, Sept. 2021. doi: 10.3847/2041-8213/ac0a81.

Roberts, D.A., Goss, W.M., Kalberla, P.M.W. et al. High resolution HI observations of 3C 58. *A&A*, 274:427–438, July 1993.

Rodríguez Concepción, A.E. and Quintero Angulo, G. Constraints on Bose-Einstein condensate stars as neutron stars models from new observational data. *Astronomische Nachrichten*, 345:e20240009, Feb. 2024. doi: 10.1002/asna.20240009.

Romano, J.D., Hazboun, J.S., Siemens, X. et al. Common-spectrum process versus cross-correlation for gravitational-wave searches using pulsar timing arrays. *PhRvD*, 103(6):063027, Mar. 2021. doi: 10.1103/PhysRevD.103.063027.

Romero-Shaw, I.M., Talbot, C., Biscoveanu, S. et al. Bayesian inference for compact binary coalescences with BILBY: validation and application to the first LIGO-Virgo gravitational-wave transient catalogue. *MNRAS*, 499(3):3295–3319, Dec. 2020. doi: 10.1093/mnras/staa2850.

Rowlinson, S., Dmitriev, A., Jones, A.W. et al. Feasibility study of beam-expanding telescopes in the interferometer arms for the Einstein Telescope. *PhRvD*, 103(2):023004, Jan. 2021. doi: 10.1103/PhysRevD.103.023004.

Saleem, M., Rana, J., Gayathri, V. et al. The science case for LIGO-India. *Classical and Quantum Gravity*, 39(2):025004, Jan. 2022. doi: 10.1088/1361-6382/ac3b99.

Salmi, T., Vinciguerra, S., Choudhury, D. et al. The Radius of PSR J0740+6620 from NICER with NICER Background Estimates. *ApJ*, 941(2):150, Dec. 2022. doi: 10.3847/1538-4357/ac983d.

Savchenko, V., Ferrigno, C., Kuulkers, E. et al. INTEGRAL Detection of the First Prompt Gamma-Ray Signal Coincident with the Gravitational-wave Event GW170817. *ApJL*, 848(2):L15, Oct. 2017. doi: 10.3847/2041-8213/aa8f94.

Schutz, B. *A First Course in General Relativity*. 2009.

Shamohammadi, M., Bailes, M., Flynn, C. et al. MeerKAT Pulsar Timing Array parallaxes and proper motions. *MNRAS*, 530(1):287–306, May 2024. doi: 10.1093/mnras/stae016.

Shapiro, S.L. and Teukolsky, S.A. *Black holes, white dwarfs and neutron stars. The physics of compact objects*. 1983. doi: 10.1002/9783527617661.

Shaw, B., Keith, M.J., Lyne, A.G. et al. The slow rise and recovery of the 2019 Crab pulsar glitch. *MNRAS*, 505(1):L6–L10, July 2021. doi: 10.1093/mnrasl/slab038.

Shklovskii, I.S. Possible Causes of the Secular Increase in Pulsar Periods. *Soviet Ast.*, 13:562, Feb. 1970.

Singh, A., Papa, M.A. and Dergachev, V. Characterizing the sensitivity of isolated continuous gravitational wave searches to binary orbits. *PhRvD*, 100(2): 024058, July 2019. doi: 10.1103/PhysRevD.100.024058.

Skilling, J. Nested Sampling. In Fischer, R., Preuss, R. and Toussaint, U.V., editors, *Bayesian Inference and Maximum Entropy Methods in Science and Engineering: 24th International Workshop on Bayesian Inference and Maximum Entropy Methods in Science and Engineering*, volume 735 of *American Institute of Physics Conference Series*, pages 395–405. AIP, Nov. 2004. doi: 10.1063/1.1835238.

Skilling, J. Nested sampling for general Bayesian computation. *Bayesian Analysis*, 1(4):833 – 859, 2006. doi: 10.1214/06-BA127. URL `https://doi.org/10.1214/06-BA127`.

Smits, R., Lorimer, D.R., Kramer, M. et al. Pulsar science with the Five hundred metre Aperture Spherical Telescope. *A&A*, 505(2):919–926, Oct. 2009. doi: 10.1051/0004-6361/200911939.

Smits, R., Tingay, S.J., Wex, N. et al. Prospects for accurate distance measurements of pulsars with the Square Kilometre Array: Enabling fundamental physics. *A&A*, 528:A108, Apr. 2011. doi: 10.1051/0004-6361/201016141.

Soni, K., Vijaykumar, A. and Mitra, S. Assessing the potential of LIGO-India in resolving the Hubble Tension. *arXiv e-prints*, art. arXiv:2409.11361, Sept. 2024. doi: 10.48550/arXiv.2409.11361.

Speagle, J.S. DYNESTY: a dynamic nested sampling package for estimating Bayesian posteriors and evidences. *MNRAS*, 493(3):3132–3158, Apr. 2020. doi: 10.1093/mnras/staa278.

Spiewak, R., Bailes, M., Barr, E.D. et al. PSR J2322-2650 - a low-luminosity millisecond pulsar with a planetary-mass companion. *MNRAS*, 475:469–477, Mar. 2018. doi: 10.1093/mnras/stx3157.

Stappers, B.W., Keane, E.F., Kramer, M. et al. The prospects of pulsar timing with new-generation radio telescopes and the Square Kilometre Array. *Philosophical Transactions of the Royal Society of London Series A*, 376(2120): 20170293, May 2018. doi: 10.1098/rsta.2017.0293.

Staubert, R., Trümper, J., Kendziorra, E. et al. Cyclotron lines in highly magnetized neutron stars. *A&A*, 622:A61, Feb. 2019. doi: 10.1051/0004-6361/201834479.

Steltner, B., Papa, M.A., Eggenstein, H.B. et al. Einstein@Home All-sky Search for Continuous Gravitational Waves in LIGO O2 Public Data. *ApJ*, 909(1):79, Mar. 2021. doi: 10.3847/1538-4357/abc7c9.

Steltner, B., Papa, M.A., Eggenstein, H.B. et al. Deep Einstein@Home All-sky Search for Continuous Gravitational Waves in LIGO O3 Public Data. *ApJ*, 952 (1):55, July 2023. doi: 10.3847/1538-4357/acdad4.

Storm, J., Carney, B.W., Gieren, W.P. et al. The effect of metallicity on the Cepheid Period-Luminosity relation from a Baade-Wesselink analysis of Cepheids in the Galaxy and in the Small Magellanic Cloud. *A&A*, 415:531–547, Feb. 2004. doi: 10.1051/0004-6361:20034634.

Sun, L., Goetz, E., Kissel, J.S. et al. Characterization of systematic error in Advanced LIGO calibration. *CQGra*, 37(22):225008, Nov. 2020. doi: 10.1088/1361-6382/abb14e.

Sun, L., Goetz, E., Kissel, J.S. et al. Characterization of systematic error in Advanced LIGO calibration in the second half of O3. *arXiv:2107.00129*, June 2021.

Svitil, K., Allen, K., Kupec, I. et al. Gravitational waves detected 100 years after einstein's prediction, Feb 2016. URL `https://www.ligo.caltech.edu/LA/news/ligo20160211`.

Swiggum, J.K., Kaplan, D.L., McLaughlin, M.A. et al. A Multiwavelength Study of Nearby Millisecond Pulsar PSR J1400-1431: Improved Astrometry and an

Optical Detection of Its Cool White Dwarf Companion. *ApJ*, 847(1):25, Sept. 2017. doi: 10.3847/1538-4357/aa8994.

Tanimoto, T., Bentz, W. and Cloët, I.C. Massive neutron stars with a color superconducting quark matter core. *PhRvC*, 101(5):055204, May 2020. doi: 10.1103/PhysRevC.101.055204.

Taylor, S.R., Baker, P.T., Hazboun, J.S. et al. enterprise_extensions, 2021. URL `https://github.com/nanograv/enterprise_extensions`. v2.4.3.

Taylor, S.R., Baker, P.T., Hazboun, J.S. et al. mattpitkin/enterprise_extensions: Keep float128 precision, Aug. 2024. URL `https://doi.org/10.5281/zenodo. 13274450`.

Tenorio, R., Keitel, D. and Sintes, A.M. Search methods for continuous gravitational-wave signals from unknown sources in the advanced-detector era. *Universe*, 7:474, 2021. doi: 10.3390/universe7120474.

Testa, V., Corsi, C.E., Andreuzzi, G. et al. Horizontal-Branch Morphology and Dense Environments: Hubble Space Telescope Observations of Globular Clusters NGC 2298, 5897, 6535, and 6626. *AJ*, 121(2):916–934, Feb. 2001. doi: 10.1086/318752.

The LIGO Scientific Collaboration, the Virgo Collaboration, the KAGRA Collaboration et al. GWTC-3: Compact Binary Coalescences Observed by LIGO and Virgo During the Second Part of the Third Observing Run. *arXiv e-prints*, art. arXiv:2111.03606, Nov. 2021.

The LIGO Scientific Collaboration, the Virgo Collaboration and the KAGRA Collaboration. Observation of Gravitational Waves from the Coalescence of a $2.5 - 4.5$ $M_\odot$ Compact Object and a Neutron Star. *arXiv e-prints*, art. arXiv:2404.04248, Apr. 2024. doi: 10.48550/arXiv.2404.04248.

Tiburzi, C., Hobbs, G., Kerr, M. et al. A study of spatial correlations in pulsar timing array data. *MNRAS*, 455(4):4339–4350, Feb. 2016. doi: 10.1093/mnras/ stv2143.

Torres, D.F., Viganò, D., Coti Zelati, F. et al. Synchrocurvature modelling of the multifrequency non-thermal emission of pulsars. *MNRAS*, 489(4):5494–5512, Nov. 2019. doi: 10.1093/mnras/stz2403.

Trimble, V. Motions and Structure of the Filamentary Envelope of the Crab Nebula. *AJ*, 73:535, Sept. 1968. doi: 10.1086/110658.

Tuyenbayev, D., Karki, S., Betzwieser, J. et al. Improving LIGO calibration accuracy by tracking and compensating for slow temporal variations. *Classical and Quantum Gravity*, 34(1):015002, Jan. 2017. doi: 10.1088/0264-9381/34/1/015002.

Ushomirsky, G., Cutler, C. and Bildsten, L. Deformations of accreting neutron star crusts and gravitational wave emission. *MNRAS*, 319(3):902–932, Dec. 2000. doi: 10.1046/j.1365-8711.2000.03938.x.

van der Swaluw, E. and Wu, Y. Inferring Initial Spin Periods for Neutron Stars in Composite Remnants. *ApJL*, 555(1):L49–L53, July 2001. doi: 10.1086/321733.

van Straten, W., Demorest, P. and Oslowski, S. Pulsar Data Analysis with PSRCHIVE. *Astronomical Research and Technology*, 9(3):237–256, July 2012. doi: 10.48550/arXiv.1205.6276.

Verbiest, J.P.W. and Lorimer, D.R. Why the distance of PSR J0218+4232 does not challenge pulsar emission theories. *MNRAS*, 444:1859–1861, Oct. 2014. doi: 10.1093/mnras/stu1560.

Verbiest, J.P.W., Bailes, M., van Straten, W. et al. Precision Timing of PSR J0437-4715: An Accurate Pulsar Distance, a High Pulsar Mass, and a Limit on the Variation of Newton's Gravitational Constant. *ApJ*, 679(1):675–680, May 2008. doi: 10.1086/529576.

Verbiest, J.P.W., Weisberg, J.M., Chael, A.A. et al. On Pulsar Distance Measurements and Their Uncertainties. *ApJ*, 755:39, Aug. 2012. doi: 10.1088/0004-637X/755/1/39.

Verma, P. Probing gravitational waves from pulsars in brans–dicke theory. *Universe*, 7:351–355, Jul 2021. doi: 10.3390/universe7070235. URL `https://www.mdpi.com/2218-1997/7/7/235`.

Viets, A. and Wade, M. Subtracting Narrow-band Noise from LIGO Strain Data in the Third Observing Run. *LIGO T2100058* `https://dcc.ligo.org/LIGO-T2100058/public`, 2021.

Viets, A.D., Wade, M., Urban, A.L. et al. Reconstructing the calibrated strain signal in the advanced ligo detectors. *Classical and Quantum Gravity*, 35(9): 095015, apr 2018. doi: 10.1088/1361-6382/aab658. URL `https://dx.doi.org/10.1088/1361-6382/aab658`.

Vigeland, S.J., Deller, A.T., Kaplan, D.L. et al. Reconciling Optical and Radio Observations of the Binary Millisecond Pulsar PSR J1640+2224. *ApJ*, 855: 122, Mar. 2018. doi: 10.3847/1538-4357/aaaa73.

Walker, A.R. The Large Magellanic Cloud and the distance scale. *Ap&SS*, 341 (1):43–49, Sept. 2012. doi: 10.1007/s10509-011-0961-x.

Wang, G., Ni, W.T., Han, W.B. et al. Alternative LISA-TAIJI networks. *PhRvD*, 104(2):024012, July 2021. doi: 10.1103/PhysRevD.104.024012.

Weisskopf, M.C., Brinkman, B., Canizares, C. et al. An Overview of the Performance and Scientific Results from the Chandra X-Ray Observatory. *PASP*, 114(791):1–24, Jan. 2002. doi: 10.1086/338108.

Woan, G., Pitkin, M.D., Haskell, B. et al. Evidence for a Minimum Ellipticity in Millisecond Pulsars. *ApJL*, 863(2):L40, Aug. 2018. doi: 10.3847/2041-8213/aad86a.

Xu, H., Chen, S., Guo, Y. et al. Searching for the nano-hertz stochastic gravitational wave background with the chinese pulsar timing array data release i. *Research in Astronomy and Astrophysics*, 23(7):075024, jun 2023. doi: 10.1088/1674-4527/acdfa5. URL `https://dx.doi.org/10.1088/1674-4527/acdfa5`.

Yamamoto, K., Uchiyama, T., Miyoki, S. et al. Current status of the CLIO project. In *Journal of Physics Conference Series*, volume 122 of *Journal of Physics Conference Series*, page 012002. IOP, July 2008. doi: 10.1088/1742-6596/122/1/012002.

Yao, J.M., Manchester, R.N. and Wang, N. A New Electron-density Model for Estimation of Pulsar and FRB Distances. *ApJ*, 835:29, Jan. 2017. doi: 10.3847/1538-4357/835/1/29.

You, X.P., Hobbs, G., Coles, W.A. et al. Dispersion measure variations and their effect on precision pulsar timing. *MNRAS*, 378(2):493–506, June 2007. doi: 10.1111/j.1365-2966.2007.11617.x.

Zachariou, N., Fegan, S., Watts, D. et al. Hyperons in neutron stars: studies of hyperon spectroscopy and the hyperon-nucleon interaction with the K-long Facility. *Philosophical Transactions of the Royal Society of London Series A*, 382(2275):20230124, July 2024. doi: 10.1098/rsta.2023.0124.

Zhang, C.M., Wang, J., Zhao, Y.H. et al. Study of measured pulsar masses and their possible conclusions. *A&A*, 527:A83, Mar. 2011. doi: 10.1051/0004-6361/201015532.

Zhou, S., Gügercinoğlu, E., Yuan, J. et al. Pulsar Glitches: A Review. *Universe*, 8(12):641, Dec. 2022. doi: 10.3390/universe8120641.

Zimmermann, M. and Szedenits, Jr., E. Gravitational waves from rotating and precessing rigid bodies - Simple models and applications to pulsars. *PhRvD*, 20:351–355, July 1979. doi: 10.1103/PhysRevD.20.351.